ABSTRACT

Title of Document: INVESTIGATION OF SWIRL DISTRIBUTED COMBUSTION WITH EXPERIMENTAL DIAGNOSTICS AND ARTIFICIAL INTELLIGENCE APPROACH

Rishi Roy, PhD, 2022

Directed By: Dr. Ashwani K. Gupta
Distinguished University Professor
Department of Mechanical Engineering

Swirl Distributed Combustion was fundamentally investigated with experimental diagnostics and predictive analysis using machine learning and computer vision techniques. Ultra-low pollutants emission, stable operation, improved pattern factor, and fuel flexibility make distributed combustion an attractive technology for potential applications in high-intensity stationary gas turbines. Proper mixing of inlet fresh air and hot products for creating a hot and low-oxygen environment is critical to foster distributed combustion, followed by rapid mixing with the fuel. Such conditions result in a distributed thick reaction zone without hotspots found in (thin reaction front) of conventional diffusion flames leading to reduced NOx and CO emissions. The focus of this dissertation is to develop a detailed fundamental understanding of distributed combustion in a lab-based swirl combustor (to mimic gas turbine can combustor) at moderate heat release intensities in the range 5.72- 9.53 MW/m^3-atm using various low-carbon gaseous fuels such as methane, propane, hydrogen-enriched fuels. The study of distributed combustion at moderate thermal intensity helped to understand the fundamental aspects such as reduction of flame fluctuation, mitigation of thermo-acoustic instability, flame shape evolution, flow field behavior, turbulence characteristics, variation of Damköhler number, vortex propagation, flame blowoff, and

pollutant and CO_2 emission reduction with gradual mixture preparation. Initial efforts were made to obtain the volumetric distribution ratio, evolution of flame shape in terms of OH* radical imaging, variation of flame standoff, thermal field uniformity, and NO and CO emissions when the flame transitions to distributed reaction zone.

Further investigation was performed to study the mitigation of flame thermo-acoustics and precession vortex core (PVC) instabilities in swirl distributed combustion compared to swirl air combustion using the acoustic pressure and qualitative heat release fluctuation data at different dilution CO_2 dilution levels with and without air preheats. Proper orthogonal decomposition (POD) technique was utilized to visualize the appearance of dynamic coherent structures in reactive flow fields and reduction of fluctuation energy. Vortex shedding was found responsible for the fluctuation in swirl air combustion while no significant flame fluctuation was observed in distributed combustion. Distributed combustion showed significantly reduced acoustic noise and much higher stability quantified by local and global Rayleigh index. This study was extended with hydrogen-enriched methane (vol. = 0, 10, 20, 40% H_2) to compare the stability of the flow field in conventional air combustion and distributed combustion. Results were consistent and distributed reaction zones showed higher flame stability compared to conventional swirl air combustion.

The study of lean blowoff in distributed combustion showed a higher lean blowoff equivalence ratio with gradual increase in heat release intensity, which was attributed to higher flow field instability due to enhanced inlet turbulence. Extension of lean blowoff (ϕ_{LBO}) was observed with gradual $\%H_2$ which showed decrease of lean blowoff equivalence ratio in distributed reaction zones. Additionally, the reduction in ϕ_{LBO} was achieved by adding preheats to the inlet airstream for different H_2 enrichment cases due to enhanced flame stability gained from preheating. Examination of non-reactive flow field with particle image velocimetry (PIV) was performed to

understand the fundamental differences between swirl flow and distributed reaction flow at constant heat release intensities. Higher rms fluctuation leading to healthy turbulence and higher Reynolds stress were found in distributed reaction flow cases signifying enhanced mixing characteristics in distributed combustion.

Reduction of pollutant emission was an important focus of this research. Measurement of NO and CO emission at different mixture preparation levels exhibited significant reduction in NO emission (single digit) compared to swirl air combustion due to mitigation of spatial hotspots and temperature peaks. Additionally, better mixing and uniform stoichiometry supported reduced CO emissions in distributed combustion for every fuel. With increased H_2 in the fuel, NO gradually increased for air combustion while reduction of NO was found in distributed combustion due to decrease in thermal and prompt NO generation.

Finally, the use of machine learning and computer vision techniques was investigated for software-based prediction of combustion parameters (pollutants and flame temperature) and feature-based recognition of distributed combustion regimes. The primary goal of using artificial intelligence is to reduce the time of experimentation and frequent manual interference during experiments in order to enhance the overall accuracy by reducing human errors. Such predictions will help in developing data-driven smart-sensing of combustion parameters and reduce the dependence on experimental trials.

Investigation of Swirl Distributed Combustion with Experimental Diagnostics and Artificial Intelligence Approach

By

Rishi Roy

Dissertation submitted to the Faculty of the Graduate School of the

University of Maryland, College Park, in partial fulfillment

of the requirements for the degree of

Doctor of Philosophy

2022

Advisory Committee:

Professor Ashwani K. Gupta, Chair
Professor Kenneth H. Yu, Dean's representative
Professor Stanislav I. Stoliarov
Professor Bao Yang
Professor Nikhil Chopra

Dedication

I dedicate this dissertation to my beloved parents Mr. Pradip Roy and Mrs. Sumita Roy for their constant love, affection, and support.

Acknowledgment

It is an absolute honor for me to write my Ph.D. dissertation. First, I would like to express my sincere gratitude to my dissertation advisor Professor Ashwani K. Gupta for introducing me to a very exciting and relevant research topic in the clean and sustainable energy domain called Colorless Distributed Combustion. His immense technical knowledge, research experience, and encouragement guided me through every step of my PhD career toward success. It is my privilege to work under the supervision of such an erudite personality for my doctoral research.

I would like to thank my dissertation committee members Professor Kenneth H. Yu, Professor Stanislav I. Stoliarov, Professor Bao Yang, and Professor Nikhil Chopra for their valuable guidance and suggestions on my research proposal. Professor Yu helped me significantly in understanding the concepts of combustion instability, air-breathing propulsion, and other related topics during my PhD coursework.

Special thanks to all my past and present colleagues from the Combustion Laboratory. This research would not have been possible without their support, especially my colleague who directly worked with such as Late Joseph, Serhat, Eliza, Arthur, Quentin, Khuong, Trevor, and Ahsan. Kiran and Hemant have been extremely supportive during my crucial time of writing the dissertation.

I am grateful to our research sponsor the Office of Naval Research (ONR), the National Science Foundation for the financial support. I would also like to convey thanks to the Summer Graduate

Research Fellowship and the Ann G. Wylie Dissertation Fellowship for supporting my research financially.

I am blessed to have an extremely supportive family that encouraged me every single day during my PhD. I give all the credit to ‘Ma’ and ‘Baba’ (my beloved mother and father) for carefully growing me up and supporting me up to the highest academic degree. I am also thankful to my elder brother Indranil and sister-in-law Sreejata for cheering me up during my long academic journey in graduate school.

Table of Contents

List of Tables

List of Figures

Chapter 1: Introduction

1.1. Background

Energy is an essential thermodynamic requirement to sustain any activity in this universe. Currently, the global current energy landscape is heavily dominated by fossil fuels (over 80%) [1]. According to the predictions given by the U.S. Energy Information Administration [2], the global energy consumption in the last decade (2010- 2020) using natural gas, petroleum, and coal was respectively ~140, 160, and 200 quadrillion British Thermal Units (1 BTU = 1.055 kJ). This statistic also predicts a continued dependence on fossil fuel-based energy conversion for several forthcoming decades. Figure 1.1 shows the trends of variation in energy production from different sources as a function of time (in years). According to such predictions, energy production in 2050 will continue to have 22% contribution from natural gas, 27% from petroleum, and 20% from coal with a net energy requirement of 900 quadrillion BTUs. This indicates a nearly 50% increase in global energy demand within the next three decades to support all human activities. Increasing energy demand is inevitable to the growing world population and consequent human activities. However, such dependence on fossil fuels is highly concerning due to alarming increase of greenhouse gases (primarily CO_2) and harmful pollutants (NOx, CO, soots) in the atmosphere. Continuous emission of carbon dioxide has resulted in an approximate increase of 100 ppm of CO_2 in the atmosphere over the last 1.5 centuries [3]. Carbon dioxide acts like a heat absorber and hence, such increase in CO_2 concentration resulted in an increase of more than 1^oC temperature rise of atmospheric temperature [4] resulting in severe consequences of melting of polar ice caps, increase in sea levels, and deadly wildfires. Different strategies and measures are defined worldwide to fight climate change and global warming. The aggressive goal set by the United

States and other countries to achieve net zero carbon emissions (or even net negative emissions) by 2050 can only be realized through innovation and technological breakthroughs in the clean energy space. Additionally, the enforcement of stringent regulations and emission standards can help in expediting the decarbonization goals.

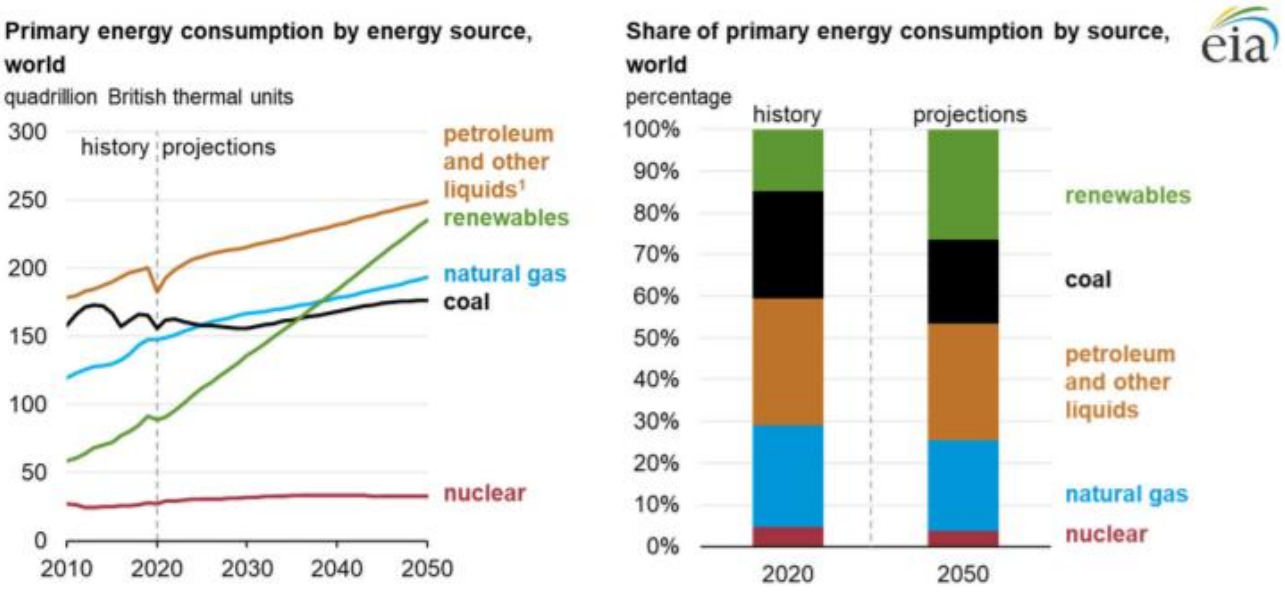

Fig. 1.1. Current and future prediction of global energy consumption from different resources [2]

This thesis primarily investigated the characteristics of a novel clean combustion technology called distributed combustion [5] for stationary gas turbine applications. The perspective of this work is to study stable combustion strategies in power generation while achieving significantly reduced emission of pollutants and greenhouse gases (mainly CO_2). Gas turbines are the commonly used energy conversion devices for power generation and propulsion applications (in aircraft) using combustion. The thermodynamic cycle used in Gas turbines is the Brayton cycle which is shown in Figure 1.2. This cycle mainly involves 4 thermodynamic processes namely (a)

Isentropic compression of Inlet air in the compressor (b) constant-pressure heat addition by combustion (c) Isentropic expansion of high temperature and high-pressure gases in turbine, and (d) finally, heat rejection in the exhaust. The combustor in gas turbine operates at high-temperature and pressure and fosters high thermal intensity (output power per unit of combustor volume) reactive flow fields. The operating pressure of a stationary gas turbine combustor is approximately 15atm with inlet mixture temperature is about 700 K [5]. The operating pressure and temperature within the combustor can have significant effect on the characteristics of flame, shape and structure of flames, output thermal intensity, the reaction chemistry with different fuel properties as well as the efficiency. Such parameters strongly influence the configuration and design of the combustor. The effect of pressure on output thermal intensity can be studied by investigating the output flame power per unit combustor volume per atm pressure (in unit of MW/ m^3-atm). In the lab-scale, investigating thermal intensity of combustion with such unit is advantageous to experimentally simulate the desired output thermal intensity while taking the pressure effect into account. This means, the MW/ m^3 achieved at a higher combustor pressure can be fostered by just increasing the heat release per unit volume without altering the combustor pressure. Such an approach makes the investigation relatively simpler in the lab by eliminating the requirements of designing high-pressure facilities.

The present dissertation investigates fundamental aspects in distributed combustion at low and moderately high thermal intensity (in the range 5.72- 9.63 MW/ m^3-atm) with different low-carbon and zero-carbon gaseous fuels. The concept of distributed combustion relies on the principles of high temperature air combustion (HiTAC) wherein the temperature of fresh reactant is increased to above the auto-ignition temperature by entraining hot reactive species to dilute the oxidizer [6]. In lab-scale distributed combustion is fostered by careful preparation of the inlet fresh

mixtures by diluting with gases such as CO_2, N_2, or steam and also preheating the mixture sometimes. Diluent gases act like heat sinks within the reaction zone and assists in mitigating the hotspots and peak-temperatures and fostering uniform thermal field at low overall oxygen concentration.

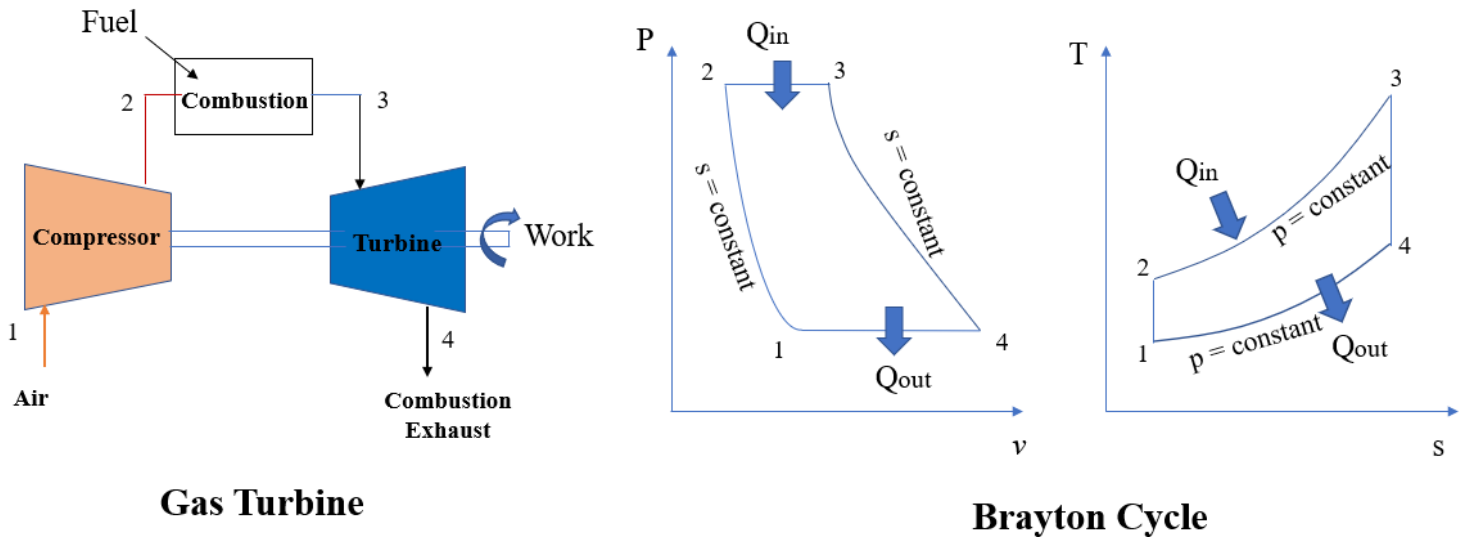

Fig. 1.2. Schematic diagram of Brayton cycle used in gas turbines.

The thermal effect of dilution results in a reduced flame luminosity or chemiluminescence intensity from the reaction zones. Hence, such combustion technology is also called 'Colorless Distributed Combustion' or CDC. The advantage of using CDC in gas turbine combustors are enhanced uniformity of thermal field (or pattern factor), decreased combustion noise and enhanced flame stability, significant reduction of pollutants (NOx and CO) and reduced CO_2 emission resulting from decreased fuel-consumption at high-intensity.

1.2. Objective of this dissertation

The present dissertation focuses on fundamental aspects of a novel low-emission combustion technology called colorless distributed combustion (CDC) with swirl flow stabilization for potential applications to stationary gas turbines. While the previous works on CDC from the Combustion Laboratory at the University of Maryland was dedicated towards the development of distributed combustion for furnace and gas turbine combustors [5, 7]. These studies were conducted in the range of 2- 200 MW/ m^3-atm thermal intensity with rectangular combustor geometries using controlled aerodynamics stabilization (with non-premixed jet flames) and with various swirling geometries. The studies mainly aimed to demonstrate CDC operations, emission reduction behaviors, and some flowfield diagnostics in distributed combustion. In the contrary, the focus this current research is study distributed combustion at a more fundamental level in a swirl-assisted combustion setup with moderately high thermal intensity range. The vision for such work is to gain in-dept understanding on flame stability, thermo-acoustic nature, flowfield turbulence, vorticity dynamics, blowoff characterization, and emission behavior in distributed combustion. Swirl-assisted combustion was investigated in order to study practical gas turbine can-combustors at lab-scale. Additionally, the use of artificial intelligence in distributed combustion is novel. To the best author's knowledge, computer vision (with deep learning) was not studied for the recognition of conventional swirl combustion and distributed combustion yet. Knowledge gained from should immensely help in transitioning to high-intensity distributed combustion or gas turbines. In summary, the primary objectives of this dissertation are:

(a) To understand fundamentally the difference between flow fields between swirl air combustion and swirl distributed combustion using the lab scale swirl combustion facility.

(b) Experimentally investigate the flame stability aspects of swirl distributed combustion as compared to swirl distributed combustion.

(c) Studying the role of different fuel chemistry such as methane, propane, hydrogen, and hydrogen-enriched fuels on swirl distributed reaction zone shape, stability with the goal of fuel-flexible CDC development.

(d) Investigation of pollutant and CO_2 emission reduction using swirl distributed combustion from conventional swirl air combustion.

(e) Demonstrate the use of artificial intelligence (AI) techniques (machine learning and computer vision) to expedite experimentation, design of AI-based virtual sensing, and developing image and audio-based recognition of distributed combustion in real-time.

1.3. Gas Turbine Combustor Design Considerations

As the main objective of the present research is to investigate distributed combustion in relation to gas turbines, it is essential to review the important design parameters of a gas turbine. A comprehensive review of gas turbine design is found in Lefebvre, A. H [8]. Some of the important design parameters are (a) Reduced combustion noise and instabilities (b) Wide operational and stability limits, (c) Low emissions of pollutants and smoke (d) Fuel-flexible operation (d) Low-pressure loss (e) Enhanced uniform thermal field (pattern factor) (f) High combustion efficiency (g) Reliability of operations.

1.3.1. Stable Combustion: One of the important requirements for gas turbine combustors is the stability of combustion. In gas turbines, combustion instability causes serious operational

issues such as flow field fluctuation, flame blowoff, and even catastrophic failures [9]. These challenges are common in low emission lean combustion systems [10, 11]. Hence, the primary challenge to develop new combustion technologies is to achieve low pollution emissions while maintaining the stability of the reaction zone and minimizing combustion dynamics. Future low emission, high intensity gas turbine combustors that use must take combustion stability into account. The combustion instabilities in gas turbines are governed by several factors in swirl flames such as thermo-acoustic instability, flow field oscillation, variation in equivalence ratio, etc. [11, 12]. With the right combustor design and proper combustion strategies, the inherent instabilities in traditional swirl flames can be mitigated.

1.3.2. Wider lean limits Operation: The other important factor is to maintain wider operational limit of combustion within the combustor. While lean operation is preferred for low-emission operations, operating close to the lean limits may have an impact on the stability of the combustion as a result of severe flow and temperature field fluctuations and local flame blowoff incidents. While the reduction of pollutant emission is essential during combustion processes, the mitigation of flame instability is crucial to the development of high performance, efficient gas turbines. Failure to maintain stable combustion severely affects the life of the combustor. Therefore, paying closer attention to flame instabilities and blowoff characteristics from fundamental viewpoints is necessary for the design of any new gas turbine combustion technologies. Understanding the operational limits of combustion technologies also helps with design modifications for the creation of stable gas turbine combustor with ultralow emissions.

1.3.3. Reduced Emission: Stringent regulations on pollutant emissions (NOx, CO, UHC, soot) drive gas turbine manufacturers to focus strongly on low-emission combustor development. Figure 1.3 depicts the NOx and CO emissions with respect to combustor firing temperatures [13]. It is evident that NOx emission strongly rises with firing temperatures greater than 1500 K. Gas turbine generally works at elevated temperature (~ 1600 K) where the NOx emission is very high. As observed, at lower firing temperature (which results with much leaner operation) near blowoff instabilities show up steadily within the reaction zone. This signifies that advanced combustors need to be carefully operated at a range of temperature to avoid high NOx formation and near blowoff instabilities.

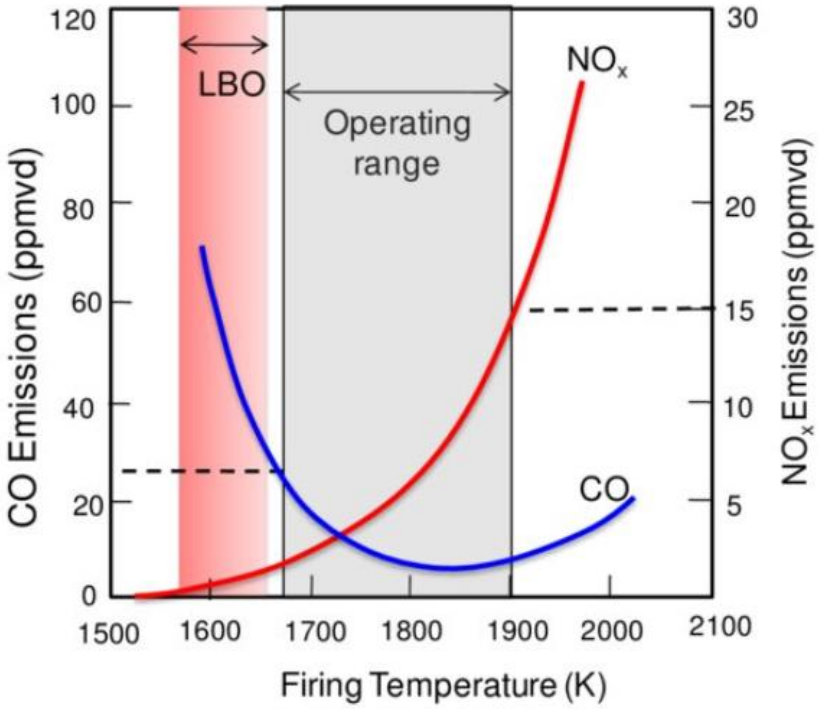

Fig. 1.3. Schematic diagram of Brayton cycle used in gas turbines [13].

Additionally, the formation of CO is mech higher at lower temperatures (< 1700K). Hence, design of gas turbine operations to optimize emission reduction is an important factor into consideration.

Unburned hydrocarbon emissions directly relate to combustion efficiency and almost 100% combustion efficiency is desired from the gas turbine combustors for fuel savings. In terms of equivalence ratios (ϕ), higher CO emissions are observed at both low and high equivalence ratios and NOx emissions are high at higher equivalence ratios up to $\phi = 1$ and decreases in rich conditions. To operate at an acceptable range, there is a small operational window where emissions can be controlled. According to the Environmental Protection Agency (Federal Register, 2006), the NOx emissions for land-based gas turbines needs to be strictly within 15- 42 ppm for gas turbines with capacity up to 250 MW [14]. While pollutant emission is crucial to the development of advanced gas turbines, an important consideration is to attain reduced carbon footprints. Emission of CO_2 is reduced by implementing better combustion strategies and by using low-carbon fuels and alternative fuels (biofuels, sustainable aviation fuels) etc.

1.3.4. Uniform Thermal Fields: An important aspect of gas turbine thermal management is to design proper cooling of turbine blades. It is essential to control the combustor outlet temperature to protect the health of the turbine blade and reduce thermally induced stresses in the blades [8]. It may not be sufficient to only control the mean blade temperature, local variations in radial and circumferential temperature from the average temperature can lead to formation of hot spots resulting in failure of turbine parts [15]. The goal of such blade design is to reduce the temperature at the root to protect the blade attachment to the shaft and at blade tip to maintain proper clearance at the wall. Pattern factor quantifies the non-uniformity in temperature distribution at the combustor exit and is given by equation 1.1.

$$\text{Pattern factor} = \frac{({T_{max}}^{out} - {T_{avg}}^{out})}{({T_{avg}}^{out} - {T_{avg}}^{in})} \tag{1.1}$$

Figure 1.4 shows the actual vs. design temperature collected from previous research studies [15]. A properly designed blade temperature should have the actual profile to match the design profile. The role of internal entrainment or mixture preparation investigated in this research is to reduce the hotspots while promoting uniform thermal fields within the reaction zone. Such thermal field uniformity in combustion zone results in enhanced pattern factor development desired for the healthy operation of gas turbines.

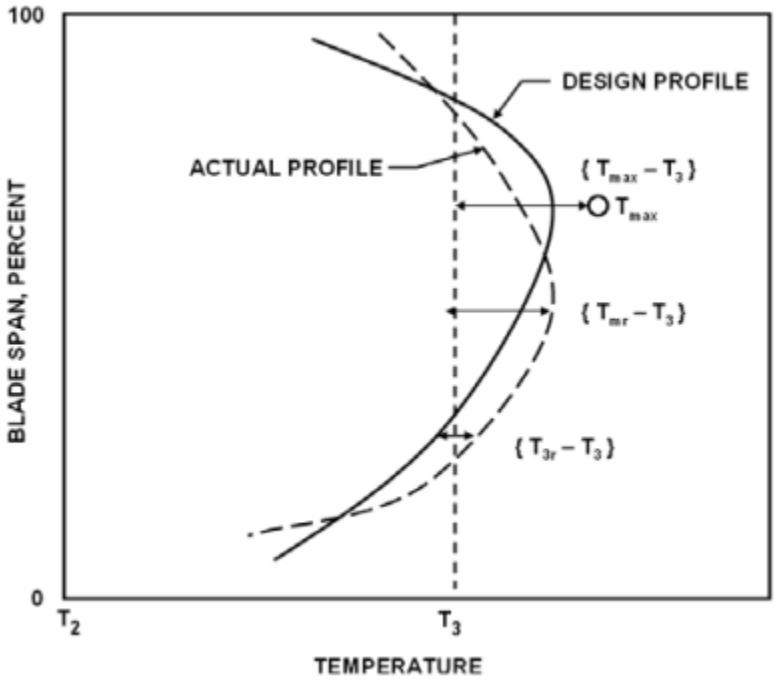

Fig. 1.4. Temperature profile at the exit plane of the turbine blades [15]

1.3.5. Fuel Flexible Operation: Fuel flexible operation is desired to operate gas turbines with a range of fuel chemistry without much alteration of configuration. Such characteristics are also highly desired for combustors to reduce pollutants and CO_2 emission (especially with hydrogen blend fuels). Aircraft gas turbines generally use kerosene fuels (such as Jet-A or JP-8), and natural gas is used in stationary gas turbines. Additionally, the use of synthetic gases, blends, hydrogen, and even ammonia was studied in the swirl combustors. The flexibility of burning alternative fuels

and biofuels has become crucial due to decarbonization motivation and the continuous depletion of fossil fuel reserves.

1.4. Current Low-emission Gas Turbines

Tackling the NOx and CO emission is one of the most important challenges in designing low-emission combustors. As NOx formation increases with hotspot and near at near-stoichiometric condition, current technologies try to operate at lean conditions to avoid the temperature peaks. Study of NOx formation during combustion is extremely important combustor significantly due to its harmful effects of smog formation, acid rain and ozone layer depletion [16]. NOx is primarily the mixture of nitric oxide (NO) and nitrogen dioxide (NO_2). However, NO is the major portion of NOx (~90%). Understanding the NOx formation pathways is key to mitigate such undesired species in the combustion exhaust. Different NO formation mechanisms are explained briefly.

1.4.1. NOx Formation Pathways

1.4.1.1. Thermal NO

As the name suggests, this NOx formation pathway is influenced by the temperature of the reaction zone. Thermal NO is formed due to oxidation of atmospheric nitrogen and is triggered at high temperatures. The important equations involving NO formation are mentioned below:

$$O + N_2 \longrightarrow NO + N; \quad (1.2)$$

$$O_2 + N \longrightarrow NO + O; \quad (1.3)$$

Such chemical pathways are extremely favored above 1850 K and the NO formation rate rises exponentially. Generally, the NO is favored line early with residence time. But achieving chemical

equilibrium is difficult in gas turbine combustors due to very fast flow timescale which does not support the reactions to achieve equilibrium. Thermal NO is the major contributor of total NO formed and generally forms in the post combustion zone. In swirl flames, the hotspots create temperature peaks resulting in higher formation of thermal NOx (above the temperature of 1850K). Hence, avoidance of hot spots can significantly reduce thermal NO emissions.

1.4.1.2. Prompt NO

Another NO formation pathway is known as the 'prompt NO' which may form in the reaction zone even before the formation of thermal NO [17]. Prompt NO formation predominantly arises from the reaction between CH radical and molecular nitrogen producing hydrogen cyanide (HCN) through the reaction channel:

$$CH + N_2 \rightarrow HCN + N \quad (1.4)$$

$$C + N_2 \rightarrow CN + N \quad (1.5)$$

$$HCN + O \rightarrow NCO + H \quad (1.6)$$

$$NCO + H \rightarrow NH + CO \quad (1.7)$$

$$NH + H \rightarrow N + H_2 \quad (1.8)$$

$$N + OH \rightarrow NO + H \quad (1.9)$$

As observed, such mechanism is governed by the existence of CH radical in combustion zone. Hence, use of low carbon fuels may help in reducing the possibilities of formation of prompt NO. Hydrogen enrichment to fuel also helps in reducing the formation of prompt NO.

1.4.1.3. Fuel NOx

In this mechanism, NO is created primarily due to oxidation of nitrogen in the fuel. Such mechanism is observed in solid fuels (such as coal), liquid distillates, and ammonia fuels. In this reaction mechanism the fuel nitrogen converts to HCN and NH_3 followed by oxidation of these radicals that finally leads to NO formation. The later part of this mechanism is similar to prompt NO formation pathways. In oxidizing environments, such NO promotes the formation of NO_2.

1.4.1.4. N_2O intermediate and NNH Pathway

Some other NO formation pathways involve the formation of nitrous oxide (N_2O) as intermediate species [7] and NNH radicals. The O radical with nitrogen reacts to form N_2O as the intermediate species. Further oxidation of N_2O generates NO. The reaction pathways are as follows:

$$O + N_2 + M \rightarrow N_2O + M; \quad (2.0)$$

$$H + N_2O \rightarrow NO + NH; \quad (2.1)$$

$$O + N_2O \rightarrow NO + NO; \quad (2.2)$$

The NNH intermediate pathway also starts from N_2 to form NO via the NNH intermediate formation as given by $N_2 \rightarrow NNH \rightarrow NO$.

1.4.2. CO Formation

Incomplete combustion leads to the formation of CO due to the unavailability of oxygen to oxidize to CO_2. An important reason for such incomplete combustion is also short residence time.

If the flow timescale inside the combustion is short, the conversion of CO to CO_2 is not allowed enough time and formation of CO in the exhaust. Also, the high-temperature dissociation of carbon dioxide leads to generation of carbon monoxide near stoichiometric conditions. At very lean conditions, inadequate mixing between air and fuel also leads to incomplete combustion forming higher concentration of CO [8]. CO emissions are highly influenced by local stoichiometry, variation of equivalence ratio within the reaction zone.

The design of combustor plays an important role in controlling CO emission due to residence time. If the reaction rate is slow such that oxidation is incomplete due to residence time, CO formation increases from combustion.

1.4.3. Current low NOx Gas Turbines

This section discusses the current widely used low NOx strategies in gas turbines. Most of the gas turbine technologies try to avoid the peak NOx formation regime (near stoichiometric) by implementing different operational strategies. Few popular strategies include lean premixed combustion (LP), Rich-burn quick-quench lean-burn (RQL), Lean direct injection (LDI), etc. as explained below:

1.4.3.1. Rich-burn, quick-quench, lean-burn (RQL)

The concept of technology was introduced in 1980 as a way to reduce NOx from gas turbines [18] and it is currently used by Pratt and Whitney for commercial development of aeroengines [19]. In this technology, first a stable combustion is fostered with rich burning state in the primary zone (at $\phi = 1.8$) by producing energetic hydrogen and hydrocarbon radical species. Rich burning minimizes the production of nitrogen oxides due to the relative low temperatures and

insufficient oxygen containing intermediate species. Later, rapid mixing and quenching occurs by additional air to avoid combustion occurring near stoichiometric conditions with higher propensity of NOx formation. Lean mixture composition is formed using excess air where reaction is re-initiated. Thermal NOx formation rates are lower in lean conditions due to low flame temperature. The operational equivalence ratio in lean condition is ~ 0.5-0.7.

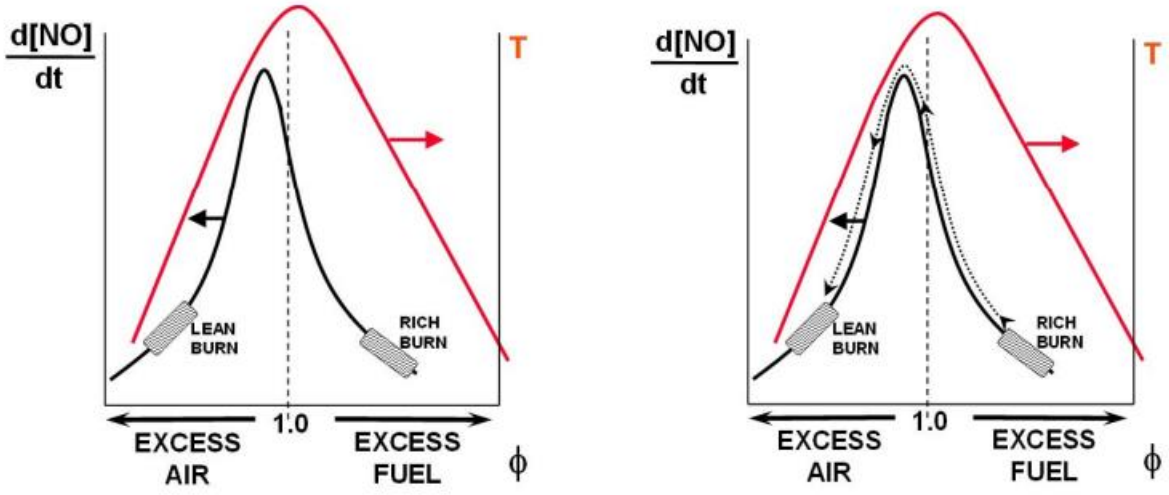

Fig. 1.5. NOx formation pathway (left) and RQL combustion strategy [19].

Very fast quenching is essential to move from the rich regime to the lean regime without going through the high temperature peak involving high NOx route. However, any off-design performance may lead to high pollutants emission. RQL may not produce very low NOx as desired due to difficulties in reaching very lean limits.

1.4.3.2. Lean Premixed Combustion (LP)

Lean Premix combustion is designed to operate with thoroughly mixed air and fuel to form a lean mixture before combustor that avoids hotspot formation [7, 20]. The atmospheric nitrogen (from inlet air) acts as a diluent, as the upstream mixing of fuel and air happens in fuel-lean

conditions. Near perfect mixing in LP technology is key to achieve ultra-low NOx as combustion happens without hotspots and the possibility of reducing thermal NOx is significantly lowered. Figure 1.6 compares the difference in operation of LP combustors vs. conventional combustors.

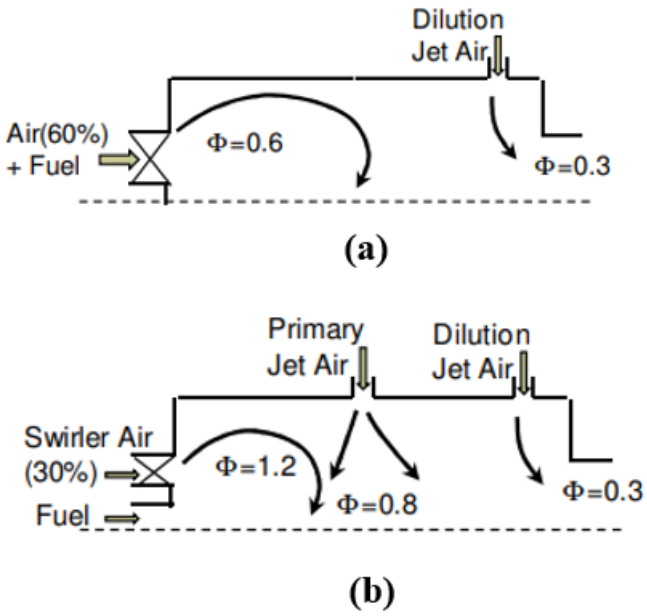

Fig. 1.6. Schematics of (a) Lean-premixed combustors and (b) Conventional non-premixed combustion strategy (taken from [7])

When liquid fuel is used for LP combustion, it is prevaporized first and such technology is called Lean Premixed Prevaporized (LPP). Despite having great emission reduction capability, the LP combustion faces significant problems of combustion instability such as pressure fluctuation, heat release fluctuation, and blowout due to near lean limit operations. Flame flashback in low velocity regions is another problem that poses severe safety challenges in practical systems. Such challenges are the important limitations in LP technologies intended for land-based and aviation gas turbines.

1.4.3.3. Lean direct injection

Lean Direct Injection (LDI) is a type of lean premixed combustion with potential application in aerospace gas turbine proposed by NASA Glenn Research Center [21-24]. The important feature offered by the LDI technology is the short mixing length to reduce the risk of flashback and certainly the reduction of NOx. Operating in non-premixed combustion mode is the lean direct injection combustor. In this technology, the fuel is directly injected into the flame zone without separately premixing. The whole intake air of the combustor except for liner cooling is delivered to combustion dome. The LDI operates overall fuel-lean avoiding any possible rich flame front. LDI reduces NOx emissions by minimizing local flame temperature avoiding local near-stoichiometric operations. Low NOx is achieved using multipoint fuel injection systems, and each of these systems contains a swirler to provide quick turbulent mixing and recirculation for flame stabilization. While LDI has shown good promise of NOx reduction, this technology faces instability challenges of traditional lean premixed systems.

While the current technologies are trying to control pollutants (NOx, CO, UHC, Soot) with different technologies, these technologies face challenges of instabilities (thermo-acoustic, hydrodynamics etc.). Such instabilities may even lead to failure of combustor materials over the period of operation. Mitigating such problems is extremely important for high intensity combustion application while producing lowest possible pollutants. Hence, it is to be a tradeoff between establishing low-NOx lean combustion technologies and stable combustion operations. Additionally, the reduction of carbon footprint is an important task in research and engineering communities. Significant attention should be given to technological innovation for developing fuel-flexible gas turbines capable of running on low/ zero carbon fuels (hydrogen, ammonia) and

providing fuel savings. Hence, the motivation for new combustion research is to focus on significantly reducing emissions (greenhouse gases and pollutants) while making sure the combustion operation is stable providing longer combustor life.

1.5. Use of Artificial Intelligence in Combustion Research

While the experimental diagnostics provides possibly the best representation of different combustion modes, physics-based modeling (such as computational fluid dynamics or CFD) may also provide realistic understanding of the combustion physics and simulate combustion in desired geometrical configurations. However, both these techniques have limitations. Experimental methods can sometimes be very time consuming and expensive due to the involvement of sensitive instruments. Additionally, experimental processing and post-processing time may also be very long. CFD not only requires computational power and storage capacity, but the accuracy of prediction heavily depends on the complexity of geometry and proper meshing development to achieve accurate and faster convergence of computation [25]. Such CFD computations may face severe difficulties to model complex geometries and are typically not reproducible for different conditions without altering the boundary conditions. Data-driven statistical analysis is an alternative effective method for analyzing such outcomes that can provide high accuracy while saving a significant amount of computational time [26]. Hence, predictive analysis in low-emission combustion is of growing interest in the combustion research community. Machine learning is generally used for efficient and accurate prediction of parameters. In general, such machine learning frameworks help to predict a target parameter based on input training parameters using statistical correlations. Machine learning is required for prediction when there exist no defined correlations between input and target data. Such modeling assists in regression analysis and

classification of data. Besides fundamental investiagtions with machine learning, such predictions can be utilized to develop data-driven smart-sensing of combustion parameters (pollutants, species, temperature, etc.) that can reduce the dependence on experimental trials. The classification task is intended to classify different sets of data and recognize combustion parameters based on training data. Image and audio-based classification is also performed along with feature extraction using computer vision schemes. For such purpose, deep learning is utilized to develop convolutional neural networks (CNN), which are widely used for feature extraction, and classification tasks using images and audio [27]. This research demonstrates the use of CNN to develop classification using training image and audio samples. This work is the foundation of feature-based recognition of combustion states to develop perception. The extention of such concepts will lead to the development of feature-based decision-making for AI-assisted advanced control systems with autonomous perception abilities. The broader goal is to reduce the time of experimentation, and limit frequent manual operations during the experiment (such as flow control, software calibration, flame ignition, and manual mixture preparation/ dilution) in order to enhance the overall accuracy by reducing human errors. Efforts have been made during this research to demonstrate a synergy between experimentation and machine learning that can be utilized to predict flame temperature, and pollutant emission from the post-flame zones. CNN has been utilized to develop recognition of different combustion modes (mainly new/ unknown combustion regimes) based on image and audio data acquired from the experimental facility considered. This thesis investigated machine learning to develop AI-based virtual ‘smart-sensing’ of combustion parameters. Computer vision is utilized to develop advanced control systems to be deployed in real combustion facilities capable of running autonomously to control combustors. Advanced control systems are essential to avoid injection delay, enhance mixing of fuel-air resulting in reduced emissions and improved efficiency.

Chapter 2: Literature Review

This chapter reviews past research works related to ultra-low emissions combustion technologies including colorless distributed combustion. Such technologies are focused on applications primarily in gas turbine combustors and furnace applications. These technologies employed either traditional flame stabilization mechanisms such as swirling stabilization or discrete and direct injection of fuel and air jets in a non-premixed setting at high velocity within the confined combustion chamber avoiding the requirement of traditional flame stabilization. To achieve low emission in the exhaust, different strategies were investigated such as (a) combustion at low equivalence ratio or lean combustion and (b) combustion at lower global oxygen concentrations. The operational difference between these strategies is that the former one is achieved using air dilution of the reaction zone whereas the latter one is obtained by internal recirculation of hot-product gases. The key components of such hot products are CO_2, N_2, and H_2O vapor. Hence, such low oxygen reactive environment can also be achieved by mixture preparation of the inlet preheated airstream with CO_2/ N_2/ H_2O vapor of a combination of these gases. Several research in the past demonstrated low emission combustion technologies using the above strategies. The concept of low oxygen reaction relies on the principles of High Temperature Air Combustion (HiTAC) [28, 29, 30] which is also known as Flameless Oxidation (FLOX) [31, 32] [33, 34], Moderate and Intense Low Oxygen Dilution (MILD) combustion [35- 37] and Colorless Distributed Combustion [5, 38- 40]. Some of the similar technologies are High Intensity Low Emission (HILE) burner [41], Stagnation Point Reverse Flow (SPRF) combustor [42, 43] and Trapped Vortex Combustor (TVC) [44, 45] where the fuel is directly injected into the combustion

recirculation zone. Another type of low-emission combustor is Princeton Asymmetric Whirl Combustor (PAWC) [46], where fuel is directly injected strongly swirling fluid motion.

HiTAC has revolutionized industrial furnace technology by demonstrating ultra-low NOx and CO emissions [28] and fuel savings resulting in reduced CO_2 emissions. HiTAC is primarily focused on lower thermal intensity furnace-type applications (< 1MW/m3-atm) compared to CDC which may range up to 50MW/m3-atm or more for gas turbine applications [47]. For HiTAC, the inlet mixture temperature is generally above the auto-ignition temperature of the reactants. However, such combustion is different from preheated air combustion (e.g., excess enthalpy combustion) in which the flame temperature increases. For HiTAC, the reaction zone temperature remains unaltered despite the addition of air preheats. Due to auto-ignition, the mixture ignites spontaneously which eliminates the need for traditional flame stabilizations in HiTAC. The operating characteristics of HiTAC differ from the MILD combustion. In the review paper by Cavaliere, A. and de Joannon, M., [48], MILD combustion was defined as the process where inlet temperature of reactants (T_{in}) is above auto-ignition temperature (T_{ai}) and the temperature rise in combustion process is lower than the auto-ignition temperature of reactant mixture. They differentiated MILD combustion from HiTAC combustion by suggesting that in HiTAC the temperature rise in combustion process (ΔT) is greater than the auto-ignition temperature of reactants even though the temperature of reactants is higher than the auto ignition temperature of the reactant mixture. Cavaliere, A. and de Joannon [48] mentioned MILD combustion as the subset of HiTAC. The conditions for MILD combustion and HiTAC can be identified from table 1.

Table 2.1. Conditions for MILD combustion and HiTAC

Combustion	Inlet Conditions	Operating Condition
MILD	$T_{in} > T_{ai}$	$\Delta T < T_{ai}$
HiTAC	$T_{in} > T_{ai}$	$\Delta T > T_{ai}$

In a recent review by Perpign et al. [49] regarding FLOX combustion, the distinction between FLOX and MILD combustion was discussed using the hypothesis of Evans et al. [50] that was based on the proposition made by Oberlack et al. [51] for premixed flamelets. A debated assumption is taken that FLOX does not show auto-ignition and extinction characteristics. Evans et al. [50] also concluded that the definition by Cavaliere, A. and de Joannon [48] was not correct because that included both 'auto-igniting' and 'gradual combustion flames' for the analysis. In 1997, Wunning, and Wunning [52] introduced the name flameless oxidation (FLOX) as a technique to suppress thermal NO_x by avoiding hot spot regions in the furnace. Under the conditions of internal gas recirculation, combustion was observed without any visible or audible flame and hence it was named flameless oxidation (FLOX). It was suggested that air preheating is not a strict requirement to achieve flameless oxidation; however, in this study, high air preheat temperatures were used (about 1100K). It was also mentioned that flameless mode can be achieved not only by discrete injection of fuel and air but also by common injection as well as in premixed mode. The flameless mode resulted in about 16 dB noise reduction as compared to the flame mode. Both regenerative, as well as recuperative burners, were successfully demonstrated. A reverse flow regenerative (FLOX REGEMAT® 350) burner that had a cycle time of 20s where three honeycomb regenerators alternately cool the flue gases and the heat the combustion air was tested [53]. NO_x

emission of about 11ppm was reported with air preheat temperature of about 1100K and thermal intensity of 0.07MW/m^3-atm at a length scale of 92 inch.

Note, while HiTAC is in operation in furnace applications (approximately 7867 furnaces worldwide use HiTAC burners [54]), the potential of MILD and FLOX technologies is still investigated in academic and pilot scale research facilities, especially for gas turbine combustors. Generally, combustors below 1 MW/m3 -atm thermal intensity are used in furnace applications while thermal intensity between 1- 10MW/m3 -atm and above are intended for high thermal intensity applications including gas turbine combustor application [47, 55, 56]. A representative plot of thermal intensity distribution for various gas turbine combustors (see Figure 2.1) can be found in ref. [7] that was collected from different references [33, 42, 44, 45, 55, 56, 57, 58]. It is interesting to see that combustor with high thermal intensities (greater than 100 MW/m3 -atm) was investigated at very lean burning conditions ($\phi = 0.2$) whereas, lower thermal intensity combustors (5- 10 MW/m3 -atm) were studies near stoichiometric conditions.

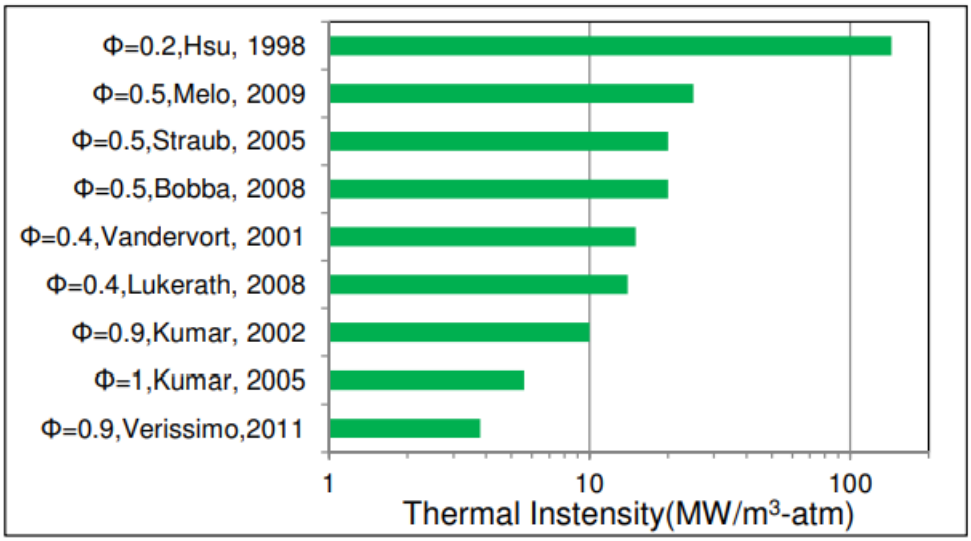

Fig. 2.1. Thermal intensity distribution of different gas turbine combustors (taken from ref. [7])

This can be attributed to the fact that lower entrainment of hot products at low and moderate thermal intensities affects the flame stability at very lean conditions compared to higher thermal intensities. Hence, near stoichiometric lean conditions are considered at low to moderate MW/m3 -atm. This is consistent with the low thermal intensity operations in furnaces where most of the investigations were carried out by different researchers in the equivalence ratio range of $\phi = 0.8 – 1$ [6, 32, 37, 59]. When low-emission gas turbines are concerned, the state-of-the-art technologies heavily focus on reduced nitrogen oxide emissions or NOx. A popular example is Dry low NOx (DLN) combustors which is also known as Dry low emission (DLE) combustors [57]. These combustors are widely in application in General Electric engines such as GE-6F, 7FA land based gas turbine, GE DLN 2.6, 2.6+, 7F DLN 2.6+ FLEX including Solar Turbines, Siemens combustor etc. DLN technology uses lean premixed combustion (LP) to minimize NOx emission. GE DLN combustor offeres single digit NO_X (< 9 ppm) and reduced CO_2 at elevated pressure, temperatures (~ 16atm and combustor exit temperature of 1561 K) with wide Fuel flexibility including the use of hydrogen blends (5-20%) [60]. Recently, Kawasaki Heavy Industries, Ltd and Obayashi Corporation in Japan demonstrated successful operation of 100% H_2-fired DLN combustors [61]. These combustors also use fuel staging for operations at part load conditions. Khalil [7] demonstrated the NOx emission from different industrial gas turbines based on the data published by the Environmental Protection Agency [62] as shown in Fig. 2.2. As observed, these combustors mainly used LP combustion, steam injection, or non-premixed versions.

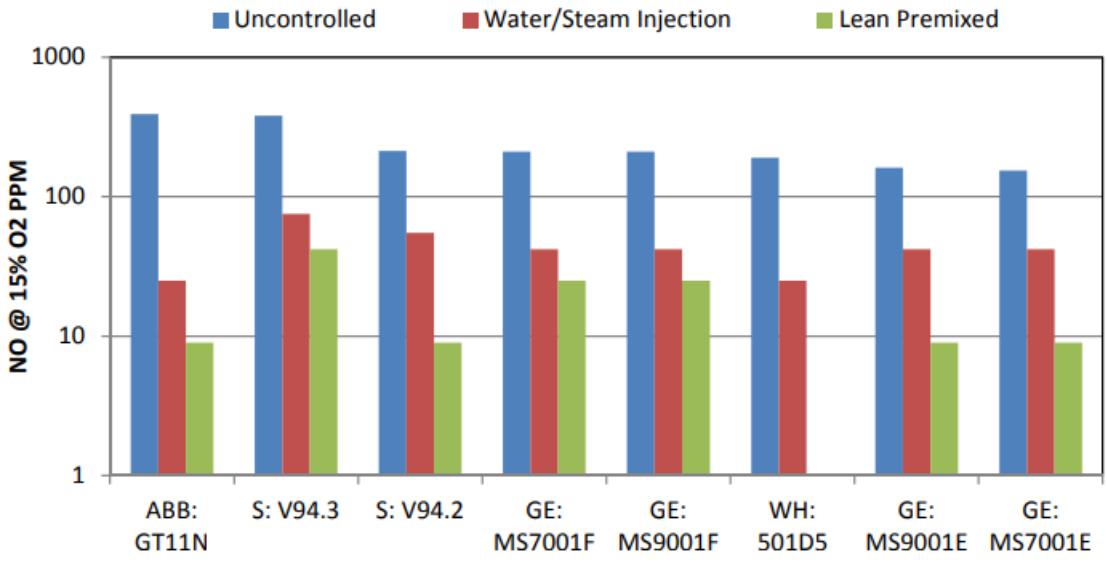

Fig. 2.2. NOx emission from different industrial gas turbines (taken from ref. [7])

Lean premixed combustion showed far better emission reduction compared to other technologies (< 9 ppm). However, steam inject also provides reasonable reduction of exhaust NOx compared to the non-premixed gas turbines. Note that, steam dilution is somewhat analogous to inlet mixture preparation using CO_2 or N_2 and may lead to distributed combustion-like conditions. Hence, a better way of investigation is to foster distributed combustion at lean premixed version to exploit the advantage of both the technologies shown in Fig. 2.2.

2.1. Requirements of Low-emission Gas Turbine Combustors

It is essential to review the requirements of gas turbine combustors for developing new combustion technologies as the working principle of these combustors vary from traditional industrial burners. Some important considerations of gas turbine combustors are mixing at shorter length scales (compared to furnaces), enhanced pattern factor, flame stability, and reduced NOx and CO emissions. The length-scale consideration can be explained by the theory proposed by

Hottel and Hawthorne et al [63] on diffusion in laminar expanding jet flames with hydrogen. According to them, the length of an expanding jet flame with a fixed exit diameter varies monotonically with Reynolds number (Re) in the laminar regime (see Fig. 2.3). With increasing Re, the flame length gradually increases to the maximum up to the transition limit (Re ~ 2000) and then starts to shorten in turbulent regime. The height of jet flames becomes independent of the Re at highly turbulent regimes.

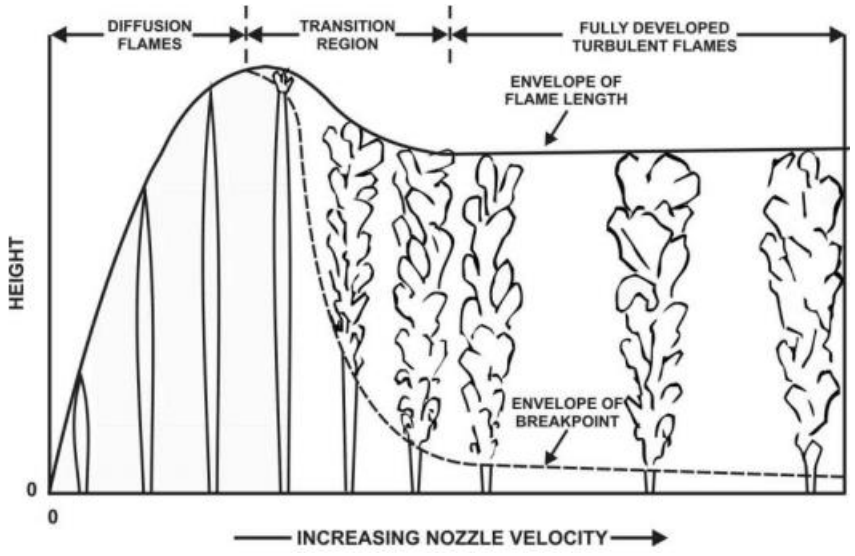

Fig. 2.3. Variation of non-premixed flame length at various Reynolds number regimes. (taken from ref. [63])

High thermal intensity gas turbines require enhances mixing for stable and efficient combustion at compact spaces supported by very high turbulence intensity of the flow field. Such requirements are an important consideration for gas turbine combustors to operate at high turbulence. Figure 2.4 depicts the length scale of different combustors found in previous studies [5]. It should be noted that lower-size combustors are intended for gas turbine combustion while larger-size combustors are typically used in furnace applications. It was reported that low thermal intensity combustors of

0.02MW/m^3 -atm has a length scale of 246 inch [37] and combustor operating at high thermal intensity ~ 144 MW/m^3 -atm has length scale of 1.6 inches [44]. Such observations support the explanation provided in Fig. 2.2 showing the effect of higher thermal intensity (inducing greater overall turbulence) on combustor lengths.

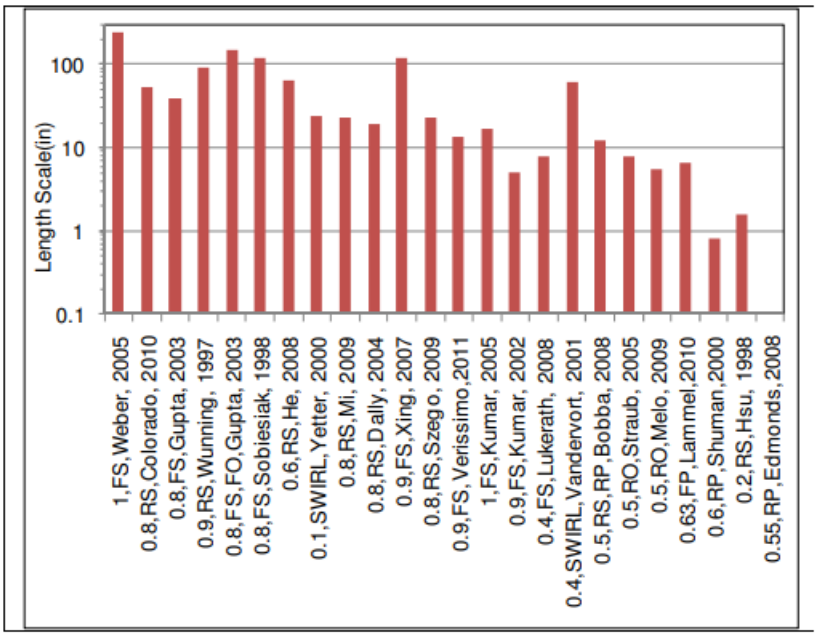

Fig. 2.4. Variation in length scale of combustors collected from different literature. (taken from ref. [44])

Another important consideration for gas turbines is the operation at high temperature and pressure. For gas turbines, the compresses air (from compressor stages) includes high temperature ~ 600K and above atmospheric pressures. It is very important to study HiTAC family combustion at high pressure as the role of diluent is yet to be investigated at such operating conditions. Notably, high pressure investigation of flameless combustion was performed by Luckerath, R., et al., [33] at 20 atm, which was the first investigation of FLOX at high pressure, to the best of our knowledge.

Finally, the emissions are the most important focus in gas turbine research. Figure 2.4 shows the NOx emissions for different combustor considered for research. Higher NO emission was found

from high-intensity combustors which was attributed to higher thermal NOx production due to increased in-flame temperature. In general, the NO emissions for these combustors are generally below 10 PPM which is along the line of GE DLN combustor performances. It is important to note that residence time within the combustor influences NOx formation. Lower residence time due to high injection velocity leads to lower NO emissions, as the short duration within the combustor prevent the reaction pathways from reaching equilibrium where high NO is produced.

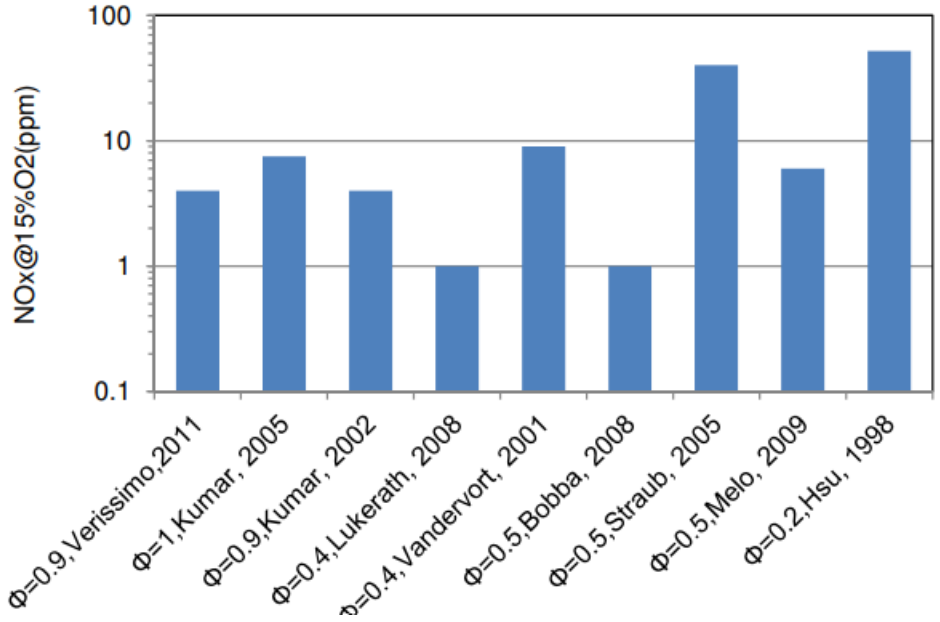

Fig. 2.5. NOx formation from different low-emission combustors [7].

2.2. Fundamentals of Colorless Distributed Combustion

2.2.1. Motivation from HiTAC

Colorless distributed combustion or CDC is based on the concept of High temperature air combustion (HiTAC). The concept of HiTAC can be well explained in comparison to furnace opration as illustrated by the Fig. 2.6. In conventional furnace, a concentrated flame is established

by direct mixing of fuel and air so that flame is anchored near the nozzle exit and bounded by the region of stoichiometric composition marked by (F*A) in Fig. 2.6 b. Such an arrangement leads to high flame temperature hotspot formation resulting in high thermal NOx production [Miller, J. A. and Bowman, C. T., 1989; Correa, S., M., 1992]. Here the flame stabilization happens due the heat transfer between product (B) and fresh mixtures by the entrainment effect which sustains the ignition.

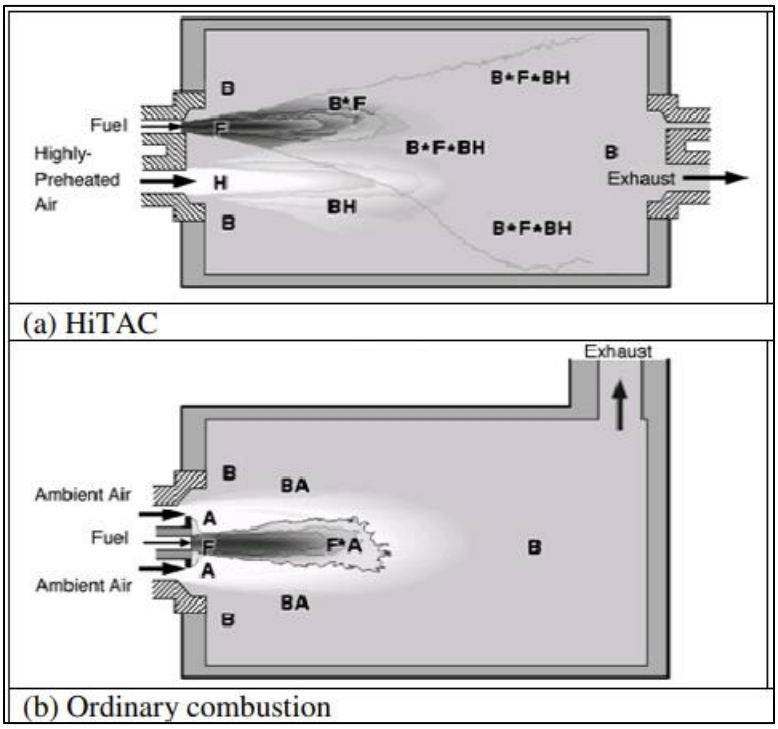

Fig. 2.6. Difference between (a) high temperature air combustion (HiTAC) and (b) ordinary combustion with schematic illustation [6].

In HiTAC, a discrete injection of highly preheated air (H) and fuel (F) jet is conceptualized, which does not require traditional flame stabilization methods (bluff body, swirl stabilization). As exhibited in Fig. 2.6 a, both fuel and air streams first entrain the product gases (B) avoiding direct mixing between the fuel and air streams. Additionally, some changes in the fuel composition due

to pyrolysis, breakdown, and evaporation during mixture preparation period may also occur in such conditions. Reduced reaction rate is established between fuel and entrained products (B*F) and the main reaction primarily occurs in the mixing zone of fuel and diluted air with significant burned gas (B*F*BH). Due to the high entrainment of burned gas, the low oxygen concentration results in major shifts in flow field characteristics such as turbulence, shear stress, strain rates and reaction rate resulting in wider reaction and reduced chemiluminescence. Such effects on flame appearance at low-oxygen concentration and preheating were dicussed by Gupta *et al.* [6] in the context of HiTAC. Figure 2.7 shows the variation of global flame chemiluminescence and flame shape and the operation window of HiTAC as a function of the recirculation ratio.

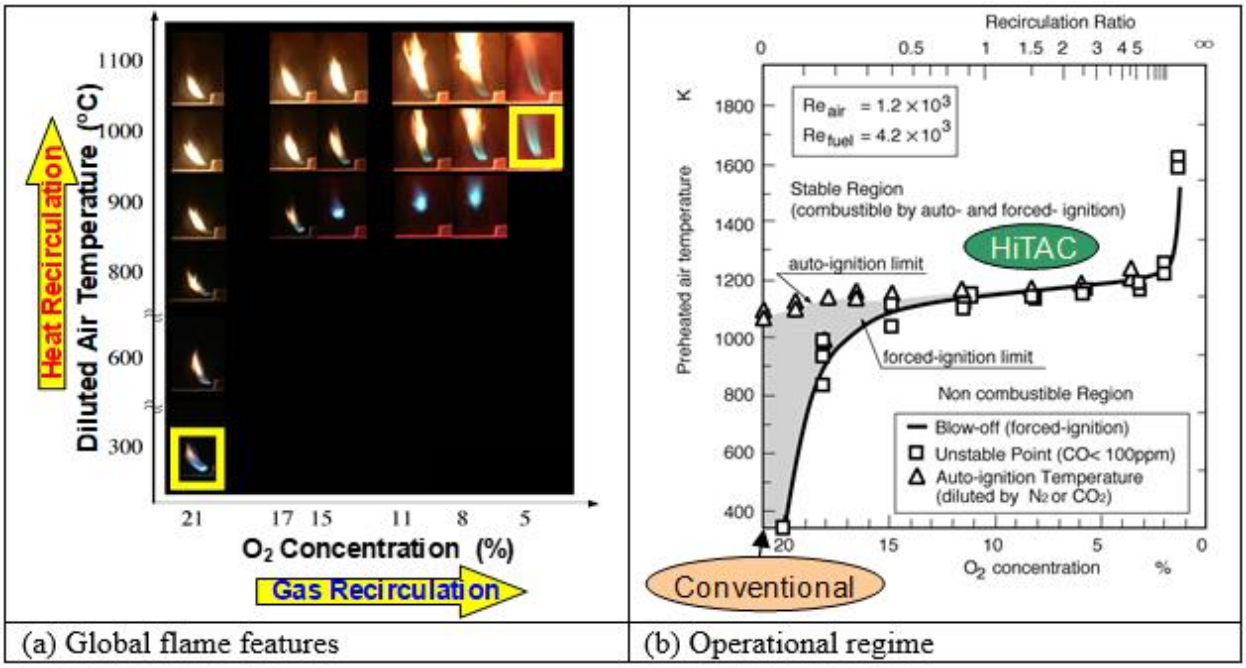

Fig. 2.7. Effect of air preheats and oxygen concentration on (a) global flame behavior (b) operational regime of propane-air flames in HiTAC [6].

While the visible chemiluminescence gradually increased with air preheat temperature due to increased reaction rate, the luminosity of the reaction zone was found to be decreased at lower O_2.

This is due to the decrease in radiation from the reaction zone due to the entrainment effect which helps to mitigate the peak temperature and hot gas pockets within the reaction zone. Additionally, with reduced O_2 concentrations, the reaction takes place over a wider volume making it distributed reactions. Figure 1.2(b) shows the limit of operation of distributed combustion as the oxygen concentration is decreased. The solid line in the figure marked the boundary between forced ignition and non-ignition regimes. The temperature must be raised above the auto-ignition temperature to sustain combustion under low O_2 levels.

2.2.2. Colorless Distributed Combustion

Inspired by the concept of HiTAC, the high-intensity combustion called colorless distributed combustion (CDC) is being investigated at the Combustion Laboratory of the University of Maryland for potential application in gas turbines. Past works involved the development of distributed combustion and studying different combustor configuration (rectangular and swirling) with distributed combustion [5, 7]. In the last decade, CDC investigations mainly involved demonstration and development of distributed combustion at different ranges of thermal intensity (from 5 to 198MW/m3 -atm). The primary focus was to exhibit a reduction of NOx and CO from different combustor facilities adapted for CDC. These combustors involved lengthscales in the range of 1- 10 inches [7]. Most of the investigations found NO emissions below 9 ppm and CO emissions less than 100 ppm (normalized at 15% O_2) from the lab-based facilities. From 2012 onward, CDC combustion was investigated in relation to gas turbines using gaseous and liquid fuels. In many cases, swirl stabilized combustion was investigated to mimic gas turbine can combustors [64- 66]. While the main focus of these experiments was the exhibition of reduced pollutants, the works by Khalil et al. [64, 67, 68] and Feser et al., [69], and Karyeyen et al. [70-

72] focused on flow field characteristics, noise reduction, utilization of laser-based diagnostic such as particle image velocimetry (PIV), planar laser induced fluorescence (PLIF), and use of gaseous and liquid fuels to demonstrate fuel flexibility in CDC combustors [73]. In many studies, mixture preparation was utilized by preheating and diluting the inlet mixture stream with inert gases such as CO_2 and N_2 to attain CDC from conventional air swirl combustion [68, 72]. CO_2 and N_2 being the key components in the product gases, diluting the inlet stream helps to simulate the entrainment effect with required preheating. Swirling motion of flow helps primarily to stabilize the flow fields in such cases and internal entrainement of products happens due to the existence of inner and corner recirculation zones. Note that, dilution with CO_2 or N_2 is different from air dilution (which is standard practice). While the air dilution is performed to achieve lean operation by reducing the global equivalence ratio, the CO_2 or N_2 is performed to reduce the % O_2 in the inlet composition keeping the mixture ϕ constant [73]. Some of the important aspects investigated in relation to swirl-assisted CDC so far are discussed in the following sections.

2.2.3. Study of reactive flow field in Swirl-assisted CDC

Several previous studies involving swirl distributed combustion demonstrated the change in chemiluminescence when the conventional air swirl flame transitions to distributed combustion [39, 65, 66, 69]. Some of the studies captured gradual broadening of reaction zones at different lean equivalence ratios with OH* radical imaging (at 307 ± 10 nm) at with direct flame imaging. Figure 2.8 shows direct flame chemiluminescence intensity distribution at different O_2 levels found in past studies due to dilution of inlet airstream with N_2–CO_2 mixture exhibiting lower chemiluminescence intensity due to reduced flame radiation. As observed, the traditional shape of the swirl reaction zone disappears gradually when dilution is applied.

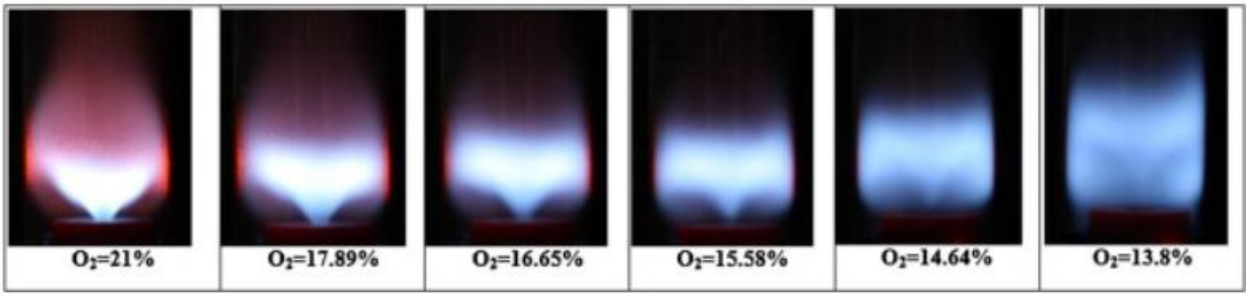

Fig. 2.8. Direct flame imaging at different %O_2 levels and lean $\phi = 0.9$ [66].

At different lean ϕ values, a similar trend was observed for the flame shape. Note that the hotspots and spatial color gradients in swirl air flame gradually diminished to a ver uniform reaction zone with reduction in % O_2 due to dilution. At O_2 = 14.64 and 13.8%, highly distributed, low luminoscity volumetric reaction zone was observed at $\phi = 0.9$. Such reaction zones were generally referred as CDC.

In addition to invetigations of chemiluminescence, the location of flame and reactive flow field was studied using PLIF for both swirl and distributed combustion [66, 73, 74]. These studies found significant differences in both cases. For conventional swirl flame, the reaction zone was observed around the shear layer of the entry jet where the velocity fluctuations and OH-PLIF fluctuations coincided. In contrast, the reaction zone located further away from the region of velocity fluctuations around the entry jet signifying the establishment of a uniform thermal field. These works of OH-PLIF also showed the difference in flow field with and without dilution (of CO_2) [73]. Figure 2.9 depicts OH-PLIF signal distribution to compare conventional air swirl flame (at ϕ

= 0.9), CO_2 diluted distributed flame (at ϕ = 0.9), and air diluted swirl flame (at ϕ = 0.6) along with calculated flame boundary (shown by white outline).

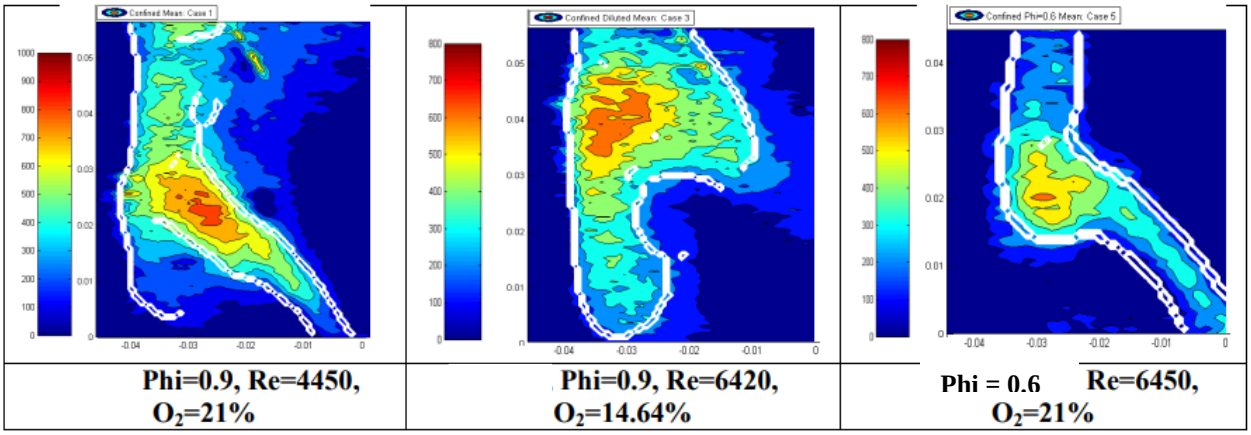

Fig. 2.9. Distribution of OH-PLIF signals in air swirl flame (at ϕ = 0.9 and 0.6) and distributed swirl flame [73].

The authors reported a V-shaped reaction zones for the air swirl flames with and without air dilution. Similar representation was not demonstrated for the CO_2 diluted reaction zone, rather a relatively wider reaction zone was observed. CO_2 diluted reaction zones results in slow reaction rate and thicker flame front in distributed combustion.

2.2.4. Noise reduction in Swirl-assisted CDC

Noise is generally referred to the combustion noise which may signify high acoustics noise level (dB) during combustor operation and may also indicate instabilities. While the reduction of pollutant NOx, CO, UHC and carbon footprints are important considerations, noise reduction is another important challenge for stationary and aviation gas turbines. Past works by Khalil et al. investigated deduction of combustion noise and fluctuation reduction in swirl-assisted distributed

combustion [64, 67]. These studies measured the acoustic responses from the flame in traditional swirl air combustion and distributed combustion using microphone data. The Fast Fourier transformation (FFT) of the acoustic response was measured to obtain the dominant frequency and magnitude of peak amplitude as shown in Fig. 2.10. When CDC was fostered, the peak at ~500 Hz dramatically decreased. In addition, the frequencies at the 200 Hz range were significantly reduced at an oxygen concentration of 15.58% and below until that disappeared in CDC (O_2 = 13.8%). Hence, it was evident that CDC played a key role in combustion noise reduction. The study of oxy-methane swirl distributed combustion (with CO_2 dilution) in ref. [67] was intended to find out the stability regime in oxy-combustion combined with CDC with global oxygen varying between (O_2 = 12- 38%).

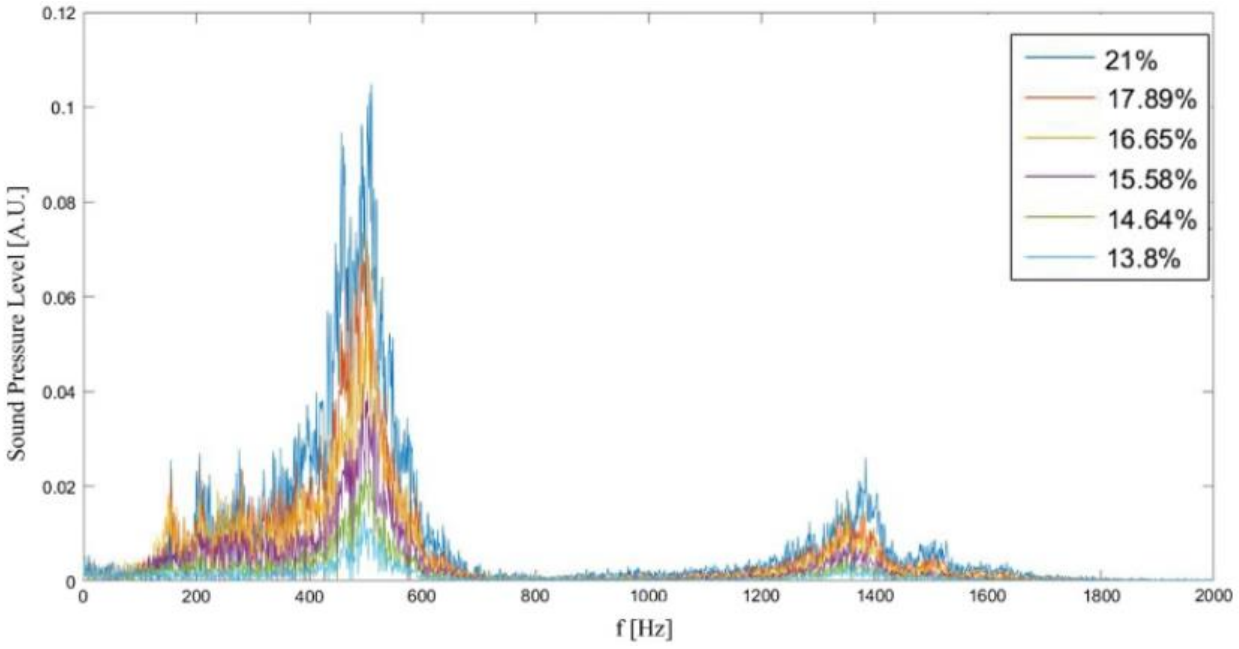

Fig. 2.10. Acoustic frequency response for different Oxygen concentrations with N_2-CO_2 dilution [64].

According to the findings, the majority of the heat release fluctuations for oxy-CO2-fuel combustion happened below 60 Hz. Increasing CO_2 dilution caused flame fluctuation to rise in amplitude up to a maximum of 28% O_2 concentration in the oxidizer. A more steady flame in CDC resulted with further increase in dilution gases lowering in O_2 concentrations. The region of fluctuation was also identified. The oscillations were contained to the flame's outer recirculation zone and shear layer with O_2 concentrations between 35% and 31%. For O_2 = 30%–28% range, the entire flame oscillated and changed from one mode to another with large oscillation amplitude. Another mode was identified with relatively stable operation in the range of O_2 = 26%–23% with further dilution. The flame began to move downstream and back upstream while retaining its general shape when the oxygen content fell below 23%.

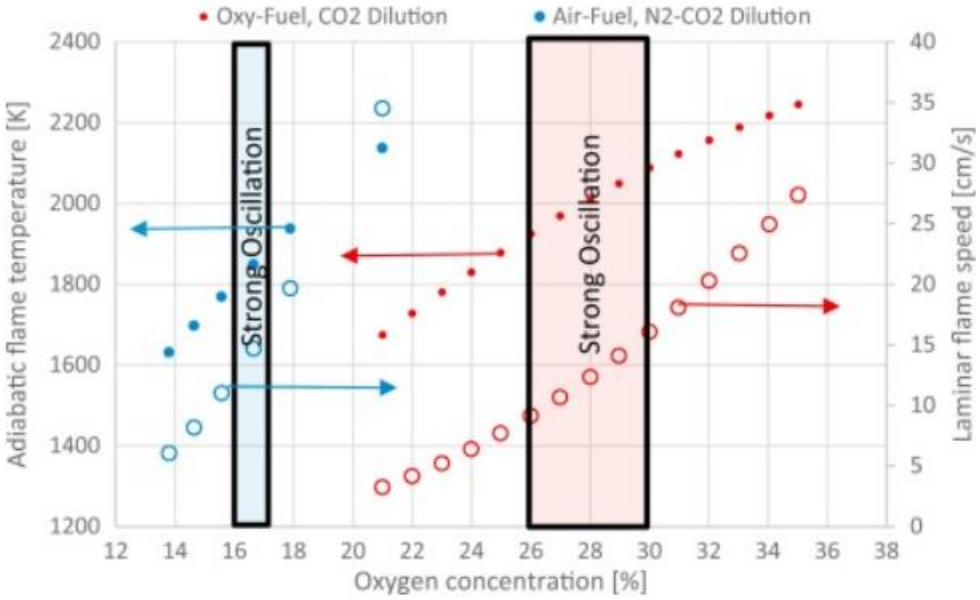

Fig. 2.11. Strong oscillations regimes identified for both flames for N2-CO2 diluted CH4-air and CO2 diluted CH4-O2 flames with adiabatic flame temperature and laminar flame speed variation at different oxygen concentrations [67].

The work by Kahlil and Gupta [64] also tried to qulitatively indicate possible existence of thermo-acoustic behavior in swirl combustion and its decline in CDC. Thermo-acoustic nature was predicted by observing the existence of a common peak frequency of heat release and acoustic pressure fluctuation. However, no detailed explanation of pressure and heat release fluctuations (in and out-of-phase oscillation) was provided. Figure 2.11 showed the variation of adiabatic flame temperatures between 1924 and 2088 K and flame speeds between 9 and 16 cm/s indicating strong oscillations between O_2 = 26 to 30% . The authors attributed such observations of the O_2 range to the favorable density gradient and the beginning of the flame transfer to the outer recirculation zone. The adiabatic flame temperature for the intermittency range (ϕ = 0.61-0.65) was reported as 1682-1753 K, which is a little lower than the range shown in Fig. 2.11 for methane-air.

2.2.5. Distributed Combustion Index

Efforts were made to develop a distributed combustion index (DCI) using parameters such as recirculation ratio (of reactive species), injection velocity, air and fuel injection configuration, and operational equivalence ratio, temperature and pressure by Khalil and Gupta [75]. They reported that the late injection of fuel resulted in a diffusion flame with high emissions and premature ignition of air and fuel due to improper entrainment of hot recirculated reactive gases resulting in formation of conventional thin flame front and hot spots. The influence of the operating conditions, equivalence ratio and operating temperature on the distribution index was also investigated to come up with an expression of DCI. Numerical simulations were performed to verify the possibility of using relations for prediction of the pollutants emission at various operational conditions to save both experimental time and costs. They found similar trends

between the obtained correlations and recorded measurements. Later Karyeyen et al. extended the work on DCI development for both N_2 and CO_2 diluted inlet airstream using more parameters such as different oxygen concentrations, varying equivalence ratio, heat release intensity and mixture temperature [76]. This study is based on NO ppm at different dilution levels with and without preheating. For various lean equivalence ratios (ϕ =0.6- 0.9), the NO concentration was found to gradually decrease with dilution of CO_2/ N2. The outcome of this research predicted the transition O_2 concentration for CDC operation with respect to ϕ, preheats temperature to develop the DCI for different dilution cases.

2.3. Data-Driven Investigation in CDC:

In this research, we explored a purely data-driven approach to predict combustion parameters and recognition of combustion states with deep learning (convolutional neural networks). Artificial neural network (ANN) is a popular data-driven predictive modeling framework which can be reliably used to predict output parameters in combustion conditions [26]. The ANN involves multi-layer perceptron (MLP) network architecture [77] and used for data classification and regression analysis. The MLP uses input and output layers with at least one hidden layer in between and information is fed forward (from the input layer to the output) so that to make the final prediction. ANN has been utilized in combustion engineering ranging from IC engines to swirl flames for predicting combustion temperature and pollutants emissions. ANN has already been used to forecast several parameters, including scalar dissipation rate, EINOx emission, etc., in earlier investigations of premixed flames [78, 79]. ANN and other predictive methodologies such as Response surface methodology (RSM) were examined by researchers in the past [80] to estimate

brake thermal efficiency (BTE), brake specific fuel consumption (BSEC), and nitrogen oxides (NOx) from a biodiesel-ethanol fueled single cylinder engine. According to their findings, the ANN model predicted data with reduced statistical errors and significantly higher agreement between experimental and predicted data than the RSM. Niu et al. [81] used Support Vector Machine (SVM) and ANN modeling to analyze the performance characteristics of marine diesel engine combustion (efficiency, fuel consumption, pollutants emission). They discovered that SVM offers a better prediction model for little datasets. In the past, swirl flame imaging and ANN modeling were used to detect flame temperature and NOx content [82]. In this study, ANN was used for the probabilistic classification of combustion states. Images intensities were correlated with experimentally measured NOx concentration to determine any possible connection between them using feature extraction. Other studies [83, 84] have concentrated on using experimental data to forecast the efficiency, exhaust temperature, and pollutant emissions from engines and gas turbines. Adewole et al. [85] also used simple ANN modeling to forecast the flame temperature and pollutants emission for a low-swirl burner design using the equivalence ratio and swirler vane angle as inputs. Hence, the use of machine learning in combustion research is steadily growing to predict various combustion parameters. However, data-driven approach has not yet been investigated much in distributed combustion. This research was aimed at developing a predictive modeling approach based on past reasearch in the field of machine learning (regression and classification) to help developing a data-driven prediction approach for smart virtual sensing and perception of combustion regimes.

Chapter 3: Experimental Methodology

This chapter describes the design of the experimental combustion facility and different experimental diagnostics employed during this research. The following sections include a detailed description of the experimental swirl burner, different instruments employed to measure various combustion parameters and flow field conditions studied.

3.1. Design of the Experimental Facility

The current facility mimics the can combustors in gas turbines with swirl stabilization. The burner has a circular foundation with a projected outward nozzle exit of height ~20 mm from the foundation. The diameter of the nozzle exit (D) is 20 mm. The exit nozzle is fitted in a 60 mm internal diameter and 200 mm long transparent quartz tube. Hence, the effective length of the combustor was 180 mm. The combustion takes place within the quartz confinement. The quartz being transparent provides the necessary optical access for laser-based diagnostics and imaging. The top part of the quartz enclosure is covered with an aluminum section having a central opening (creating ~50% area reduction) for the exhaust gases. Figure 3.1 provides the 3-D representation of the model burner along with its cross-sectional view. A cross-sectional view of this combustor setup included in appendix C.

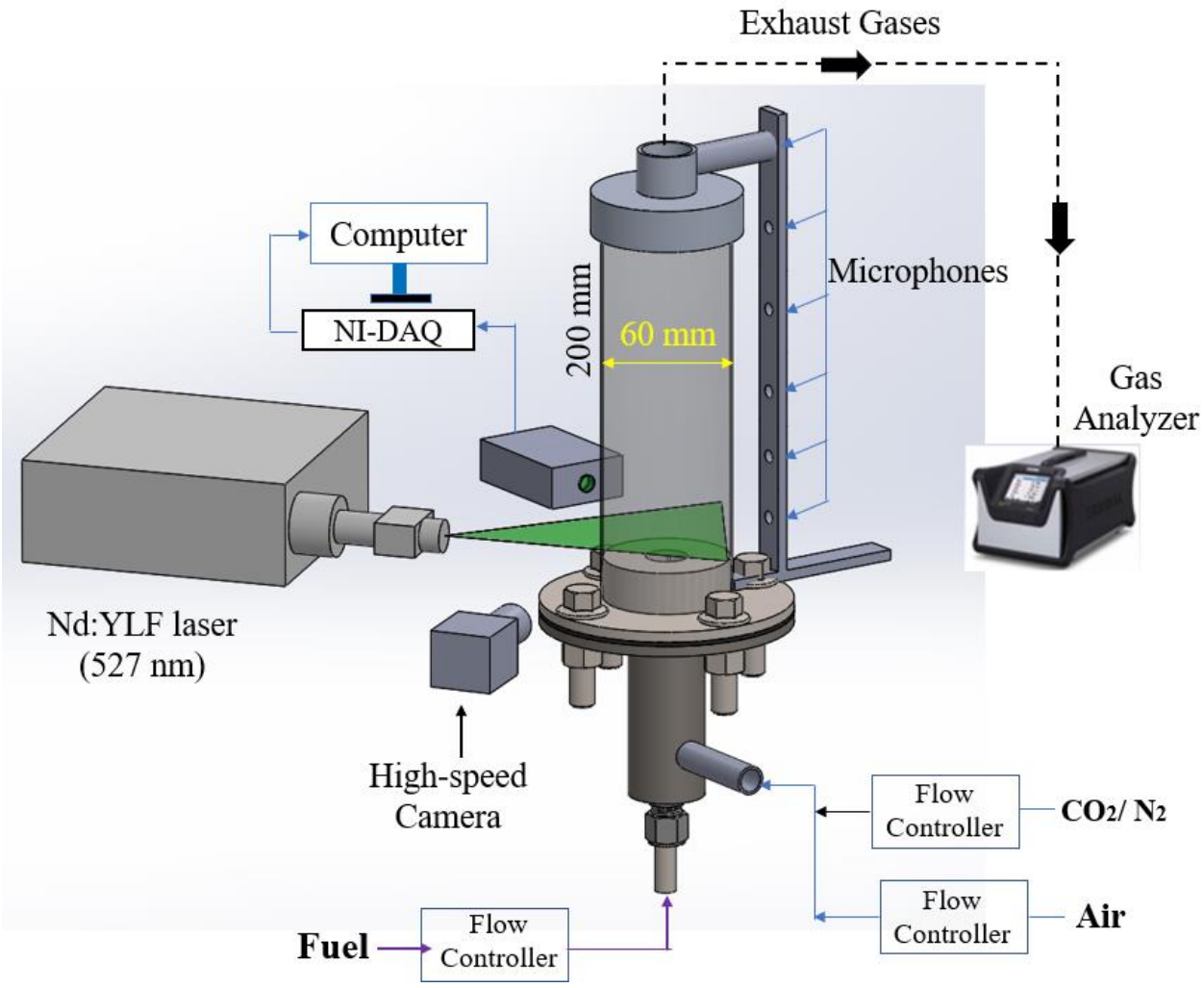

Fig. 3.1. 3D model of the experimental swirl combustion facility.

This burner involves a swirler having a swirl vane angle ($\theta = 45°$) located in the air passage near the nozzle exit. Figure 3.2 shows the image of the swirler used in this research. The function of a swirler is to distribute the momentum of an incoming fluid stream in tangential and axial direction. Hence, the nature of the flow becomes very three dimensional having a helical core [6]. Generally, the strength of a swirling flow is defined in terms of swirl number. By definition the swirl number (S) is defined as the ratio of tangential to axial flux of momentum [6].

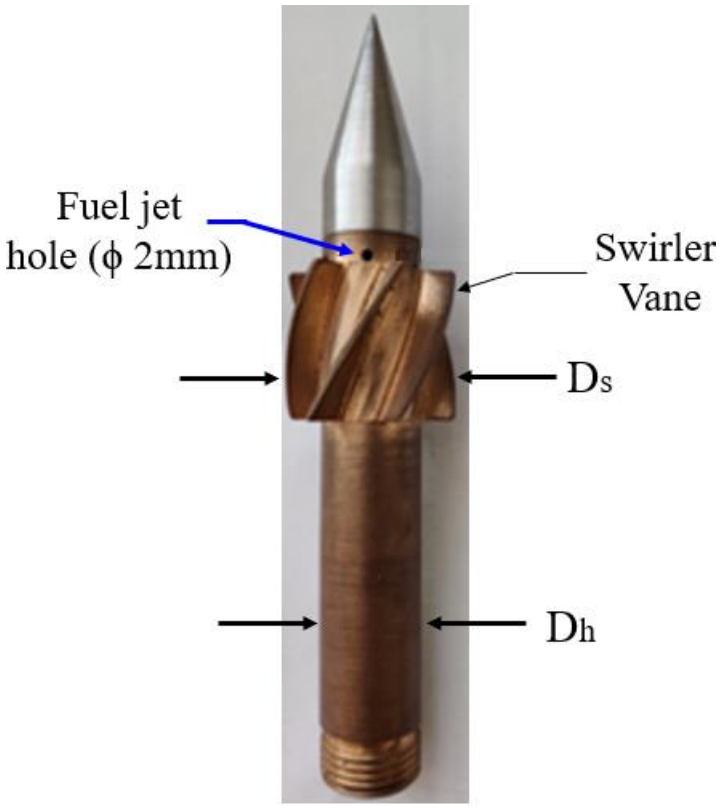

Fig. 3.2. Photograph of the swirler used in this research.

The swirl number is also calculated in terms of the characteristic diameter of the swirler. If D_s and D_h are the swirl diameter and hub diameter of any given swirler, then the swirl number is given by:

$$S = \frac{2}{3}\left(\frac{1-\left(\frac{D_h}{D_s}\right)^3}{1-\left(\frac{D_h}{D_s}\right)^2}\right)\tan\theta \qquad (3.1)$$

For the present configuration, $D_h / D_s = 0.5$, which results in a swirl number S = 0.77. If the conical shape at the top of the swirler (where the hub diameter goes to zero) is considered, the swirl number S can be approximated to $S = 2/3 \tan\theta$. This yields a swirl number S = 0.66.

The experimental facility is equipped with different instrumentation facilities such imaging cameras (iCCD and CMOS), monochromatic lasers, photomultiplier tube (PMT), microphones for

flame acoustic level measurements, data acquisition devices (National Instruments), laser timing device, and gas analyzer for real-time measurement of exhaust gas species, air preheater, electronic flow metering instruments, and data processing computers. The combustor is capable of testing combustion with different gaseous and liquid fuels (kerosene and biofuels). The current dissertation primarily focused on the utilization of important gaseous fuels such as propane, methane, hydrogen, and hydrogen enriched fuel blends with an objective of studying fuels with low-carbon and zero-carbon content and with good burning characteristics.

3.2 Flow-metering Instruments

The flowrate of diluent carbon dioxide input was metered using an AALBORG gravimetric flow controller (having an accuracy of ± 1.5% full-scale reading, repeatability ± 0.25% full-scale reading) with the scale being 0-15 SLPM. The primary airstream was controlled using an OMEGA flow controller with an accuracy of ± 0.8% of the reading, and ± 0.2% of full scale reading with full scale being 1000 SLPM. The carbon dioxide was mixed with main air at far upstream of the nozzle exit to allow adequate time for good mixture preparation before introducing in the combustor.

3.3 Camera System

High-speed imaging of the reaction zone at different conditions was obtained using the IDT OS9 high-speed camera (incorporated with a 50 mm, f/1.2 Nikkor lens) at 3 kHz framing rate. While the image acquisition performed well without any spectral filtering, a 527 nm bandpass filter (bandwidth 20 nm) was applied during imaging. Spectral filter was found to be more

important in reactive diagnostics (to filter out chemiluminescence signatures from the flame) and it was not required in non-reactive cases.

3.4. Microphone

Small microphones were positioned around the burner's edge to gather the acoustic data. The microphone placed at the exit opening of the burner provided the best signal-to-noise ratio (SNR). Another microphone located farther away from the experimental setup continuously recorded the background noise signal. The background noise was subtracted from the recorded signals and the results obtained are presented here. A high-speed data acquisition (National Instruments DAQ system, NI-9324) was used during the experiments. The data acquisition was performed using LABVIEW software at a sampling rate of 25 kHz. The microphones were calibrated with known signals from a microphone calibration system.

3.5. Laser Hardware and Related Software for Processing

A Litron LD30-527 PIV pulsed laser (Nd:YLF) was used to create the laser sheet. A planar laser sheet was generated from the 527 nm wavelength laser beam having a diameter of ~1 mm using sheet forming optics.

3.6. Particle Image Velocimetry (PIV)

Non-reactive flow field has been studied using particle image geometry (PIV) for both swirl-assisted air combustion and distributed combustion. PIV system is composed of the Litron high-speed laser system coupled with the frame-straddling 416 x 688 pixel high-speed IDT OS9 camera

that operated at 3000 frames per second acquisition rate. A fluidized bed seeder was used for flow seeding in this study. Alumina (Al_3O_2) seeding particles with a nominal diameter of ~3 μm were used. The % seeding air was calibrated to get the required seeding density as needed. The seeding air percentage was ~15 % that was bypassed from the main airstream and mixed downstream to keep the total flowrate constant. The pulse separation between the laser pulses (50 μs) was decided depending upon the mean flow velocity in different combustion conditions. The Mie scattering images were processed using the Provision- XS (IDT) software package. A 24x24 pixel interrogation window was considered by default by the processing software that uses cross-correlation algorithm. The spatial resolution of the velocity field was 0.2 mm/pixel. In this study, high-speed PIV was utilized to extract better features of the flow field that is generally not possible to derive a low processing frequency. Also, it was found in our study of mitigation of thermo-acoustic instability that a peak frequency at 176 Hz was responsible for such instability in swirl flame in this combustor configuration. Additionally, higher frequency modes were also observed related to the acoustic modes of the combustor. Hence, a low-speed laser system was not employed in this study. Different number of image pairs in the range 5- 3000 were processed to obtain desired velocity profile of the swirl flame. Figure 3.3 demonstrates the axisymmetric velocity profiles derived by processing different image pairs. The accuracy of results obtained with different varying image pairs was examined by the relative changes in velocity (change in velocity = velocity obtained with image pair 1 - velocity obtained with image pair 2) as shown in fig. 3.4.

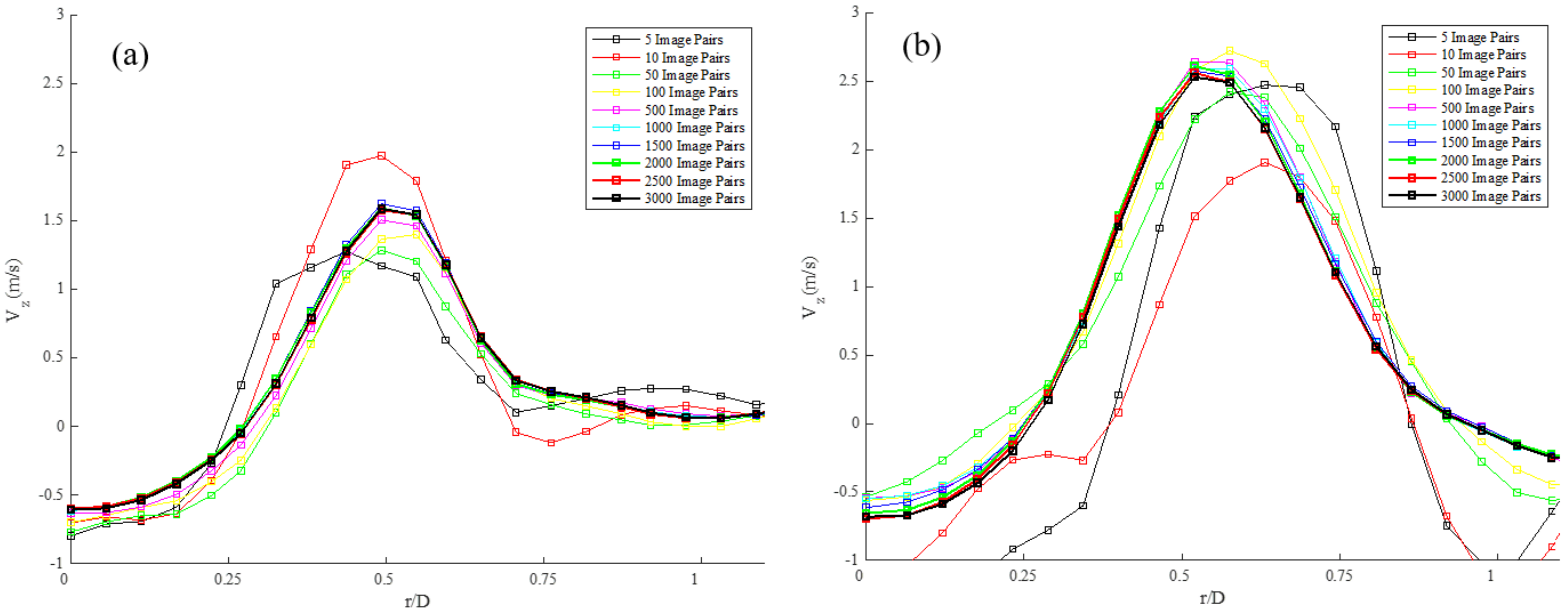

Fig. 3.3. Axial velocity profiles generated with different number of image pairs for (a) swirl air combustion and (b) swirl distributed combustion.

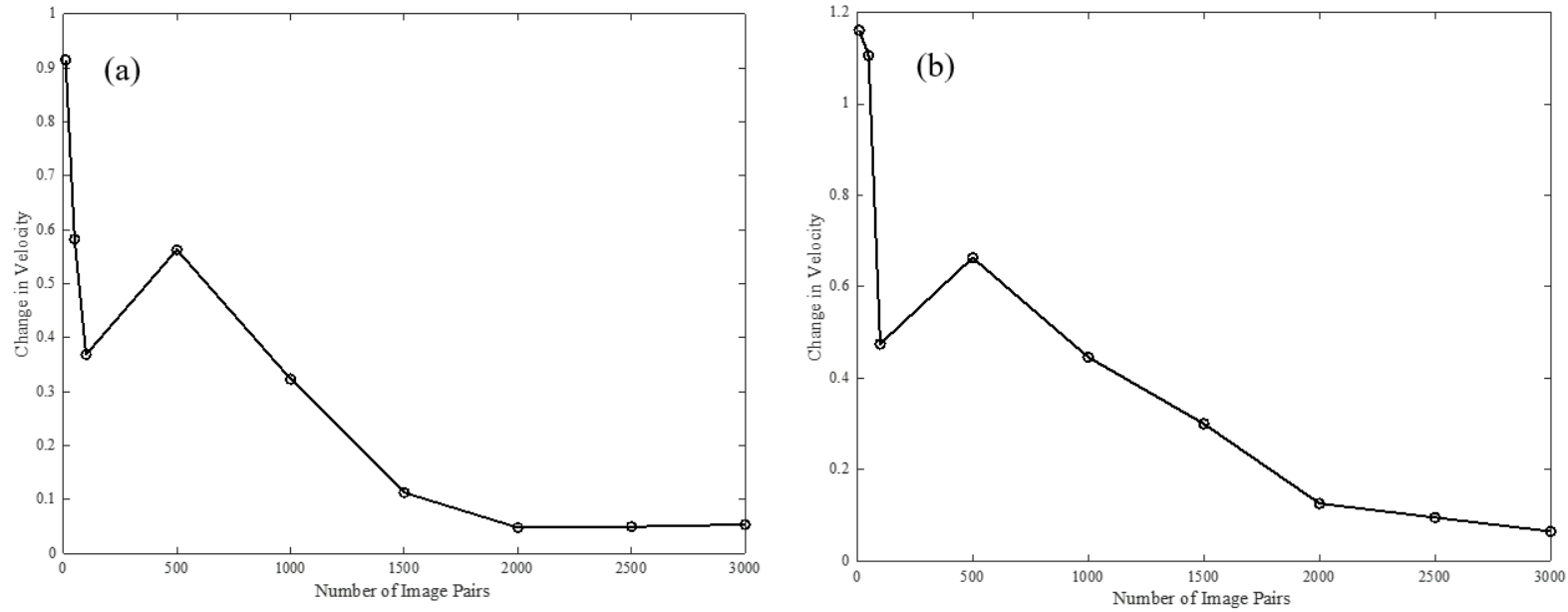

Fig. 3.4. Relative changes in axial velocity magnitudes between consecutive image pairs for (a) swirl air combustion and (b) swirl distributed combustion.

From the fig. 3.3 it can easily be observed that the velocity profile of the swirl air flame and the swirl distributed combustion is distorted with low number of image pairs (< 500 pairs) due to under sampling of the data in both cases. Above 1000 image pairs the profiles looked reasonable. However, the accuracy of velocity data needed to be verified to decide the optimized case. From the fig. 3.4 the relative change in velocity magnitude was observed. For swirl air combustion, the relative differences were mitigated with 2000 image pairs onwards. However, the swirl distributed combustion showed continuous decrease in relative velocity up to 3000 image pairs. The least value change of velocity was observed at 3000 image pairs. Hence, 3000 image pairs were considered to the be optimized case for the post processing while maintaining the Nyquist Stability Criterion [86].

Chapter 4: Flame Structure and Emission in Distributed Combustion

Study of flame shape evolution in distributed combustion was of great fundamental interest. This chapter primarily focuses on appearance of swirl distributed combustion with gradual mixture preparation using flow field dilution with CO_2 and N_2 resulting in distributed reaction within the swirl combustor. The flame shape is determined using the OH* chemiluminescence signal distribution captured with iCCD imaging adapted with spectral filtering at 307±10 nm. The spatial and structural evolution of different gaseous hydrocarbon flames along with their distributed behavior in the swirl combustor was investigated using the flame boundary approach.

4.1. Flame structure evolution while approaching distributed combustion regime

Flame shapes at different O_2 concentrations were examined using propane, methane, and hydrogen enriched methane-oxidizer compositions. Figure 4.1 shows different flame shapes using normal air (at O_2 ~ 21%) without any diluent. The spatial distribution of OH* chemiluminescence intensity are presented in color bar with a scale of 0-1000 a.u.

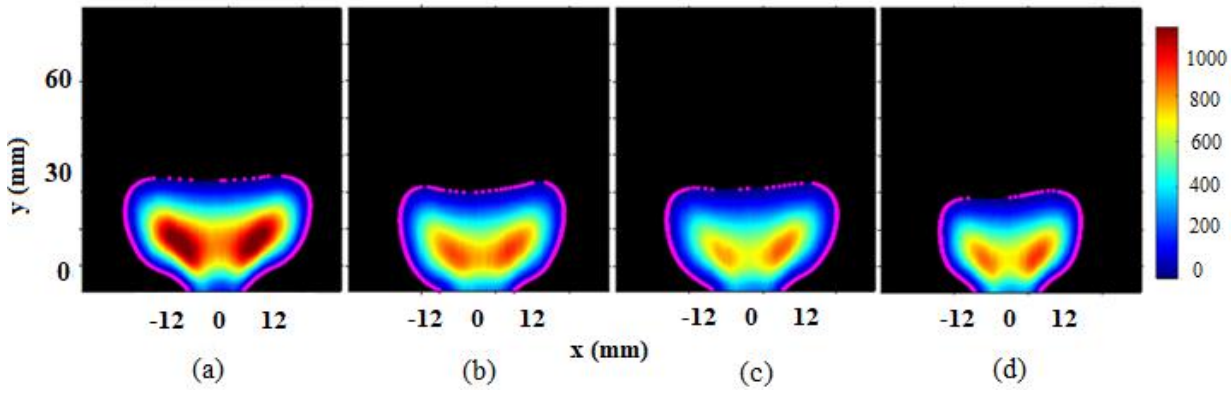

Fig. 4.1. Representation of undiluted (a) propane (b) methane (c) 20% HEM, and (d) 40% HEM flames using normal air as the oxidizer (at O_2 ~ 21%).

The results depict the expected luminosity of propane-air swirl flame to be higher than the corresponding methane or hydrogen-enriched methane flames. Higher energy release per unit volume of propane-air flame than the methane-air flames [87] provided high OH* chemiluminescence signal intensity (strongest at the center), see Figs. 4.1. a and b. Hydrogen enriched methane flames showed a gradual decrease in flame length, as compared to propane and methane flames. This is attributed to enhanced reactivity and higher flame speed of the combustible mixture associated with the increase in hydrogen content to methane. Similar observations of reduced flame length were reported in the previous studies [88, 89] of hydrogen enriched methane swirl flames. To further understand the flame shape and size, two-dimensional flame area was evaluated from the chemiluminescence images of different fuel mixtures under normal air-combustion condition (O_2 ~ 21%). The results are shown in table 4.1.

Table 4.1. Calculated flame area of different flames using normal air as oxidizer

Fuel-air	Propane-air	Methane-air	20% HEM	40% HEM
Area (mm^2)	1034.91 ± 10	895 ± 7	888 ± 5	712 ± 5

The results on flame area shown in table 4.1 manifests that the burning area (or volume in three dimension) for the propane-air composition is highest among all the different hydrocarbon flames reported here.

The gradual transition of flames to CDC mode was examined using OH* chemiluminescence imaging at different flow dilution levels (using CO_2 or N_2). Figure 4.2 exhibits the shape and relative location of the different flame boundaries for each O_2 concentration using CO_2 as the diluent. Decrease in O_2 concentrations provided a gradual broadening of the flame area. Such widening of the flame is accompanied with a gradual decay of the concentrated OH* zone (red)

near the central part of the flame (see Fig. 4.2a, at O_2 ~ 21%) to a uniformly distributed low intensity signal extended over the entire flame volume (see last column of flames in Fig. 4.2). This indicates that the flame gradually approached distributed combustion regime. Similar observations on flame widening and near colorless swirl flame in distributed combustion were reported in ref. [90]. The reduction in spatial concentration gradient of OH* with the decrease in O_2 level in the fresh mixture signifies a gradual reduction of reaction rate per unit flame volume to increase the net burning volume of the flame. A nearly uniform OH* signal distribution for propane flame occurred at O_2 ~ 17%, whereas it occurred at 18% for methane flame. The flame images at O_2 = 16%, correspond to final unextinguished state in the reactive flow field. Global flame extinctions were observed at O_2 < 16% with a slight change in blow-off equivalence ratios (ϕ_{bo}) among the fuel-oxidizers examined. The ϕ_{bo} for propane flame was observed to be higher than methane and HEM flames. The reduction of reaction rate due to the addition of diluent caused decrease in flame speed and hence, the flame lifts off from the burner exit plane. Lift-off caused the shape of flame base to gradually change from point shaped flame to a nearly flat shape. For the propane and methane flames, the pointed base was observed up to O_2 = 16%, which is attributed to near blow-off flame quenching. A similar flame evolution was demonstrated in Fig. 4.3, using N_2 as the diluent gas. Gradual flame broadening with decrease in visible flame signature, flame lift-off with flow dilution (or decreasing O_2 concentration) are consistent with the previous observations made using CO_2 as the diluent gas. The flame blow-off limits extended with N_2 dilution (see Fig. 4.3). Stable flame was observed until O_2 = 14% (while it was 13% for 40% HEM fuel) unlike CO_2 dilution case where the flame sustained only up to O_2 = 16%. This was attributed to higher heat capacity value of CO_2 as compared to N_2 which provided greater reduction of flame speed and the overall temperature [91] at a relatively higher O_2 concentration. Hence, the N_2 diluted flow field

provides stable flames over an extended range of O_2 concentration due to its delayed transition to CDC mode as compared to the CO_2 dilution case.

The flame lift-off heights (h) at different O_2 concentration using the two different diluents are presented to help understand the stability and reactivity of swirl-stabilized flames.

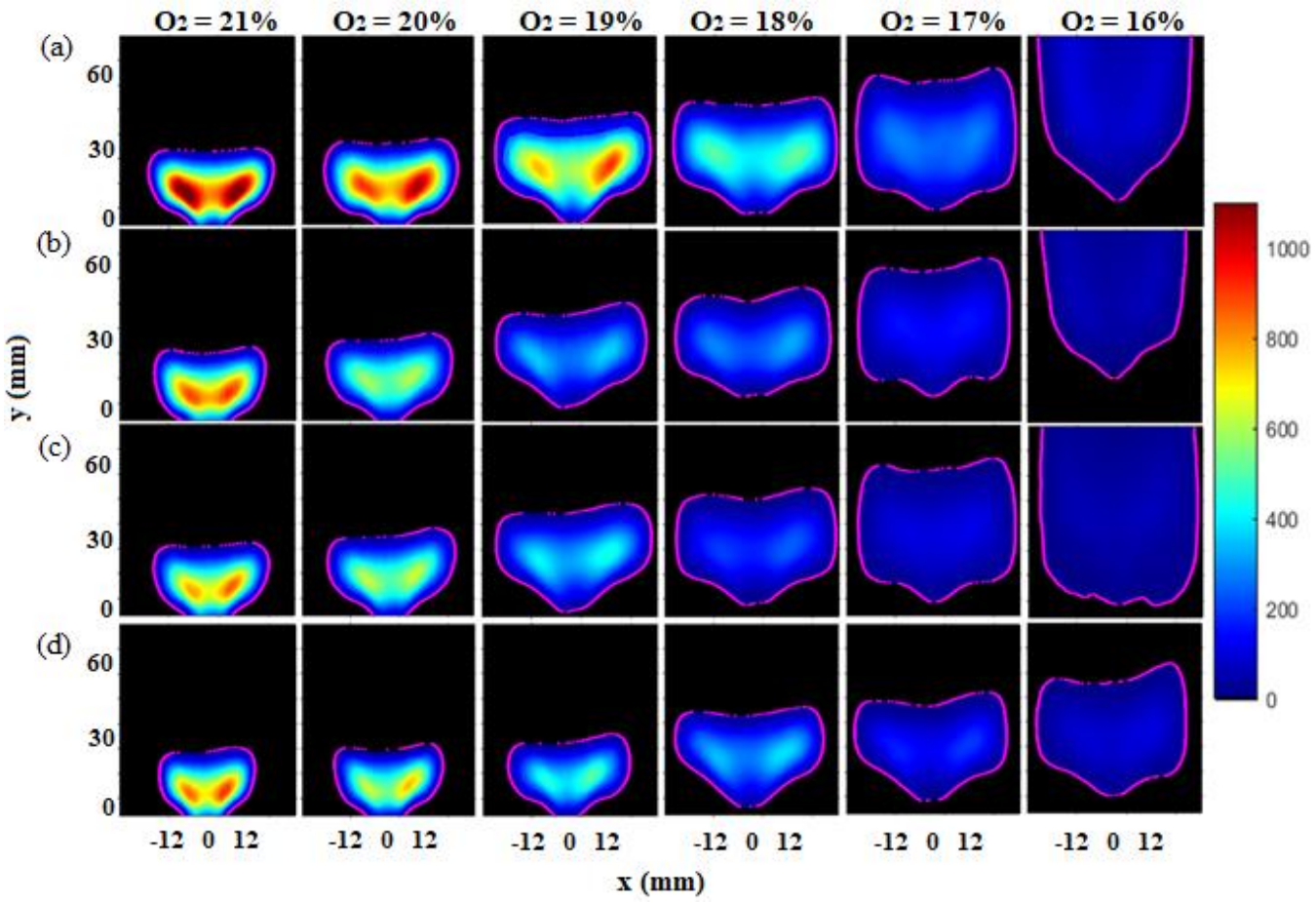

Fig. 4.2. OH* chemiluminescence with overlaid flame boundary for (a) propane, (b) methane (c) 20% HEM, and (d) 40% HEM flames at different O_2 concentrations using CO_2 as diluent.

The normalized lift-off height (with respect to the burner exit diameter, D) were evaluated from the distance between the burner exit and flame base as marked by the derived flame boundary

for each flow condition. The results are represented in Fig. 4.4. The results show that below a certain threshold value of O_2 concentration (~ 20% for CO_2 and 19% for N_2 diluted cases) all flames reveal some lift-off from the burner exit. The lift-off heights for the CO_2 diluted flow field are higher than the N_2 diluted flow field. As mentioned earlier, the higher heat capacity of CO_2 provided greater reduction of flame speed and subsequently, higher flame lift-off heights than the N_2 dilution case. The methane flame revealed the highest lift-off value for both the diluents. This was conjectured to be associated with the reduction of mixture reactivity, which was highest for methane as compared to other fuels for every O_2 concentration reported here.

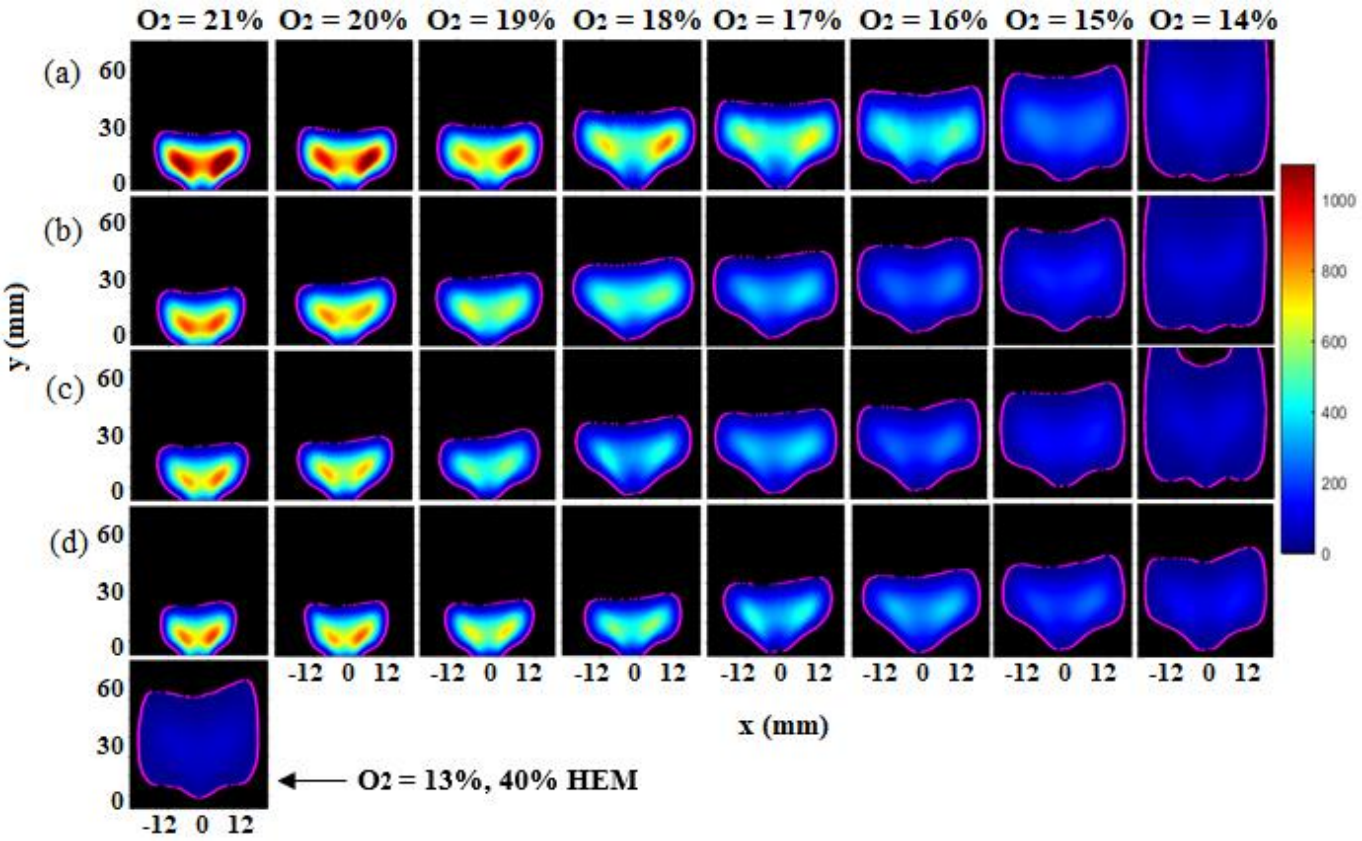

Fig. 4.3. OH* chemiluminescence with overlaid flame boundary for (a) propane, (b) methane (c) 20% HEM, and (d) 40% HEM flames at different O_2 concentrations using N_2 as diluent.

The reduction in flame speed for methane mixture was highest among the fuels that resulted in largest flame lift-off distance for all O_2 concentration examined. Hydrogen enriched methane flames showed less flame lift-off height than pure methane flame. This is directly attributed to increased reactivity and the flame speed due to the addition of H_2 with methane, which helped to stabilize the flame close to the burner exit.

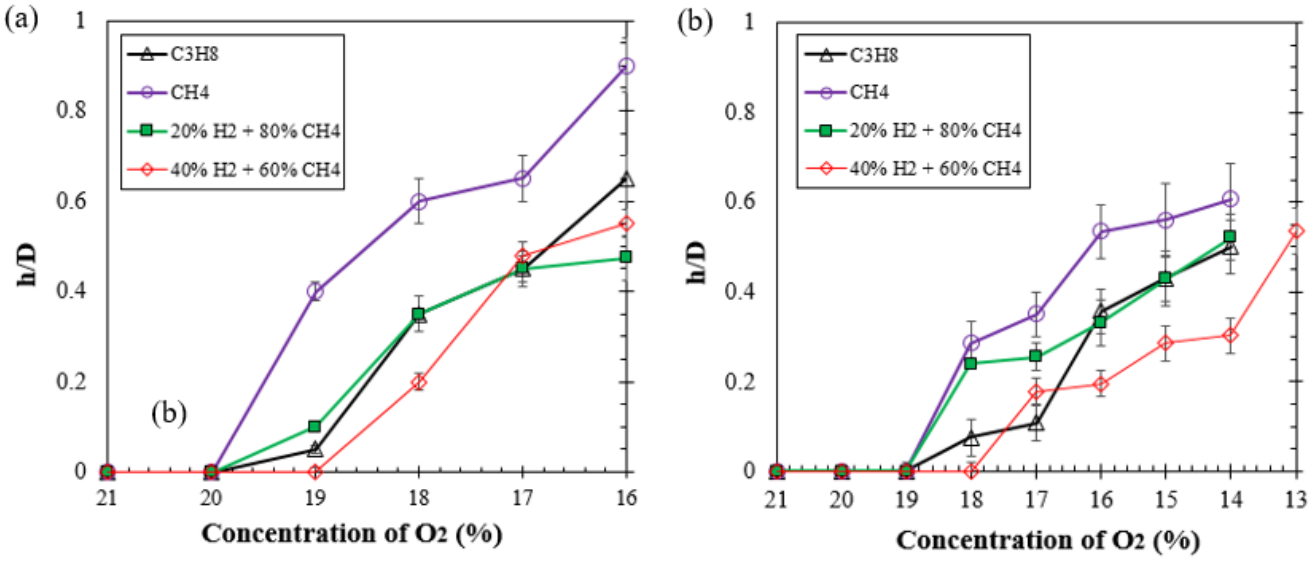

Fig. 4.4. Normalized lift-off heights for different fuel-oxidizer flames at different O_2 concentrations with (a) CO_2, and (b) N_2 as inlet flow diluent.

4.2. OH* signal intensity-based CDC mode detection

Chemiluminescence signal intensity variation at different O_2 concentrations was analyzed to detect the initiation of CDC. The ratio of rms to mean OH* signal intensity (I_{rms} / I_m) was measured for every O_2 level and presented in Fig. 4.5. Propane flame images are overlaid on the plot to compare the spatial intensity variation corresponding to different O_2 levels. The highest

intensity fluctuation (rms = 20-25% of mean intensity) is observed in air combustion condition (O_2 ~ 21%) for different flames. Propane flames have the highest I_{rms} / I_m values, signifying a relatively higher spatial OH* intensity variation than other flames. The value of I_{rms} / I_m gradually decreased with decrease in O_2 concentration of the fresh reactant mixture for both CO_2 and N_2 diluted flow cases. Such reduction in rms intensity fluctuation was expected from the gradually diminishing of spatial gradient of OH* distribution to form uniform spatial distribution approaching CDC. The slope of the I_{rms} / I_m curves gradually changed to zero at $O_2 \leq 17\%$ and 15% for CO_2 and N_2 dilution cases, respectively.

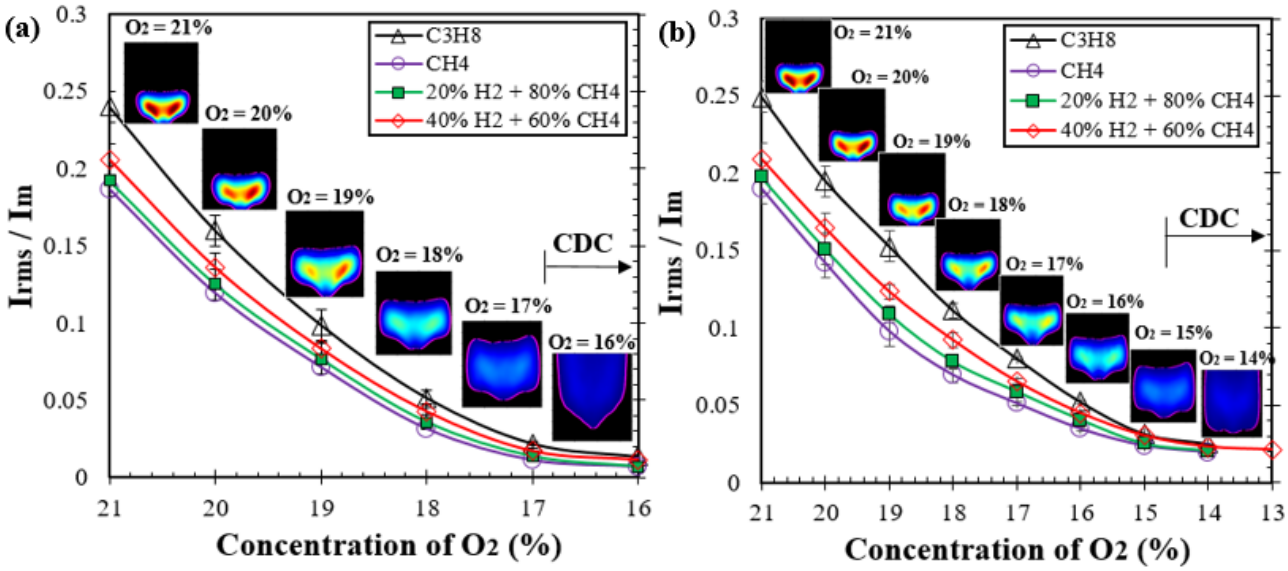

Fig. 4.5. RMS to mean OH* signal intensity (I_{rms} / I_m) variation with O_2 concentrations for different flames with (a) CO_2, and (b) N_2 as inlet flow diluent. (Propane flames are overlaid)

The corresponding rms intensity values of different flames were found to become less than 2% of their mean intensity. This indicated an almost negligible spatial variation of OH* signal in flames below the above given O_2 levels. The uniformity of OH* concentration gradient in CDC is

confirmed from the overlaid propane flame images. The results infer that distributed combustion starts at O_2 ~ 17% and 15% for CO_2 and N_2 diluted flow fields and exists until the flame blow-off.

4.3. Calculation of distribution ratio

A quantitative analysis of the OH* chemiluminescence images help assists to understand the distribution behavior of flames in a swirl burner. Distribution Ratio (DR) is defined as the ratio of the observed flame area (A_f) from the chemiluminescence image at any particular O_2 concentration to the initial flame area (A_i) at normal air condition, O_2 ~ 21%, so that:

$$\mathrm{DR} = \frac{\mathrm{A_f}}{\mathrm{A_i}} \tag{1}$$

The magnitude of A_f was obtained by measuring the area within the flame boundary derived from the chemiluminescence image. The A_i values are given in table 4.1. The concept DR is important to understand the distributed behavior of different swirl flames at transition to CDC. Simultaneous examination of DR and OH* intensity fluctuation (I_{rms} / I_m) is useful to detect the CDC regime in terms of flame expansion. Figure 4.6 shows the variation of DR and I_{rms} / I_m with different O_2 concentrations for CO_2 and N_2 diluted flow field. A gradual increase in DR value was observed with decrease in O_2 concentrations for both diluent gases. The results show the following power-law behavior of flame expansion for both CO_2 and N_2 diluted flow fields:

$$\mathrm{DR_{CO2}} = 445762 * [\mathrm{O_2}]^{-4.273}; \mathrm{R^2} = 0.9998 \tag{2}$$

and,

$$\mathrm{DR_{N2}} = 9414.4 * [\mathrm{O_2}]^{-3.021}; \mathrm{R^2} = 0.9960 \tag{3}$$

At the initiation of CDC mode determined from the OH* signal intensity analysis (in section 3.3), the DR possesses a value of ~ 2.5 for all the flames. This signifies that flames undergo an expansion

of at least 2.5 times of their initial volumes (in normal air combustion) before transitioning to CDC. The different combustion modes for these flames can be expressed by the following DR values:

$$DR = 1 \quad \text{for air combustion } (O_2 \sim 21\%)$$

$$DR \geq 2.5 \quad \text{for distributed combustion}$$

The final values of DR showed significant volumetric expansion of flames under distributed combustion conditions. Expansion of nearly three times of the initial volumes (in air combustion) was found for different flames using CO_2 as diluent while it was more than 3.5 for the N_2 dilution case. Approximate flame distribution can be measured using the above-stated DR models for different diluents. The DR values are more sensitive to the flame edge location at lower O_2 concentration. In CDC mode, an average change of 10.5% of DR value for every 20% offset of threshold value (from Otsu threshold) was noted from the sensitivity analysis.

The above calculation of DR is based on 2D flame areas. Flame areas were obtained by imaging the flame in its mid-plane. This might not always provide a true measure of the volumetric distribution of flames. We calculated the actual volume of the flames by solid revolution of 2D images in Matlab® to calculate a volume-based DR. A multiplication factor (M_c) to convert the mean DR (area) values to mean DR (volume) was calculated, such that:

$$\text{DR (volume)} = M_c * \text{DR (area)} \qquad (4)$$

The DR (volume) and the M_c values are reported in table 4.3 along with the DR (area) values for different flow dilution cases. The volume-based DR from table 3 manifests that the flame expands more than 4 times (for CO_2) and nearly 5 times (for N_2) of their initial volumes under CDC mode. Note that DR may vary with swirl distribution in the burner. The DR values of methane and 20% HEM flames in CDC are higher than the propane flame. This is due to relatively lower A_i values and comparable sizes of these flames to those of propane flame under CDC. The 40% HEM flame

showed a slightly different expansion nature (especially with N_2 dilution) due to its significantly smaller flame shape (A_f) at every O_2 level. Such smaller shape is from the result of high mixture reactivity and flame speed due to higher H_2 content in the mixture. Stable OH* chemiluminescence image for 40% HEM mixture was recorded with up to O_2 = 13% as compared to 14% for other fuel-oxidizer mixtures examined using N_2 dilution.

Table 4.2. DR (volume) and Multiplication factor (Mc) at different flow dilution levels

O_2 (%)	CO_2 dilution case			N_2 dilution case		
	DR (area)	DR (Volume)	Multiplication factor (M_c)	DR (area)	DR (Volume)	Multiplication factor (M_c)
21	1	1	1	1	1	1
20	1.228	1.430415	1.164833	1.109152	1.296279	1.168712
19	1.47	2.058124	1.400085	1.27	1.523972	1.199978
18	1.94	2.673674	1.378182	1.48849	1.999213	1.343114
17	2.48	3.501241	1.411791	1.770545	2.434335	1.374907
16	3.12	4.145295	1.32862	2.11	3.096282	1.467432
15	--	--	--	2.55	3.713924	1.456441
14	--	--	--	3.41	4.861688	1.425715
13	--	--	--	4.12	4.880121	1.184495

Such extension of flammability limit can be explained using the concept of DR and corresponding lift-off information shown in Fig. 4.4. The lifted flame is more unstable than an attached flame and the degree of instability increases with increase in lift-off heights [92].

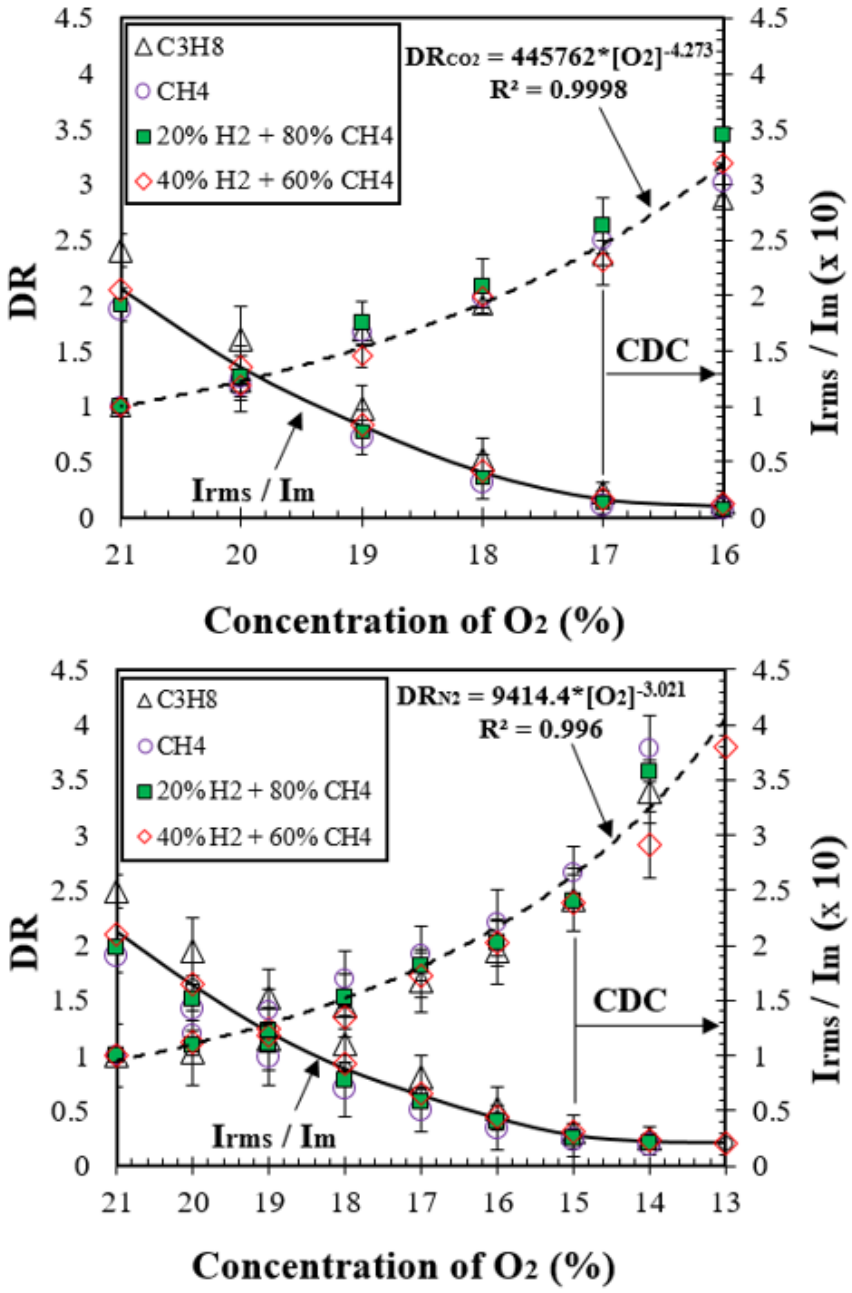

Fig. 4.6. Distribution Ratio (area-based) for different hydrocarbon flames at different O_2 concentrations using (a) CO_2 and (b) N_2 as the diluent.

The normalized lift-off height for 40% HEM with N_2 (see Fig. 4.6 b) dilution is seen to be lower than other flames under consideration. At O_2 = 14%, the lift-off distance of this flame was less than 50% of the other hydrocarbon flames. This revealed that the flame stabilized relatively close to the burner exit. The lowest magnitude of DR (at O_2 = 14%) among different hydrocarbon flames describes a relatively narrow shape of this flame due to an energetic and stable burning characteristic. Such stable burning behavior even at O_2 = 14% helps this particular flame to sustain for longer time.

4.4. NO and CO emission

The emission of NO and CO under normal air combustion and distributed combustion were obtained. The concentrations of NO and CO corrected to 15% O_2 concentration (ppm) under air combustion (at O_2 ~ 21%) are given in table 4.3. Flame temperature has pronounced effect on NO_x formation [93]. The NO emission from methane-air flame is seen to be lower than the propane-air flame which has higher flame temperature. The concentration of NO gradually increased with the increase in hydrogen enrichment to methane.

Table 4.3 NO and CO (corrected to 15% O_2) concentrations in normal air-combustion

Fuel-air	Propane-air	Methane-air	20% HEM	40% HEM
NO (ppm)	20.29	13.23	13.44	13.93
CO (ppm)	56.44	52.12	24.6	28.64

In ref. [89], this increase of NO was attributed to the increase in local flame temperature from hydrogen addition as well as broadening of post combustion zone. The formation of NO and CO was examined in relation to DR at each O_2 concentration to understand the pollutants emission

when approaching CDC. The NO and CO concentrations were normalized with respect to their initial concentrations (given in table 4.3) and expressed as NO* and CO*. Figure 4.7 shows the NO*, CO*, and DR at different O_2 levels using CO_2 as the flow diluent. The variation of DR, NO* and CO* helps to understand the effectiveness of combustion at different O_2 levels. The NO* decreased for every fuel with an increase in flow dilution when approaching the distributed combustion regime. An average reduction of 90% (96% for propane and 40% HEM flames) of the initial NO concentration (under normal air combustion mode) was observed when the flame transitions to CDC. The gradual reduction of NO level is related to the drop in overall adiabatic flame temperature with increasing flow dilution. The adiabatic flame temperatures at different flow dilution levels were supported by using Chemkin-Pro coupled with GRI-3.0 [94] for methane and HEM flames. The results on the average adiabatic temperature of these flames are shown in Fig. 4.8 at different dilution levels for both the diluents. As expected, the average flame temperature gradually decreased with an increase in flow dilution for both the diluents. The rate of temperature decrease was higher for the CO_2 diluted flames due to the higher heat capacity value of CO_2 resulting in greater reduction of temperature with flow dilution. In addition to NO*, the CO* levels were also reduced to about half of their initial values, when flames transitioned to CDC. This is attributed to gradual reduction of varying stoichiometry and sharp temperature gradient (that exist in conventional fuel-air flames) with decrease in O_2 level. An improved mixing and uniformity in combustion is fostered across the combustor which results in reduction of CO*. Note that CO* suddenly increased at some intermediate O_2 levels. This is due to the dissociation of CO_2 to CO at high temperatures. Such a sudden rise in CO level was further investigated using simplified chemical analysis of the present flame. The analysis was performed using Chemkin-Pro coupled

with GRI 3.0 for a sample case of 20% hydrogen enriched methane where such rise (in CO level) was prominent.

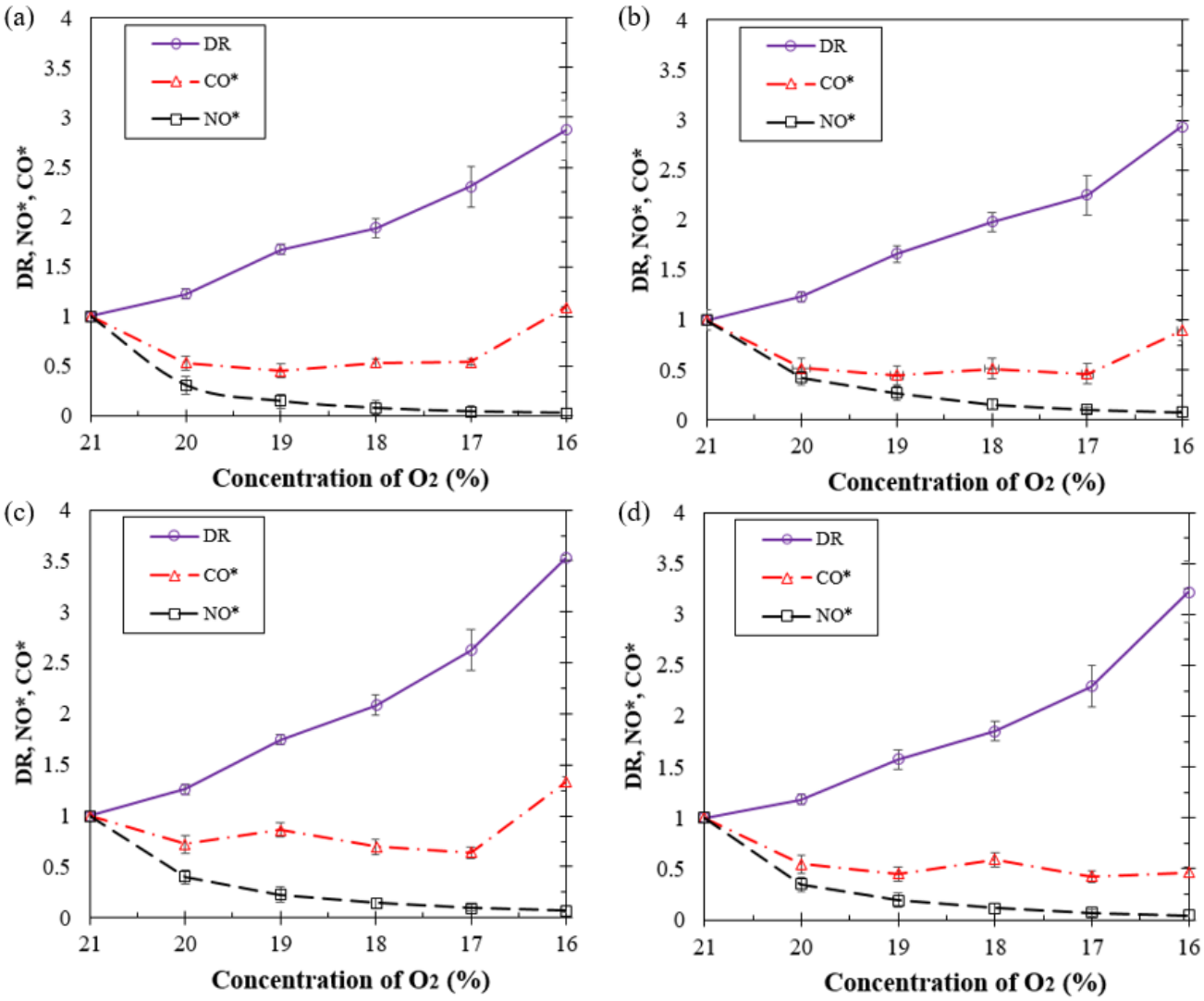

Fig. 4.7. Normalized NO (or NO*) and CO (or CO*) and DR (area-based) for (a) propane, (b) methane, (c) 20% HEM and (d) 40% HEM flame at different O_2 concentrations using CO_2 as flow diluent. (All corrected to 15% O_2 concentrations)

A similar trend of high CO level at intermediate O_2 level was demonstrated by the Chemkin simulation. Analysis of reaction pathways revealed the presence of a particular reaction step: $CH_2(S) + CO_2 \leftrightarrow CO + CH_2O$ for the diluted flow cases. Here the $CH_2(S)$ represents singlet methylene [95].

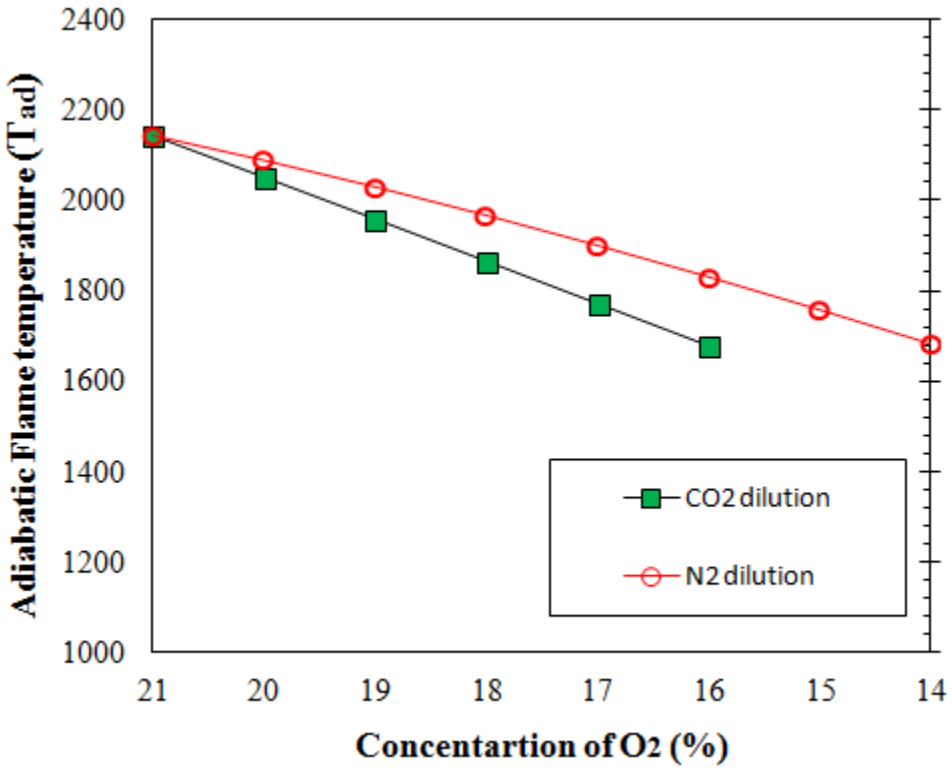

Fig. 4.8. Average adiabatic flame temperature (T_{ad}) at different flow dilution levels for methane and HEM flames.

This specific reaction step was absent in normal combustion mode with pure air as the oxidizer. Additionally, this reaction step was prioritized with an increase in dilution levels. For the O_2 concentrations corresponding to the sudden rise of CO, the direction of the above-stated reaction was in the forward direction that favored the CO formation. This supports the role of this particular reaction step in enhanced CO production. The effect of flow dilution with N_2 on NO and CO

emission was also examined. Figure 4.9 shows the NO* and CO* emission behavior at different O_2 concentrations. The observation commensurate with the CO_2 diluted flow field case.

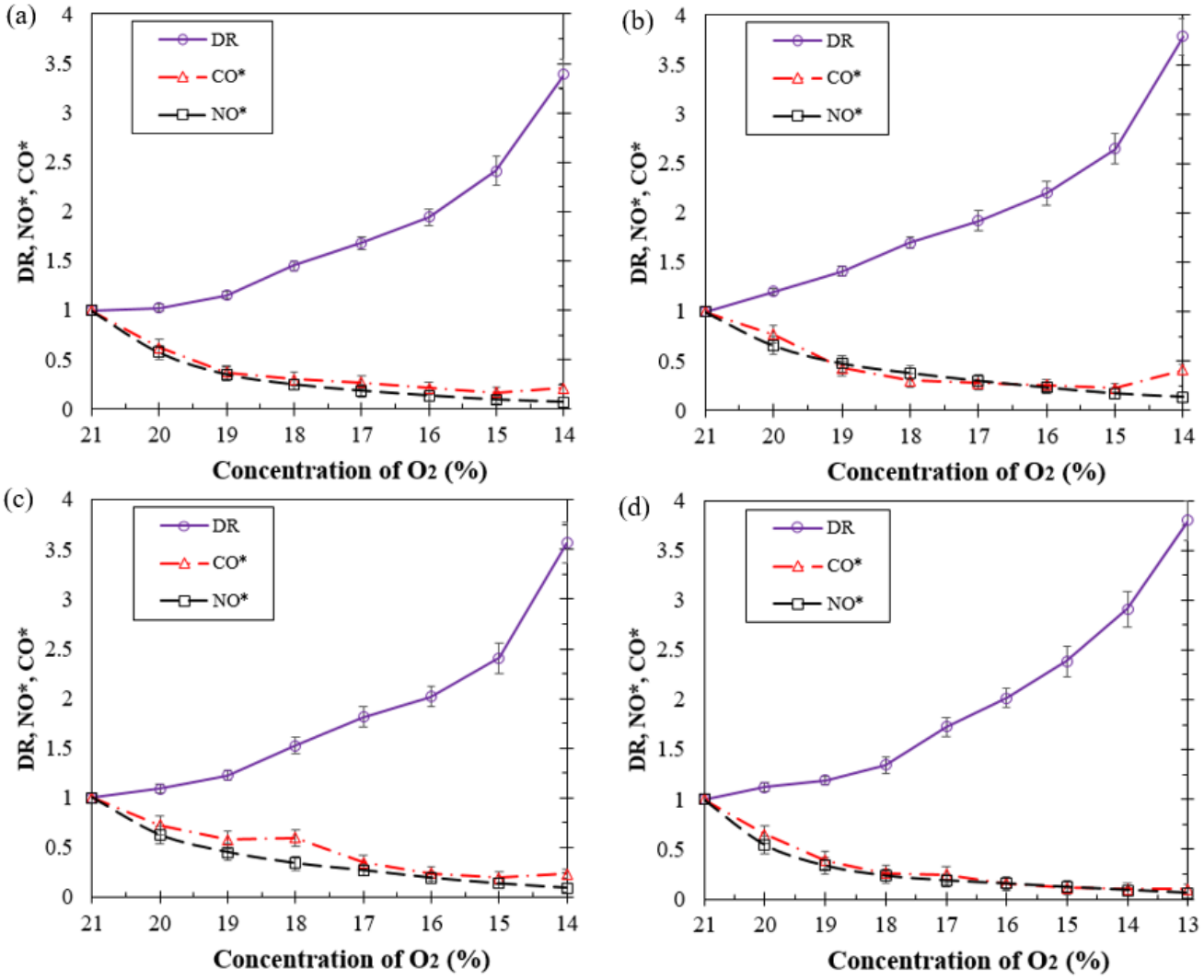

Fig. 4.9. Normalized NO (or NO*) and CO (or CO*) and DR (area-based) for (a) propane, (b) methane, (c) 20% HEM and (d) 40% HEM flame at different O_2 concentrations using N_2 as flow diluent. (All corrected to 15% O_2 concentrations)

Decrease in the O_2 level decreased the NO* and CO* while increasing the DR. The additional CO production from the dissociation of CO_2 at intermediate O_2 levels was absent in N_2 dilution case.

4.5. Summary

Distributed combustion was investigated in a swirl burner (at 5.72 MW/m^3-atm thermal intensity) was carried out using four different gaseous fuels, namely, propane, methane, 20% hydrogen enriched (80% methane) and 40% hydrogen enriched (60% methane) methane. The primary motivation of this study was to understand the global flame behavior and pollutant emission in distributed combustion. Flames were recorded by imaging the OH* chemiluminescence signatures. Resulting flame images were examined at different O_2 concentrations (corresponding to different dilution levels) when approaching distributed combustion condition. The rms OH* signal intensity fluctuation reduced from ~ 20-25% to less than 2% of mean intensity when CDC mode was achieved. Flame expansion with respect to their initial volume (in air combustion) provided a better understanding of the role of chemical composition of different fuels under CDC. The lift-off height for CO_2 diluted CDC flow field was observed to be higher than the N_2 diluted flow field. Higher heat capacity value of CO_2 promoted greater reduction of flame speed that subsequently caused higher flame lift-off. The pollutants emission (normalized NO and CO concentrations) showed a significant reduction when the flames approached distributed combustion mode.

Chapter 5: Investigation of flame fluctuation reduction in distributed combustion.

This chapter characterizes the stability of swirl distributed combustion compared to the conventional swirl air combustion. Results were primarily based on the high-speed chemiluminescence imaging, acoustic measurements, and qualitative heat release measurements (using PMT coupled with CH* filter) performed for both the combustion case. The flow field conditions are mentioned in appendix D. Results from this work are explained in the next sections.

5.1. Results and Discussion

Experimental results obtained are reported in this section. The high-speed chemiluminescence imaging results are explained in section 5.1.1. Section 5.1.2 provides the POD analysis on different reaction zones (at different O_2 concentrations) while section 5.1.3 presents the analysis of reaction zone acoustic and chemiluminescence signals.

5.1.1. High-speed Chemiluminescence Imaging

The dynamics of reaction zones were examined between normal air combustion and distributed combustion using chemiluminescence imaging at high-speed. Figure 5.1 represents the instantaneous chemiluminescence images for swirl flames in air combustion (at $O_2 \sim 21\%$) as well as the distributed combustion (at $O_2 = 17$ and 16%). Every 6^{th} instantaneous image captured at 3 kHz is presented so that the separation between images represents a 2ms time interval. The dotted yellow line at the bottom of each image shows the burner exit-plane (at y = 0). The normal swirl flame possessed a nearly axisymmetric 'V'-shaped flame base with a conical top structure (see Fig. 2a, t = 0 ms). The second image in Fig. 2a indicated the development of two axisymmetric vortices on both sides of the flame. The next two images demonstrated the growth pattern and roll-

up (along the shear layers) of these vortices with time. The red triangular markers (in 2, 4, and 6 ms images) tracked the mean axial location of the vortex in each image. Note that the flame base gradually lifted off at 2 ms and moved approximately 10 mm downstream of the burner exit (at 4 ms). As the vortices continued to propagate downstream, the flame base started moving back to the burner exit at 6 ms.

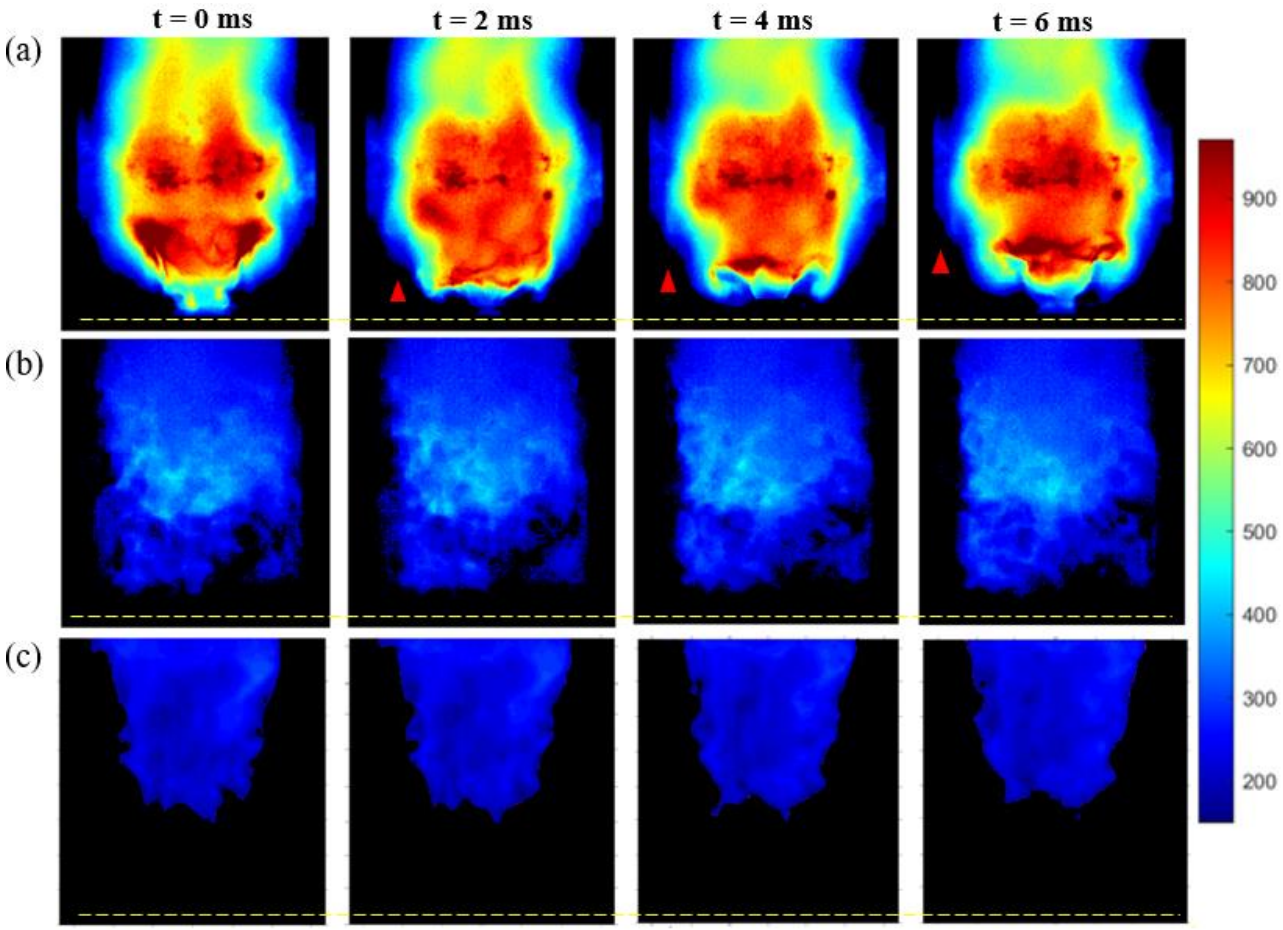

Fig. 5.1. Instantaneous broadband chemiluminescence of (a) normal swirl flame (O_2 ~ 21%), and distributed flames at (b) (O_2 ~ 17%) and (c) (O_2 ~ 16%). The yellow dotted lines represent the burner exit plane location. The red triangles in the top row represent the axial location of the symmetric vortices.

Such detachment and reattachment of flame base continued indefinitely for the present swirl flame at O_2 ~ 21%. The time-series of the flame base oscillations were collected from chemiluminescence

images at three O_2 levels (21, 17, and 16%). The mean flame base was located using the flame edge technique similar to ref. [96] The peak oscillation frequencies for different flames were obtained using Fast Fourier Transformation (FFT) and shown in Fig. 5.2. It is observed that the normal swirl flame had a peak base fluctuation at 176 Hz (see Fig. 3a).

The approximate vortex-shedding frequency of normal swirl flame was calculated (from chemiluminescence image tracking) to be in the range of 166- 187 Hz. This shedding frequency was observed to vary from cycle to cycle within the stated range.

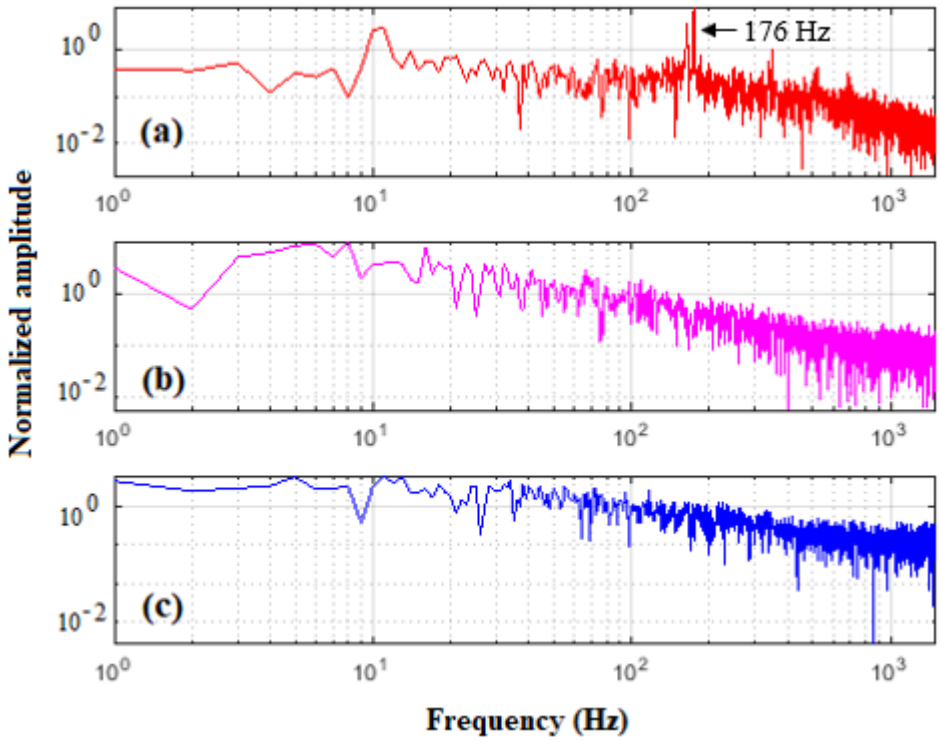

Fig. 5.2. Spectrum of flame base fluctuation for (a) normal swirl flame (O_2 ~ 21%), and distributed flames at (b) (O_2 ~ 17%) and (c) (O_2 ~ 16%).

Hence, a reasonable correlation existed between the vortex-shedding phenomenon and flame base oscillation for the normal swirl flame at O_2 = 21%. Besides such base fluctuations, a self-sustained

periodic vertical motion of the reaction zone (as observed from the supplemental video) was also observed in this flame.

Figure 5.1 b showed a volume-distributed combustion with reduced chemiluminescence intensity for O_2 = 17%. Such an appearance indicated the onset of distributed combustion in the current experimental setup. Distributed combustion at O_2 = 17% did not manifest any prominent vortex shedding, unlike the normal swirl flame. A constant average stand-off height of ~ 6mm was maintained in this case. This stand-off distance observed from the base in distributed combustion appeared mainly due to the dilution of main airstream with CO_2. The appearance of periodic structures near the burner exits in the normal swirl flame disappeared with the RZ stand-off (generated due to CO_2 dilution) in distributed combustion. No significant fluctuations were also noticed in the base of this RZ. The existence of some dark fragmented pockets observed near the base was attributed to localized extinction. Such extinction and reignition events near the RZ root did not affect the global stability of RZ. At O_2 = 16%, distributed combustion showed a stable stand-off distance of ~25-30 mm from the burner exit. The RZ adopted the shape of a nearly 'inverted cone' due to substantial quenching of the RZ root and the side edges. The spectrum in Fig. 3b and c showed a remarkable difference in RZ base oscillation behaviors between normal swirl combustion and the distributed combustion. No distinguished oscillation peaks were observed in distributed combustion at O_2 = 17 and 16%. Such observation signified that distributed combustion promoted a stable RZ base compared to normal air combustion.

It is important to note that a gradual drop in adiabatic flame temperature (T_{ad}) occurred from diluting the main airstream with CO_2 while fostering the distributed combustion. Further efforts were taken to examine the chemiluminescence signatures at different dilution levels while

maintaining a constant adiabatic flame temperature (T_{ad}) of 2100 K (similar to the T_{ad} of the undiluted flame at O_2 = 21%). The primary purpose of keeping such constant T_{ad} was to examine the effect of CO_2 dilution on RZ luminosity independent of any thermal effect (caused by the change of T_{ad}). The equivalence ratio (of 0.9) and heat release intensity (= 5.72 MW/m^3-atm) were unaltered during this study. The top row in Fig. 5.3 represents the instantaneous images of reaction zones at different O_2 levels with variable T_{ad} while the bottom row represents similar images at T_{ad} = 2100 K. The luminosity of RZ decreased in both cases with CO_2 dilution. However, such decrease in luminosity was noticeably higher for the variable T_{ad} case compared to the constant T_{ad} case. The RZ stand-off height was observed to be relatively smaller for the constant T_{ad} case, which is reasonable and expected because of the higher flame speed due to preheating of the inlet air. At O_2 = 16%, this stand-off distance became prominent for the variable T_{ad} case while a relatively small stand-off was observed for the constant T_{ad} case. The stand-off distances with and without constant T_{ad} can be better understood in connection with the laminar flame speed (S_L) information calculated at different dilution levels using Chemkin-Pro simulation. The S_L gradually decreased from ~ 0.26 m/s to 0.039 m/s with dilution (with change in O_2 concentration from 21% to 16%) when the T_{ad} was varied. This result supports the observation of increasing the RZ stand-off with gradual CO_2 dilution (Roy and Gupta 2020). When T_{ad} was kept constant (at ~ 2100 K) by preheating the inlet airstream, S_L gradually increased from ~ 0.26 m/s to 1.05 m/s (with change in O_2 = 21% to O_2 = 16%). Such an increase in S_L supports the observation of negligible RZ stand-off (in distributed combustion) with constant T_{ad}. Hence, the preheating of inlet air has predominance over the chemical effect (caused by CO_2 dilution) on S_L (which was seen to decrease gradually with dilution for the variable T_{ad} case). This is convincing as the gradual increase of

preheat temperature enhances the decomposition of CO_2. Hence, the effect of CO_2 dilution on S_L becomes weaker than the enhancement of overall reaction rate due to high preheating.

The decrease in RZ luminosity was further quantified by calculating the average chemiluminescence (broadband) intensity for each dilution case with variable as well as constant T_{ad} cases. These intensities were normalized by the average intensity in the undiluted case (O_2 =21%).

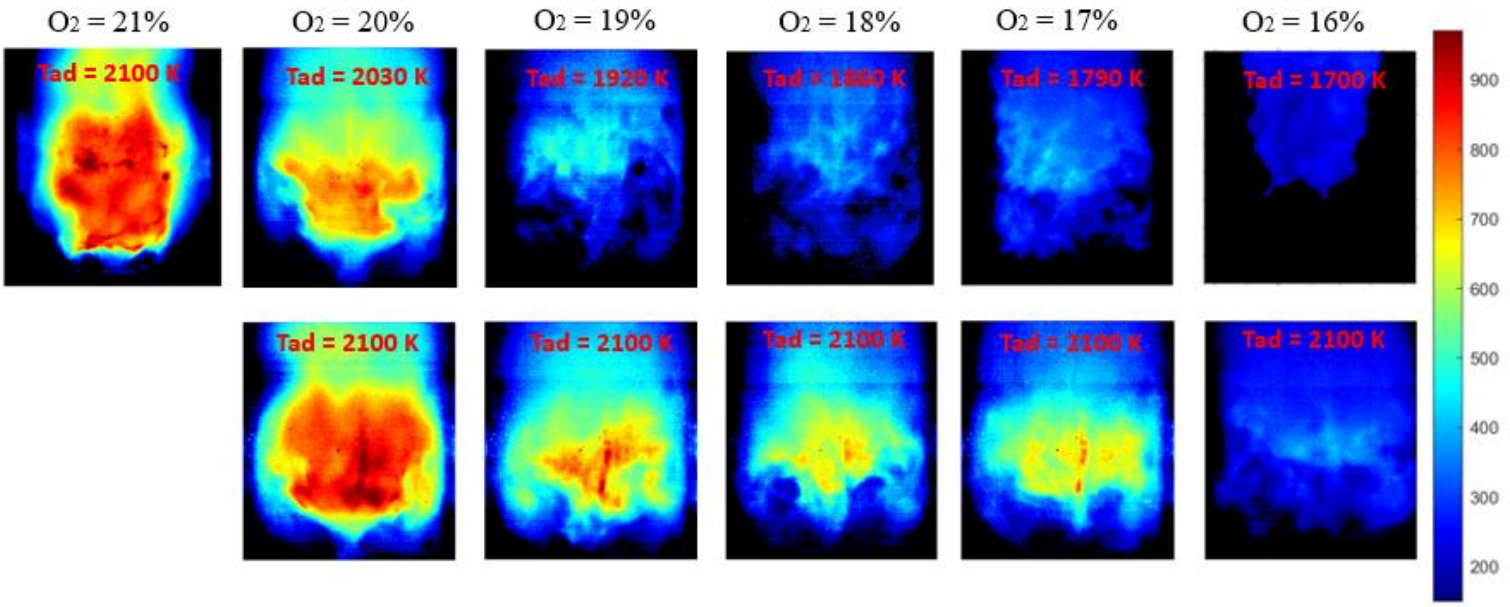

Fig. 5.3. Instantaneous flame chemiluminescence at different O_2 concentrations with gradually decreasing (top row) and constant (bottom row) adiabatic flame temperature.

The results are plotted in Fig. 5.4. The reduction in chemiluminescence intensity for the decrease in T_{ad} case was higher than the constant T_{ad} case for all the O_2 levels examined. At distributed combustion (O_2 = 16%), the normalized chemiluminescence intensity decreased by ~40% compared to O_2 = 21% with constant T_{ad} while a drop of ~70% was observed for decrease in T_{ad}

case. The observed decrease in intensity for constant T_{ad} case was mainly due to CO_2 dilution, whereas the gradual decrease in T_{ad} played an important role in reducing the luminosity of the reaction zones for the variable T_{ad} case.

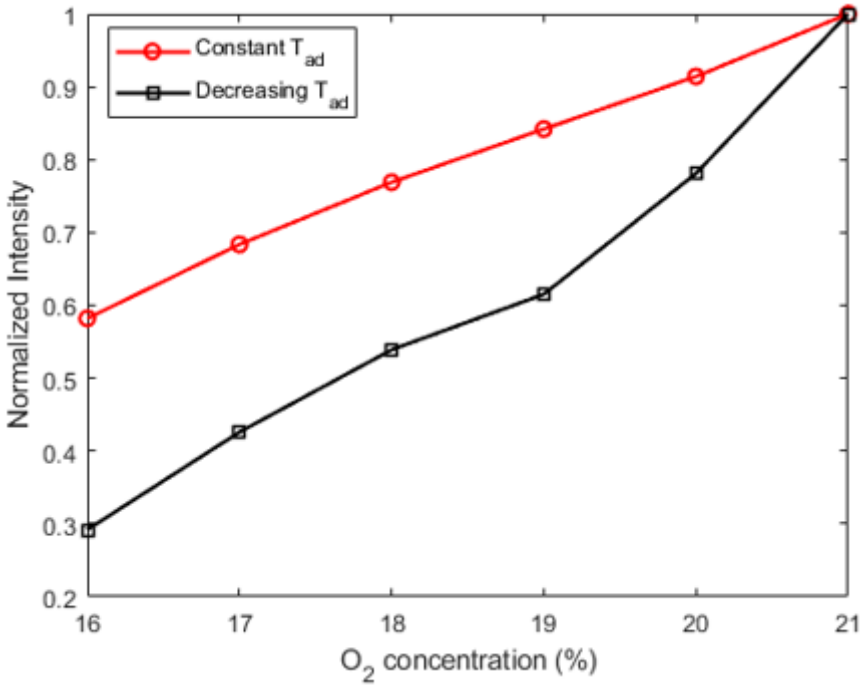

Fig. 5.4. Average chemiluminescence intensity at different O_2 dilution levels for the constant and gradually decreasing adiabatic flame temperature (normalized with respect to the average intensity in undiluted case)

5.1.2. Proper Orthogonal Decomposition:

An analysis of RZ oscillation from normal air-combustion to distributed combustion was performed using proper orthogonal decomposition (POD). POD is a mathematical tool that decomposes an ensembled data series into spatial modes [97, 98]. For example, POD applied to

any instantaneous flow field realizations $u(x,t)$ produces a set of orthogonal base functions $\phi_n(x)$ (or eigenmodes) modulated by time coefficients $a_n(t)$. Hence, a reconstruction of such instantaneous realizations becomes possible that can be given by the expression:

$$u(x,t) = a_o\phi_o(x) + \sum_{i=1}^{\infty} a_n(t)\phi_n(x) \quad (5.1)$$

Where the term $\phi_o(x)$ in equation 1 indicates mode 'zero' or the mean RZ structure obtained from chemiluminescence. The other modes represent various dominant patterns of fluctuations present in the RZ. The term '$u(x,t)$' represents the temporal variation of chemiluminescence intensity at different O_2 levels.

In this work, POD modes were calculated for both normal air combustion (O_2 ~ 21%) and distributed combustion (at O_2 ~ 17% and 16%) using chemiluminescence images. Figure 5.5 compares the first 6 POD modes (shown in decreasing energy order) between normal air combustion (at O_2~ 21%) and distributed combustion (at O_2 ~ 16-17%). Higher-order modes (beyond mode 6) were not presented as they contained less than 25% of the highest RZ fluctuation energy (in mode 1). Mode 0 from normal swirl flame (see Fig. 5.5a) showed symmetric, conical mean flame structure with reactions occurring within the inner recirculation zone. Two very small corner recirculation zones were visible on both sides of the flame. Such a conical structure changed to a volumetric distributed reaction zone structure at O_2 = 17%. Two weak, vertically elongated, faint corner recirculation zones were also observed surrounding the lifted RZ base. At O_2 = 16%, the mean RZ adopted a lifted 'V' shape. A remarkable difference in fluctuation patterns between normal swirl combustion and distributed combustion was manifested in mode 1 (see the second column of Fig. 5.5). Mode 1 fluctuation in normal swirl flame was strongly dominated by vortex shedding and fluctuating reaction zone (see Fig. 5.5a). In contrast, the distributed combustion (at O_2 = 17%) showed only mild spatial fluctuations in mode 1. The fluctuating reaction zone (as

found in swirl flame) was absent near the distributed combustion case, which contributed to enhanced stability in distributed combustion.

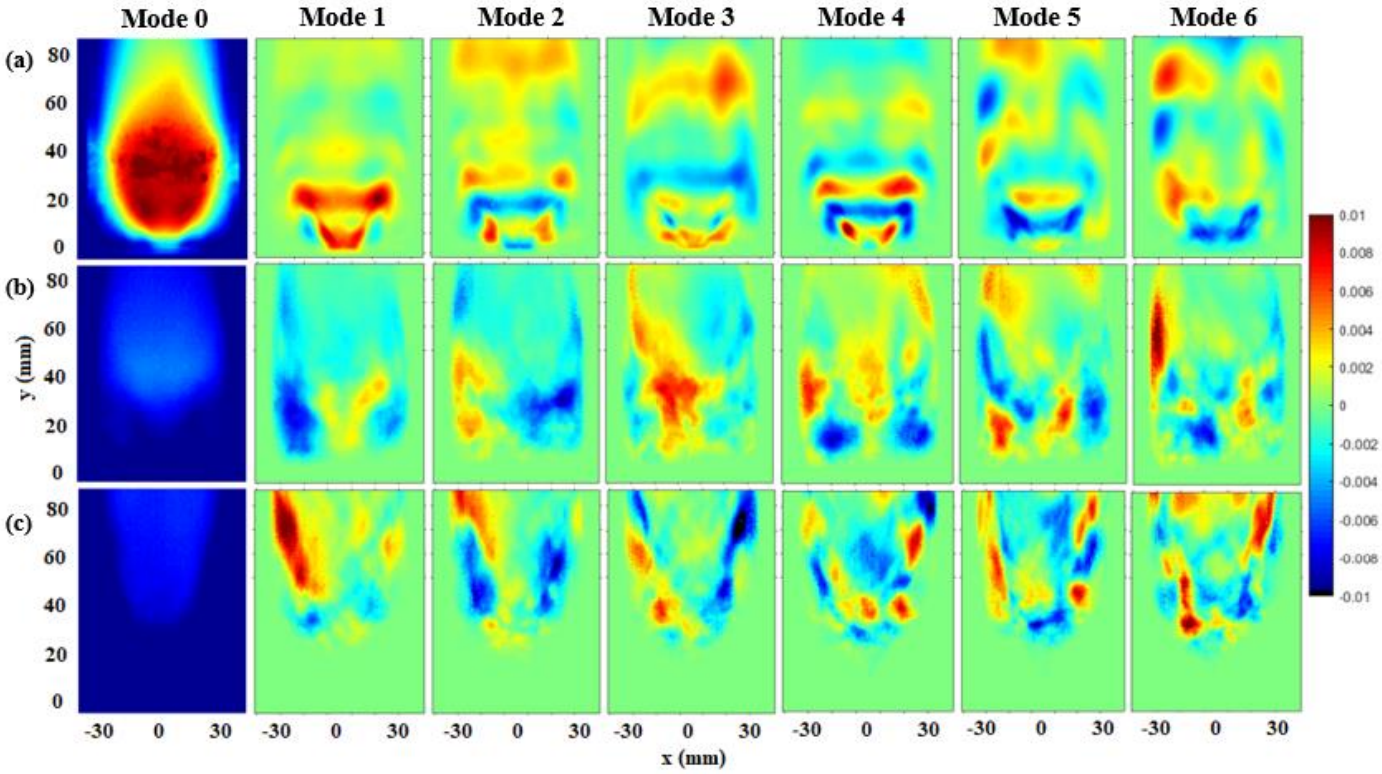

Fig. 5.5. POD modes 0-6 for (a) normal-air combustion (O_2 ~ 21%), and distributed combustion at (b) (O_2 ~ 17%), and (c) (O_2 ~ 16%).

At O_2 = 16%, mode 1 indicated some fluctuations along the edges of the lifted RZ, see Fig. 5.5 c. A bright patch of signal along the left edge of the RZ with negligible signal intensity on the right edge was observed in mode 1. This intense bright edge shifted to the right side of the RZ in mode 3. Such three-dimensional vortical motions appeared due to the existence of precessing vortex cores (PVC) found in swirl flames [99-101]. This is also supported by a similar explanation provided by [102] in their study of swirl-stabilized methane flame. In modes 2-4, the normal swirl flame illustrated shedding of axisymmetric ring-vortex (alternate blue and red horizontal stripes)

that displaced the reaction zone periodically. Modes 5 and 6 had a lower overall contribution to fluctuation, which resulted from alternate vortex shedding along the edges. Compared to normal air combustion, modes 2-6 in distributed combustion also demonstrated very different oscillation patterns.

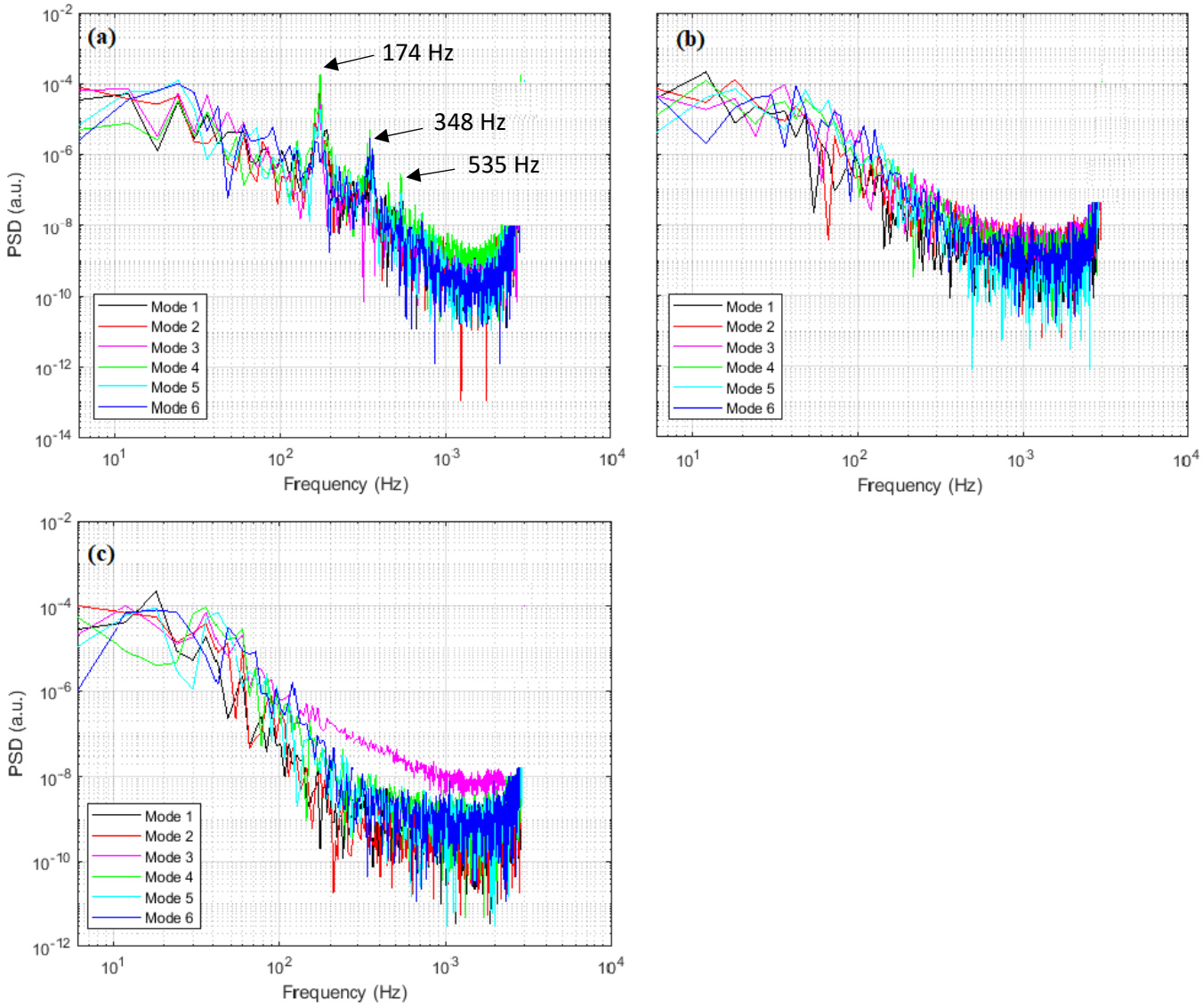

Fig. 5.6. Power spectrum of POD modes 1-6 for (a) normal-air combustion (O_2 ~ 21%), and distributed combustion at (b) (O_2 ~ 17%) and (c) (O_2 ~ 16%).

The PSD of the fluctuation observed in each POD mode was calculated for normal air combustion and distributed combustion. Such calculations help to quantify the RZ fluctuations in different combustion regimes. Figure 5.6 compares the PSD of modes 1-6 at O_2 = 21, 17, and 16%. In normal combustion (O_2 = 21%), a distinguished fluctuation peak existed for every POD mode at 174 Hz with mode 4 providing the highest magnitude (see Fig. 5.6a). A second peak exists around 348 Hz for all the modes except mode 3. Mode 4 of the normal swirl flame possessed another peak at ~ 535 Hz. In contrast, no such fluctuation peaks were manifested from the PSD of the distributed combustion (at O_2 = 17%). Such observation signifies that distributed combustion had no dominant mode of fluctuations. A similar PSD without any distinct peak was also observed for the distributed combustion at O_2 = 16%. The mode 5 and 6 of distributed combustion at O_2 = 17 and 16% displayed some mild, discrete peaks in the frequency range (f) of 40-50 Hz. The Strouhal number (St= f*D/ Um) calculated using the burner exit diameter (D) and the average inlet velocity (Um) was in the range of 0.22- 0.24. Such 'St' values indicated a slight influence of von-Karman vortex shedding in these modes. These results demonstrated that distributed combustion exhibited no remarkable fluctuation compared to the normal air swirl flame. It should be noted that the existence of any thermo-acoustic instability cannot be concluded based on the peaks observed in Figs. 5.2 and 5.6 only. The thermo-acoustic instability is mainly dependent on RZ dynamics and acoustic properties of the combustor. The primary objective of these figures was to compare the RZ base behavior and the chemiluminescence fluctuation characteristics between the conventional swirl-assisted combustion and the novel distributed combustion.

The energy contents of different POD modes were further obtained in normal air combustion as well as distributed combustion. The purpose of showing this plot was to highlight how the

fluctuation of energy gradually decreased when distributed combustion was established from a conventional swirl-flame. The chemiluminescence images were normalized by their respective maximum intensity values so that any abrupt change in intensity (as sometimes found in distributed combustion) did not influence such energy calculations. POD was calculated using these normalized images. Such energy distribution in the first 20 modes is presented in Fig. 5.7. Reduction in RZ oscillation (in terms of energy content) was observed in every mode when distributed combustion was fostered from the normal swirl flame.

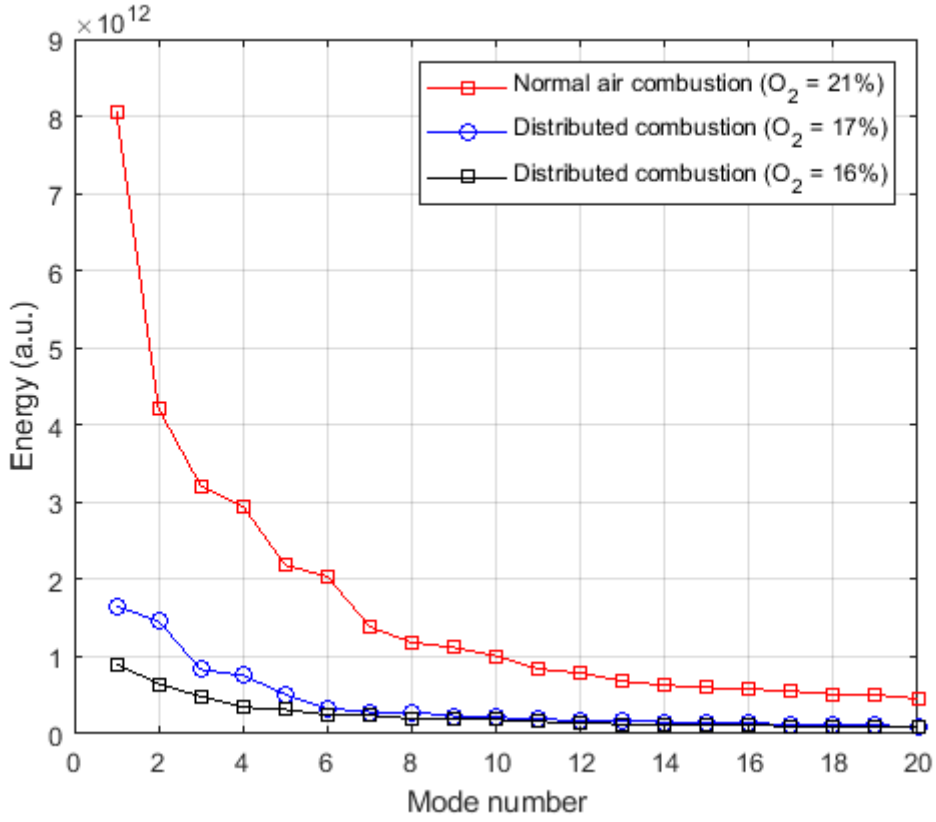

Fig. 5.7. Energy contents in flame fluctuation of first 20 POD modes in normal-air combustion (at O_2~ 21%), and distributed combustion (at O_2 ~ 17% and 16%).

The energy in mode 1 was reduced by ~ 60% from the normal swirl combustion to distributed combustion. Starting from mode 2, the difference between the energy contents in normal combustion and distributed combustion became marginal. After mode 12, both normal air combustion and distributed combustion possessed almost the same fluctuation energy. Such an energy plot of fluctuation directly supports the evidence of reduced oscillations in distributed combustion as compared to normal air swirl combustion.

5.1.3. Reaction Zone Acoustics and PMT Signal Analysis:

The reduction of fluctuation in distributed combustion was further investigated using simultaneous acoustic and PMT signals. The goal was to understand whether any thermo-acoustic coupling existed (in normal air flame) that gradually diminished when approaching the distributed combustion. The acoustic pressure was represented by the microphone signal while the qualitative heat release was indicated by PMT signal. The acoustic and PMT signals are shown in Fig. 5.8 for the sequential decrease in O_2 concentration from 21% to16%. The shape of the acoustic signal gradually changed from a time-varying sinusoid to a limit-cycle oscillation with decrease in O_2 concentrations. The amplitude of the signal was reduced from ~ 90 dB (in normal combustion) to 20 dB (in distributed combustion, Fig. 5.8f). The zoomed view of acoustic signal in Fig. 5.8 f shows the nature of such signal variation in 20 ms at distributed combustion regime. Such a reduction in acoustic signal signifies the advantage of distributed combustion in reducing combustion noise. A noticeable reduction of amplitude was also observed for the PMT signal; however, the PMT signal mostly lost its sinusoidal nature near distributed combustion. The reduction in PMT signal amplitude is as expected due to the distribution of heat release throughout

the combustor volume resulting in reduced reaction rate. To understand the thermo-acoustic nature of reaction zones, the fluctuation component of acoustic pressure (p') and the heat release (q') were analyzed at various O_2 levels.

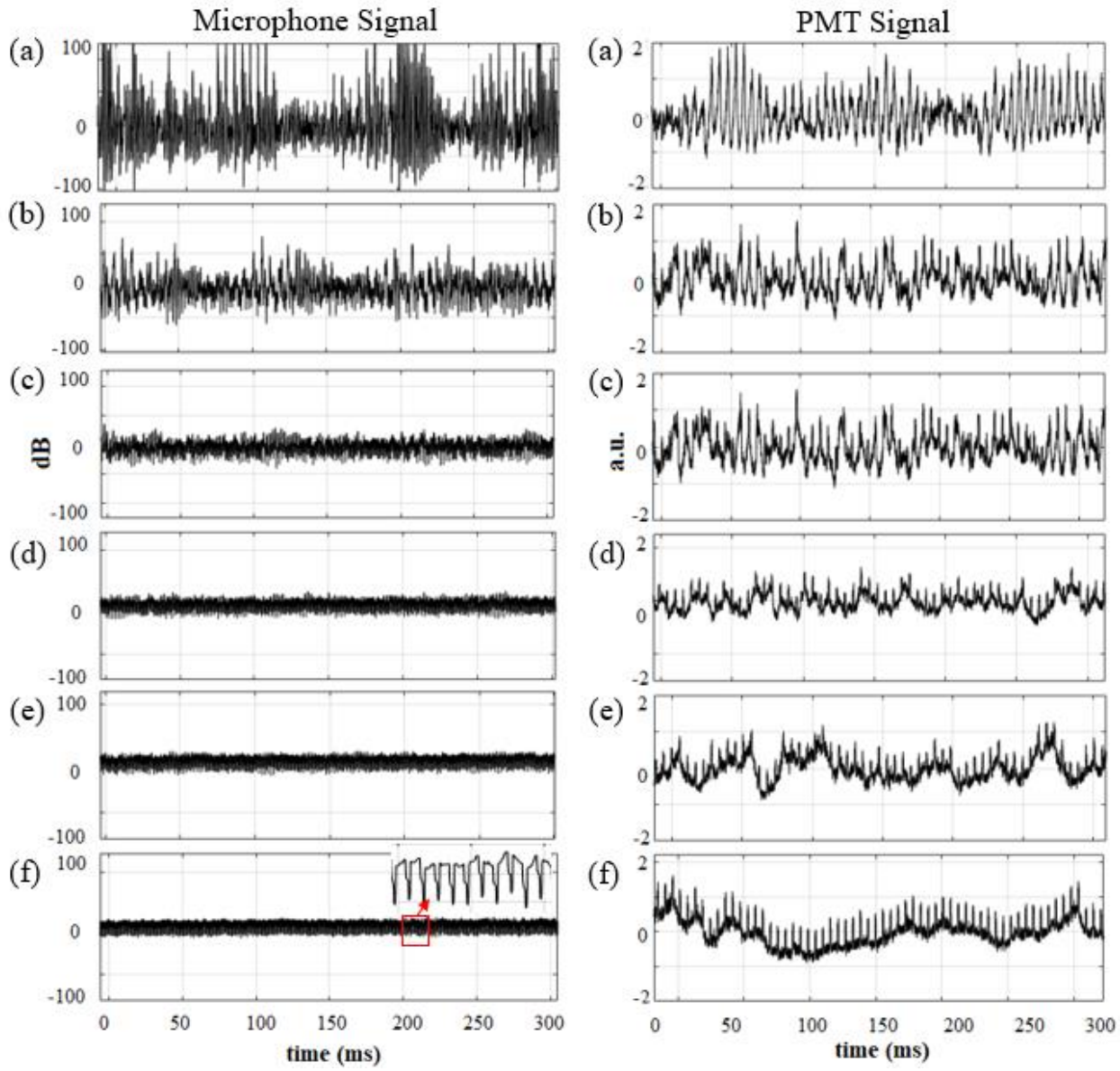

Fig. 5.8. Temporal evolution of microphone signal and PM signal at (a) O2 = 21%, (b) O2 = 20%, (c) O2 = 19%, (d) O2 = 18%, (e) O2 = 17%, and (f) O2 = 16%.

The results obtained on PSD of p' and q' are shown in Fig. 5.9. For the normal air flame (at O_2 = 21%), the PSD of p' and q' showed common peaks at 174 Hz, 350 Hz, and 540 Hz, respectively. The 174 Hz peak was of specific interest as a similar peak was observed in the power spectral density of POD modes as well the RZ base fluctuation (shown in Fig. 5.2 a). Such a peak further supports the possibility of thermo-acoustic coupling in normal swirl flames at O_2 = 21%. The possible explanation for the 540 Hz peak is the existence of precessing vortex core (PVC) (64, 100, 101, 103). However, it is important to note that PVC can only influence thermo-acoustic instabilities in combustion when it exists in acoustic resonance near the burner exit [104]. None of the acoustic modes of the current combustor (based on the geometry) overlapped with the PVC frequency (540 Hz) found during this study. Hence, such naturally occurring PVC did not play any major role in influencing the instability in this combustor. The self-sustaining instabilities in the current swirl flame (at O_2 = 21%) were mainly due to the existence of the thermo-acoustic coupling that influenced the periodic vortex shedding observed from the chemiluminescence imaging.

An approximate calculation of Helmholtz frequency was also performed by assuming the burner geometry acts like a Helmholtz resonator. The calculated Helmholtz frequency (~ 375 Hz) was rather close to the 350 Hz peak observed in PSD. The amplitude of 174 Hz peak gradually decreased with decrease in O_2 levels. Such observation is consistent with the results shown in Fig. 5.8 illustrating the gradual reduction of acoustic and heat release signals. Figure 5.9 shows very good support for the possible thermo-acoustic coupling at 174 Hz in normal swirl flame that diminished approaching the distributed combustion. The absence of the acoustic peak in distributed combustion can be interpreted as a very weak correlation or almost no correlation between heat release and acoustic signal fluctuation to support diminished thermo-acoustic couplings near distributed combustion. The peak at 540 Hz still existed in distributed combustion

with reduced amplitude indicating the existence of PVC. Further, the power spectral densities of p' and q' at different CO2 dilution levels was investigated at a constant adiabatic flame temperature of Tad = 2100 K with the objective of examining the effect of CO_2 dilution on RZ instability.

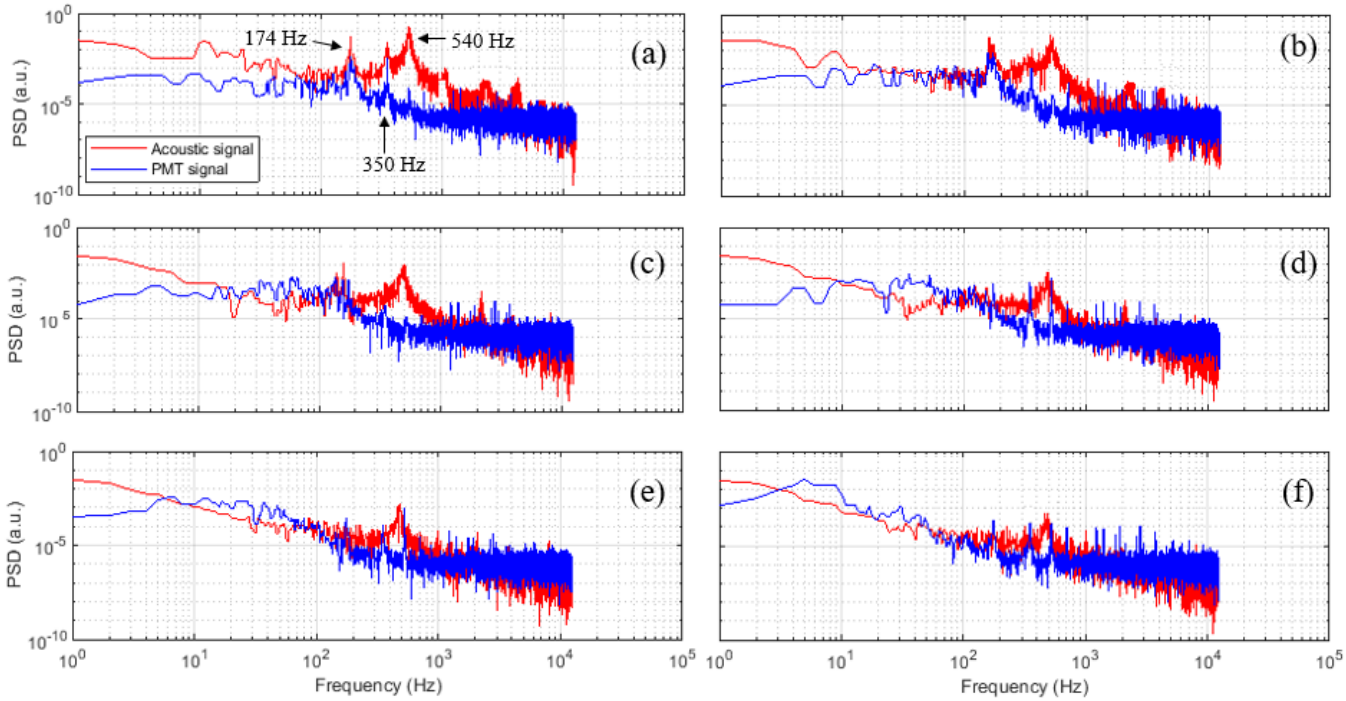

Fig. 5.9. Power spectrum of p' and q' signals at (a) O2 = 21%, (b) O2 = 20%, (c) O2 = 19%, (d) O2 = 18%, (e) O2 = 17%, and (f) O2 = 16%.

The p' and q' spectra with constant T_{ad} were very similar to the one where T_{ad} was not constant. However, an early suppression (at O_2 = 19%) of the thermo-acoustic peak (~174 Hz) along with the gradual diminishing of the PVC peak (~540 Hz) were observed. The preheating of inlet air to maintain a constant Tad helped in reducing the amplitude of the heat release fluctuation peak and the PVC peak from the early stages of dilution. Hence, the observations with constant Tad were

consistent with the previous case (wherein the Tad gradually decreased with dilution) that the instabilities in the present swirl flame were gradually suppressed with CO_2 dilution.

The possibility of thermo-acoustic coupling was further analyzed by examining the Rayleigh's criterion as given in ref. [10]. For this purpose, the existence of some weak 174 Hz peak for both p' and q' was assumed near distributed combustion. The limit-cycle fluctuations of p' and q' signals were compared at first to qualitatively understand their phase differences in normal air combustion and distributed combustion. These signals were bandpass filtered near 174 Hz to obtain such limit-cycle fluctuations. Figure 5.10 represents a part of the bandpass filtered p' and q' signals simultaneously. It was observed that the bandpass filtered signals were fairly sinusoidal. The p' signal was apparently in phase with q' at O_2 = 21%. In distributed combustion, those signals were clearly out of phase. Such observation signified the existence of thermo-acoustic coupling that disappeared in distributed combustion. A quantitative understanding of thermo-acoustic coupling was obtained by calculating the line-of-sight Rayleigh index for every RZ considered. The mathematical formulation of Rayleigh's criterion (over one period) is expressed as:

$$g(x) = \int p'(x,t)\, q'(x,t) dt \tag{2.2}$$

A local Rayleigh index was calculated by evaluating equation (2) at several different points within the combustor. CH* chemiluminescence images (captured with the bandpass filter centered at 430 ± 10 nm) were used to obtain the spatial distribution of local Rayleigh index. The CH* signals were normalized by the respective maximum intensities to ensure that the local and global Rayleigh index values were unaffected by the drop in chemiluminescence signal intensity near the distributed combustion. However, it is important to note that CH* chemiluminescence may not represent the actual heat release.

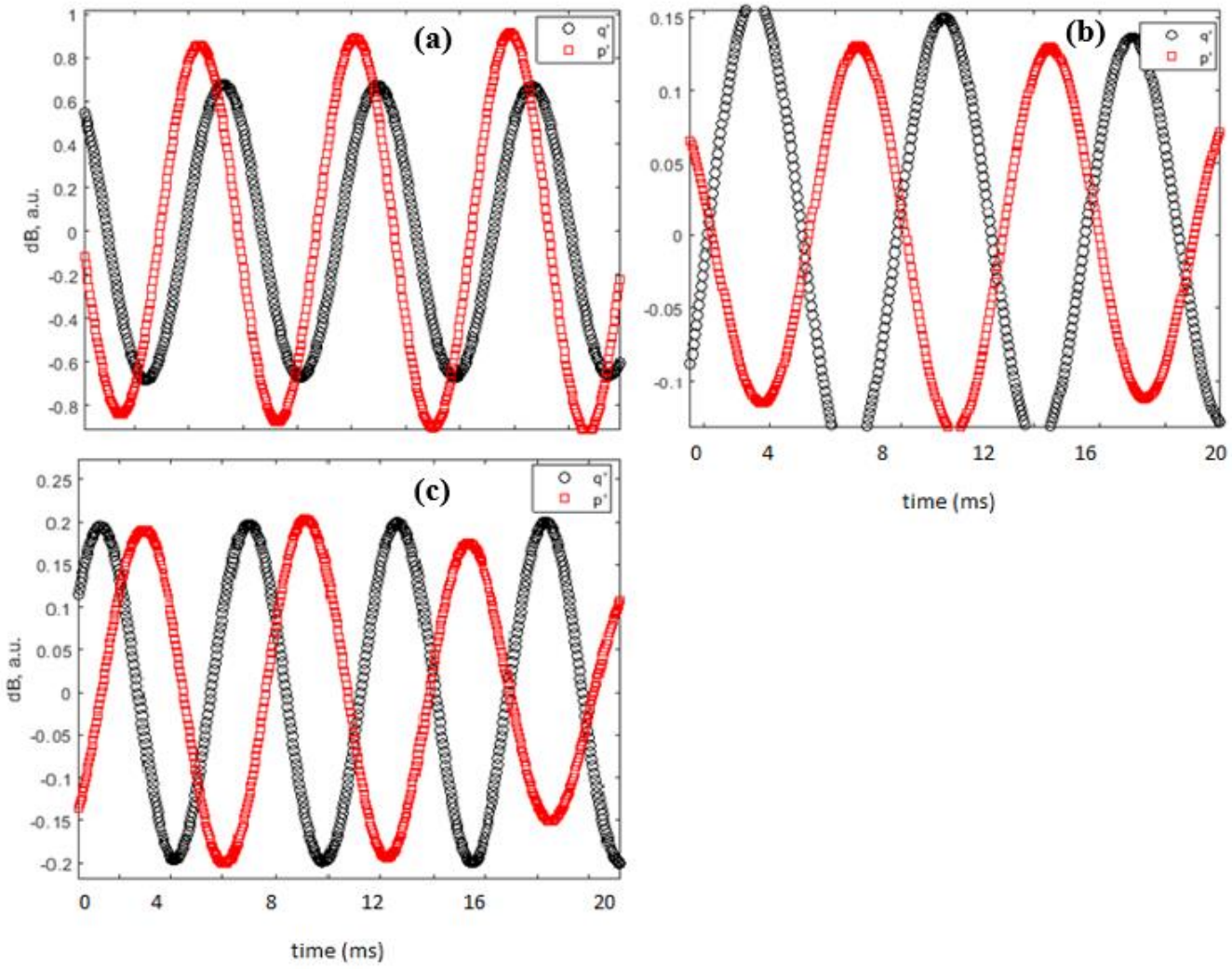

Fig. 5.10. Simultaneous representation of the limit cycles of p' and q' in (a) normal air combustion (O2 ~ 21%), and distributed combustion at (b) (O2 ~ 17%) and (c) (O2 ~ 16%).

Hence, care must be taken while performing quantitative analysis with such data. The positive value of Rayleigh index indicates a positive thermo-acoustic coupling, which assists in self-sustaining or growing of an instability. On the contrary, a negative value indicates the dampening of instability. Figure 5.11 illustrates the spatial distribution of local Rayleigh index within the combustor volume for RZ at O_2 = 21, 17, and 16%. The Rayleigh index possessed positive values in the reaction zone for normal swirl flame (see Fig. 5.11 a). The peak positive value was distributed along both flame shear layers indicating a strong thermo-acoustic coupling that

influenced the shear layer instability. A similar sign of Rayleigh index observed on both shear layers was previously attributed to the formation of toroidal structures by Kang et al. [105]. They postulated that the toroid forms at locally lean flame zones where shear layer entrainment occurs leading to flame instabilities. For the present flame (at O_2 = 21%), most of the 'driving parts' of flame instabilities were located from y = 0 to y ~ 30 mm. The value of the local Rayleigh index was observed to reduce gradually at downstream locations (at y > 30 mm). Unlike the normal swirl flame, the spatial value of the Rayleigh index was remarkably low (mostly negative or zero) for the distributed combustion (Fig. 5.11 b, c). However, a weak positive index value was observed along the RZ edges (mild green hue). Such localized instabilities are linked with 3-D vortical motion of the RZ explained in section 3.2. Such observations of weak spatial Rayleigh index indicate the existence of 'dampening instability' characteristics in distributed combustion resulting in higher combustion stability.

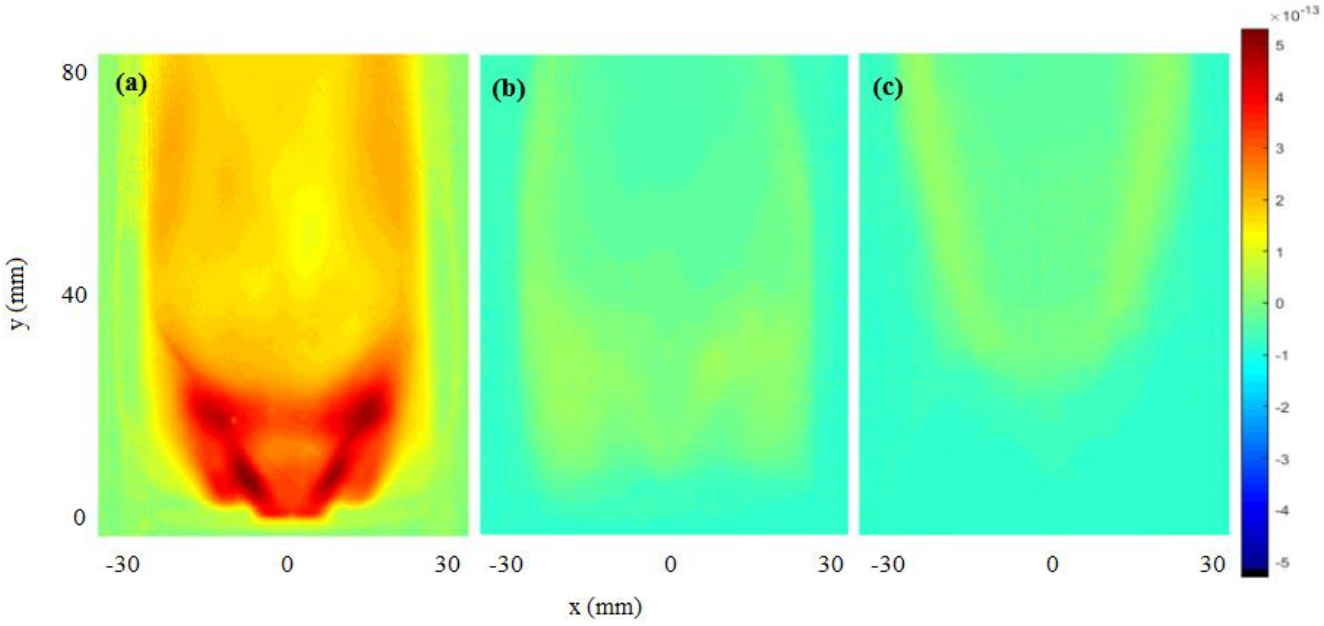

Fig. 5.11. Local Rayleigh index distribution at (a) O2 = 21%, (b) O2 = 17%, and (c) O2 = 16%.

A global Rayleigh index was further estimated to understand the overall stability of RZ at various O_2 concentrations. The integrated value of equation (2) over the entire data set provided the global Rayleigh index, $G(x)$. The results obtained on global Rayleigh index, $G(x)$ as a function of O_2 concentration are presented in Fig. 5.12. In this case, the value of the global Rayleigh index was reported near the burner exit location (flame root) for both swirl combustion and the distributed combustion cases. A positive value of G was seen for O_2 = 21 and 20%.

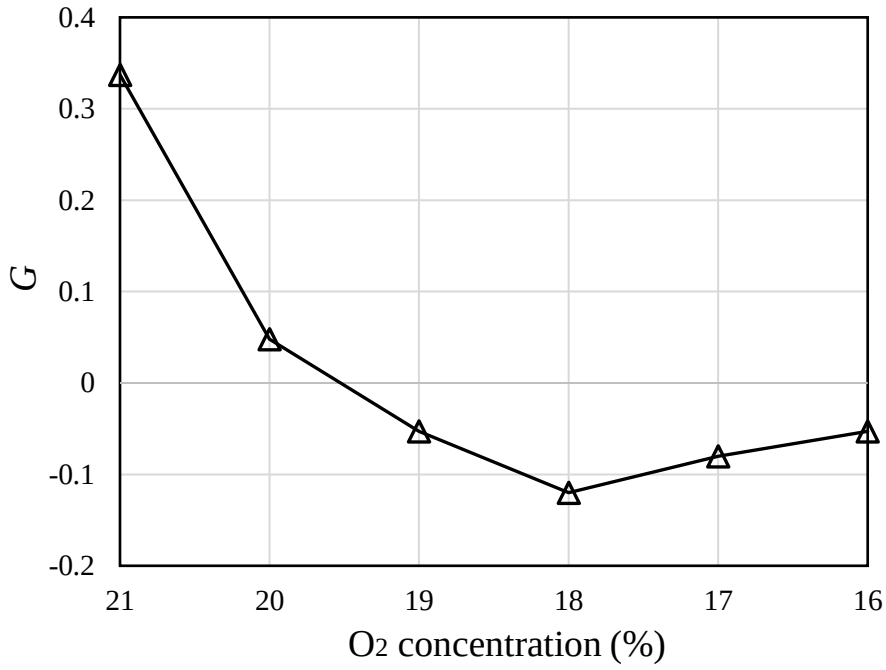

Fig. 5.12. Global Rayleigh index at different O_2 concentrations

This is as expected since the results shown in Fig. 5.10 a also exhibited an 'in phase' p' and q' signals. Also, a highly positive local Rayleigh index was observed in most of the reaction zone in Fig. 5.11 a. These observations adequately support the existence of thermo-acoustic couplings in normal swirl flame leading to self-sustained oscillations of reaction zones but absent in distributed combustion. The $G(x)$ possessed a negative value for O_2 = 19-16% reaction zones indicating an

'out of phase' fluctuation of heat release and acoustic fluctuations. The lowest magnitude of $G(x)$ observed at O_2 = 18% can be attributed to the very low amplitude of both p' and q' signals that resulted in an overall low '$G(x)$' value. The negative value of $G(x)$ in distributed combustion confirms the absence of thermo-acoustic couplings leading to enhanced stability in distributed combustion. These results highlight distributed combustion as a promising gas turbine combustion technology that results in low noise and absence of combustion instability.

5.3.3. Summary

The fluctuations of RZ at various O_2 concentrations were examined to evaluate RZ stability of normal air combustion (O_2 = 21%) and distributed combustion (O_2 = 17 and 16%). Experiments were carried out in a swirl-assisted burner configuration using methane fuel (at an equivalence ratio of 0.9) using CO_2 as flow diluent. High-speed imaging of broadband chemiluminescence was performed to distinguish the global dynamics of normal swirl combustion and distributed combustion. Such imaging showed shear layer vortex-shedding from normal air swirl flames at frequencies in the range of 166- 187 Hz. The fluctuation of RZ base (~ 174 Hz) was attributed to the occurrence of such vortex shedding. In contrast, distributed reaction zones exhibited relatively stable RZ bases. POD analysis was carried out to understand the dominant dynamic structures contributing to RZ fluctuation at various O_2 concentrations. The POD modes demonstrated different vortex patterns, which showed the presence of dominant fluctuations in conventional swirl flames. In contrast, mild spatial fluctuation patterns were noticed in distributed combustion. The energy distribution of various POD modes showed a significant reduction of fluctuation energy (~ 60%) that contributed to higher RZ stability of distributed combustion. The calculation of PSD for the amplitude fluctuations in different POD modes highlighted peak fluctuation frequencies at 176 Hz and 350 Hz at O_2 = 21%. Distributed combustion showed no such peaks in

any mode signifying the absence of any dominant fluctuation patterns. The acoustic signal reduced remarkably in distributed combustion indicating decreased combustion noise. The reduction of heat release was attributed to the broadening of the reaction zone resulting in a decreased reaction rate. The power spectrum of heat release (q') and acoustic signal fluctuation (p') demonstrated a common peak at 174 Hz. This peak gradually diminished with the decrease in O_2 levels. The effect of CO_2 dilution on RZ chemiluminescence, CH* chemiluminescence fluctuation spectrum, and dynamic pressure fluctuation was also examined at a constant adiabatic flame temperature of 2100 K (same as that of the undiluted flame). The objective here was to investigate the effect of CO_2 dilution independent of any thermal effect (caused by the variation of T_{ad}). The results showed that the RZ luminosity drop was relatively higher for all the dilution levels with decrease in T_{ad} as compared to constant T_{ad} case. Suppression of thermo-acoustic peak occurred relatively earlier along with a gradual decline of the PVC peak amplitude at constant T_{ad}, which was attributed to preheating of the inlet air. The local Rayleigh index calculation showed a highly positive index value along the flame shear layers of normal swirl flame. The distributed combustion exhibited low overall distribution of Rayleigh index throughout the RZ volume. Furthermore, the global Rayleigh index was calculated for different O_2 levels. At O_2 = 21 and 20%, positive Rayleigh index values were observed signifying the continuation of self-sustained instability. However, distributed combustion demonstrated a negative Rayleigh index that indicated the dampening of such instability.

Chapter 6: Performance of Swirl Distributed Combustion with Hydrogen-enriched Methane: Stability, Blowoff, and Emissions.

The performance of distributed combustion was examined with various hydrogen-enriched methane fuel blends to investigate the effect of low-carbon fuels from distributed combustion. The primary idea was to reduce CO_2 along with pollutants NO and CO. While emission reduction is important, it is essential to investigate flame stability especially with the gradual increase in $\%H_2$. The stability discussion is primarily based on POD analysis of the chemiluminescence signal distribution for swirl air combustion and swirl distributed combustion with different hydrogen-enrichment. The possibility of thermo-acoustic is also examined with gradual hydrogen enrichment levels in air combustion and distributed combustion. Results from this chapter assist in developing low-emission, high stability distributed reaction for advanced gas turbines. The experimental conditions are given in appendix D. The results of this study in explained below.

6.1. Results

Section 6.3.1 provides the result of flame chemiluminescence imaging while section 6.3.2 discusses the heat release and acoustic signatures from different reaction zones. Proper orthogonal decomposition (POD) analysis is given in section 6.1.3 followed by the characterization of lean blowoff limits in section 6.1.4. Comparison of emission characteristics in swirl and distributed combustion is given in section 6.1.5.

6.1.1 High-speed Chemiluminescence Imaging of Reaction Zones

At a framing rate of 2000 frames per second, high-speed chemiluminescence signatures were captured (without any spectral filtering) for both traditional swirl combustion and distributed combustion with incremental H_2-enrichment of methane fuel. Such imaging was performed to compare the appearance of reaction zones at different $\%H_2$ addition to fuel for both swirl combustion and distributed combustion. These reaction zones were imaged at different $\%H_2$ while keeping the diluent flowrate (CO_2 in this case) the same as that required for the distributed combustion case with pure methane fuel (i.e., 0% H_2). The primary motivation here was to compare the effect of dilution on swirl-assisted distributed reaction zones with different hydrogen enrichment of the fuel. Figure 5.1 shows the shape of global reaction zones at different hydrogen-enrichment obtained from chemiluminescence imaging (without any spectral filtering). These images represent the average of 500 instantaneous chemiluminescence images taken for each category (top row shows for swirl combustion and bottom row for distributed combustion). The dotted (brown) line under each row represents the exit plane of the burner nozzle. As observed, the flame shape gradually changed with $\%H_2$ addition for both the swirl and distributed combustion. The reaction zone in swirl combustion (top row in Fig. 5.1) gradually showed brighter chemiluminescence intensity with increase in hydrogen enrichment. The shape of the flame did not change significantly between 0-20% H_2-enrichment. However, a narrower flame shape having elongated corner recirculation zones (CRZ) was observed at 40% H_2 enriched swirl flame case. The behavior of reaction zones were observed using videography developed with these images. A self-sustained periodic vertical oscillation of the reaction zone (as shown in the supplemental video) was observed in all cases of swirl combustion. Periodic shedding of vortex from both sides of the flame was also observed for these cases.

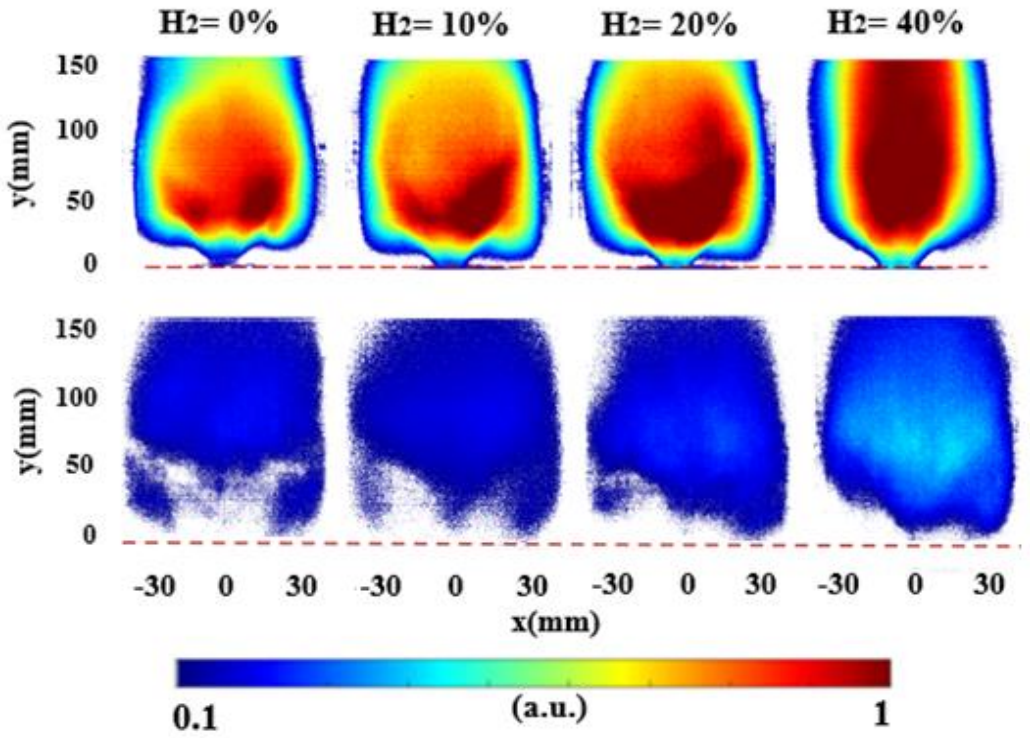

Fig. 6.1 Average high-speed chemiluminescence images (line-of-sight) of (a) conventional swirl combustion, and (b) distributed combustion at different hydrogen enrichment to methane fuel. Red dotted lines indicate the nozzle exit plane.

In our earlier work [106], vortex shedding was found to influence the oscillation of reaction zones for the pure methane fueled swirl combustion (H_2 = 0%). Distributed combustion showed significantly reduced chemiluminescence intensity for all cases between 0-20% H_2-enrichment compared to the swirl flame cases. The distributed flame was found to be lifted from the nozzle exit due to increased velocity of inlet jet. The distributed reaction zone associated with 40% H_2-enriched case was found to be brighter and narrower than the other distributed combustion cases. At this condition, the reaction zone behavior started to depart from the distributed nature, showing a rather narrow reaction zone similar to that observed in swirl combustion case. Such observations in 40% H_2-enriched methane fuel signify that the flowrate of diluent CO_2 corresponding to the

distributed combustion case with pure methane was not sufficient to establish distributed reaction zones with this fuel. This resulted in the observed difference of the shape and reaction zone (with CO_2) for the 40% hydrogen enrichment case, as compared to the other distributed reaction cases.

Reduced standoff height and a narrower flame shape were the results of the increased flame speed and reactivity due to gradual addition of hydrogen to the fuel mixture. Periodic vortex shedding observed for the swirl combustion was absent in distributed combustion (at different $\%H_2$ enrichment). This is similar to our previous findings [106]. These periodic vortex shedding can be observed from the instantaneous chemiluminescence images so that their instantaneous behavior delineates the presence and temporal evolution of such vortical structures and hence not observed in the average value of flame images.

6.1.2 Heat Release and Acoustic Signatures

Using photomultiplier (PMT) and microphone signals for various H_2-enriched situations, heat release and audio characteristics in conventional swirl combustion and distributed combustion were explored qualitatively. The PMT was incorporated with a CH* narrow band filter (at 432 ± 5 nm FWHM). This CH* radical is qualitatively regarded as a heat release rate marker. Figures 5.2 and 5.3 show the time-series of microphone and PMT signals for swirl combustion and distributed combustion at different $\%H_2$ enrichment levels. The results show significant reduction in the amplitude of fluctuation in distributed combustion. With initial hydrogen enrichment, the acoustic amplitude of the swirl flame (see Fig. 5.2a) increased up to the case of 20% H_2 enrichment along with the audible signatures from the flame. At 40% H_2-enrichment, this acoustic amplitude decreased as compared to the 20% H_2 enrichment case; in addition, the flame shape also decreased.

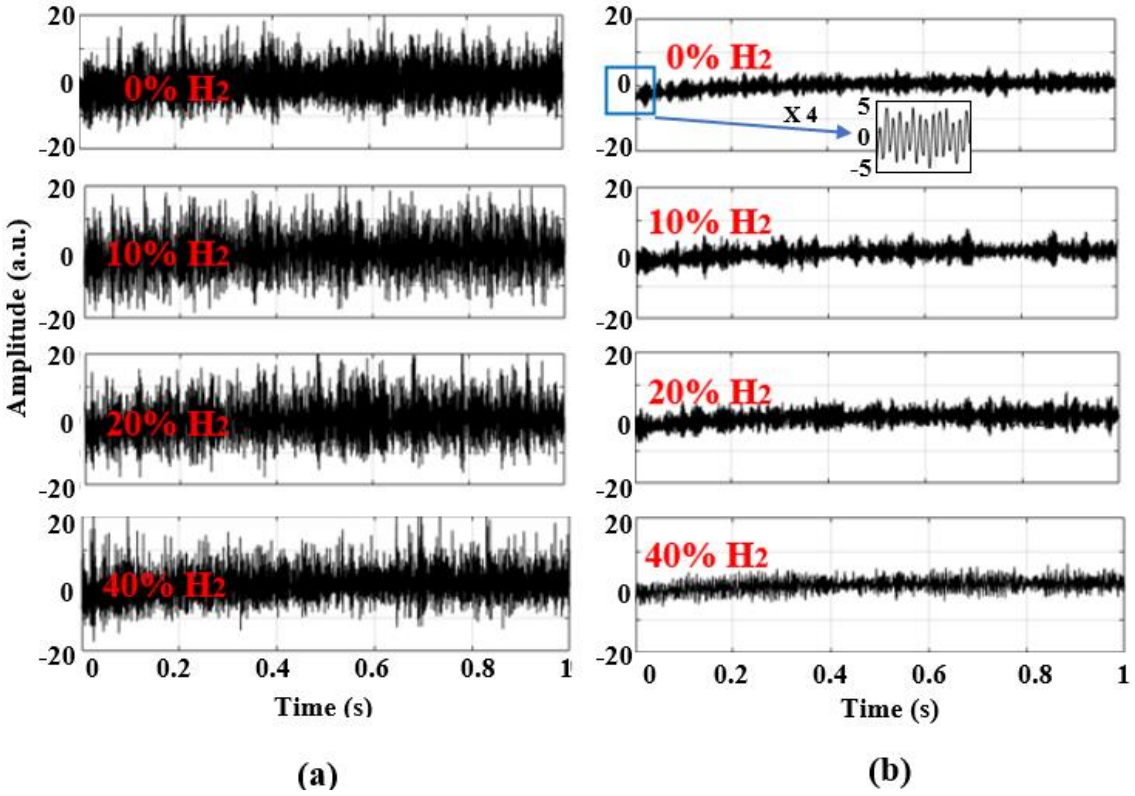

Fig. 6.2 Temporal evolution of microphone signal at different hydrogen enrichment to methane for (a) swirl combustion, and (b) distributed combustion.

For every $\%H_2$ enrichment case, the acoustic amplitude in distributed combustion was lower than the conventional swirl flame. The results show that when distributed combustion is implemented, the acoustic amplitude decreases by more than 70%. Hence, the distributed reaction zone with hydrogen-enriched methane assists in reducing the acoustic noise compared to the conventional swirl combustion case. Similar observations were observed from PMT signal on the reduced heat release in distributed combustion, see Fig. 6.3. Approximately over 60% reduction in the PMT signal was observed in distributed combustion regime. Reduction of PMT signal is

indicative of the reduced flame luminosity in distributed combustion regime and also supports the decay of heat release fluctuation.

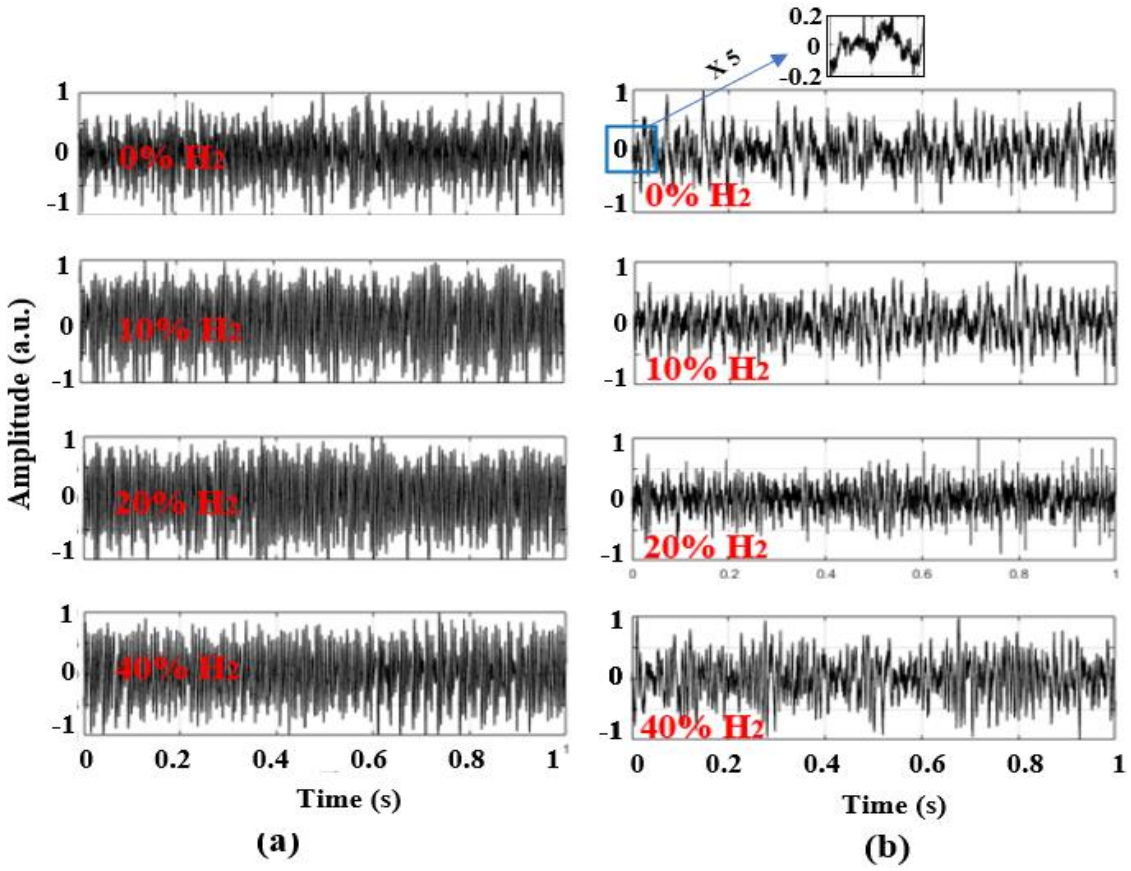

Fig. 6.3 Temporal evolution of PMT signal at different hydrogen enrichment to methane for (a) swirl combustion, and (b) distributed combustion.

When compared between the different %H_2 cases in distributed combustion, the 40% H_2 enriched case showed relatively higher periodic fluctuations in the PMT signal. Such behavior indicates that this reaction zone is not completely distributed and has less uniform thermal fields (unlike distributed combustion).

Power spectral density (PSD) was calculated simultaneously from $p'$and q' signals for each case. Figure 6.4 shows the PSD plot for the conventional swirl flames with different % H_2 enrichment. The acoustic signal fluctuation showed multiple frequency peaks in different cases of %H_2 enrichment. For the pure methane case (Fig. 6.4a) with 0% hydrogen enrichment, three distinct peaks observed were at 175, 350, and 530 Hz. Such peaks were also observed in our previous study wherein the 350 Hz was found to be similar to Helmholtz resonator frequency, the 530 Hz peak was related to the Precessing vortex core (PVC), and the 175 Hz was found to generate the thermo-acoustic coupling [106]. This thermo-acoustic coupling was found to be influenced by the periodic vortex shedding nature of the swirl combustion. With gradual H_2 enrichment of methane from 10-40%, similar observations of common peaks for $p'$and q' were made. The acoustic peaks observed at higher frequency ranges (> 530 Hz) was correlated with the acoustic modes of the current combustor [103]. The amplitude of these acoustic mode peaks increased at higher % hydrogen in the fuel that was also perceived from the audible signature of the reaction zones during experiments. The common peak frequency (for $p'$and q') was slightly shifted to lower frequency (i.e., towards left in the plot) with gradual H_2 enrichment to methane fuel. Existence of different frequency peaks were also observed by Wicksall and Agrawal [107] at different H_2 enrichment levels in swirl flame using H_2 enriched methane or propane fuels.

Along with the 157 Hz peak, a smaller peak of 197 Hz was observed at 40% H2-enrichment. The addition of hydrogen in methane influenced this common frequency of fluctuation for both the acoustic signal and the PMT signal (or the qualitative heat transfer). Similar information of PSD of $p'$and q' was obtained in distributed reaction zones with gradual H_2 enrichment as shown

in Fig. 6.5. The common peak of $p'$and q'(at 175 Hz) observed in conventional swirl flame (Fig. 5.4) vanished in distributed combustion that was fostered purely with methane (see Fig. 6.5a).

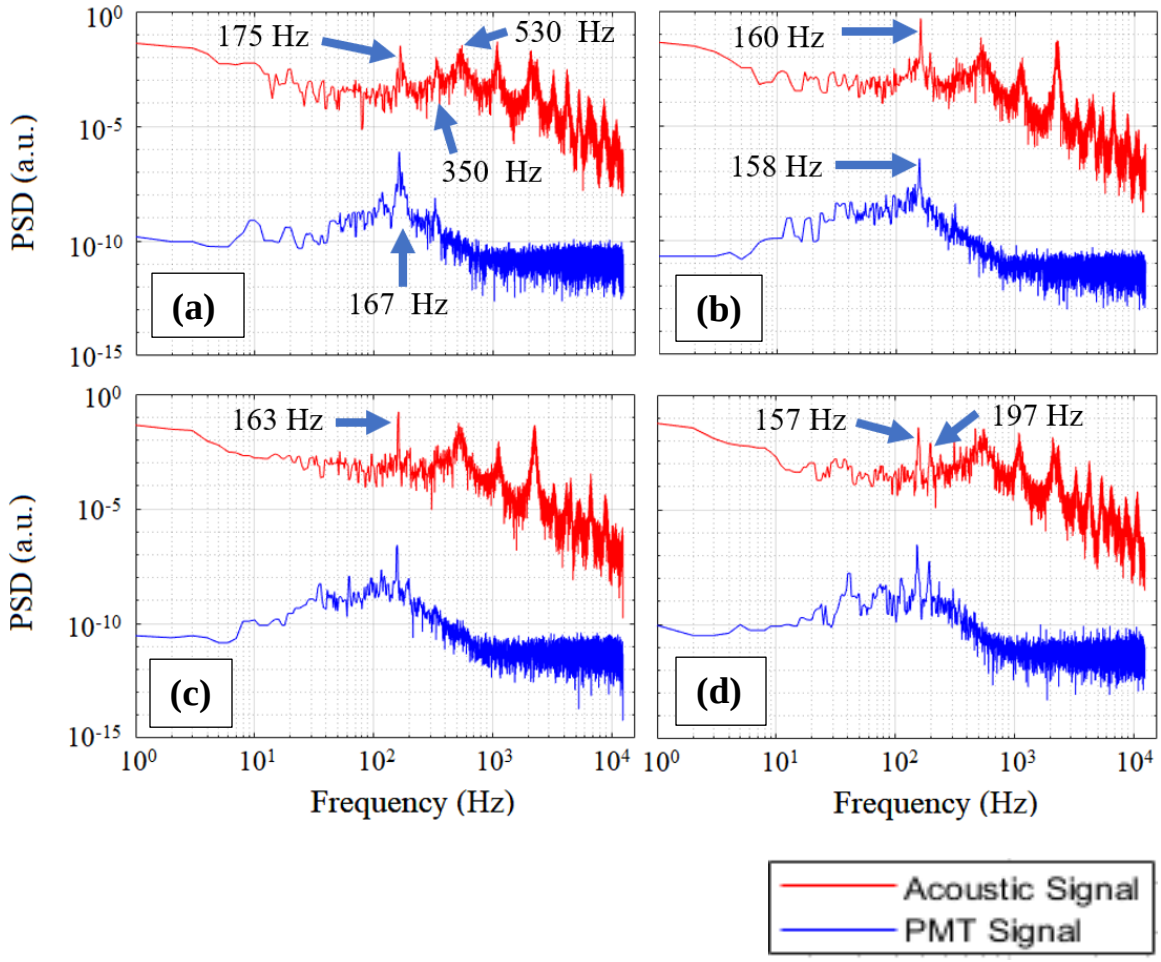

Fig. 6.4 Power spectral density (PSD) of the acoustic and PMT signal fluctuations for conventional swirl flame (at O_2~19%) reaction zones with (a) 0%, (b) 10%, (c) 20%, and (d) 40% hydrogen enriched methane.

The decline of peaks suggests that the thermo-acoustic instability in distributed combustion was dampened resulting in decreased reaction zone fluctuation [106] to support stable combustion and lower noise levels. However, the peak signifying the existence PVC and higher frequency peaks were still observed in distributed combustion. With gradual increase of % H_2 enrichment,

the acoustic fluctuation peak of PVC shifted slightly to lower frequency (towards left in the figure) indicating the effect of hydrogen addition on the hydrodynamic structures of swirling distributed combustion.

Note that after 40% hydrogen enrichment, a minor common peak of the $p'$and q' signals returned (around 129 Hz) (see Fig. 6.5d). The existence of such peaks indicated a slight reduction of flowfield stability (which is a characteristic of non-distributed reaction zone). This is because the reaction zone in this condition was not completely distributed and the observation of common peak of $p'$and q' can be correlated with the existence of weak thermo-acoustic coupling at 40% hydrogen enrichment to methane. Distributed combustion for this condition was actually achieved with a higher flowrate of diluent CO_2 (with 18.25 LPM). This reveals that fuel property can have some effect on establishing distributed combustion. Figure 6.6 shows the PSD of $p'$and q'signals for the distributed combustion case with 40% hydrogen enriched methane and with increased dilution of 18.26 LPM of CO_2. As observed, the common peak of $p'$and q'signal observed near 129 Hz in Fig. 6.4d disappeared for the distributed combustion case using 18.25 LPM CO_2 dilution (see Fig. 6.6). The only minor peaks observed were related to the acoustic modes of the combustor along with a very weak peak associated with the PVC. The results show that any possible thermo-acoustic coupling is dampened in this condition. This condition is considered as the actual distributed combustion fostered with CO_2 dilution for the 40% H_2- enriched methane fuel case. Such results explain the existence of a 129 Hz peak in Fig. 6.5, which is due to the non-distributed nature of the reaction zone with 14.55 LPM CO_2.

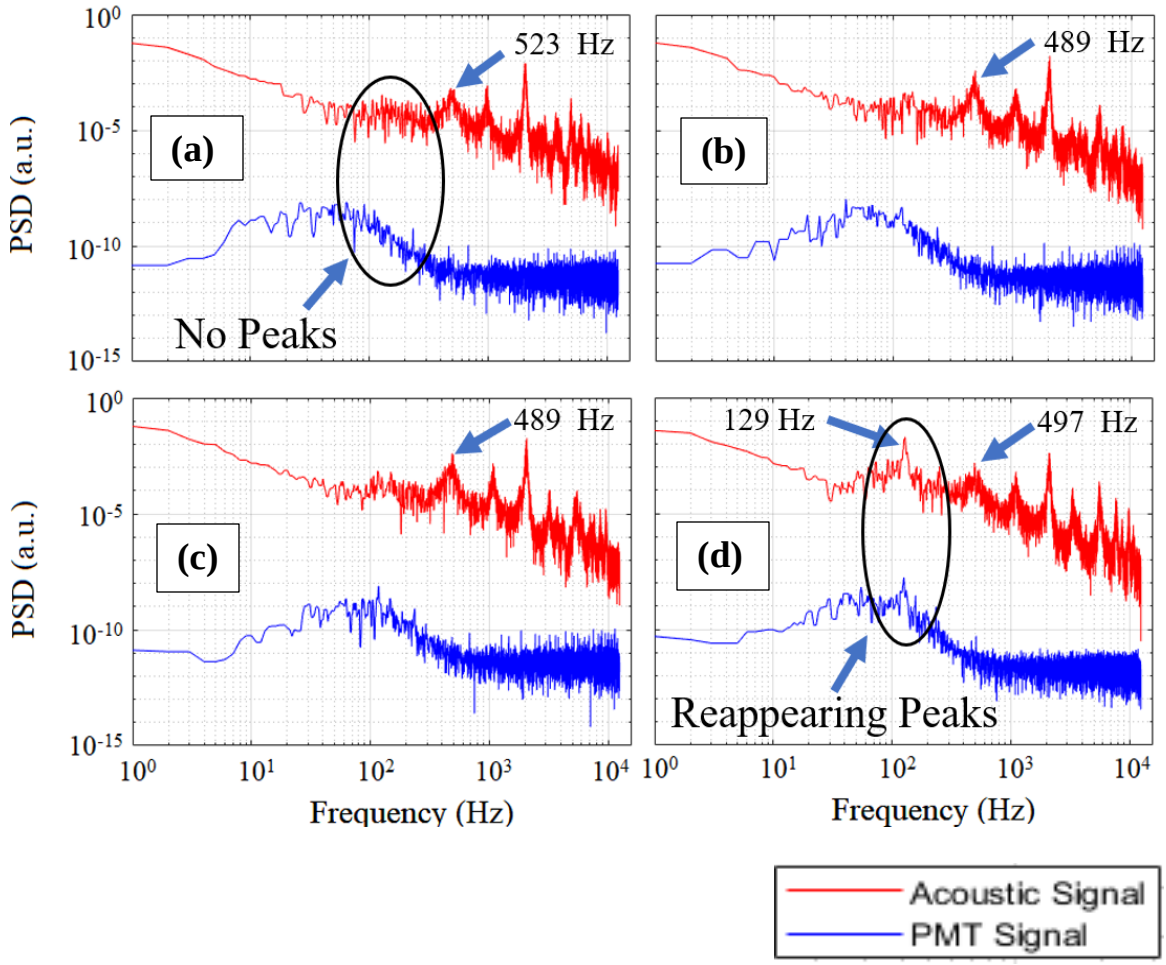

Fig. 6.5 Power spectral density (PSD) of the acoustic and PMT signal fluctuations for distributed combustion (at o2~17%) reaction zones with (a) 0%, (b) 10%, (c) 20%, and (d) 40% hydrogen-enriched methane (with 14.55 LPM CO_2 diluent).

The input airstream was not preheated prior to conducting this trial. Similar PSD studies of $p'$and q' were carried out in our earlier work [106] with preheating of the input air to support conditions suitable to gas turbines. It was found that the air preheating helps in diminishing thermo-acoustic coupling with gradual dilution at relatively earlier stage of dilution compared to non-preheat cases. Also, the intensity of the PVC peak gradually declined with preheating of air.

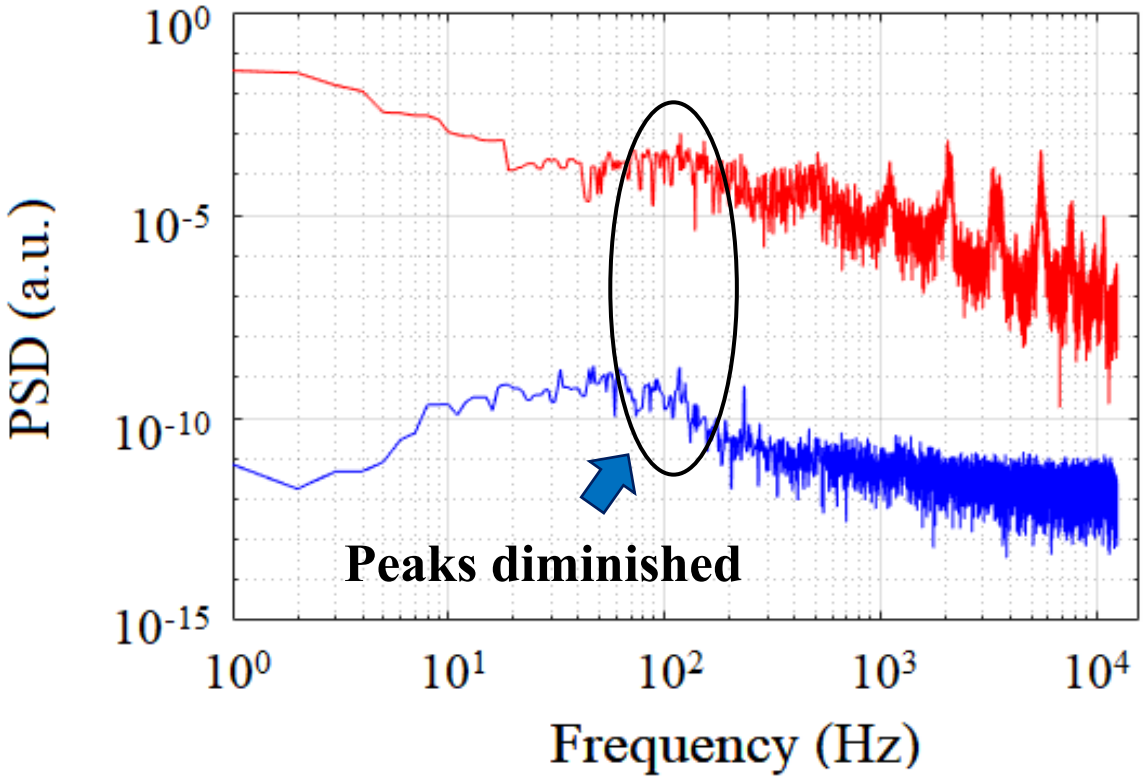

Fig. 6.6 Power spectral density (PSD) of the acoustic and PMT signal fluctuations for distributed combustion with 40% hydrogen-enriched methane using 18.25 LPM CO_2 diluent.

6.1.3 Proper Orthogonal Decomposition Analysis:

Previously, the utilization of POD helped us to visualize and compare the dominant structures (vortex shedding, flame whirling) in swirl combustion and distributed combustion with pure methane [106] as found in chapter 5. POD was utilized in this work to understand and observe the formation of structures in reaction zones with hydrogen enriched methane. The specific questions that are of interest here are: (a) what is the effect of fluctuating structures on reaction zone stability? and (b) can we better understand the departure of distributed combustion behavior for the 40% H_2-enriched methane case in the case of 14.55 LPM CO_2 dilution?

To determine POD modes at various levels of %H_2-enrichment, the instantaneous chemiluminescence images (high-speed photos) were selected as the instantaneous parameter u (x, t). The pure methane fueled case (H_2 = 0%) was studied in the past [106], which showed vortex shedding along shear layers in swirl combustion that influenced the thermo-acoustic instability. However, distributed reaction zones showed significantly low fluctuation without any considerable vortex shedding. To understand the effect of hydrogen fuel on reaction zones, the first four POD modes with 10% H_2-enriched methane are shown in Fig. 6.7.

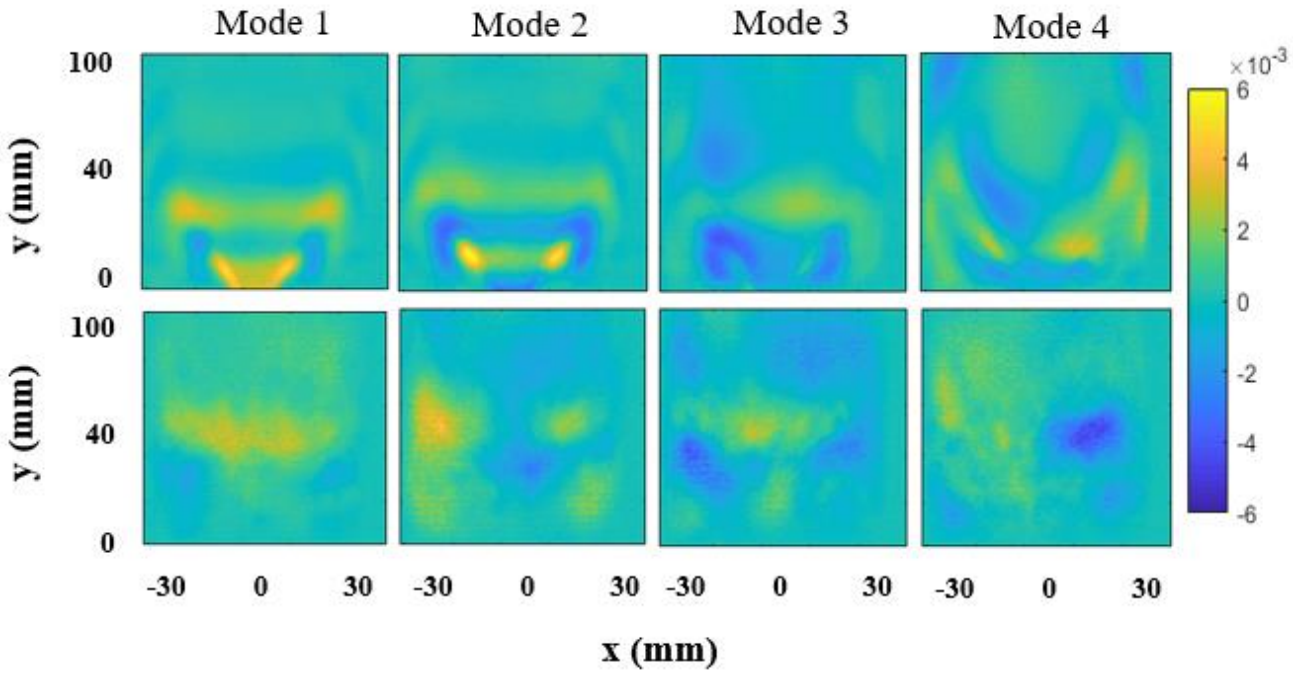

Fig. 6.7 First four POD modes of the conventional swirl combustion (top row) and distributed combustion (bottom row) with 10% hydrogen-enriched methane using 14.55 LPM CO_2 dilution.

The first four modes contained significant energy of fluctuations (~ 5- 30%) and are presented according to decreasing energy levels. Hence, mode 1 possessed the highest fluctuation energy. The appearance of different vortex shedding patterns were also observed in the conventional swirl combustion (see the top row of Fig. 6.7). Mode 1 and 2 in swirl combustion

exhibits vortex shedding along the shear layers near the burner exit. Modes 2 also showed the alternate ring vortex propagation in swirl combustion mode (blue and yellow horizontal patches). Such vortex shedding was partly present in mode 3 also. Mode 4 showed rotating structures (as observed on both sides) which signify the whirling nature of the reaction zone. Hence the vortex shedding, and rotational characteristics are the primary contributors to flame fluctuation in swirl combustion. In contrast, the current distributed combustion case (see bottom row of Fig. 6.7) showed no significant vortex shedding, indicating improved flame stability in distributed combustion. Further investigation was carried out to obtain the power spectral density (PSD) of these POD modes that can reveal the influence of vortex shedding and rotational structures in flame fluctuation behavior. Figure 6.8 shows the PSD plots of POD modes for both swirl and distributed combustion with 10% H_2-enriched methane. As observed, the POD modes for swirl combustion possessed a fluctuation peak at 162 Hz, which is very close to the ~160 Hz peak observed from the PSD analysis of $p'$and q' signals (shown in Fig. 6.4 b) for this case. This indicates that the vortex shedding behavior in swirl combustion with 10% hydrogen-enriched methane influenced the possible thermo-acoustic coupling found from the PSD of $p'$and q' signals. In contrast, no such major fluctuation peak was observed in distributed combustion (see Fig. 6.8 b) that confirmed the reduced flame fluctuation in distributed combustion regime. The mild fluctuation observed in the PSD of different modes of distributed combustion can be attributed to the rotational behavior of the reaction zone. Hence, this result supports the disappearance of peaks in the PSD of $p'$and q' signals (Fig. 6.5 b) indicating the diminished thermo-acoustic instabilities in distributed combustion. A similar vortex shedding influenced flame fluctuation was observed in our previous work for the swirl flames with pure methane [106].

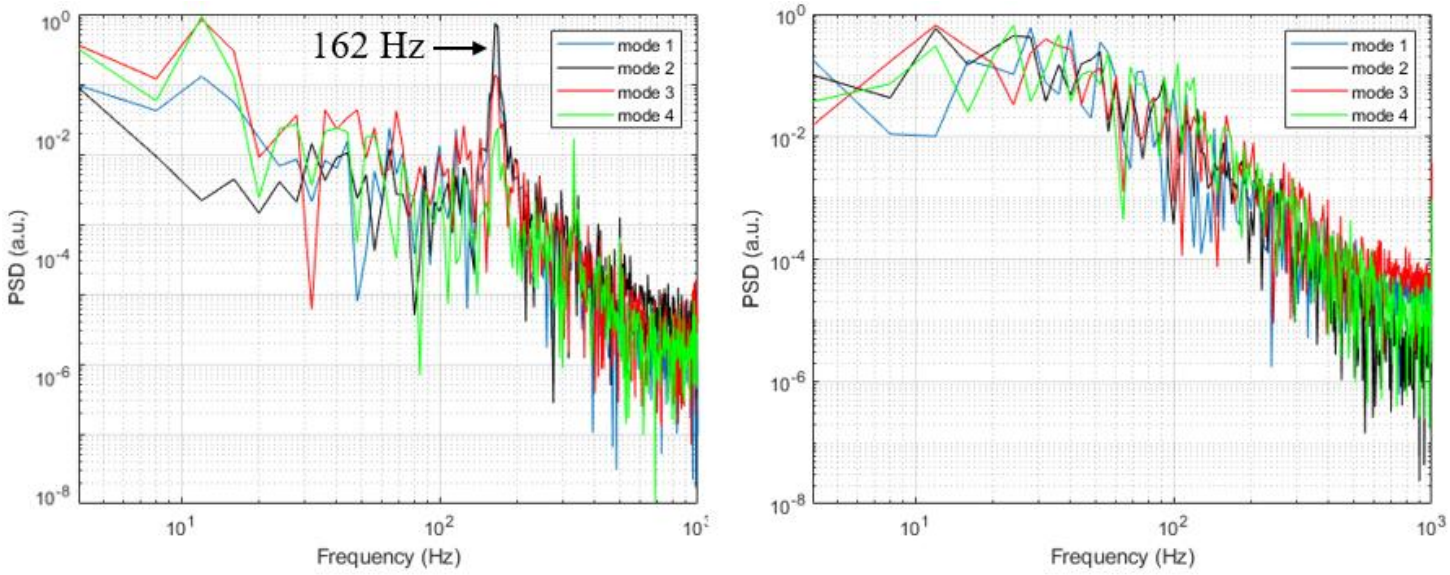

Fig. 6.8 Power spectral density of the first four POD modes of the (a) conventional swirl combustion (top row) and (b) distributed combustion (bottom row) using 10% hydrogen-enriched methane with CO_2 dilution.

A correlation between the vortex shedding frequency and the POD fluctuation frequency was found in that study. No major vortex shedding in distributed combustion was observed in that work supporting the reduction of flame fluctuations in distributed combustion. Hence, the present result is consistent and supportive of our previous experimental results. A similar behavior was observed with distributed combustion using 20% hydrogen-enriched methane.

Further, the POD modes were obtained for the distributed combustion case with 40% hydrogen-enriched methane and CO_2 dilution (14.55 LPM) to analyze the observed departure of this case from the distributed combustion behavior. Figure 6.9 exhibits the first 4 modes of both swirl and distributed combustion with 40% hydrogen-enriched methane using CO_2 dilution. In this case, the swirl combustion also showed a high influence of vortex shedding. While the propagation of vortices along the reactive shear layers was observed in modes 1 and 2, modes 3 and 4 showed

ring vortex at downstream locations. For the present distributed combustion case (bottom row of Fig. 6.9), appearance of prominent structures was again observed. Such vortex shedding can be clearly observed in modes 3 and 4 of distributed combustion (with small dark blue and yellow patches highlighted in the figure).

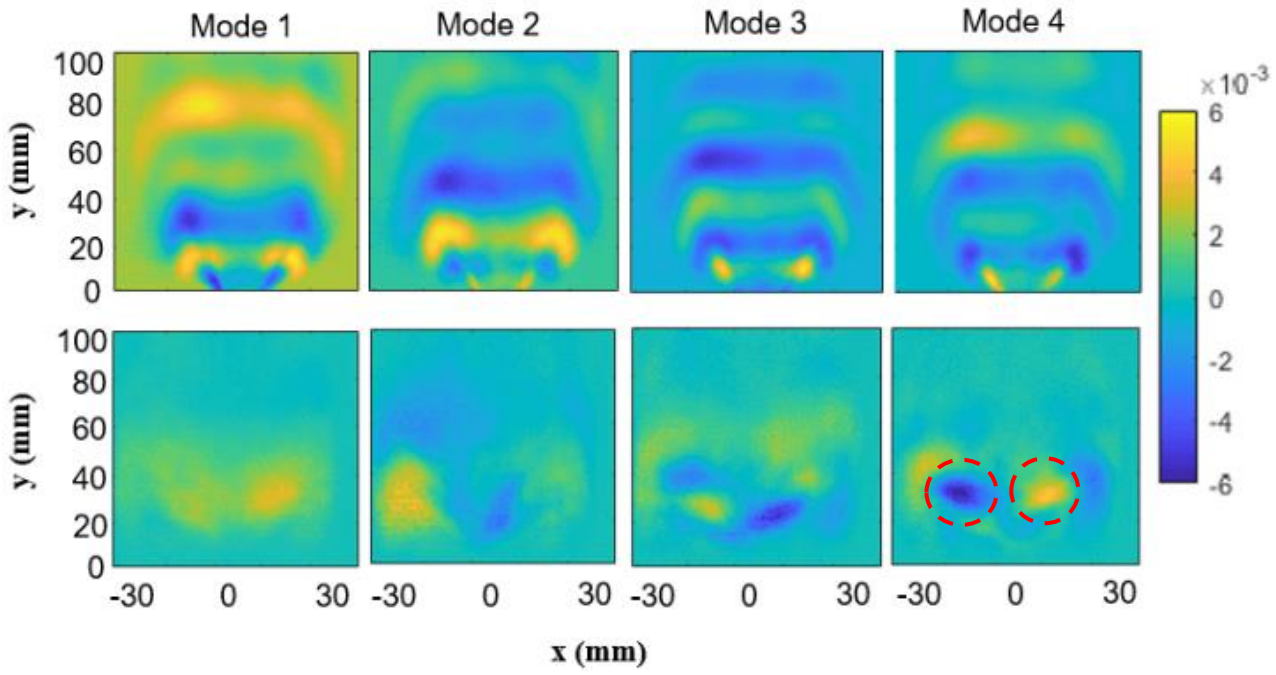

Fig. 6.9 First four POD modes of the conventional swirl combustion (top row) and distributed combustion (bottom row) with 40% hydrogen-enriched methane and 14.55 LPM CO_2 dilution.

The appearance of structures in the current case (with 40% hydrogen-enriched methane and 14.55 LPM CO_2 dilution) can be attributed to vortex shedding, which causes a fluctuating reaction zone. These structures were not seen in the case of distributed combustion with 10% hydrogen-enriched methane, see Fig. 6.7. This investigation was extended by obtaining the PSD of these modes. The PSD of spatial modes helped in understanding whether this vortex shedding influenced the fluctuation of the reaction zones. The PSD analysis (see Fig. 6.10) showed the existence of a peak at 180 Hz for the different modes in swirl combustion. This peak exists between

the two peaks at 157 Hz and 197 Hz as observed from the PSD analysis of $p'$and q' signals (see Fig. 6.4 d). This indicates that the vortex shedding behavior in swirl combustion with 40% hydrogen enriched methane influenced the possible thermo-acoustic coupling found from the PSD of $p'$and q' signals. Reduced fluctuation in distributed combustion mode was observed as compared to the swirl combustion cases.

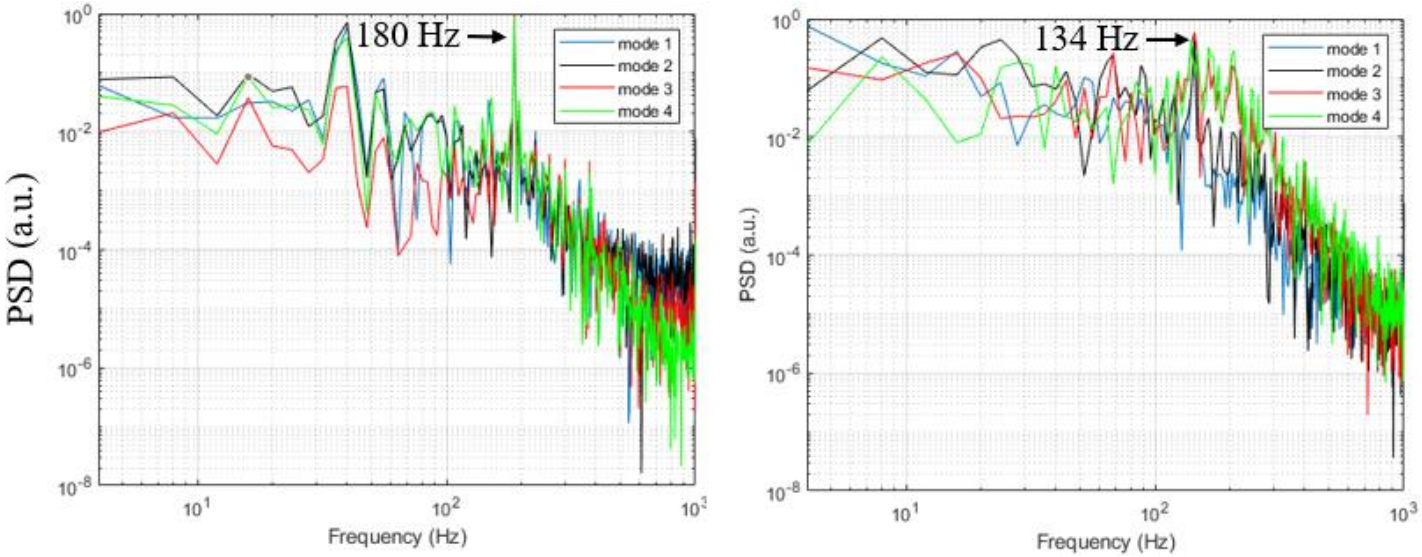

Fig. 6.10 Power spectral density of the first four POD modes of the conventional swirl combustion (left) and distributed combustion (right) with 40% hydrogen-enriched methane with CO_2 dilution.

The PSD plot of distributed combustion did, however, show a peak about 134 Hz, which is close to the peak seen in the PSD plot with $p'$and q' signals at 129 Hz (see Fig. 6.5 d). This is a good confirmation for the observed flame fluctuation and departure of distributed combustion behavior with 40% hydrogen enriched methane and 14.55 LPM CO_2 dilution. Such analysis indicates that the fluctuation in distributed reaction with 14.55 LPM CO_2 dilution was influenced by the vortex shedding found from the POD analysis in Fig 6.9. Hence, this case does not represent a purely distributed reaction zone. It is important to note that higher flow of diluent (18.25 LPM

CO_2) was required to properly foster distributed combustion with 40% H_2-enriched methane fuel as reported in section 6.2. Increasing hydrogen content in the fuel mixture gradually increased the amounts of water vapor while it reduced CO_2 in the combustion exhaust. Such increase in vapor increases the specific heat of the combustion exhaust resulting in higher enthalpy content (in the product) that is transported to the flame root due to swirling nature of this reaction zone. Hence, localized thermal fluctuations are expected resulting in observed deviation from the distributed nature with 14.55 LPM dilution of CO_2 and higher diluent flow was required to produce uniform distributed reaction zones. However, further investigation needs to be made to properly understand the influence of higher vapor content on distributed reaction zones, which was not the primary focus of this research.

6.1.4 Lean Blowoff Characteristics in Distributed Combustion with H_2-Enriched Methane

Lean combustion technologies must consider the blowoff limit while determining the operational limit. Conventional stationary gas turbines often operate with equivalence ratio as low as ~ 0.3 [15]. However, at very lean equivalence ratios, combustion may suffer from instabilities and flame blowoff. Hence, the knowledge of lean blowoff limits in distributed combustion is essential to implement this technology in real gas turbine combustors.

In this work, lean blowoff equivalence ratios (ϕ_{LBO}) for traditional swirl combustion and distributed combustion at various H_2 enrichments to methane were compared. Air preheating was performed (between 373-573K) for the distributed combustion cases to determine how much reduction in ϕ_{LBO} could be achieved (on the leaner side) to enhance the wider operational window. Figure 6.11 exhibits the variation of blowoff equivalence ratio with gradual H_2 enrichment to methane fuel. In each case, the ϕ value was decreased from an initial value of 0.9 to the

corresponding ϕ_{LBO} by adding more air while keeping the fuel flowrate constant. The ϕ_{LBO} gradually decreased with hydrogen enrichment to methane for both swirl combustion and distributed combustion cases. Gradual reduction of ϕ_{LBO} using hydrogen-enriched methane was also reported in a past study [108] and it was attributed to enhanced flame speed moving the reaction zone close to the nozzle exit and increase in adiabatic flame temperature (AFT) and strain rates from the hydrogen addition. The addition of hydrogen reduces the density of the fuel mixture to result in enhanced flame speed. An increase in reaction rate (or flame speed) makes the reaction zone more energetic resulting in enhanced stability of the reaction zone to much-reduced equivalence ratios wherein the lean blowoff occurs. The increased flame speed with $\%H_2$ was also verified with Chemkin-Pro© simulation coupled with GRI-mech 3.0 reaction mechanism [94]. Laminar flame speed computation showed a reduction of flame speed (average) from~ 0.35 m/s to 0.027 m/s when distributed reaction zones were fostered from conventional swirl flame for different hydrogen enrichment cases. As observed, blowoff in distributed reaction zones occurred at relatively high ϕ values than the conventional swirl flames for our quest in seeking near stoichiometric combustor operation. With increasing hydrogen content in the fuel blend, the ϕ_{LBO} of distributed reaction zones approached the ϕ_{LBO} of the conventional swirl flame fostered with pure CH_4 having 0% H_2 enrichment. Further reduction of ϕ_{LBO} in distributed combustion was desired to achieve wider lean operation characteristics similar to conventional swirl combustion. The reduction in ϕ_{LBO} was fostered by adding preheats to the inlet airstream. Such reduction of ϕ_{LBO} in distributed combustion was achieved by preheating the inlet airstream in distributed combustion for different H_2 enrichment cases. Gradual preheating reduced the ϕ_{LBO} in distributed combustion such that they are very similar to that of swirl combustion. The ϕ_{LBO} curve in distributed combustion at 473K nearly overlaps with that of the conventional combustion curve.

Note that this distributed combustion was fostered with 14.55 LPM of CO_2 dilution that showed a departure from the distributed nature of reaction zone at 40% hydrogen enrichment. We also examined the ϕ_{LBO} limits with 18.25 LPM of diluent and preheating. As observed, the non-preheated distributed reaction zone with 18.25 LPM of CO_2 dilution resulted in blowoff at a relatively higher ϕ value than the 14.55 LPM case. But a reduction of ϕ_{LBO} was also achieved for the 18.25 LPM dilution case with the air preheats.

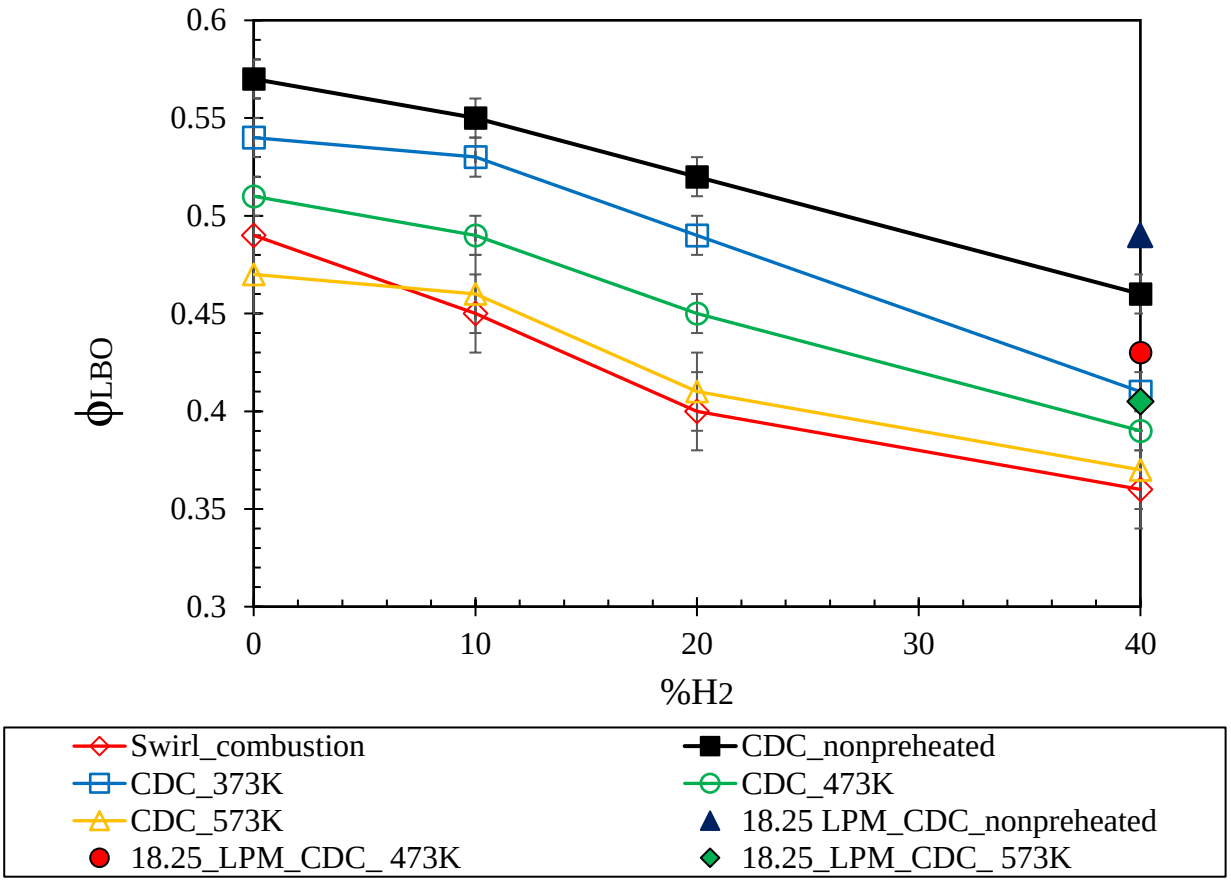

Fig. 6.11 Lean blowoff equivalence ratio variation for conventional swirl and distributed reaction zones with hydrogen-enriched methane.

Reduction of equivalence ratio to more lean equivalence ratio with air preheats was primarily attributed to the increase in flame speed and adiabatic flame temperature that provided additional stability to the reaction zones. Some previous studies [109] concluded that high-temperature flame

(due to increased preheating) are less sensitive to flame stretch because of higher flame speed resulting in reduced $\phi_{LBO.}$ The plots showing the reduction in laminar flame speed in distributed combustion (due to dilution) and increase in flame speed and temperature due to preheating is given in appendix C. The increase in water vapor formation with hydrogen-enrichment explained earlier is displayed in appendix C. In the case of distributed combustion, it is important to note that preheating is very advantageous because it raises the adiabatic flame temperature while maintaining a uniform thermal field, improving flame stability and gas turbine thermal efficiency. Hence, preheating compensates for the drop in adiabatic flame temperature that occurs from diluting the reaction zone with CO_2 or N_2.

6.1.5. NO, CO and CO_2 Emission Characteristics

Any modern combustion technology for gas turbines must consider emission reduction. One important aspect of investigating H_2-enriched methane for distributed reaction zones was to understand the nature of pollutants emission (NO, CO) and CO_2 emissions with gradual hydrogen enrichment to fuel. Reduced CO_2 emission is also a key to developing new combustion technologies that support the future decarbonization goals. A general problem of increasing H_2-enriced fuels is the increase in NOx with gradual hydrogen enrichments [110, 111]. Such an increase of NOx level was influenced by the rise of flame temperature or the geometrical configuration of the burners. The results are reported on the NO, CO, and CO_2 emissions from distributed reaction zones fostered with CO_2 or N_2 dilution of the main airstream. The measured concentrations were normalized with respect to 15% of O_2 (to comply with EPA standards) in the exhaust stream. Concertation reported at each H_2-enrichment level were the average of 2 minutes of data sampled at a rate of 60 datapoint/ minute by the gas analyzer. Figure 5.12 shows NO and

CO emissions (in ppm) from conventional air-swirl combustion as well as distributed combustion for both cases of CO_2 or N_2 dilution of the main airstream. The NO emission gradually increased with an increase in H_2 enrichment for conventional swirl combustion. Gradual H_2 enrichment in fuel makes the reaction zone more energetic, along with a gradual rise of flame temperature when %hydrogen was gradually increased. A previous study by Lantz et al. [89] on an industrial dry low emission (DLE) burner using hydrogen-enriched natural gas flames suggested such an increase of NO occurs due to the increase in local flame temperature from hydrogen addition even when the overall adiabatic flame temperature was kept constant. This study also indicated the possible influence of broadening of the post combustion zone on increased NOx due to hydrogen addition. Addition of hydrogen starts the onset of flame reactions at relatively upstream locations close to the exit nozzle. Hence, the observed rise of NO ppm is reasonable for the conventional swirl flame at O_2~21%. A similar trend was observed in a study on distributed combustion performed in a rectangular combustor setup by Kim et al. [112].

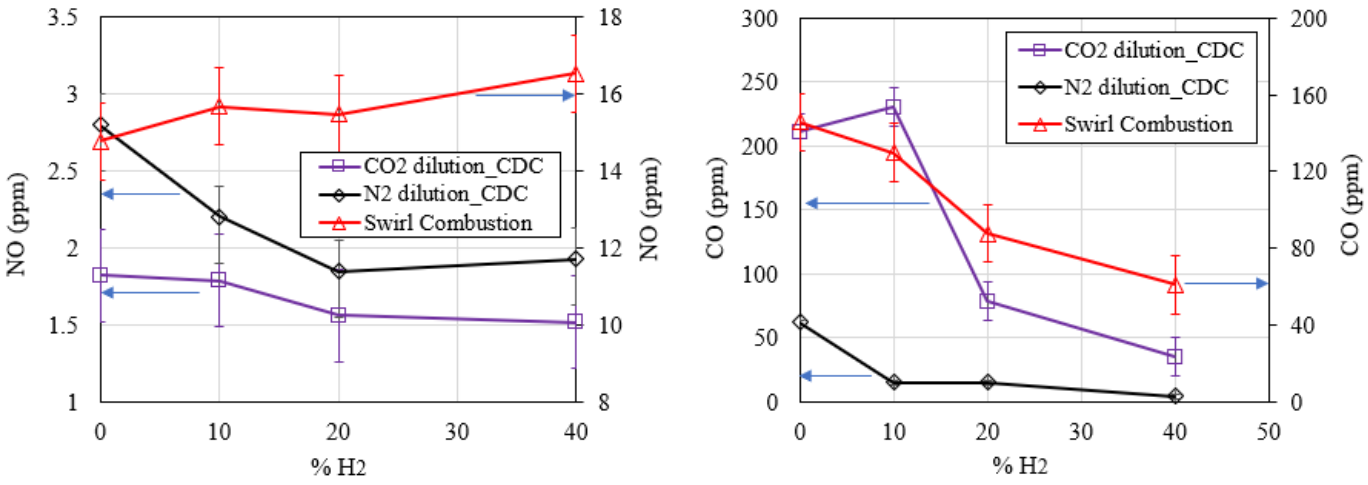

Fig. 6.12 Emission of (a) NO and (b) CO with CO_2 and N_2 dilution of the main air stream. NO and CO Concentrations reported here are corrected to 15% O_2 concentration.

In swirl air combustion with hydrogen-enriched methane, the thermal-NO process ($O + N_2 \longleftrightarrow NO + N$; $N + O_2 \longleftrightarrow NO + O$) is the main contributor to NO generation. On the contrary, the NO emission from the diluted reaction zones (with CO_2 or N_2) was found to decrease with gradual hydrogen enrichment. Gradual dilution of reaction zones decreases the flame temperature resulting in decreased NO emission in the exhaust stream of the distributed combustion. The adiabatic flame temperature was found to decrease from ~2050 K to 1520 K for different $\%H_2$-enriched methane cases as observed from Chemkin-Pro© simulation. The NO (ppm) for the N_2 diluted flowfield case was slightly higher than that of CO_2 dilution case, which is related to the higher heat capacity of CO_2 that provided lower combustion temperature [113] and hence lower NO in that case (with CO_2 dilution). The other factor responsible for the decrease in NO concentration in distributed combustion was the reduction of 'prompt NO' formation with gradual increase of $\%H_2$-enrichment to methane. Prompt NO formation predominantly arises from the reaction between CH radical and molecular nitrogen producing hydrogen cyanide (HCN) through the reaction channel:

$$CH + N_2 \rightarrow HCN + N \tag{6.2}$$

Later this HCN is oxidized to NCO which is converted finally to NO. The details of these reaction mechanisms can be found elsewhere [114]. Reduction of NO in distributed combustion was investigated with Chemkin-Pro© simulation. Results revealed that gradual increase in % hydrogen in fuel increases the consumption of CH through another reaction channel given by:

$$CH + H_2 \rightarrow H + CH_2 \tag{6.3}$$

Such consumption of CH radical through equation 3 reduced the coefficient of sensitivity of the reaction given by equation (2) with gradual $\%H_2$-enrichment. Hence, the prompt NO formation is suppressed with gradual increase of hydrogen content in fuel. Other NO formation pathways involve NNH mechanism ($N_2 \rightarrow NNH \rightarrow NO$) and N_2O intermediate mechanism ($N_2 \rightarrow N_2O$

→ NO) were also observed in our computation. But these mechanisms did not show major impact on NO formation in distributed combustion compared to prompt NO pathway. Normalized sensitivity coefficients are included in appendix A.4. Influence of similar reaction mechanisms on NO reduction was mentioned by Li et al. [115] for the study of MILD combustion with methane/hydrogen blend fuel. However, the N_2O intermediate mechanism was found to be the dominant mechanism of NO formation in that study.

For both dilution cases, a steady decrease in CO emission occurred along with an increase in H_2-enrichment. The CO emission for the CO_2 diluted distributed combustion was higher than the N_2 diluted case and for some $\%H_2$ in conventional swirl combustion (H_2 = 0- 20%). This is attributed to the use of CO_2 as the diluent, which undergoes high-temperature dissociation to CO. The overall decrease of CO concentration in the exhaust from distributed combustion for each hydrogen-enriched case indicated the reduction of variable stoichiometry, enhanced mixing, and the uniformity of combustion behavior across the entire combustor volume. At lower hydrogen-enrichment (~0-10%), the CO_2 diluted cases showed higher CO in distributed combustion compared to swirl combustion. Higher carbon content of fuel mixture, high-temperature dissociation of diluent CO_2, and lower residence time of combustion [70] are the possible source of such rise in CO concentration. Hence, the distributed combustion with H_2 enrichment is advantageous for the reduction of toxic pollutants, such as NO and CO.

The CO_2 emission from the exhaust of the distributed reaction zone with H_2 enriched methane was examined for both the diluents (CO_2 and N_2).

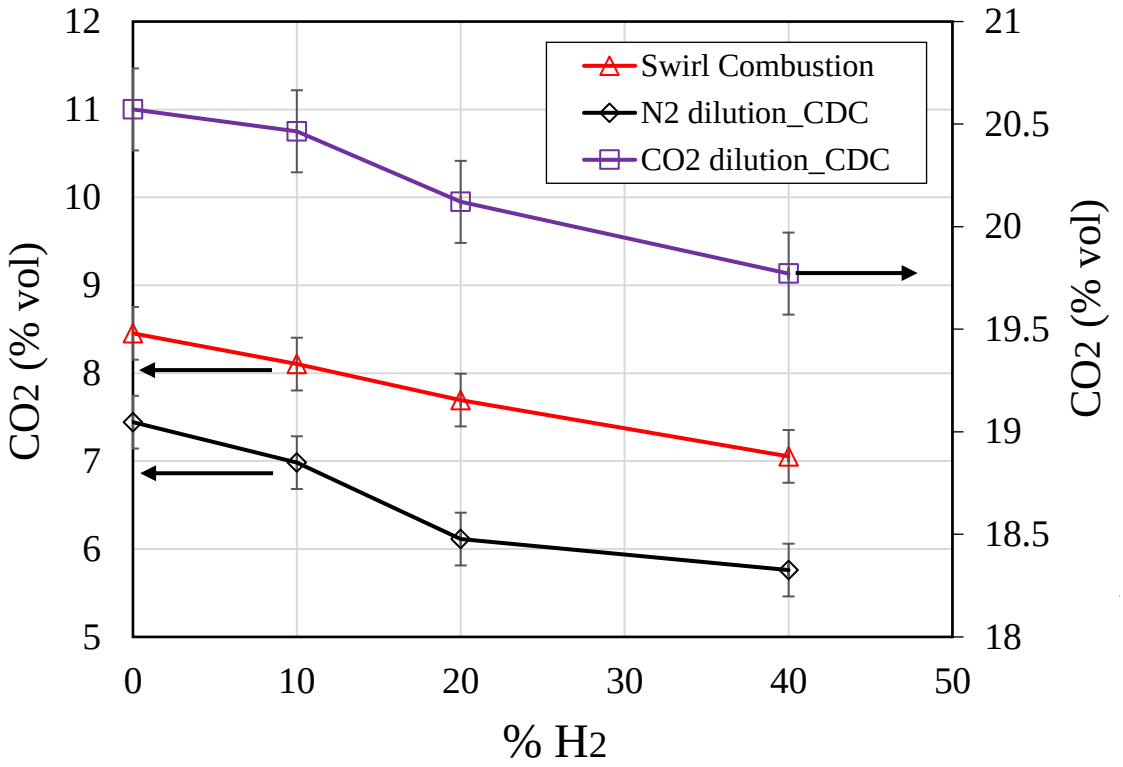

Fig. 6.13 Measured CO_2 concentration in the exhaust with CO_2 and N_2 dilution of the main air stream.

Figure 6.13 shows the change in CO_2 concentration caused by the gradual enrichment of H_2 to methane. As observed, the CO_2 concentration gradually decreased with an increase in $\%H_2$ content in methane in both conventional swirl combustion and distributed combustion. This observation of decreased CO_2 emission is consistent for both the diluents (see Fig. 6.13). The effect of low carbon content of the fuel clearly signifies the reduced CO_2 formation in the combustion exhaust for these cases. The CO_2 emission in the exhaust from CO_2 diluted distributed reaction zones were found to be higher than the N_2 diluted flowfield cases. Dilution of flowfield with CO_2 is primarily responsible for such enhanced CO_2 emission in the exhaust. The observed reduction of CO_2 in the exhaust from combustion of different H_2 enriched methane fuels provides the key role played by the H_2 containing fuel mixture properties.

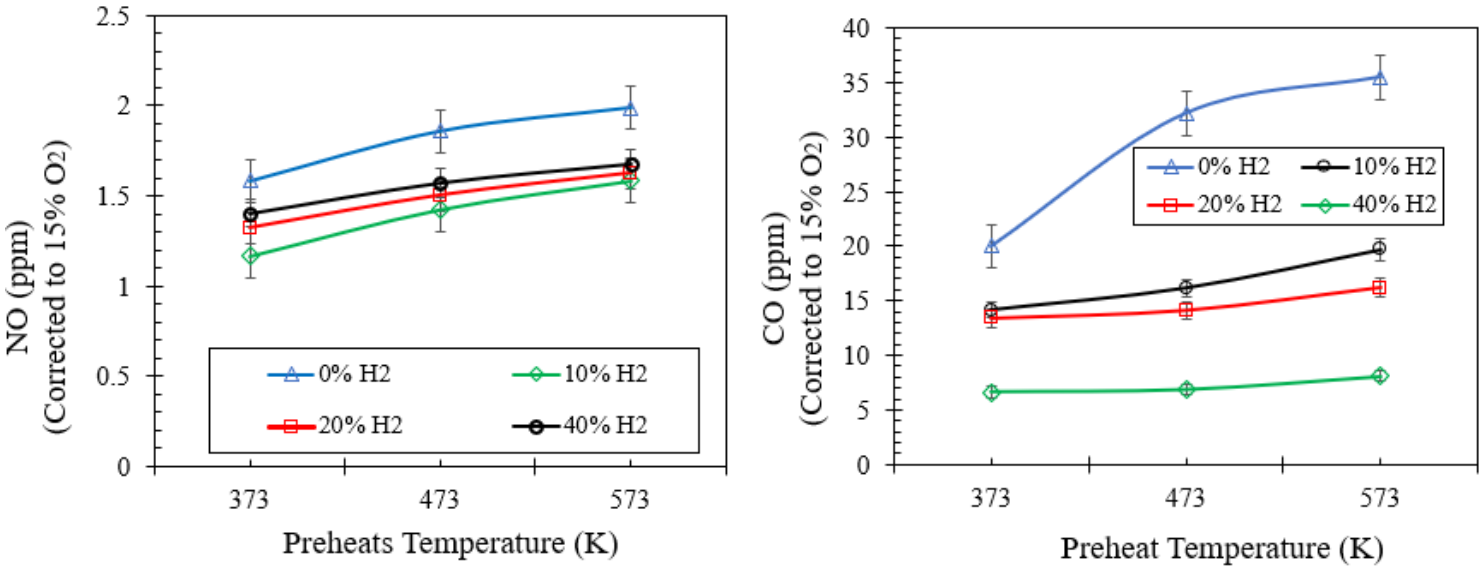

Fig. 6.14 Emission of (a) NO and (b) CO in distributed combustion with CO_2 dilution and inlet air preheating.

In order to support the emission characteristics in situations that are important to gas turbines, the emission characteristics from distributed combustion were also performed with the input air preheated. Figures 6.14 show the NO and CO concentrations from distributed reaction zones (with CO_2 dilution) with gradual preheating of inlet air in the range 373-573K. The concentration of NO increased with gradual preheating, which is reasonable due to increased flame temperature. At any given preheat temperature, the NO ppm gradually decreases with increase in $\%H_2$ enrichment. This observation is consistent with the results found without preheating (Fig. 6.12) and is attributed to the dilution effect of the main airstream. The concentration of CO also increased with gradual preheating of the inlet air. Such result is reasonable as high-temperature dissociation of CO_2 (from dilution and exhaust) increases the formation of CO [96]. In general, the CO (ppm) at any preheat temperature is relatively lower for higher $\%H_2$ enrichment in the fuel. This can be attributed to reduced carbon content in the fuel with increase in $\%H_2$ in the fuel.

Besides, the measurement of CO_2 emission at different preheat temperatures also showed reduced CO_2 emission with increase in $\%H_2$ content in the fuel at any preheat temperature. Such an outcome is consistent with the non-preheated emission results. With gradual increase of preheats, the CO_2 %vol remained almost constant or showed slight decrease that is related to high-temperature dissociation of CO_2. A similar observation of emission characteristics in distributed combustion using air preheats was made with N_2 dilution as well. The results support that distributed combustion is a novel combustion technology that provides ultra-low pollutants emission as well as reduced greenhouse (of CO_2) gas emission.

6.2 Summary

Distributed reaction was studied with hydrogen-enriched methane at 5.72 MW/m^3-atm heat release intensity. Important aspects studied were the stability of the reaction zone, blowoff, and emission characteristics of NO, CO, and CO_2. Experiments were mainly performed with CO_2 dilution while the exhaust emission measurements were performed with both CO_2 and N_2. High-speed imaging was performed at 2000 frames per second for both swirl and distributed combustion conditions with H_2 enrichment of methane fuel. Enhancement of chemiluminescence intensity with gradual increase of $\%H_2$ in the fuel mixture was observed for both the swirl and distributed combustion cases. The standoff distance gradually reduced with hydrogen enrichment of the methane fuel, and the shape of the flame became narrower for both the swirl and distributed combustion. The microphone and PMT (fitted with CH* filter) signal were collected for the different cases to obtain the fluctuation of pressure and qualitative heat release signatures from the reaction zones. Power spectral density (PSD) was evaluated from the pressure and heat release fluctuation data ($p'$and q') for the various combustion cases reported. It is important to note that CH* chemiluminescence

may not represent the actual heat release when fuel composition involves increasing $\%H_2$. Hence, care must be taken before obtaining quantitative analysis with PMT data with CH* spectral filters. Existence of a common peak for $p'$and $q'$was observed for most of the cases in regular swirl combustion indicating the possibility of thermo-acoustic coupling. On the contrary, no such common peaks near that frequency limit were observed in distributed combustion with H_2 = 0-20% enrichment. The POD analysis for this distributed combustion case demonstrated the appearance of vortex shedding characteristics in reaction zones. Such vortex shedding influenced the possible thermo-acoustic fluctuations observed from the PSD of $p'$and q' signals. The lean blowoff equivalence ratio (ϕ_{LBO}) measured for different $\%H_2$-enriched cases showed decrease of ϕ_{LBO} of distributed reaction zones with gradual $\%H_2$ enrichment (compared to the 0% H_2 enriched case) signifying the extension of lean operational limits. Measurement of NO concentration showed decreased emission in CDC for both the diluents because of the chemical effect of dilution that decreased the adiabatic flame temperature. The overall exhaust CO (ppm) emission also decreased gradually indicating enhanced mixing, and the uniformity of combustion across the combustor volume. A gradual decrease of CO_2 with $\%H_2$-enrichment for both swirl and distributed reaction zones were observed. Such reduction of CO_2 in the exhaust is due to influence of the low carbon content of the fuel from hydrogen enrichment. Such investigations of dynamic structure in reactive flow field with pure methane (chapter 5) and with hydrogen-enriched methane provided important understanding of the interaction of vortex structures with reaction zones, which inspires to visualize similar structures and its influence at higher heat release intensities. Appendix E provides the structural details (vortex propagation) of hydrogen-enriched swirl air and swirl distributed combustion at 7.63 MW/m^3-atm heat release intensity.

Chapter 7: Examination of Lean Blowoff Limits in Distributed Combustion with Varying Heat Release Intensities

This chapter discusses the results from lean blowoff (LBO) limits characterization in swirl-assisted distributed combustion. Examination was done with two different fuels such as propane and methane as the fuels at three different heat release intensities (5.72, 7.63, and 9.53 MW/m^3-atm). Detailed mechanism of flame blowoff in distributed combustion was focused. Distributed combustion regime was established using a conventional swirl-assisted burner using normal air (at O_2 ~ 21%) at rather high equivalence ratio of 0.9 (for gas turbine condition) by gradually diluting the inlet airflow with CO_2. Next, the airflow rates were varied to reduce the equivalence ratio until reaching the point of blowoff. Lean blowoff equivalence ratios (ϕ_{LBO}) in distributed combustion were recorded for both the fuels at every examined heat release intensity condition. High-speed chemiluminescence imaging was performed for stable distributed reaction zone conditions (at ϕ = 0.9) as well as at near blowoff equivalence ratio conditions. The variation of chemiluminescence signal intensities evolved from conventional swirl combustion and distributed combustion (under both stable and near blowoff conditions) were examined at near and far flowfield locations downstream of the burner nozzle exit. Furthermore, the effect of inlet airstream preheats on LBO was investigated at different air preheat temperatures of 400, 600, and 800 K that simulate gas turbine operational conditions. These results were further used to obtain the laminar flame speeds and flame temperatures at the blowoff points corresponding to the examined air preheat temperatures. The experimental conditions are mentioned in table 7.1.

Table 7.1. Flow conditions for lean blowoff study at various heat release intensities

Heat Release Intensity (MW/m3-atm)	Propane flowrate [L/min]	Methane flowrate [L/min]	Diluent CO_2 flowrate [L/min]		Air flowrate [L/min]	
			For Propane	For Methane	For Propane	For Methane
5.72	2	4.93	12	11.50	52	51
7.63	2.67	6.57	16.50	16	72	68
9.53	3	8.50	18.50	20	88	92

7.1. Results

The results are presented in this section from the different experiments reported with a focus on the fuel-lean condition in swirl-assisted distributed combustion under normal (at $\phi = 0.9$) and near lean blowoff (ϕ_{LBO}) conditions.

7.1.1. Lean Blowoff Limits in Distributed Combustion

The blowoff equivalence ratios in lean distributed combustion were examined at several different heat release intensities using propane and methane as the fuels. In all these cases, distributed combustion was fostered initially at an equivalence ratio of 0.9 and then gradually reduced until approaching the lean blowoff limit. Figure 7.1 represents the variation of lean blowoff equivalence ratios with different heat release intensities for the two fuels examined. The

lean blowoff in distributed combustion using propane fuel occurred at higher equivalence ratios than that for methane fuel at every heat release intensity. Such a difference in blowoff equivalence ratio is attributed to fuel property effects leading to the variation in flame speeds and strain rates [116]. The results show that the lean blowoff (ϕ_{LBO}) in distributed combustion gradually increased with an increase in heat release intensity for both the fuels (see Fig. 2). Such observation is attributed to the gradual increase in inlet flow-turbulence intensity that strongly enhanced with higher inlet flowrate at higher heat release intensities. The flow Reynolds numbers at the exit of the burner nozzle were 4992, 6705, 8920 (for methane) and 4886, 6750, 8128 (for propane) corresponding to the 5.72, 6.73, and 9.53 MW/m^3-atm heat release intensity. The stability of swirl flames strongly decreases with increase in turbulence levels that results in global flame extinction at higher equivalence ratios. Besides this, the decrease of flame stability can also be attributed to the heat loss to the burner wall (in this case quartz) from the flame reaction zone resulting in localized flame quenching [117, 118]. Higher heat release intensity required higher mass flow of the inlet mixture. Increasing heat release intensity enhanced the heat loss (from the reaction zone) by increased conduction and radiation effects. This paper reports on the role of variation of lean blowoff equivalence ratios in distributed combustion with heat release intensities. It is not the intent here to provide the blowoff mechanism in distributed combustion as it is beyond the scope of this work.

In a previous study [96], CO_2 dilution resulted in a gradual drop in adiabatic flame temperature and laminar flame speed when approaching towards distributed combustion similar to Wang et al. [119] Further dilution (with O_2 < 16%) created an additional drop in flame speed along with significant fluctuation of the lifted distributed reaction zone. The recent study by Roy and Gupta

[106] showed that such fluctuations in the reaction zone of distributed combustion were primarily influenced by the rotational effect of the reaction zone due to the existence of Precessing vortex core (PVC) [120- 122]. Such instabilities of reaction zone have shown to finally lead to global blowoff under fuel lean condition.

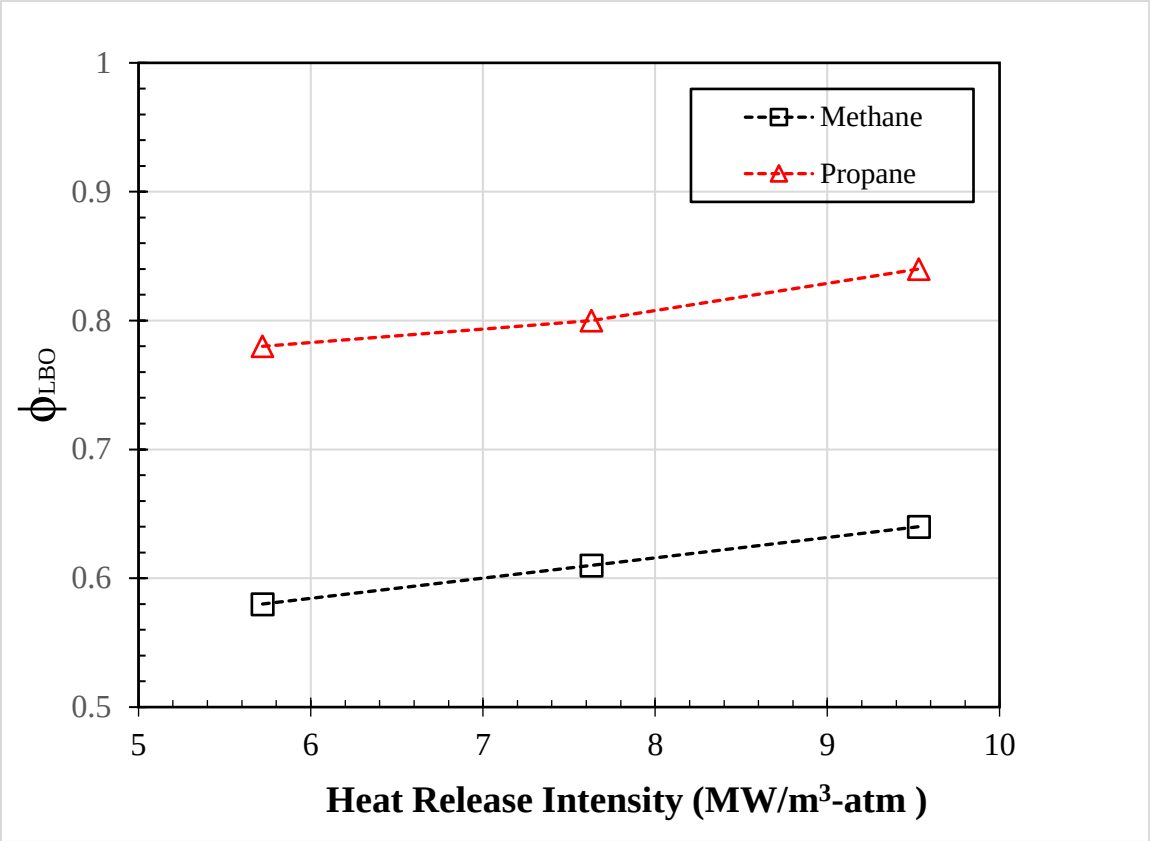

Fig. 7.1. Lean blowoff equivalence ratio at different heat release intensity in distributed combustion using propane and methane fuels.

7.1.2. Chemiluminescence Imaging Near and Away from Blowoff

Imaging of broadband flame chemiluminescence was conducted for both conventional swirl combustion and distributed combustion at various heat release intensities. Figure 7.2 shows the average chemiluminescence images. The top row of Fig. 7.2 shows the normal stable swirl combustion (at $\phi = 0.9$) while the bottom row shows corresponding distributed reaction zones, both using propane as the fuel. These images represent time-average signatures from 500 consecutive images. The results show that the reaction zone becomes wider and elongated with increase in thermal intensity of the swirl flames. The inner recirculation zone (IRZ) was also relatively longer for higher thermal intensity flames. In contrast to conventional combustion, distributed reaction zones spanned almost over the entire volume of the burner having lower chemiluminescence intensity than normal flames. Such reduction of visible signature occurred primarily due to the reduction of adiabatic flame temperature with gradual CO_2 dilution. The gradient of observed chemiluminescence signal (across the regular swirl flame) was remarkably decreased in distributed combustion. With increase in thermal intensity, the distributed reaction zones acquired gradually larger combustor volume and the flames were attached relatively closer to the nozzle exit. A very similar observation was made (in normal air combustion and distributed combustion) when methane was used as the fuel. Chemiluminescence imaging was further performed to capture the near blowoff behavior in distributed reaction zones. Figure 7.3 shows sample instantaneous images near blowoff for the heat release intensity of 9.53 MW/m^3-atm under distributed reaction condition near to just above and very close to blowoff $\phi_1 = \phi_{LBO} + 0.06$ (top row) and $\phi_2 = \phi_{LBO} + 0.02$ (bottom row). The images in each row are not consecutive so that they reveal some characteristic structures at the given conditions. Significant quenching along the right

and left side of the reaction zone at ϕ_1 resulted in change of flame shape from distributed to near V-shape.

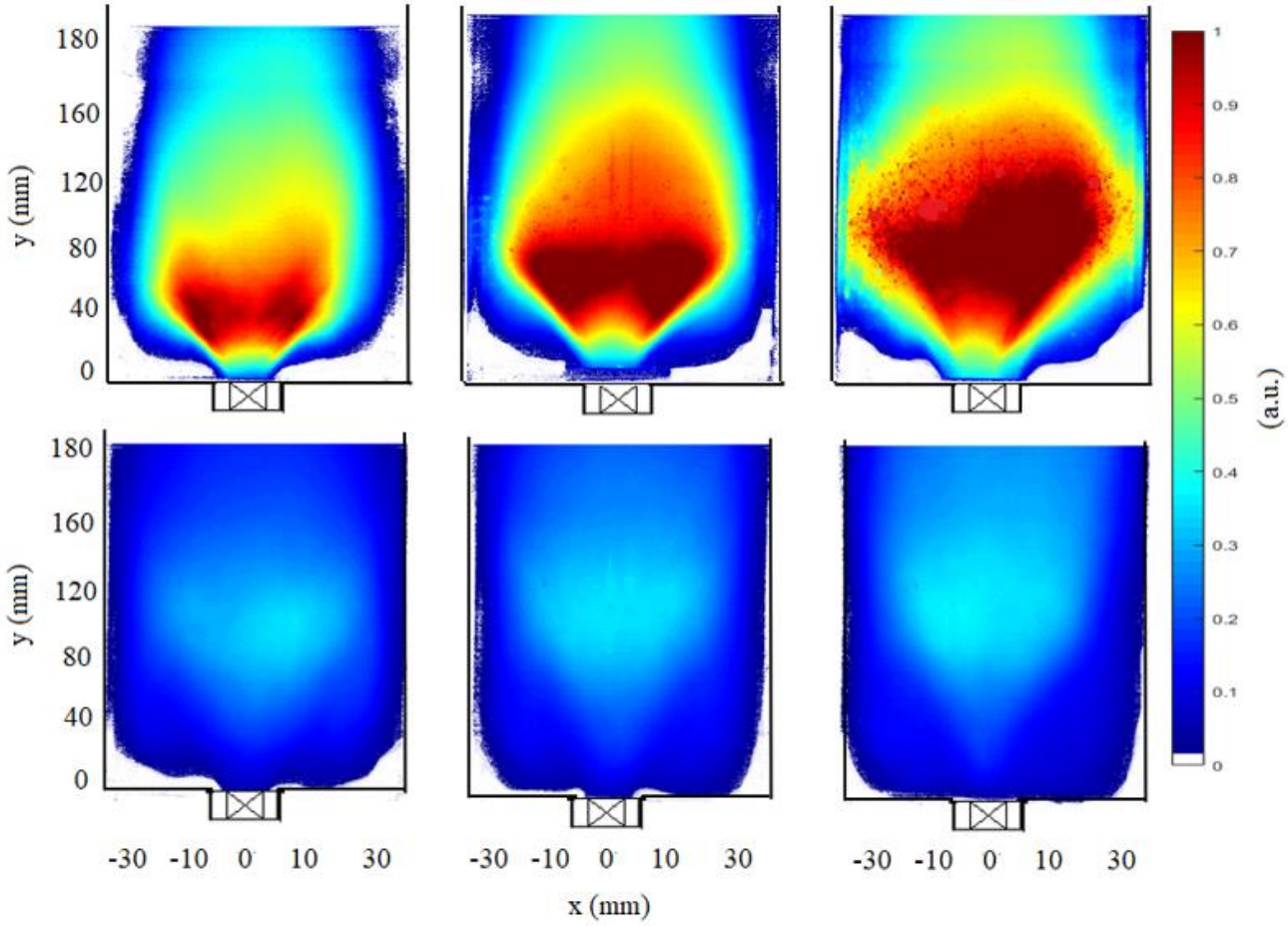

Fig. 7.2. Average of 500 chemiluminescence images of stable swirl combustion (at ϕ = 0.9) (top row) and distributed combustion (bottom row) at heat release intensities of 5.72, 7.63, and 9.53 MW/m^3-atm using propane fuel.

The middle image (of the top row) shows more overall volume of the reaction zone while the rightmost image shows significantly quenched reaction zone leading to much reduced volume. Such alteration of shapes of the reaction zone was periodic and sustained without global extinction.

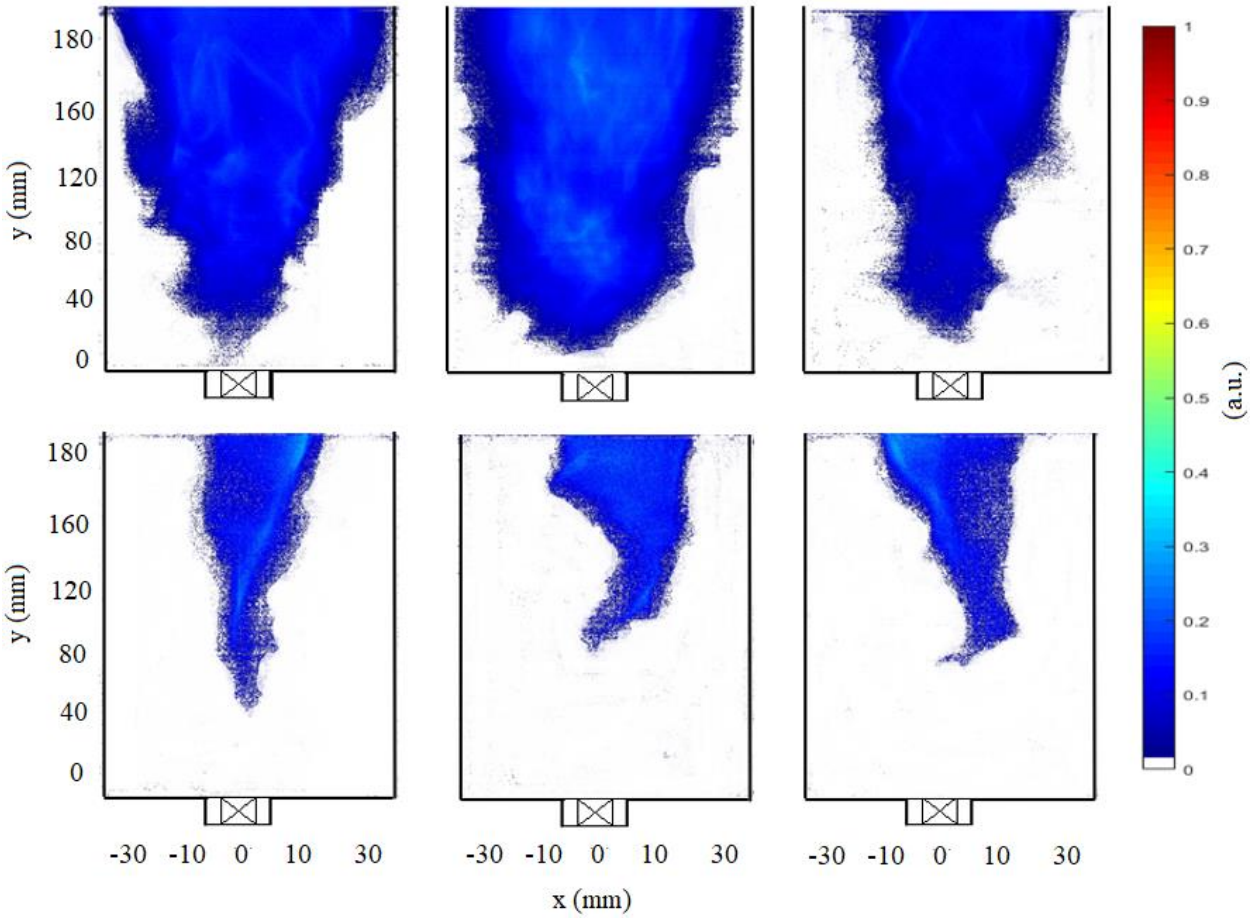

Fig. 7.3. Instantaneous chemiluminescence images near to blowoff. Top row at ϕ_{LBO} + 0.06, and bottom row at ϕ_{LBO} + 0.02 using propane fuel (at heat release intensities of 9.53 MW/m^3-atm).

Due to further quenching, the reaction zone appeared as a thin (thread-like) behavior with significant standoff height at ϕ_2. Different shapes represented at ϕ_2 showed the similar thin revolving reaction zone with some bending observed at the flame base of the reaction zone as seen from the middle image at ϕ_2. Localized wrinkling of flame surfaces (on both sides) was clearly observed which is possibly due to the complex interaction between vortical structures with the reaction zone, heat release fluctuations, and helical instabilities [123]. However, further

appropriate understanding of such an event requires non-intrusive planar laser-based investigations of such complex flowfield. Further reduction of ϕ resulted in global extinction of reaction zone at ϕ_{LBO}. Nearly similar observations were also made of the blowoff moments at lower heat release intensities except that the reaction zones observed at ϕ_1 and ϕ_2 were relatively thin and shorter in length. The near-field (at y = 25 mm) and far-field (at y = 135 mm) chemiluminescence signal intensity were also examined for 9.53 MW/m^3-atm flame to characterize the lean blowoff event. Note that the chemiluminescence reported were line-of-sight integration of the chemiluminescence signals. Hence, the local quenching near blowoff may not be true representations. Planner measurement (using laser-based diagnostics) is recommended for better investigations. Figure 7.4 shows such signal variation across the reaction zone in conventional swirl combustion, distributed combustion (at ϕ = 0.9), and at near blowoff equivalence ratio conditions. Such intensity distribution was obtained from chemiluminescence strips of one-pixel thickness spanned across the reaction zone (from left to right). In near-field, the swirl flame manifests a steep signal gradient on both sides of the flame. Two distinguished peaks observed at the top of the swirl flame's signal profile are attributed to the peak heat release zones. In contrast, the signal intensity in distributed combustion was remarkably lower and relatively uniform across the reaction zone. The small central peak in the distributed reaction zone signified slightly more heat release near that zone. The noticeable reduction of signal intensity can be observed near blowoff equivalence ratio conditions. The small centrally located peak at ϕ_1 indicated sidewise quenching of most of the reaction zone while the completely diminish chemiluminescence signal at ϕ_2 occurred due to extinguished reaction zone at that location. The far-field chemiluminescence manifested a very uniform signal intensity across the distributed reaction zone. Note that the magnitude of signal in normal swirl combustion was lower than that of the distributed combustion (at ϕ = 0.9) in the far-

field. This is because the heat release in swirl flame (at O_2 = 21%) primarily occurred at locations of between y = 30 and 90 mm. Hence, lower chemiluminescence intensity was recorded for the conventional swirl flame in the far-field. At ϕ_1 considerable chemiluminescence was noticed in the far-field, unlike the near-field. This confirms the existence of a lifted volumetric reaction zone with a nearly extinguished base (close to the nozzle exit). A similar observation can be made at ϕ_2 although with very reduced chemiluminescence signal. Similar observations of chemiluminescence distribution were made at other heat release intensities examined here.

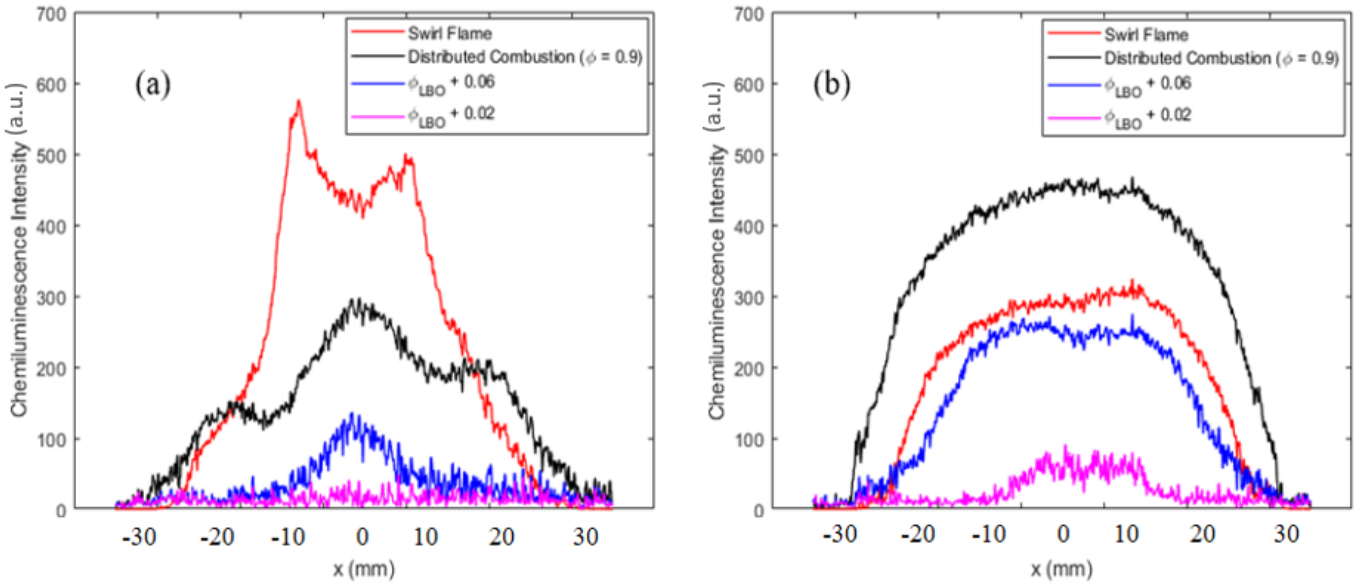

Fig. 7.4. Radial distribution of chemiluminescence intensity at (a) Near-burner exit flowfield (at y = 25 mm) and (b) farther away flowfield (at y = 135 mm) using propane fuel (at heat release intensities of 9.53 MW/m^3-atm).

7.1.3. Effect of Preheating on Blowoff

The effect of air preheats with CO_2 dilution was investigated to understand the possible influence of flame temperature drop on lean blowoff. The experimental conditions for distributed combustion (at ϕ = 0.9) were kept constant while the inlet airstream was preheated to 400, 600, and 800 K, respectively. Reduction of ϕ was carried out until reaching the blowoff conditions at different heat release intensities. Figure 7.5 shows the variation ϕ_{LBO} at different air preheat temperatures for the 5.72 MW/m^3-atm thermal intensity flame using both propane and methane fuel. The ϕ_{LBO} gradually reduced with increase in preheat temperatures of the inlet airstream for both the cases.

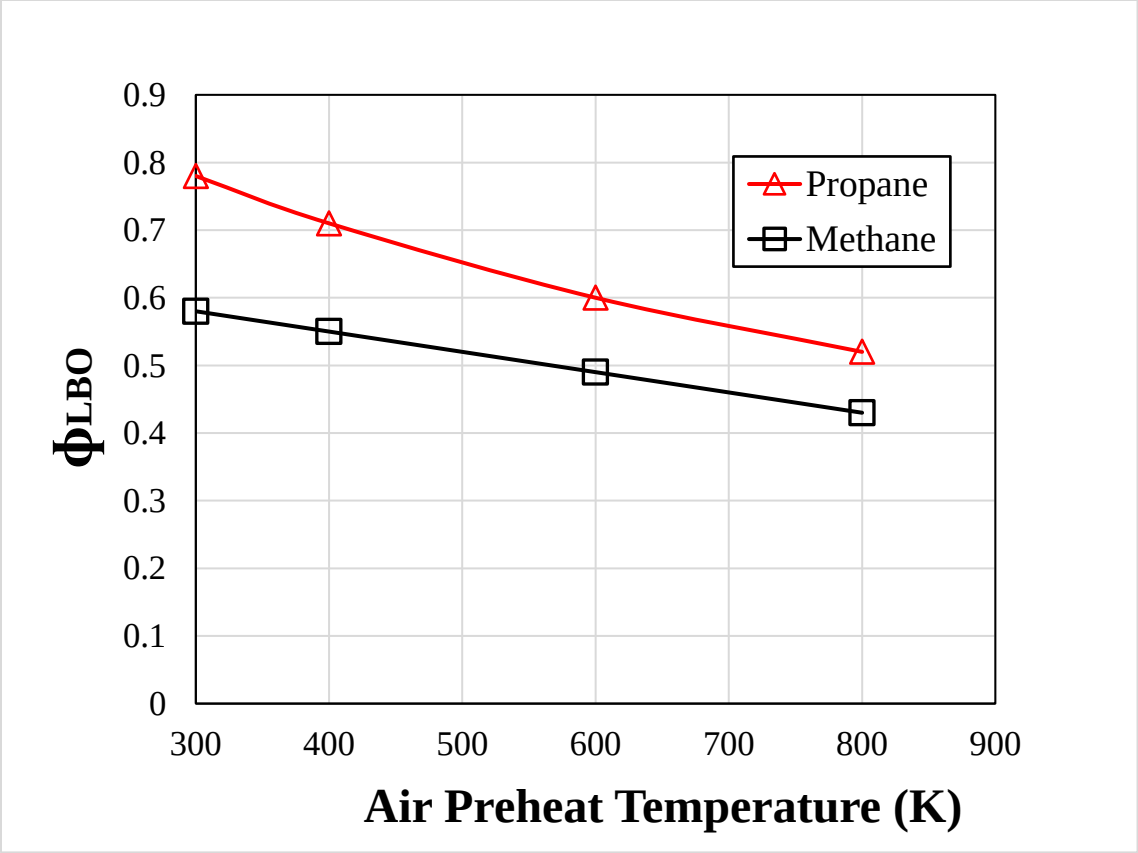

Fig. 7.5. Lean blowoff equivalence ratio of propane and methane flames with CO_2 dilution at different air preheat temperatures.

Such observation is reasonable and as expected since air preheats of inlet air enhanced the laminar flame speed that provided additional stability to the reaction zone. Hence, the flame sustained for a longer period of time with gradual preheating. To corroborate this result, the laminar flame speed (S_L) and the adiabatic flame temperature (T_{ad}) were further calculated using Chemkin-Pro simulation coupled with GRI-Mech 3.0 [94] using the sample case for methane fuel. GRI-Mech 3.0 considers 53 chemical species and 325 chemical reactions during these calculations. Figures 7.6 and 7.7 show the variations of near blowoff (at ϕ_2) laminar flame speed (S_L) and adiabatic flame temperature (T_{ad}) for methane fuel at the 3 different air preheat temperatures considered in this study.

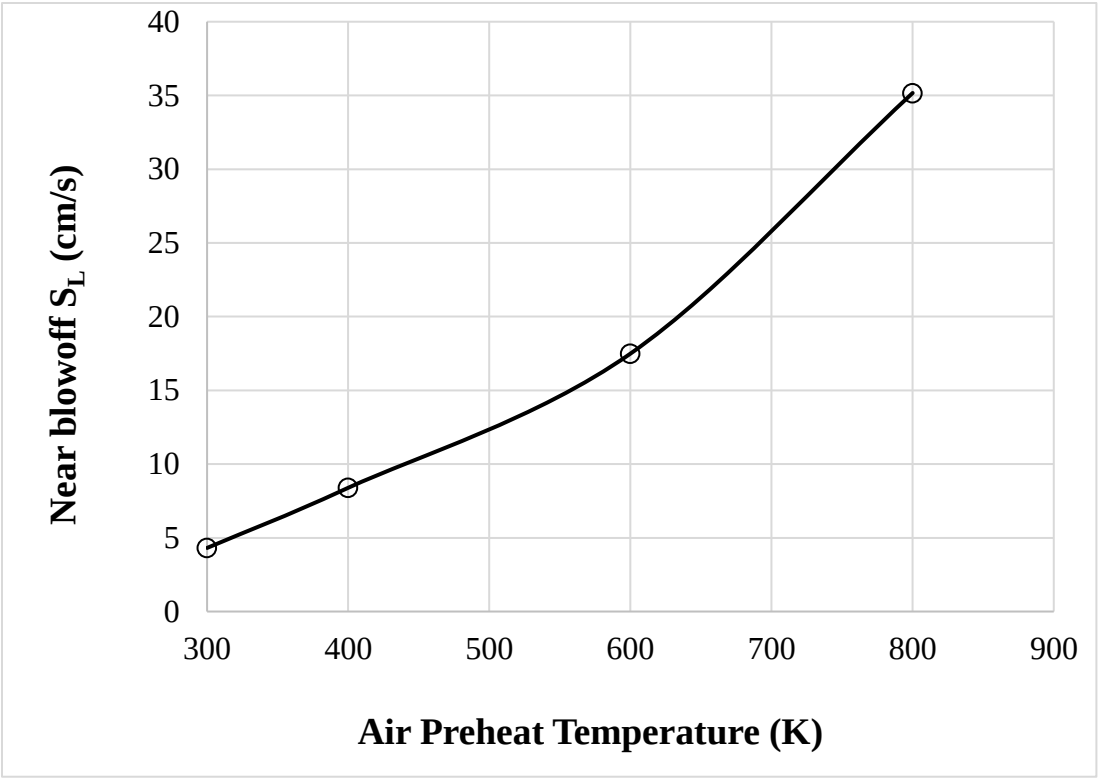

Fig. 7.6. Laminar flame speed (S_L) near blowoff (ϕ_{LBO} + 0.02) for methane fuel at different air preheat temperatures.

The results show that near blowoff S_L gradually increased with the increase in air preheat temperatures. The growth of S_L at higher air preheat temperatures (600-800 K) was faster than initial air preheats (~ 400 K). This observation is convincing as the change in S_L is impacted simultaneously by both the dilution effect of CO_2 and air preheats. The slower initial growth rate of S_L is primarily due to the influence of CO_2 dilution over air preheats. As the air preheat temperature increased, the thermal dissociation of CO_2 took place. Hence, the effect of air preheats on S_L becomes more dominant than that of CO_2 dilution.

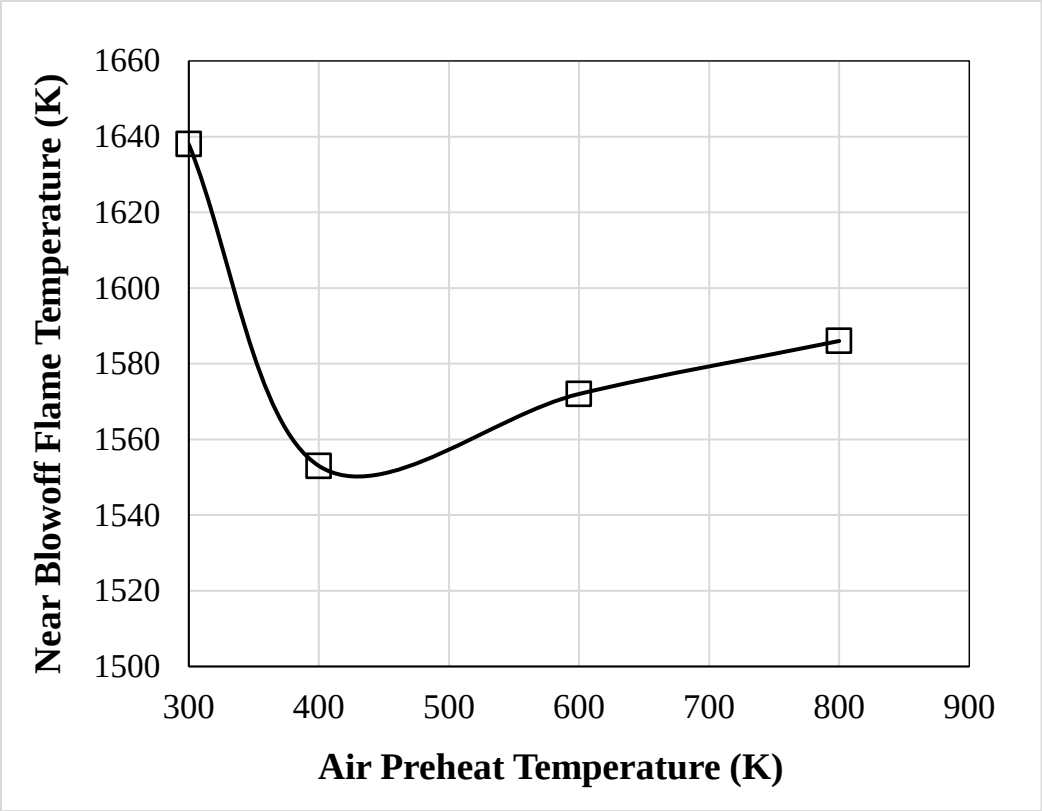

Fig. 7.7. Adiabatic flame temperature (T_{ad}) near blowoff (ϕ_{LBO} + 0.02) of methane flame for 3 different air preheat temperatures.

The competing effects between CO_2 dilution and preheating can also be observed from the variations in T_{ad} shown in Fig. 8. Up to 400 K, the predominance of CO_2 dilution tends to weaken the air preheat effect on flame temperature. The drop in ϕ (by increasing the airflow) to attain LBO provided additional reduction of flame temperature. Hence, such decrease of T_{ad} continued till ~400 K. After 400 K, the flame temperature started rising again due to increased influence of air preheats over CO_2 dilution effects. To verify this hypothesis of thermal decomposition of CO_2 at higher air preheat temperatures, the concentrations of near blowoff CO and CO_2 in the exhaust were measured experimentally (using the lab-based gas analyzer) as well as with Chemkin-Pro© simulation. Figure 9 demonstrates the mole fraction of CO and CO_2 (both measured and calculated) near blowoff (at ϕ_2) at various air preheats temperature reported.

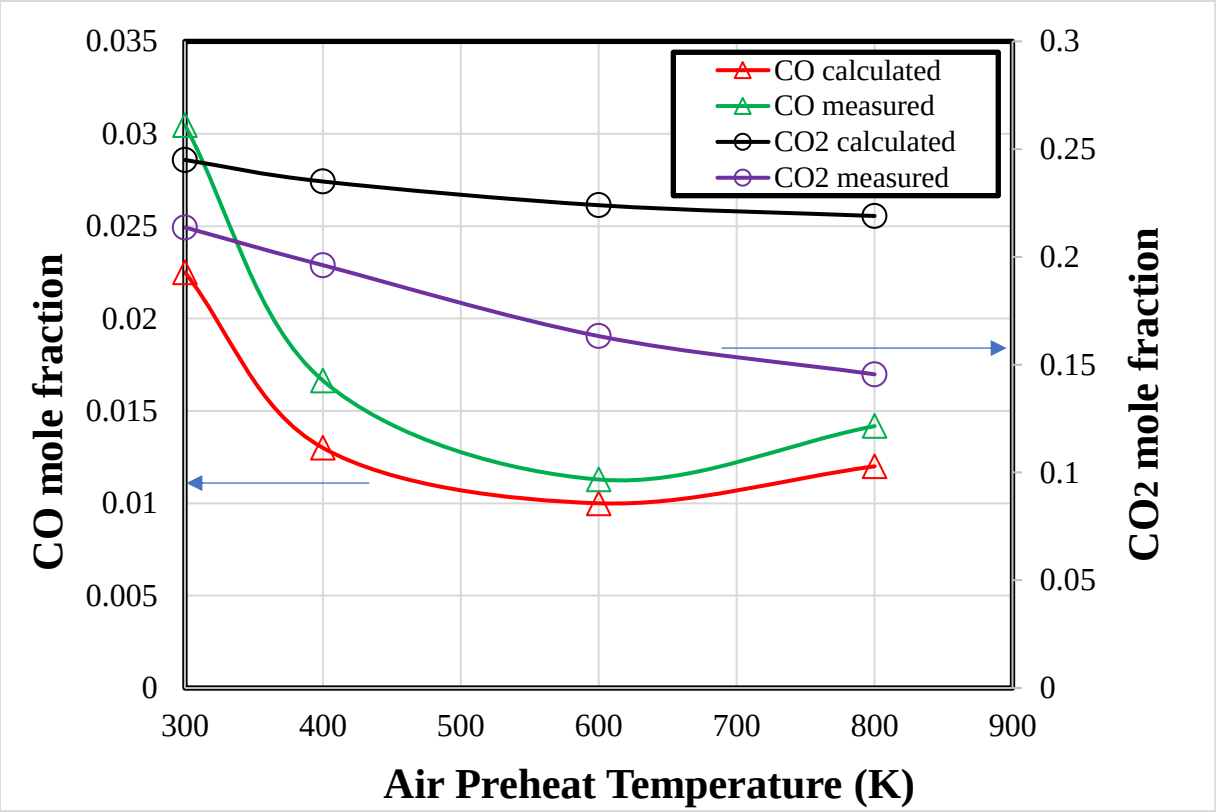

Fig. 7.8. CO and CO_2 concentrations near blowoff (ϕ_{LBO} + 0.02) at different air preheat temperatures.

When the concentration of CO_2 systematically went down with increase in preheats the CO concentration (ppm) increased at temperatures higher than 600 K. This observation was consistent between experimental measurement and Chemkin-Pro© simulation results. Such results support the high temperature decomposition of CO_2 that occurred at high air preheat temperatures in the range 600-800 K. Note that the difference in magnitudes of mole fractions (of CO and CO_2) between experimental and simulation results occurred mainly due to the difference in number of species considered for such calculation. While the Chemkin-Pro© considered 53 species, the gas analyzer reported only 6 key species in the exhaust. However, the trend of variations of near blowoff CO and CO_2 mole fractions with preheat temperatures were similar for both experimental measurement and simulation. Similar trends of near blowoff flame speed and temperature was also observed for propane fuel.

The reduction of LBO equivalence ratio with air-preheats for this particular burner is also related to enhanced stability of reaction zone as observed in our previous study [106]. The instabilities in this current swirl-burner arise primarily due to thermo-acoustic coupling and the existence of precessing vortex cores (PVC). It was observed that preheating of inlet airstream helped in significantly reducing the amplitude of heat release fluctuation (resulting in dampening of thermo-acoustic nature) and the PVC peak in power spectral density (PSD) plots. Reduction of such instability peaks helps in restoring the stabile reaction zones. Hence, the suppression of flowfield instabilities due to air preheat also played an important role in extending the life of distributed combustion by decreasing the LBO equivalence ratios. Additionally, the increase in air preheats gradually decreased the flow Reynolds number that results in reduction of inlet turbulence intensity

[124]. Reduction of turbulence intensity also helped in reduction of inherent instabilities such that the flame sustained longer period.

7.2. Summary

Lean blowoff (LBO) in distributed combustion was studied using propane and methane fuels at three different heat release intensities of 5.72, 7.63, and 9.53 MW/m^3-atm in a swirl-assisted combustor. The equivalence ratio was reduced by increasing the inlet airflow for each case. High-speed chemiluminescence signatures (performed at 500 frames/second) showed large and relatively wider reaction zones both in swirl combustion and distributed combustion at higher thermal intensity. Near blowoff, significant quenching of distributed reaction zone led to nearly a V-shape (at $\phi_{LBO} + 0.06$) and thin thread-like shape with further reduction of ϕ (at $\phi_{LBO} + 0.02$). The LBO ϕ increased gradually with increase in heat release intensity, which was attributed to higher flowfield instability due to enhanced inlet turbulence. The effect of air preheats on LBO of CO_2 diluted reaction zones were also investigated. Air preheats helped to extend the blowoff event to a lower equivalence ratio than no air preheats. Such decrease in LBO ϕ was primarily due to the additional flame stability (and enhanced flame speed) gained with air preheats. Calculation of laminar flame speed (S_L) and adiabatic flame temperature (T_{ad}) was performed using Chemkin-Pro with GRI-Mech 3.0. Above 400 K, high temperature dissociation of CO_2 becomes an important factor leading to the weakened effect of dilution on T_{ad} reduction. This resulted in increased T_{ad} (for air preheats above 400 K) due to the stronger influence of air preheats over the chemical effect.

Chapter 8: Non-reactive Flowfield Investigation in Conventional and Distributed Swirl Combustion Configuration

The knowledge of velocity field and turbulence characteristics provides important information on mixing, combustion characteristics and pollutants formation in distributed combustion. Additionally, such information helps in understanding the fundamental differences that contribute to the evolution of distributed combustion as compared to conventional swirl combustion regimes. The results obtained on the different flow field characteristics using the PIV diagnostics are presented here. Section 8.1 provides the information on velocity field (mean and rms), section 8.2 exhibits the evolution of vortex structures in different flow field, and the section 8.3 discusses the variation of Damköhler number when the non-reactive flow field transitions from conventional swirl case to distributed reaction case.

8.1. Characterization of Velocity Field within the Combustor

Figure 8.1 shows the radial variations of mean axial velocity at 3 different downstream locations (i.e., at z/D of 0.25, 0.5 and 0.75) of the burner exit. Due to axisymmetric nature of non-reactive flow field, the region of interest was examined only on one side along the longitudinal central axis of the burner (i.e., from r = 0- 25 mm on the right side of the flow field) to expedite processing time and reduce storage space requirements. Information was obtained from the time-averaged non-reactive PIV measurements performed for both swirl and distributed reaction cases. A swirling velocity field with peak magnitude near the swirling lobe that revealed forced and free vortex was prominent at different axial locations (z/D = 0.25- 0.75) in the flow. The magnitude of peak velocity increased in the non-reactive distributed reaction flow field case (see Fig. 8.1 b)

indicating a higher overall flow rates causing higher momentum flux of inlet mixture in distributed reaction.

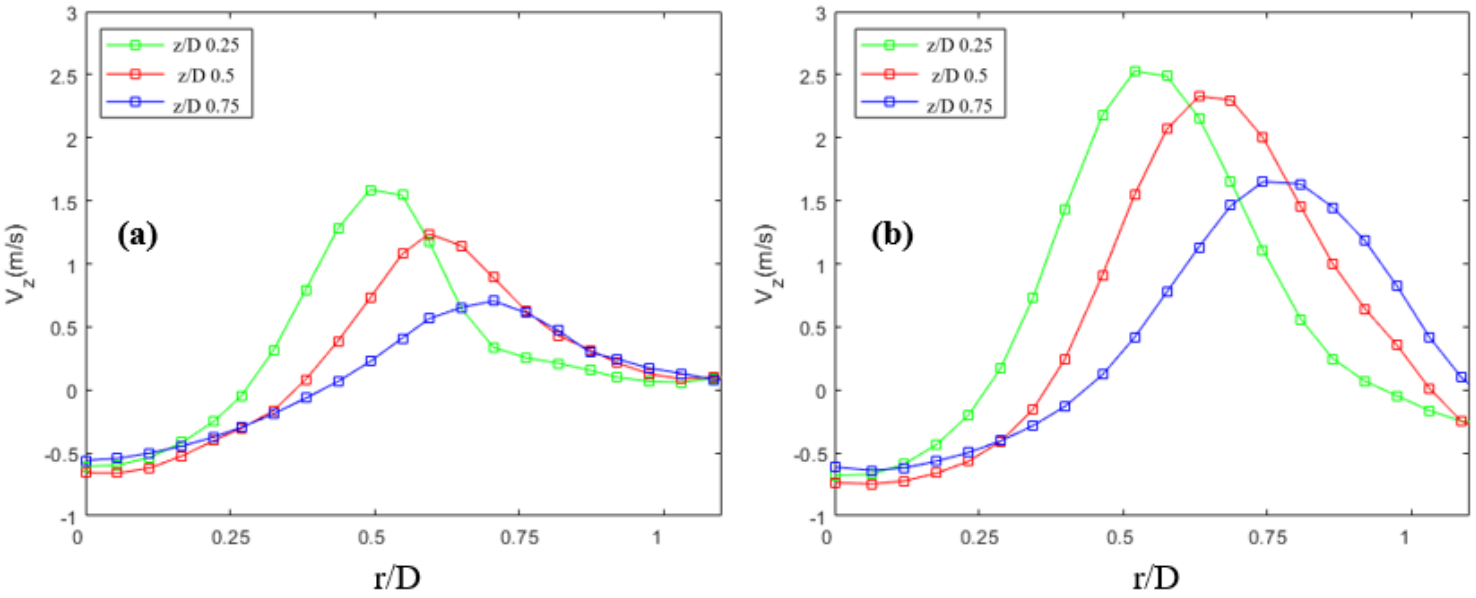

Fig. 8.1. Variation of mean axial velocity profiles in (a) conventional swirl case, and (b) distributed non-reactive flow case near the burner nozzle exit.

The velocity peaks gradually diminished with increase in axial distance and shifted outwards (towards right) in both cases indicating widening of the jet diameter due to higher side-entrainments. The distributed case showed peak at larger radial distances as compared to conventional swirl case for all the axial distances examined. The turbulence characteristics were examined for both the cases at locations near to the nozzle exit. Figure 8.2 shows the variation of mean and fluctuating (rms) velocity in the axial direction for conventional swirl and the distributed reaction flow fields at z/D = 0.25 to better understand the near field turbulence. The rms velocity profile in swirl flow case (Fig. 8.2 a) showed a more pronounced peak, while it was more uniformity distributed across the entire span of the burner in distributed reaction case having higher rms fluctuations than the swirl case. This suggests that distributed reaction condition is established

under conditions of uniform and high-turbulence flow field immediately downstream of the burner exit. Furthermore, near to the wall locations, very high turbulence in the flow field could be observed in distributed reaction cases due to reduced velocity magnitude and higher rms fluctuation as compared to the conventional swirl flow case. The axial velocity field can be better understood by overlaying the velocity vectors on the axial velocity contour (average), see Fig. 8.3.

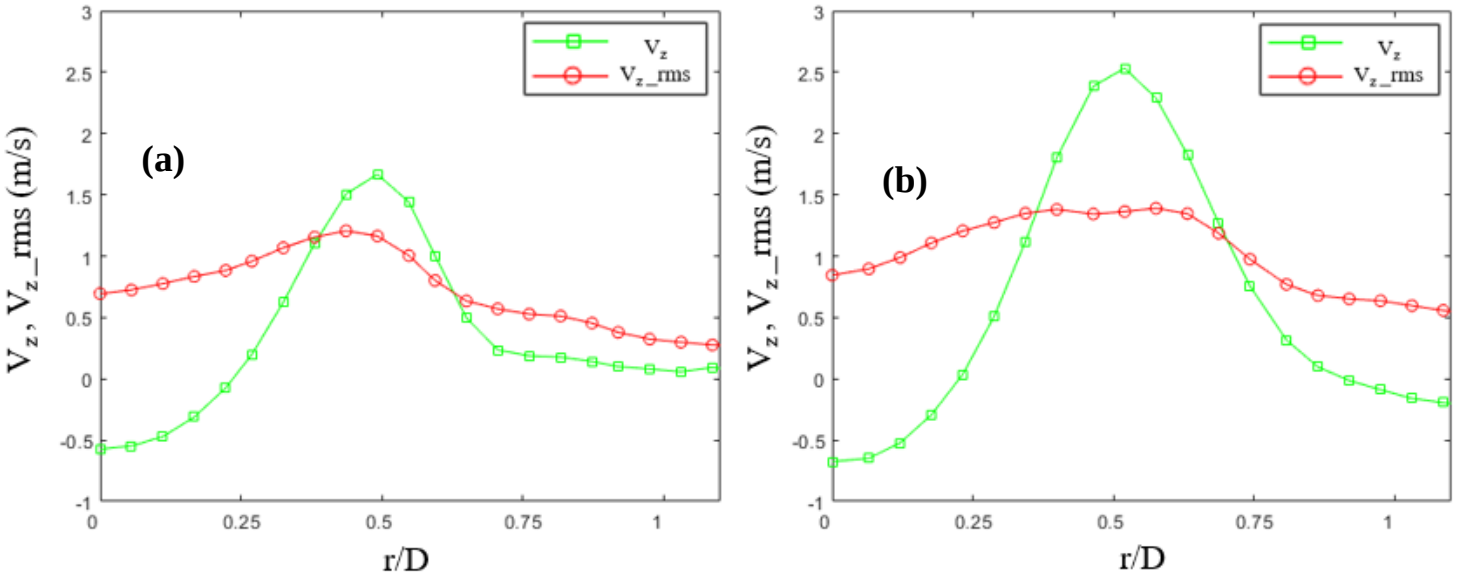

Fig. 8.2. Variation of mean and rms axial velocity profiles for (a) conventional swirl case, and (b) distributed reaction flow field case near the burner nozzle exit at z/D = 0.25.

Recirculation of fluid mass was observed at the center of the flow field for both the cases, while a wider corner recirculation of fluid was observed in distributed reaction case. Distributed reaction case showed a much higher jet influx (or momentum injection) from the exit nozzle than swirl case that lead to the formation of wider shear layers (as seen from the length and width of the red contour in Fig. 8.3). Stronger entrainment of products can be observed in distributed reaction due to the wider central recirculation as well as corner recirculation of fluids. The visualization of the distribution of velocity fluctuations (rms) throughout the flow field in each case provided an

understanding of the turbulence distribution in the two cases. Figure 8.4 illustrates the distribution of rms axial fluctuations in swirl and distributed reaction flow field cases.

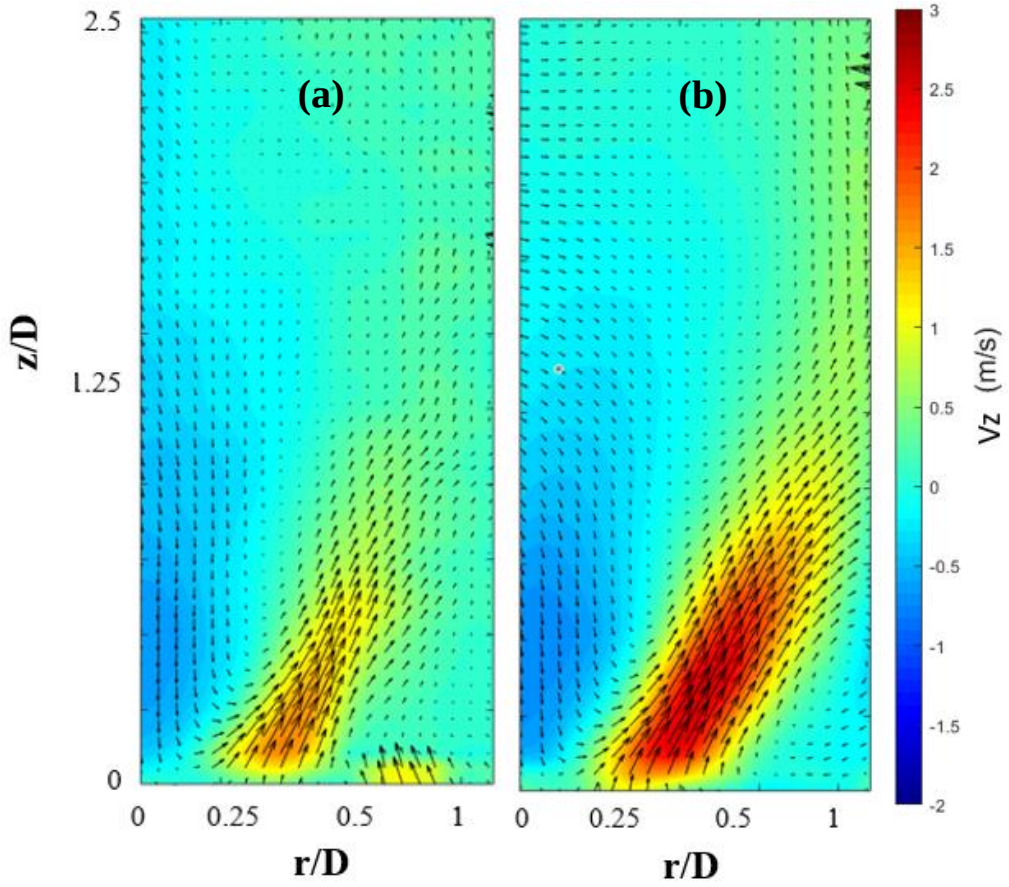

Fig. 8.3. Velocity vectors superimposed on the mean axial velocity contour for (a) conventional swirl, and (b) distributed reaction flow cases.

The results showed much stronger velocity fluctuation in distributed reaction flow case as compared to the swirl case. The peak fluctuation in swirl flow field was found to be confined to a narrow region near the peak momentum flux as shown in Fig. 8.4 a, whereas a much wider and longer region of peak velocity fluctuation was observed in distributed reaction flow field case. This observation also supports the higher observed rms velocity profile seen in Fig. 8.2 at z/D = 0.25. Higher rms velocity may be related to higher exit velocity of inlet mixture in distributed reaction case that was used to keep the heat release intensity constant. The results showed that

distributed reaction promoted higher turbulence in the entire radial plane of the burner near to the burner exit as compared to a conventional swirl case under similar heat release intensity flow conditions.

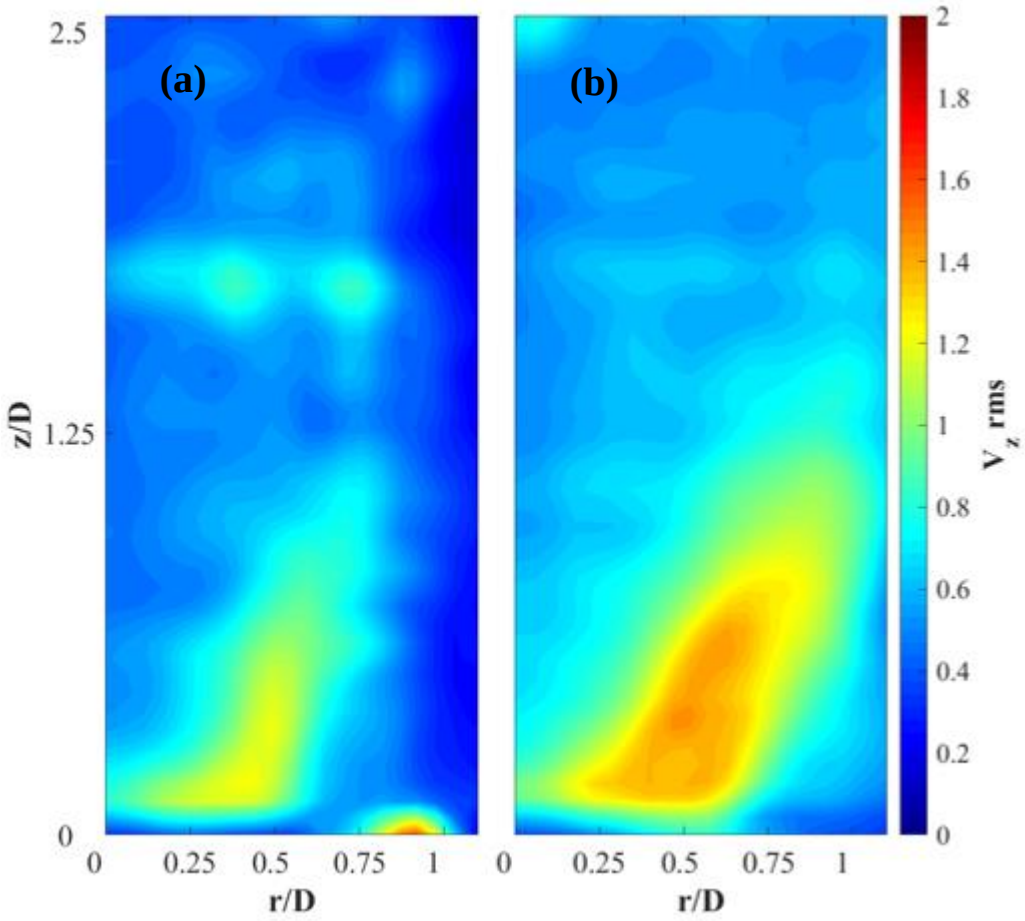

Fig. 8.4. Spatial distribution of rms axial velocity contour for (a) conventional swirl case, and (b) distributed reaction flow case.

Figure 8.5 shows the distribution of mean and rms fluctuation values of radial velocity as a function of axial distance from the burner nozzle exit. Compared to swirl flow case, the distributed reaction zone case showed higher mean velocity. At r/D = 0.25, the lowest radial mean velocity was observed due to the existence of inner recirculation lobe in that region. The velocity peak reaches

maximum near to r/D = ½ from the burner centerline for both the cases around the high jet momentum region.

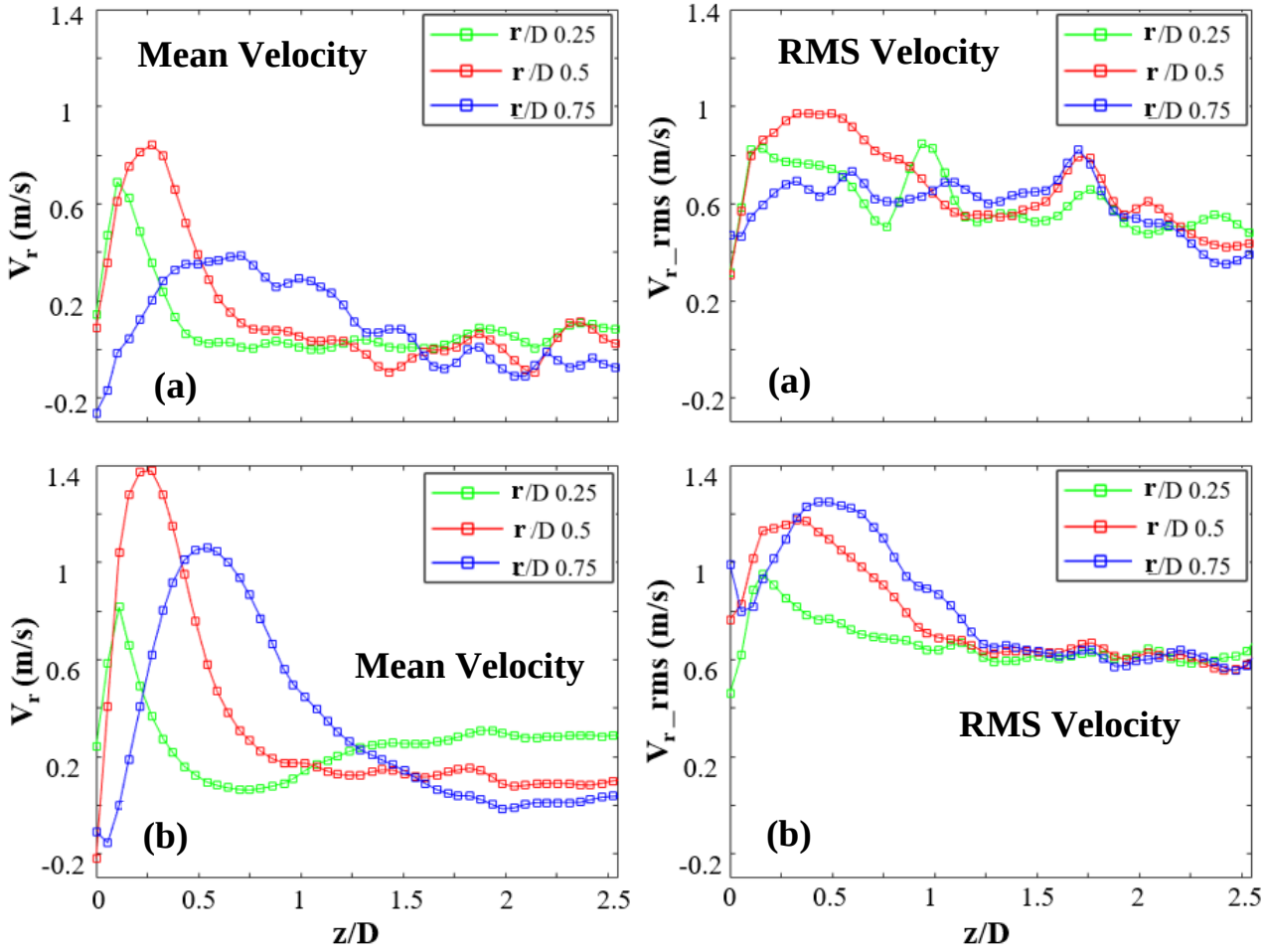

Fig. 8.5. Radial velocity profiles (mean and rms) as function of the axial distance in (a) conventional swirl flow and (b) distributed swirl flow at various distances downstream from the burner nozzle exit.

The results showed that at increased radial distances from the burner longitudinal central axis (i.e., r/D increased to 0.75), the magnitude of radial mean velocity started to decrease due to the existence of corner recirculation zone. The rms fluctuation component of radial velocity exhibited

much higher values in distributed reaction zone case as compared to conventional swirl flow case. These results directly show the establishment of stronger turbulence levels in distributed reaction zone case at all spatial locations in the flow.

8.2 Evolution of Vortex Structures within the reaction zone

The knowledge on the evolution of vortical structures in the flow, in particular near to the vicinity of the reaction zone, is essential to understand the influence of such dynamic structures on flow fields as they provide a direct role in flames under reactive flow conditions. A non-reacting vorticity field assists in determining and visualizing the detailed structures that evolve in conventional swirl flow field and CO_2 assisted diluted flow fields that lead to distributed reaction zones. Vorticity was evaluated by measuring the gradients of velocity field obtained from the non-reactive high frequency (3 kHz) PIV measurements for both swirl and distributed reaction flow field cases. Figure 8.6 shows the time-averaged vorticity fields (obtained from over 3000 instantaneous images) in both swirl and distributed reaction zone flow field cases (i.e., non-reactive cold flow conditions). The solid black lines represent the time-averaged streamlines in both cases. It was observed that the vortex breakdown occurs near the burner exit resulting in a conical-shaped flow field consisting of an inner recirculation zone (IRZ) and a corner recirculation zone (CRZ) due sudden expansion of the burner geometry. The CRZ in conventional swirl flow field is not as prominent as that under CO_2 diluted flow field of distributed reaction zone condition. The streamlines help to indicate the inner and outer shear layers near to the vicinity of IRZ and CRZ. The streamlines reveal that the flow field in swirl case (Fig 8.6 left) is more distorted and chaotic in the central zone with the existence of toroid-like structures as marked by the red rectangles.

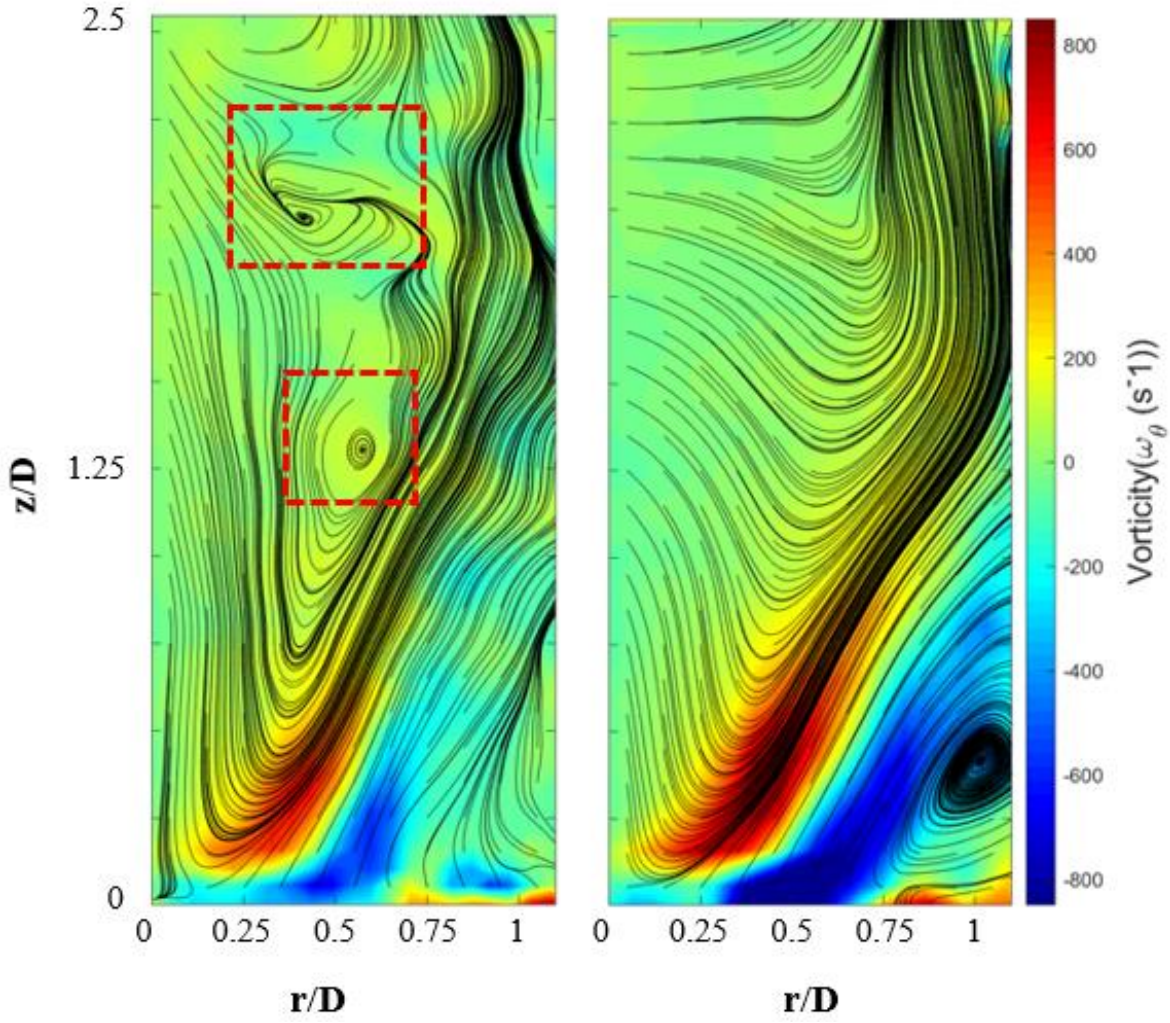

Fig. 8.6. Time-averaged streamline plot (obtained from PIV measurement) and superimposed on the contour plot of azimuthal vorticity for the non-reactive flow field in the simulated conventional swirl case (left) and distributed reaction case (right).

Possible explanation of these structures was given in other studies [125, 126] indicating the existence of hydrodynamic instabilities such as precessing vortex core, PVC [103]. Such structures were not found in distributed reaction zone flow case signifying less disturbance in flow fields caused by such structures. The hypothesis of reduced instability in distributed combustion due to absence of PVC is consistent with our previous investigation [106] which showed much reduced

amplitude of PVC peak in distributed combustion captured from the microphone signal fluctuations in reactive conditions. However, a detailed investigation is needed to check the actual influence of such structures, as this was not the focus of the present research. The red and blue vorticity contours signify counterclockwise and clockwise rotation of local fluid near to the nozzle exit. A wider flow field with prominent IRZ and CRZ was observed (by dense streamlines) in the case of distributed reaction zone flow field as compared to the conventional swirl flow field. Such observations in distributed reaction zone flow field indicate higher flow recirculation and entrainment of hot reactive species into the fresh mixture within the combustor volume.

To further understand the influence of such vortical structures on flow fields, instantaneous snapshots of vortex evolution were analyzed. Figure 8.7 shows the shedding and propagation of vortex from the burner exit obtained from 10 instantaneous consecutive snapshots in traditional swirl flow case with respect to the average streamline overlaid. Such visualizations help to understand the interaction of instantaneous structures with the average flow field (that represents an average flame front in reactive cases).

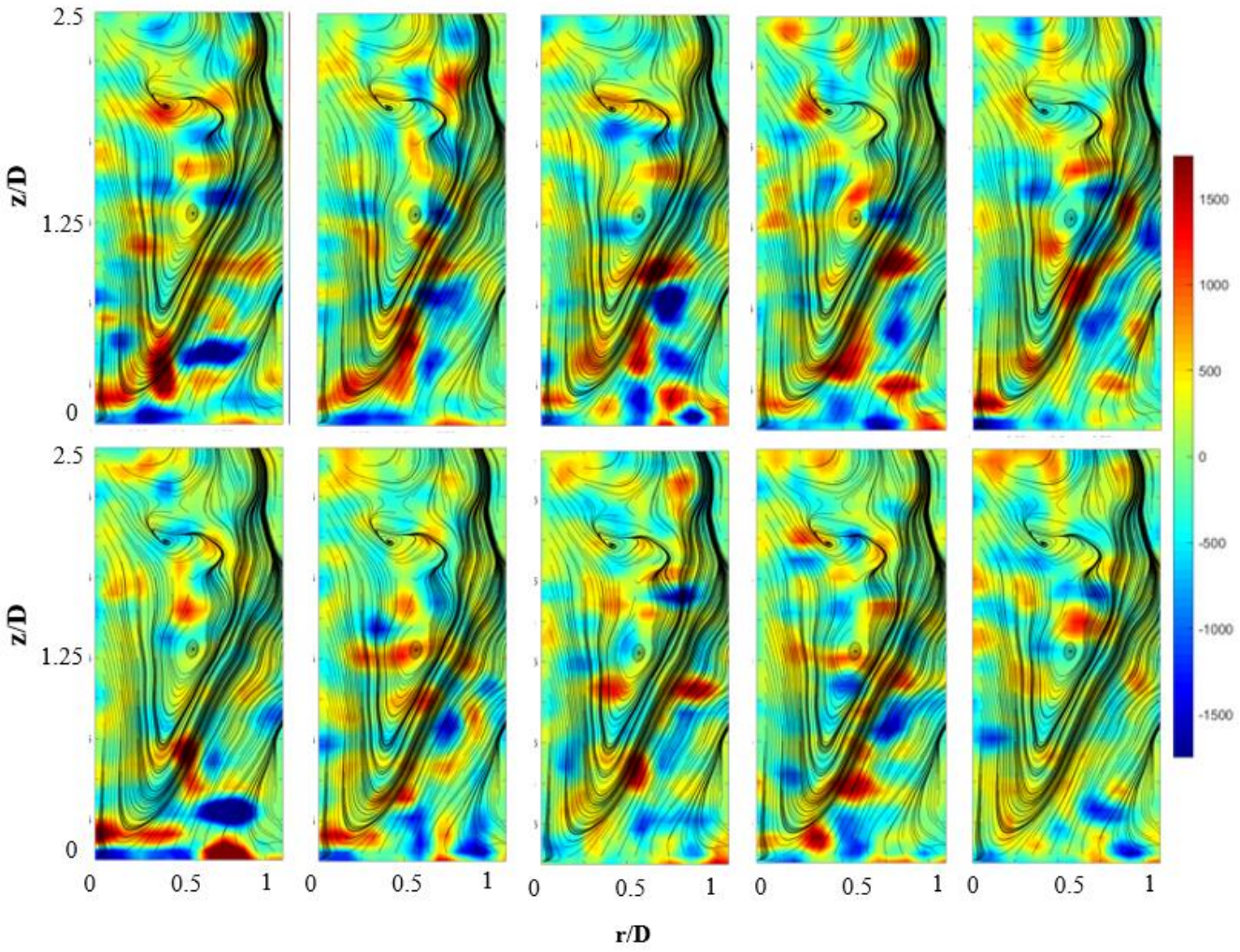

Fig. 8.7. Time-averaged streamline plot (obtained from PIV data) and superimposed on ten consecutive instantaneous azimuthal vorticity contours (shown in color) in conventional swirl flow case.

Vortex propagation was mainly observed along the mean streamlines and near the inner shear layers in these cases. Very small existence of vortical structures was observed at the corner zones and outer shear layers. Comparing frame-by-frame, vortex propagation was prominent up to z/D ~1.75 and the strength of rotation reduced further downstream (z/D ~ 2-2.5). This indicates dissipation of large vortex eddies within two jet diameters from the nozzle exit and a narrow

confined conical flow field in swirl flow case. This is consistent with the observation in reactive cases wherein a relatively short reaction zone occurs in conventional swirl reaction zone near to the burner nozzle exit.

Similar visualization was carried out with CO_2 diluted flow fields with same numbers of snapshots. The results are shown in Fig. 8.8. Higher strength of the propagating vortex can be observed from these instantaneous images. Entrainment of mixture in the outer recirculation was clearly observed in distributed reaction flow field case. In contrast the strength of vortices in swirl flow field case was well-retained up to z/D = 2.5 as compared distributed reaction zone case, see the snapshot images shown in Figs. 8.7 and 8.8. This implies the existence of a relatively wider and longer reaction zone within the combustor in distributed reaction zone having wider entrainment zones. Existence of vortex structures was observed both inside and outside the average streamlines and also along these streamlines in distributed reaction zone. Such observations can be attributed to the higher interplay between turbulent eddies with shear layers and flow fields resulting in enhanced turbulence and mixing within the distributed reaction zone case. Additionally, a higher density of large and small vortex structures was observed in distributed reaction zone as compared to conventional swirl case signifying a distribution of turbulent eddies of different length scales that aid in mixing at reduced O_2 concentrations (due to effect of dilution).

The hypothesis of existence of different length scale of turbulent eddies was verified by from the energy budget of different flow fields studied using the power spectral density (PSD) of the axial velocity. Such PSD of non-reacting flow field is compared in Fig. 8.9. The turbulent energy production in distributed reaction case is higher than the swirl flow field. Here, the focus was to

capture the existence of different length-scale of eddies and the energy transfer happening from large scale to the small-scale eddies before dissipation in both the flow fields considered.

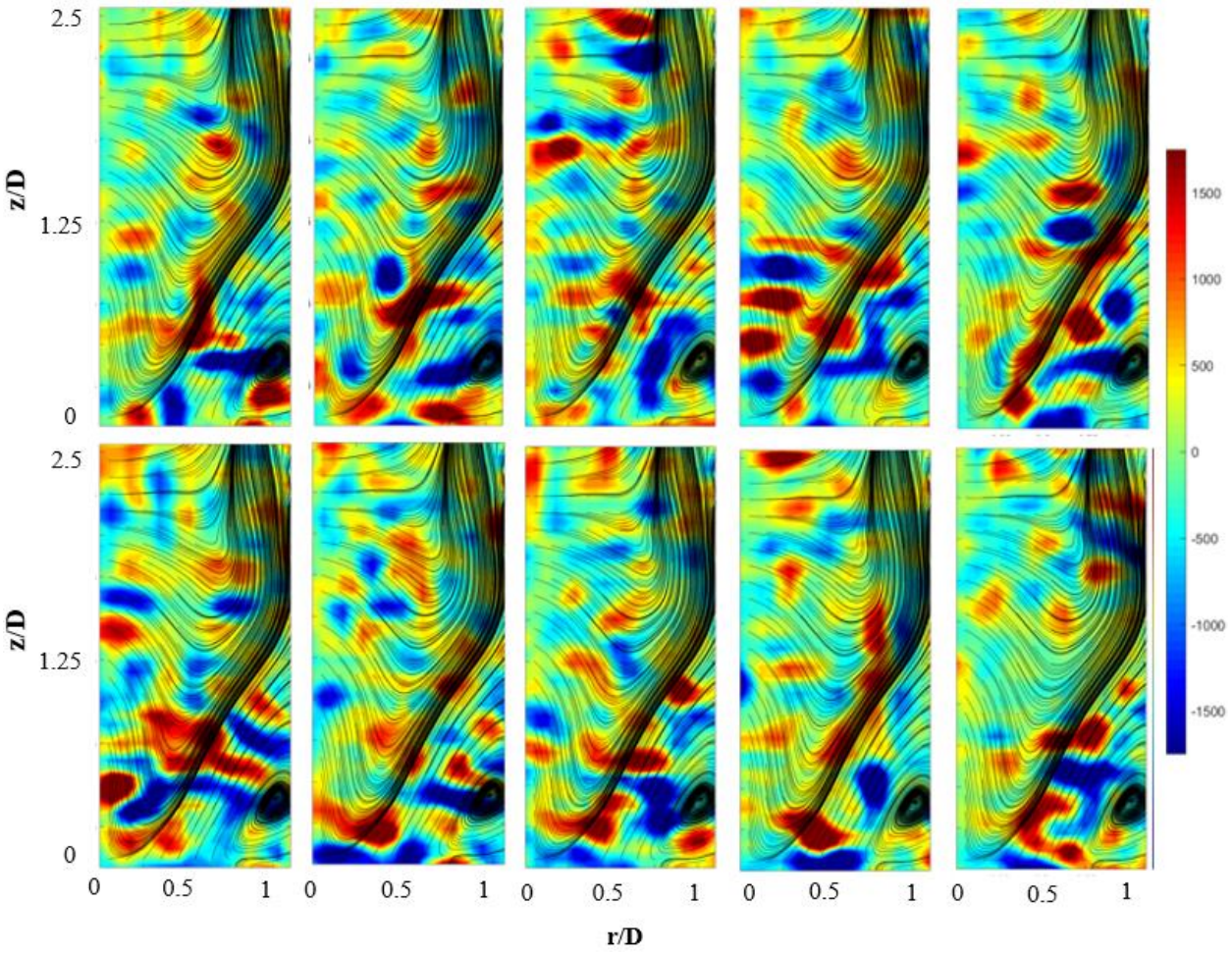

Fig. 8.8. Time-averaged streamline plot (obtained from PIV measurement) and superimposed on ten instantaneous azimuthal vorticity contours (shown in color) of distributed reaction zone conditions.

A -5/3 slope was shown on the PSD plots to indicate the inertial subrange where such transfer of turbulent kinetic energy occurs without loss. The inertial subrange in the distributed reaction case appeared at a higher frequency than the conventional swirl flow case. Additionally, the energy

dissipation regime is more defined in the distributed reaction case (than the conventional swirl flow) indicating the dominance of viscous dissipation in the non-reacting flow field established with gradual CO_2 dilution.

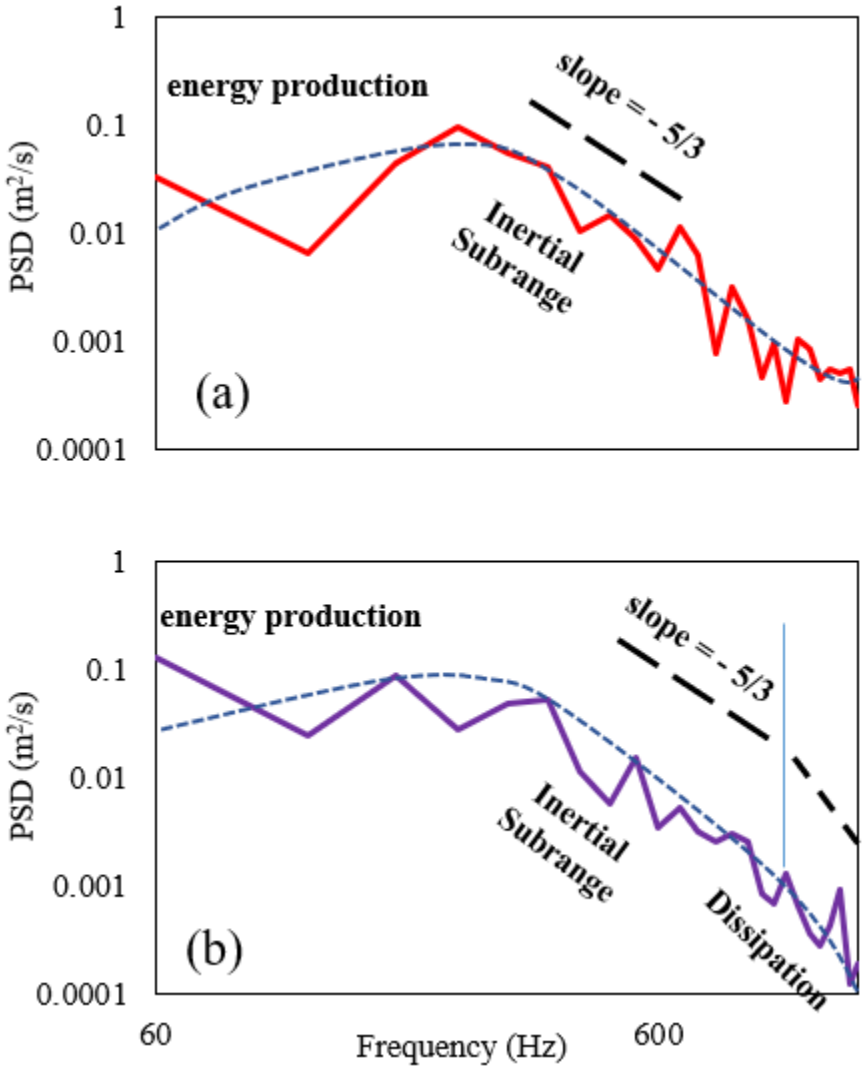

Fig. 8.9. Power spectral density of turbulence obtained from the non-reactive axial velocity field for (a) conventional swirl flow case and (b) distributed reaction case. The -5/3 slope signifies the inertial subrange of energy transfer from large turbulent eddies to smaller dissipating eddies.

Such observations signify the existence of different scales of turbulent eddies in the non-reactive distributed reaction case that supports our explanation of Fig. 8.8 showing different scales of instantaneous vorticity distribution.

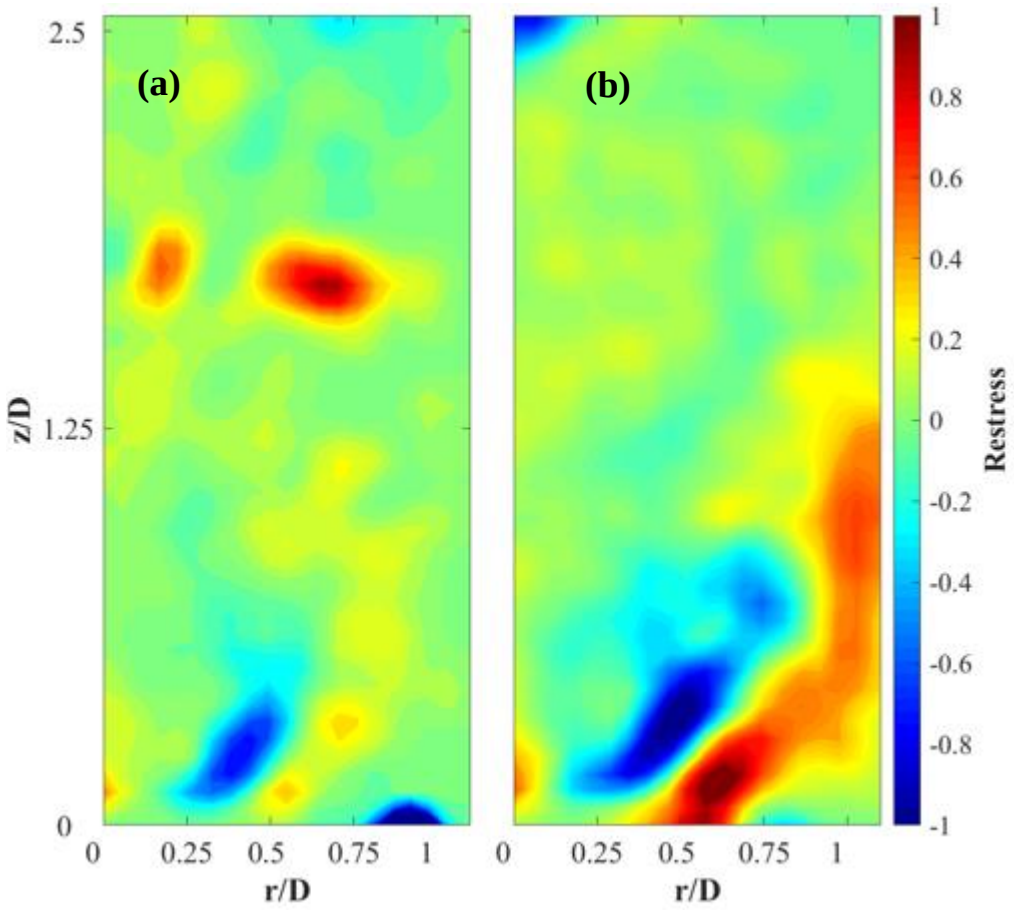

Fig. 8.10. Distribution of averaged Reynolds stress in (a) conventional swirl case and (b) distributed reaction flow case.

The results also indicated that the dissipation of small-scale eddies at lower global O_2 concentration is dominated by the effect of flow field viscosity in distributed reaction regime. A better overall

energy cascading is observed in distributed reaction than conventional swirl flow case. The observation of flattened PSD curve at higher frequencies (> 600 Hz) in conventional swirl flow signifies fixed energy density due to accumulation of turbulent energy at higher frequency bands unlike the distributed reaction case (which showed energy dissipation). Hence, viscous dissipation was prominent at higher frequency of velocity fluctuations in the non-reactive distributed flow whereas energy accumulation was observed in swirl flow cases.

It is useful to compare the distribution of stress tensor in distributed reaction due increased turbulent fluctuations observed in distributed reaction zone. Figure 8.10 shows the Reynolds stress in both swirl and distributed reaction flow field cases. The results obtained showed much higher stress distribution in distributed reaction zone case as compared to swirl flow case. A very high magnitude of stress field was found near the recirculation zones in distributed reaction flow field case. Higher Reynold stress distribution supports our hypothesis of better mixing due to higher turbulent fluctuation in distributed reaction case. Such observations in distributed reaction reported in ref. [69] also support our quantified values reported here.

8.3. Variation of Damköhler Number for Conventional Swirl and Distributed Reaction zone flows

An essential part of investigating distributed reaction zone was to help distinguish the operational regime of distributed reaction regime from conventional swirl flow regime in reactive case. A plot of the different combustion regimes was presented on the Borghi Diagram [127] to represent such differences. The Borghi Diagram is the plot of velocity fluctuation (v') normalized by the laminar flame speed (S_L) versus the integral length scale (L_T) normalized by the flame

thickness (δ_L). In this study, we considered the fuel properties of methane to evaluate S_L and L_T to project different combustion regimes on the Borghi plot. To evaluate the laminar flame speed, Chemkin-Pro© simulation was used coupled with GRI-mech 3.0 reaction mechanism that considers 53 species and 325 chemical reactions for the calculations. The velocity fluctuation data was collected from the velocity field obtained from the PIV measurements. The integral length scale was calculated by measuring the area under the curve of two-point velocity correlation as given in several other studies [128, 129]. By definition, the two-point correlation is generally given by:

$$\rho(r) = \frac{\langle (u'_i(x_o) u'_j(x_o + r) \rangle}{\langle (u'_i(x_o) u'_j(x_o) \rangle} \tag{8.1}$$

and the integral length scale (L_T) is given as [129]: $$L_T = \int_0^\infty \rho(r)\, dr \tag{8.2}$$

In the equation 1, the $\rho(r)$ represents the correlation coefficient, $u'_i(x_o)$ represents the velocity fluctuation at any point x_o in space, $u'_j(x_o + r)$ represents the velocity fluctuation at point $x_o + r$, and $\langle (u'_i(x_o) \rangle$ represents the ensemble average velocity fluctuation over time. Figure 8.11 shows the variation of ρ in the radial spanwise direction within the region of interest of PIV. The correlation coefficient curves showed that the conventional swirl flow was slightly different than the distributed flow reaction zone case indicating different length scales of the production and dissipation of turbulent kinetic energy involved within the two flow fields. Such differences are reasonable due to the highly three-dimensional and turbulent nature of the flow fields (at different densities) resulting from the swirling flow process. At locations near the nozzle exit (z/D = 0.25) the correlation coefficient diminishes to zero at a faster rate than that at far field locations (z/D = 0.5, 0.75) for both swirl and distributed reaction zone cases. The results showed that the magnitude of ρ remained very similar radially up to 0.2 jet dimeters at different axial locations near the exit

nozzle. However, they differed in magnitude after r/D = 0.25 to near wall locations due to possible involvement of different length scales in shear layers and corner recirculation bubbles. The integral length scale (L_T) was evaluated for different reaction zone regimes by taking the integral of correlation coefficients.

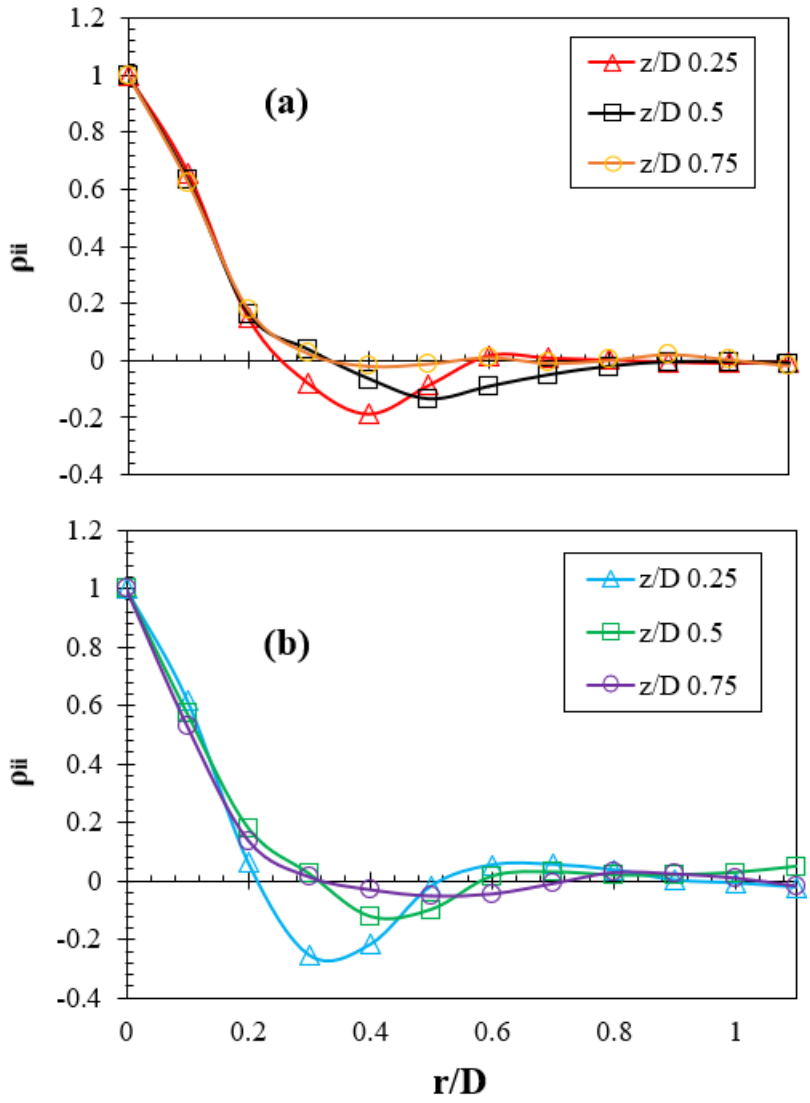

Fig. 8.11. Variation of two-point correlation coefficient in spanwise direction for (a) normal swirl flow case, and (b) distributed reaction flow case.

Figure 8.12 shows the Borghi diagram with projected different reaction zone regimes based on different Damköhler numbers. The Borghi diagram indicated the operational regime of the conventional reactive swirl flow field within the corrugated flamelet with a Karlovitch number (~1/Da) less than 1.

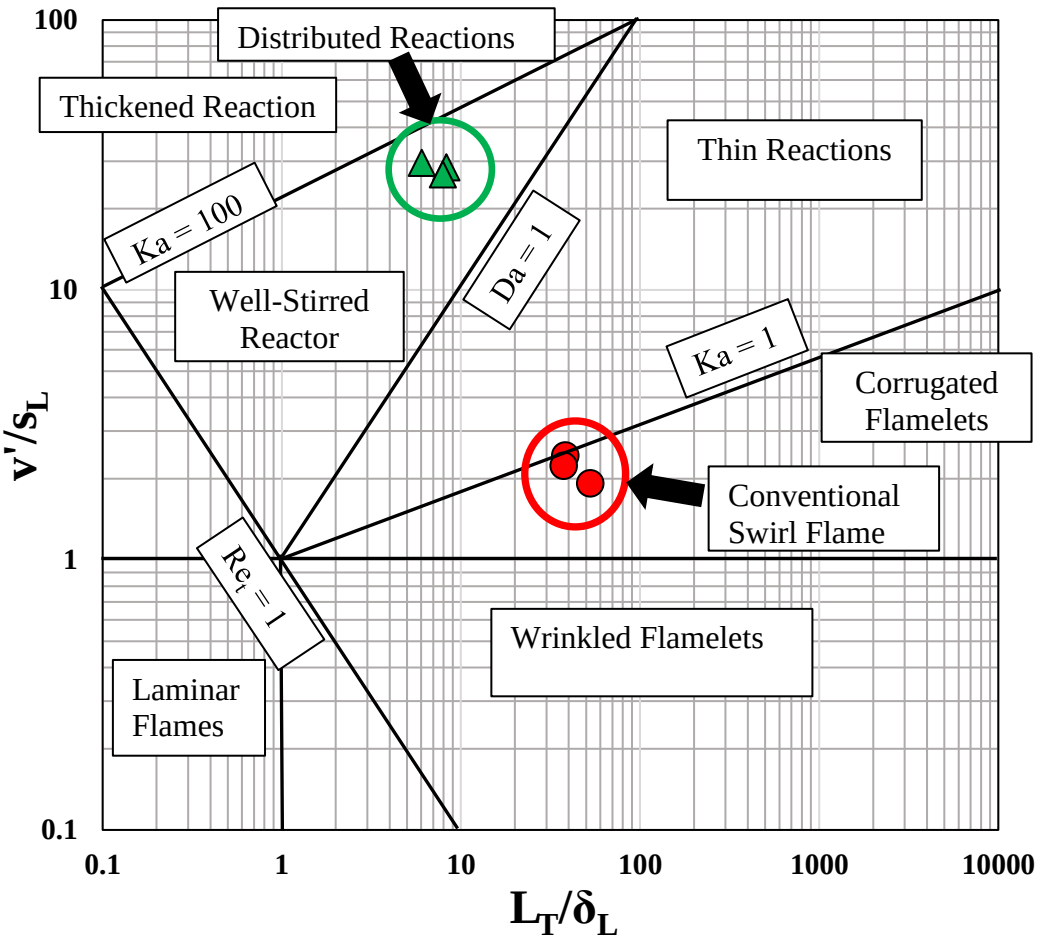

Fig. 8.12. Plot of velocity fluctuation normalized by the laminar flame speed with respect to integral length scale normalized by the flame thickness for conventional swirl and distributed reaction zone cases.

When distributed reaction flow was fostered with gradual mixture preparation (CO_2 dilution to inlet airstream), the evaluated Damköhler number became less than 1 and the reaction zone gradually moved near the thickened reaction zone (indicated by red triangles). The three points shown in both swirl and distributed reaction zone correspond to z/D = 0.25, 0.5, and 0.75.

The above observation clearly depicts a completely different regime of operation in distributed reaction zone (representing thickened reaction zone) than conventional swirl flow field. Note that the velocity fluctuations considered to evaluate different data points shown on the Borghi diagram are the average values at any z/D locations. It is to be noted that the magnitude or rms velocity fluctuations may be somewhat different for reactive PIV case and with different fuels that have different properties. Hence, verification under combustion conditions involving exothermic reactions using PIV measurement are needed to support the findings here. The results showed that distributed reaction field possessed a higher v'/S_L value than that of normal swirl flow cases. Higher magnitude of v'/S_L signify two important things such as, (a) higher rms velocity fluctuation (v'), and (b) reduced flame speed or both to occur simultaneously. The dilution of inlet flow field with CO_2 causes a reduction in flame speed was also reported in our previous chapters. Moreover, a higher v' implies reduced timescale of eddy rotation in distributed reaction zone, which can be confirmed by the value of Da < 1 (implying shorter flow time scale than chemical time scale).

As the Damköhler number is an important indicator to distinguish different reaction regimes, we investigated the spatial variation of local Da at different axial and radial locations in the flow field. Figure 13 exhibits the variation of Da for the swirl and distributed reaction flow field cases. The magnitude of Da was found to be much higher than 1 at all locations investigated in traditional

swirl flows, whereas distributed reaction zone showed Da less than 1. Such observations clearly signify spatially shorter flow time scales compared to the chemical time scales when the reaction zone transitions from normal swirl to distributed reaction zone case. The magnitude of Da increased with increase in axial distance from the burner exits in both cases. This can be attributed to higher eddy rotation time scale at far field of the burner nozzle. Such jumps in the magnitude of Da was seen at one jet diameter downstream of the nozzle exit in swirl flow, while the same was observed at two jet diameters downstream of the exit in distributed reaction zone case that signifies a volumetrically widened flow field compared to narrow reaction zone in conventional swirl flow case.

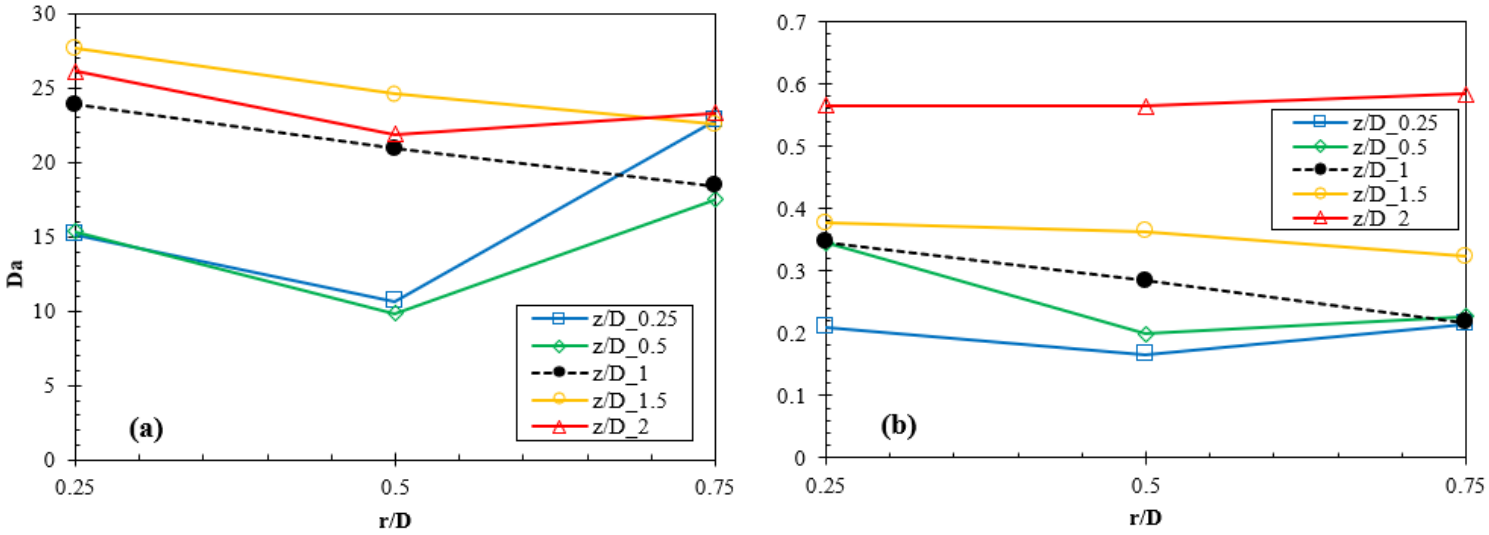

Fig. 8.13. Local variation in Damköhler number at different axial locations for (a) swirl, and (b) distributed reaction flow fields.

8.4. Summary

Flow field characteristics in non-reactive distributed reaction zone was investigated with conventional swirl flow. Non-reactive flow field was investigated in both cases using high

frequency (3 kHz) particle image velocimetry (PIV) measurements. Conditions of distributed reaction zone was established from a conventional swirl flow case using CO_2 dilution of the main airstream to emulate a 5.72 MW/m^3-atm heat release intensity flow field representing the two different regimes in the limit of non-reactive fields. Flowfield were illuminated with an Nd:YLF laser beam generating 527 nm wavelength to capture the Mie scattering images. The results showed higher average velocity peaks near the swirl lobes at different axial locations near the burner exit. Axial velocity fluctuation (rms) was of relatively higher magnitude (and also provided more uniform profile across the radial span of the combustor volume) in distributed reaction zone case than swirl flow field case. The radial velocity variation as a function of axial locations showed higher average values in distributed reaction zone case as compared to swirl flow case. The vorticity data showed the existence of a conical flow field near the burner exit due to vortex breakdown forming inner and corner recirculation zones. The corner recirculation was more prominent in distributed reaction flow case. Instantaneous vorticity evolution illustrated that in swirl conventional flow field vortex propagation was mainly observed along the average streamlines and within the inner recirculation zone, whereas in distributed reaction zone, the flow field vortex rotation was observed in corner recirculation zone and inner recirculation zones and along the mean streamlines. A higher magnitude of Reynolds stress distribution was found in distributed reaction zone as compared to traditional swirl flow case. Calculation of local Damköhler number (Da) showed values much higher than unity in swirl flow case. In contrast, the magnitude of Da was less than unity in all locations (axial and radial) within the entire flow field.

Chapter 9: Data-driven Prediction of in Distributed Combustion

This chapter discusses the use of artificial neural network (ANN) for data-driven prediction in distributed combustion. ANN was developed using data obtained from experiments. Optimization of model was considered for efficient prediction of target parameters. The next few sections explain the detailed ANN approach used for predictions in distributed combustion.

9.1. Basics of Artificial Neural Network

Artificial neural network (ANN) technology was used in our current research to develop data-driven predictive model for the current swirl-assisted distributed combustion state with experimental data. An ANN is made up of a collection of linked neurons that function as information processing units [26]. According to certain studies, ANN was modeled after the structure of the human brain [130]. However, the major goal of using such a neural network is to create any potential mathematical correlations between the input and output variables in cases where no direct mathematical correlations exist. The main benefit of such modeling is the reduction in computation time required to forecast complex correlations between variables. Figures 9.1 a and 9.1 b depict the schematics of a basic artificial neural network (ANN) with one input layer, one hidden layer, and one output layer, respectively. Vectors [x_1, x_2, ..., and x_j] along with the appropriate weight vectors [w_1, w_2, ..., and w_j] represent the different inputs of the artificial neural network. The bias and activation functions in this case are b and f, and y is the output variable. The goal of bias is to shift the activation function by adding a constant to the model input, whereas the activation function just determines whether the weighted sum of inputs in each neuron should be activated or not. The output of the ANN (at each neuron) can be described mathematically as:

$$y = f(\sum_{i=1}^{i=n} w_i x_i + \mathbf{b}) \quad (9.1)$$

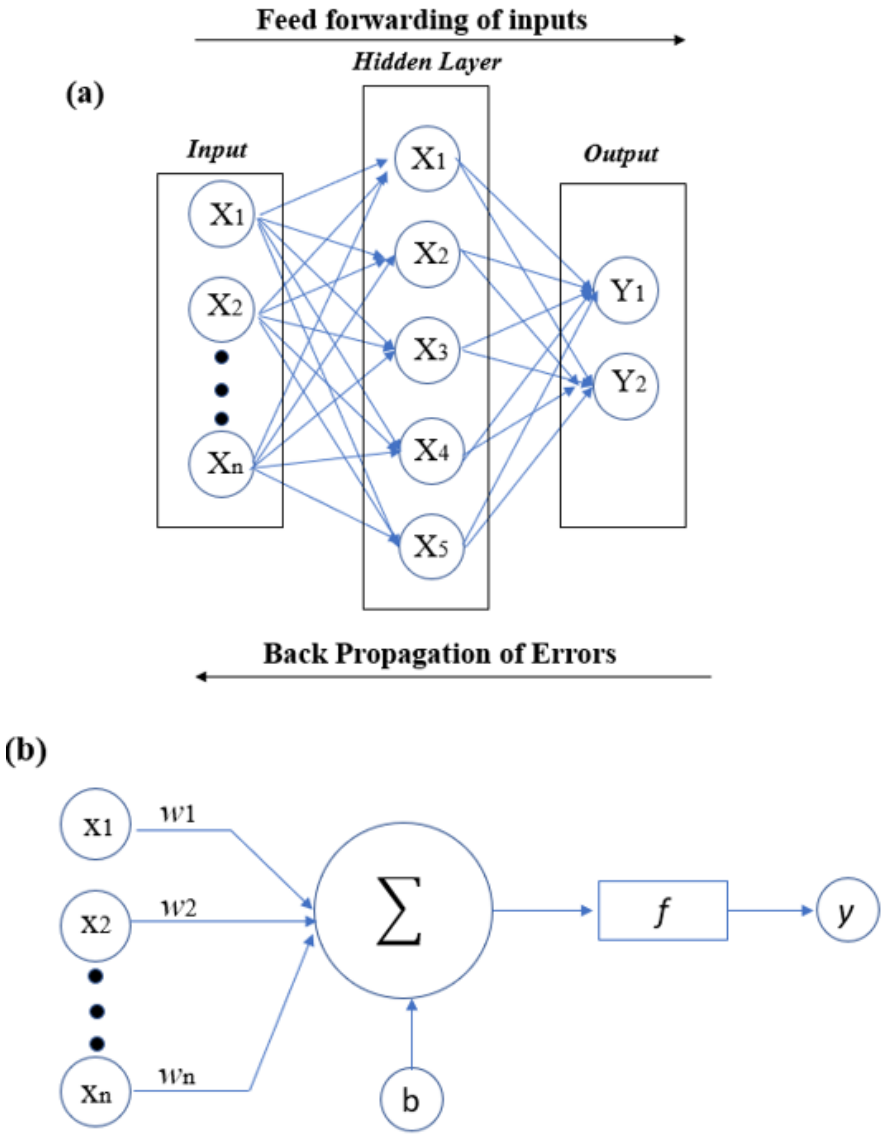

Fig. 9.1. (a) Schematics of ANN and (b) representation of an individual neuron.

The performance of any ANN is determined based on the mean square error (MSE) obtained in each iteration (of training, validation, and testing data). Here, the MSE is defined as:

$$\text{MSE} = \frac{1}{N}\sum_{i=1}^{N}(y_i - t_i)^2 \quad (9.2)$$

Here , the predicted output is y_i and the actual output is t_i are shown above, with N denoting the total number of data points. The choice of weights and biases in equation (9.1) is adjusted continuously until the MSE is very well minimized. Such adjustments are performed in each step during model training when the learning algorithm iterates thorough the entire training data. The number of times of such iteration though the whole dataset is also called 'Epochs'. Sometimes this MSE is also referred to as a quadratic cost function (CF). The value of R (coefficient of correlation with values between -1 and +1) was noted in each iteration to verify the prediction of the final model.

9.2. Results and Discussion of Data-driven Predictions

The results obtained during this study are explained below.

9.2.1. Experimental Data Collection:

The main experimental data predicted in this study were NO and CO concentrations (in ppm) at various O_2 levels (between 17 and 20%) and different inlet air flowrates. Variation of O_2 levels indicates different dilution levels while airflow variation signifies change of inlet equivalence ratio. Measurements were obtained with gradually increasing inlet air flows at every O_2

concentration until the flame extinguished. The air flowrate was adjusted to shift the methane-air mixture's inlet equivalence ratio from 0.88 (stable burning) to 0.58 (near blowoff), with a gradual decrease of 0.03. Adiabatic flame temperature (AFT) was also calculated at similar O_2 concentrations and air flowrates using Chemkin-Pro© coupled with GRI-Mech 3.0 reaction mechanism. In this work, the air flowrates and different O_2 concentrations are considered as the input variables while the AFT and the concentrations of NO and CO are the output variables to be predicted using ANN modeling. Table 9.1 demonstrates the ranges of input and output variables (actual) considered in this study. As observed from the table, the AFT reduced systematically with increasing airflow. A similar observation was made for the NO and CO concentration variations as well. This is logical as the reaction zone became increasingly diluted with cold air as the inlet air flow was gradually increased resulting in drop in flame temperature at different O_2 levels. Such drop in AFT also explains the observed reduction of NO concentration (ppm) gradually. Similarly, the CO concentration was also reduced. For the O_2 levels ranging between 17-20%, the inlet airstream was diluted with CO_2. Hence, the drop in AFT in this O_2 concentration range was due to the combined effect of dilution [106] and increasing air flowrate to reach the blowoff limits. Note that the lower bounds of NO, CO concentrations and the AFT are zero and 300 K for O_2 = 17, 18, and 19%. This is to signify that the flame blowoff had already occurred when the upper limit of air flow (78.54 LPM) was supplied to the burner for these specific O_2 levels. The AFT and the ppm of NO and CO were significantly reduced when distributed combustion (at O_2 = 17%) was fostered from the conventional swirl flame (at O_2 = 21%).

9.2.2. ANN Model Development

The basic structure of the current ANN consists of two inputs and three output variables with one hidden layer. The model was tested with hidden layer containing 10, 15, and 20 neurons with the

given data. Model development was continued with the best possible scheme having the lowest MSE and a strong R value. The model development was performed in Matlab® software. Feed forward and cascade forward networks with Levenberg–Marquardt backpropagation training algorithms were utilized (using 'trainlm' function) with different training functions combinations.

Table 9.1. Input and output variables considered for ANN modeling.

Input variables		Output variables		
% O_2	Air Flowrate (LPM)	NO (ppm)	CO (ppm)	AFT (K)
21	51.77±1 -78.54±2	13.79±3 - 1.86±2	49.78±2 - 1.42±1	2199.85±5-1569.19±10
20	51.77±1 - 78.54±2	6.33±1 – 0.51±1	41.07±2 - 1.93±0.5	2086.08±5-1023.89±5
19	51.77±2 -78.54±3	3.81±1 - 0	25.78±2 - 0	1880.08±10 - 300
18	51.77±3 -78.54±5	1.92±1 - 0	17.78±1 - 0	1788.48±10 - 300
17	51.77±3 -78.54±5	0.75±1 - 0	36.47±3 - 0	1663.88±6 - 300

Note, the cascade forward networks are similar to a feed forward network with a connection established between the input and every previous layer to the following layers. The Levenberg–Marquardt algorithm [131] was used to achieve a fast speed of model training. The entire experimental dataset was divided into three sets: training data, validation data, and testing data containing 70%, 15%, and 15% of the total dataset (with total 55 data points for each output variable). While training, normalization of data was performed for each variable (of Table 9.1) with respect to the corresponding maximums to ensure a similar range of variation in magnitude. The division of data points into the mentioned three groups was done randomly by default in Matlab using 'dividerand' command. Such randomization of data helped in minimizing the

possibility of selecting a biased training dataset that was not representative of the different input conditions considered. Table 2 shows the different training schemes and network structures used in this paper. The transfer functions tested for training were tangent-sigmoid (Tansig), and log-sigmoid (Logsig). The mathematical representation of these transfer functions is:

$$\text{Tansig (n)} = \frac{2}{1+e^{-2n}} - 1 \tag{9.3}$$

and,

$$\text{Logsig (n)} = \frac{1}{1+e^{-n}} \tag{9.4}$$

Overfitting of data was avoided by utilizing the 'early stopping criteria' as mentioned before [132]. No specific learning rate was applied in this case. Each scheme was trained several times until the lowest MSE of performance was achieved. The feed forward network with 15 neurons and Logsig was observed to be the best scheme with the lowest MSE (of 0.003723) and R = 0.95272. Hence, this scheme was selected at this stage of data prediction.

9.2.3. Effect of Different Learning Rates on Modeling:

One important aspect of machine learning model development is to optimize the model by tuning different hyperparameters for obtaining time-efficient predictions. The learning rate (LR) is a key hyperparameter that assists in updating the weight distribution for the neural network such that the cost function is minimized [133] as:

$$w_{i+1} = w_i - \alpha . \frac{\partial CF}{\partial w}\Big|_{w=w_i} \tag{9.5}$$

Here, w_i represents the weight at i^{th} iteration and α the corresponding the learning rate. The expression CF is similar to that of the MSE (given in equation 2). A very low LR results in very slow progress of model training while too high magnitude of LR may cause strong divergence of model's cost function. The importance of choice of LR can be explained using Fig. 9.2 which schematically shows how choice of LR may affect the optimization of CF with respect to weights.

Table 9.2. Training schemes used for the current ANN modeling.

Transfer Function	Network	Number of Neurons	Testing MSE	R Value	Epoch
Tansig	Feed Forward	10	0.3868	0.87868	16
Logsig		10	0.04054	0.8791	12
Tansig		15	0.03847	0.89995	15
Logsig		15	0.003723	0.95272	19
Tansig		20	0.009185	0.91602	12
Logsig		20	1.5	0.82062	13
Tansig	Cascade Forward	10	0.0757	0.88609	12
Logsig		10	0.031	0.86645	53
Tansig		15	1.17	0.86031	9
Logsig		15	0.2102	0.8833	23
Tansig		20	0.04186	0.91241	13
Logsig		20	0.022	0.8735	9

Naturally, the quadratic CF curve has a parabolic shape, and the size of the arrows corresponds to the magnitude of LR. As a result, the shorter arrows on the left side of Fig. 9.2 denote low values, while the longer arrows on the figure's right side denote greater values. The movement of the red dot in this diagram represents the evolution of CF optimization over several iterations. It has been noted that an extremely low LR requires numerous iterations to reach the CF global minimum. However, a very high LR may completely miss the point of minimum and produce undesirable results.

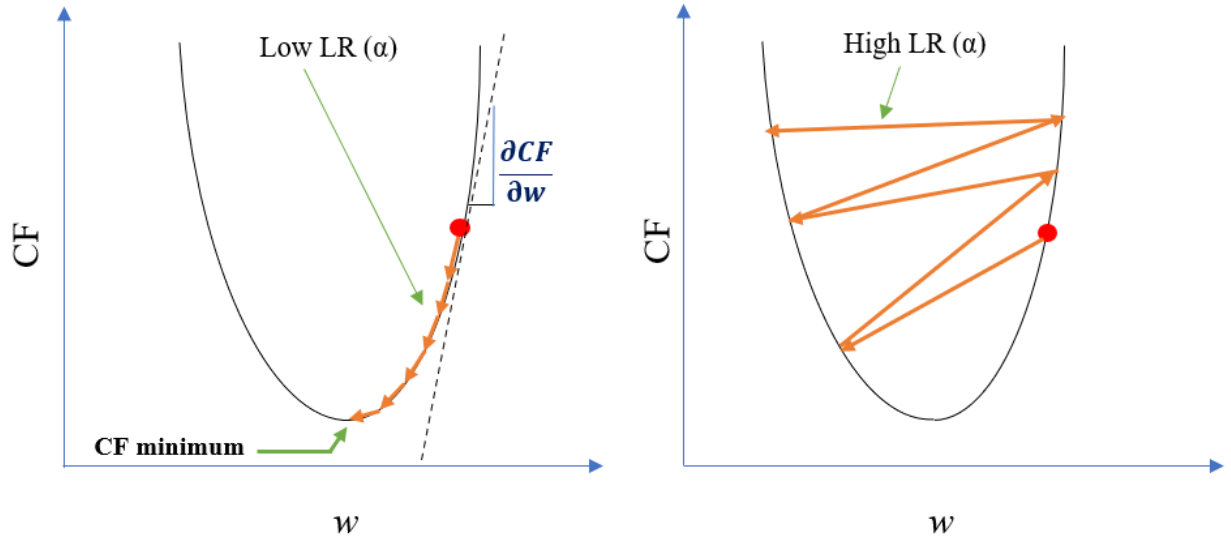

Fig. 9.2. Schematic representation of cost function optimization with respect to weight with high and low learning rates.

It is important to note that the global minimum is reached by moving in the opposite direction of the gradient ($\frac{\partial CF}{\partial w}$) and hence, the gradient (multiplied by α) is subtracted from the current weight (w_i) to obtain the i+1th weight in equation 9.5. Hence, the use of suitable α values is essential to develop a good ANN model.

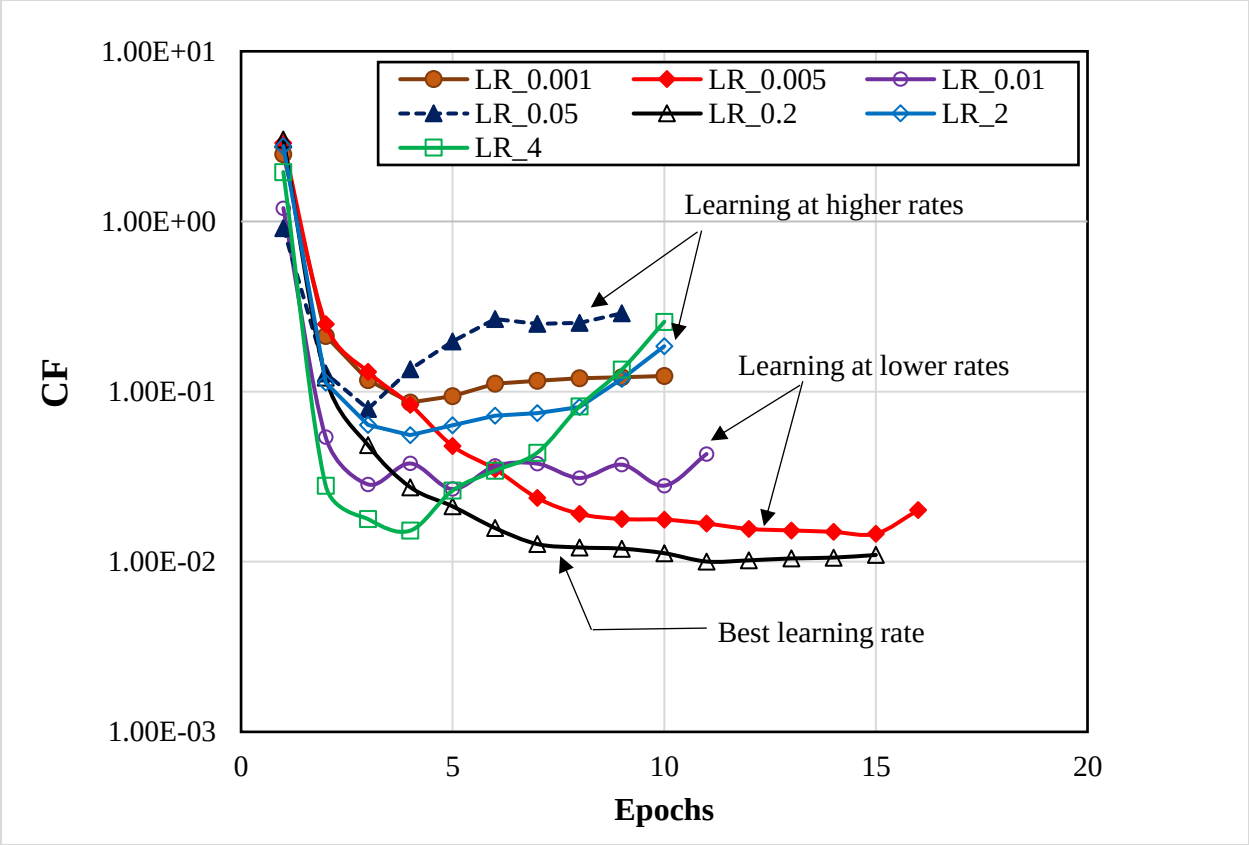

Fig. 9.3. Variation of cost function (of validation data) with various learning rates for the current ANN.

Different learning rates were tested on the optimized feed forward network to select the best learning rate for the model development. The other objective of testing with different LR is to understand its effect on the current model training. Note that the results obtained in table 9.2 were conducted without any specified LR. While using different LR values for the current ANN model, the variation of CF (of validation data) was monitored at every iteration to check how smoothly the curves converged to the point of minimum for the various LR values. The validation data was used because early stopping criteria is determined based on the validation dataset. Figure 9.3 shows the CF vs. iteration curves for different learning rate values. This plot includes representative LR

values in the lower range (0.001, 0.005), intermediate (0.001, 0.005, and 0.2), and higher ranges (LR= 2, 4) to exhibit the nature of CF variation at different LR values considered here. As observed, higher learning rates quickly converged to their corresponding minimum CF followed by steep increase CF. Very low learning rates such as 0.001 did not show a defined singular global minimum value while LR = 0.005 took much longer to converge to the lowest MSE. Such observation provides an excellent confirmation of the hypothesis explained in Fig. 9.2 that signifies the current ANN model follows the right optimization trend. The LR = 0.2 showed the lowest possible validation CF (among the other LR values) with the current dataset and converged smoothly to the point of minimum without any further abrupt increase. Hence, this LR (of 0.2) can be considered as the best learning rate for training the current data. Table 9.3 provides the testing, validation, MSE, and R values for different learning rates to lie in the range 0.001- 4, corresponding to the point of best validation. Note that the MSE at LR = 0.2 was found to be the least one with the strongest correlation indicated by R = 0.96391 for all the LR's tested. Hence, LR = 0.2 demonstrated the best performance and was selected for further model training. This LR value is neither too low nor very high. Hence, such LR is safe and accepted for the current model training without any possible performance degradation. The prediction of target variables was done with the optimized training scheme and the learning rate discussed before. The final neural network structure involved two inputs, three outputs, and one hidden layer with 15 neurons used in this study. Figure 9.4 represents the MSE of training, validation, and testing for the ANN developed with LR = 0.2. As observed, the best validation performance occurred at epoch 10. The validation MSE drops at first up to epoch 10 and then starts rising again. Hence, epoch 10 was selected as the best performance point using the early stopping criteria. The training and testing MSE decreased continuously. The testing MSE at the best performance point was 0.003343.

Table 9.3. Performance of ANN modeling with different learning rates.

LR	Epoch	Testing MSE	Testing R
0.001	10	0.006694	0.871
0.005	8	0.006212	0.9472
0.01	9	0.016	0.9096
0.05	12	0.03	0.80197
0.1	11	0.02376	0.8713
0.2	15	0.003343	0.96391
0.3	16	0.0245	0.88272
0.4	17	0.023	0.90096
0.5	8	0.0166	0.91866
1	10	0.004702	0.94128
2	11	0.02224	0.89829
3	9	0.004334	0.92137
4	8	0.023	0.89134

The corresponding R values can be observed from Fig. 9.5. In this figure, the blue, green, and red lines observed in training, validation, and testing windows are respectively the best-fit lines generated by the current ANN model. The dotted lines signify the actual target outputs obtained from the experiments. The data points located far from the best-fit lines are the outlier points.

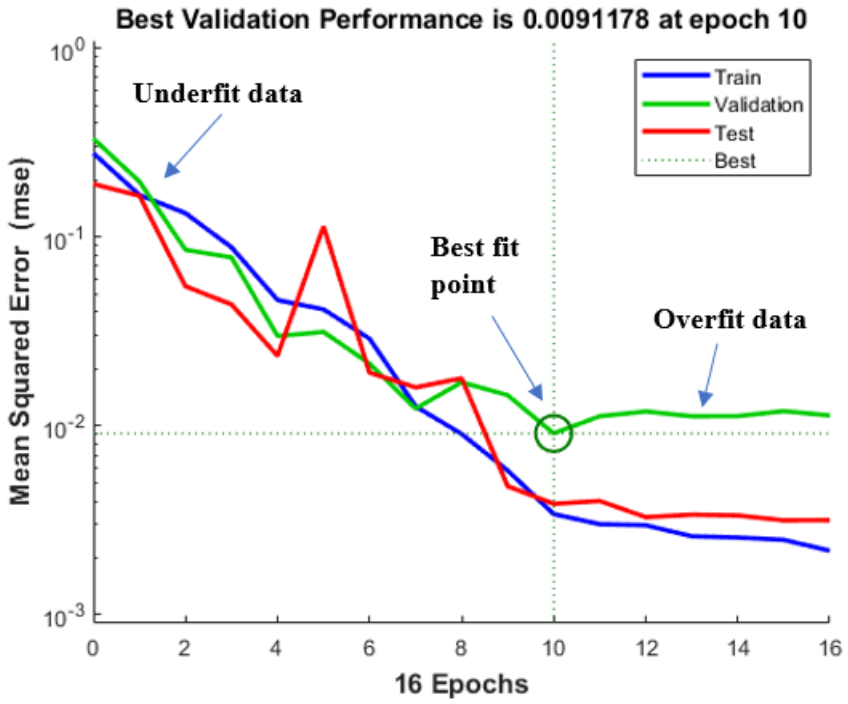

Fig. 9.4. Mean Square Error for training, testing, and validation of the ANN with LR = 0.2.

The 'R' values for the training, validation, and testing are 0.99548, 0.95193, and 0.96391, respectively. Such an observation concludes very strong relationships of model fitting with the data allocated for training, validation, and testing. Also, a strong overall correlation of R = 0.9842 was established with the current model. Hence, the current model is a well-developed ANN model for the prediction of different output parameters in distributed combustion. Table 9.4 summarizes the final weight and bias distribution in different layers for the optimized model.

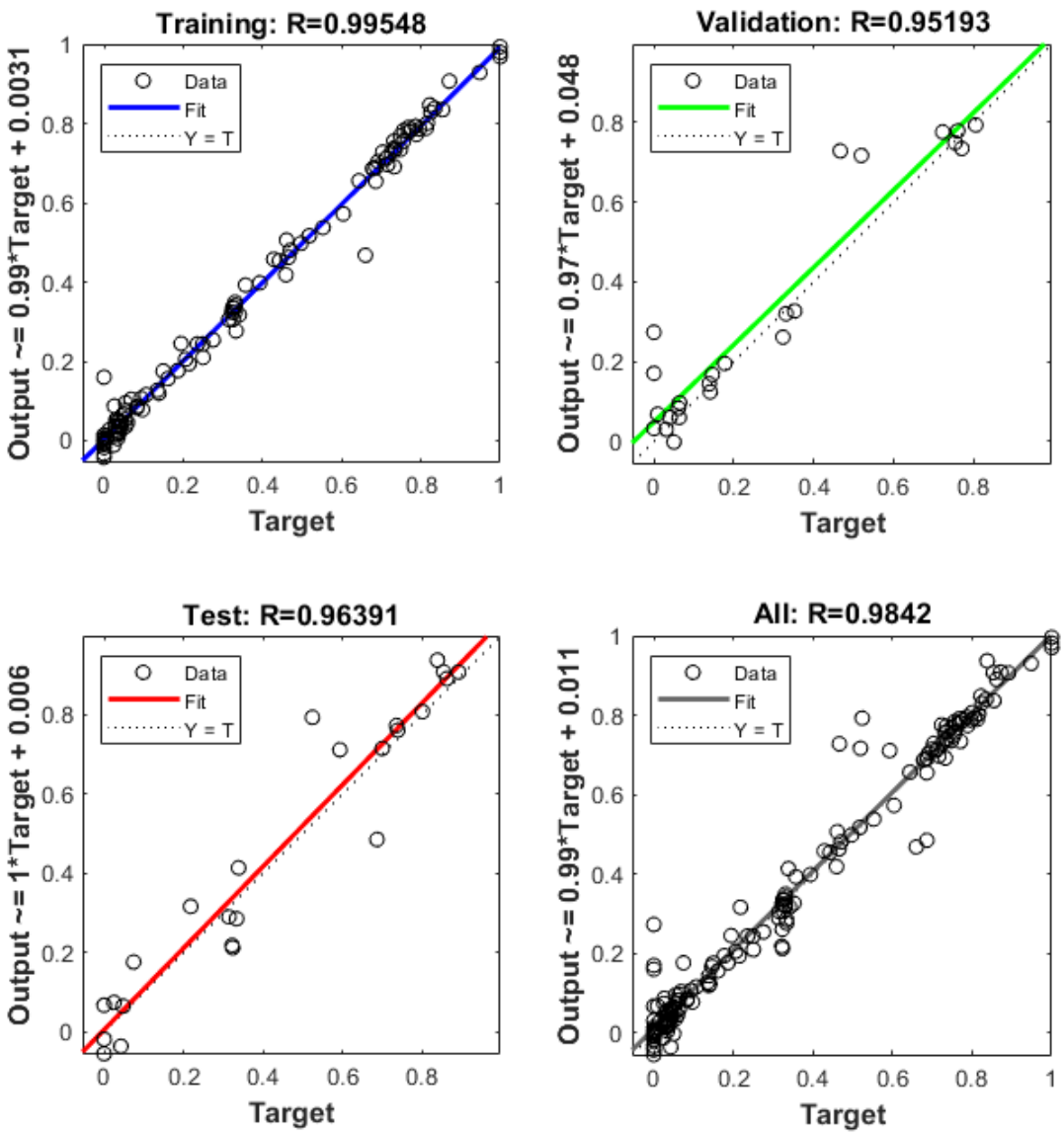

Fig. 9.5. Coefficient of correlation (R) values for training, testing, and validation of the ANN with LR = 0.2.

As expected, the input to hidden layer involved 2 sets of weights (as there were two input variables) while the hidden layer to the output layer had 3 sets of weights (due to three output variables). Note that these weights and bias values solely depend on the dataset and the training algorithms

chosen by the model developer. Hence, the current values given in table 9.4 are only representative of the current ANN model.

Table 9.4. Distribution of weights and bias values for the current ANN.

Neuron Number	Input Layer to Hidden Layer			Hidden Layer to Output Layer			
	Weight		Bias	Weight			Bias
1	-11.1531	-3.3187	10.1039	-0.36287	3.0738	0.5581	0.86061
2	-3.9873	-12.6057	7.8788	-2.4003	0.29962	1.4562	-0.84075
3	-8.8152	-5.9814	7.072	0.74397	-0.84784	0.26494	-0.0068546
4	-2.3864	-11.1513	5.9616	3.0197	-1.0796	1.333	-
5	-10.768	-3.5431	6.8168	-0.24665	-1.7849	-3.5494	-
6	-6.633	-5.6471	3.6439	-0.18784	-0.36151	3.3171	-
7	-2.4228	-9.9229	-1.7747	-0.13941	0.013887	-1.5069	-
8	-9.8745	3.4741	4.0343	-0.31019	-3.5125	-0.061388	-
9	-0.13625	8.5466	-3.1642	0.43915	-0.8196	2.4401	-
10	6.7779	6.3846	2.0707	-1.1326	0.74829	-5.7562	-
11	-12.1028	-8.8599	-3.4805	-0.66257	2.9639	-3.6483	-
12	11.3572	1.3168	5.996	0.34555	0.23649	1.754	-
13	-11.0669	-2.8581	-6.1023	0.14657	0.56029	1.0991	-
14	-9.1645	8.5017	-10.6227	-4.1109	-1.7173	-5.9777	-
15	-6.8021	-5.4323	-12.6195	0.24924	0.12151	3.1039	-

9.2.4. Use of Adaptive Learning Rate

While finding the right LR value is essential to the development of a good ANN model, it can be very time-consuming to train the model with different LR values. This issue becomes even more severe when dealing with larger dataset that may take very long to converge for each condition. Hence, adaptive learning rate [134] was utilized that automatically decides the learning rate based on the value of the CF gradient ($\frac{\partial CF}{\partial w}$) at each iteration. For example, the learning rate decreases or increases near the steeper and shallower regions of the CF curve respectively, when adaptive learning is applied. The mathematical background of adaptive learning rate can be found in ref. [134]. Adaptive learning was applied while training the current dataset by using the training function 'traingda' and turning off any predefined LR in Matlab. Figure 9.6 shows the variation of CF (validation data), gradient of CF ($\frac{\partial CF}{\partial w}$), and the LR at different epochs while training the model with current data using adaptive learning. To avoid ambiguity, this gradient CF shown here was obtained with respect to the weights and not the epochs. It is clearly observed that the model assumed lower LR values where the gradient was high and considered higher LR values for lower gradient values. This implies that the current optimizer has an inverse mathematical relationship between the learning rate and gradient of the cost function. The weight of the $i+1^{st}$ step is optimized using the inverse relationships at the i^{th} step. The choice of such optimizer is recommended for larger dataset to reduce the time of training models with different LR values. In this work, adaptive learning rate was tested with the vision to train larger size data in the future and develop predictive models with that.

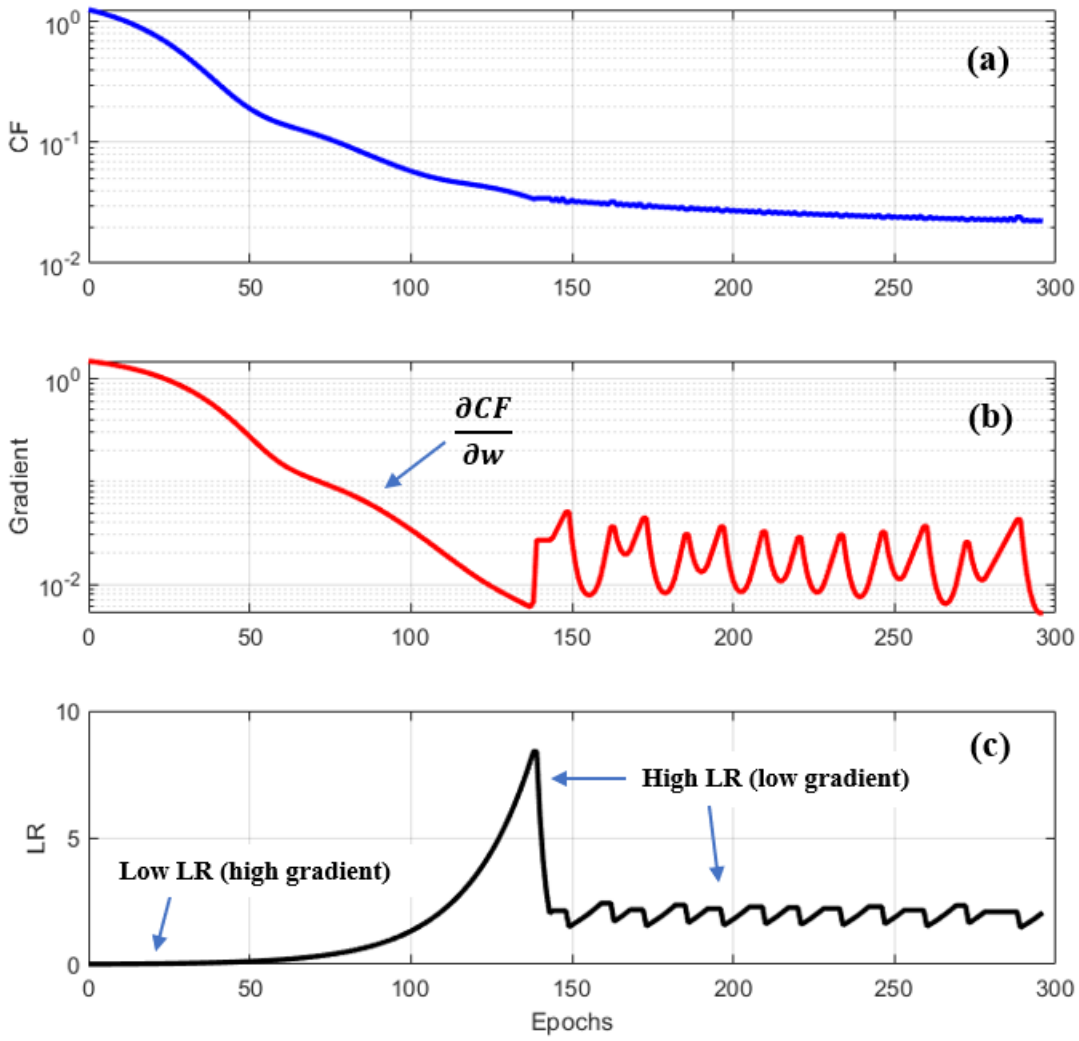

Fig. 9.6. (a) Cost function, (b) gradient of cost function, and (c) the learning rate variation with adaptive learning rate for the current ANN model.

The current algorithm properly applied adaptive learning for data training. The current model training converged at ~ 250 epochs as found from the CF (validation data) curve.

Next, the strength of correlation (R) was examined for this model with adaptive learning as shown in Fig. 9.7.

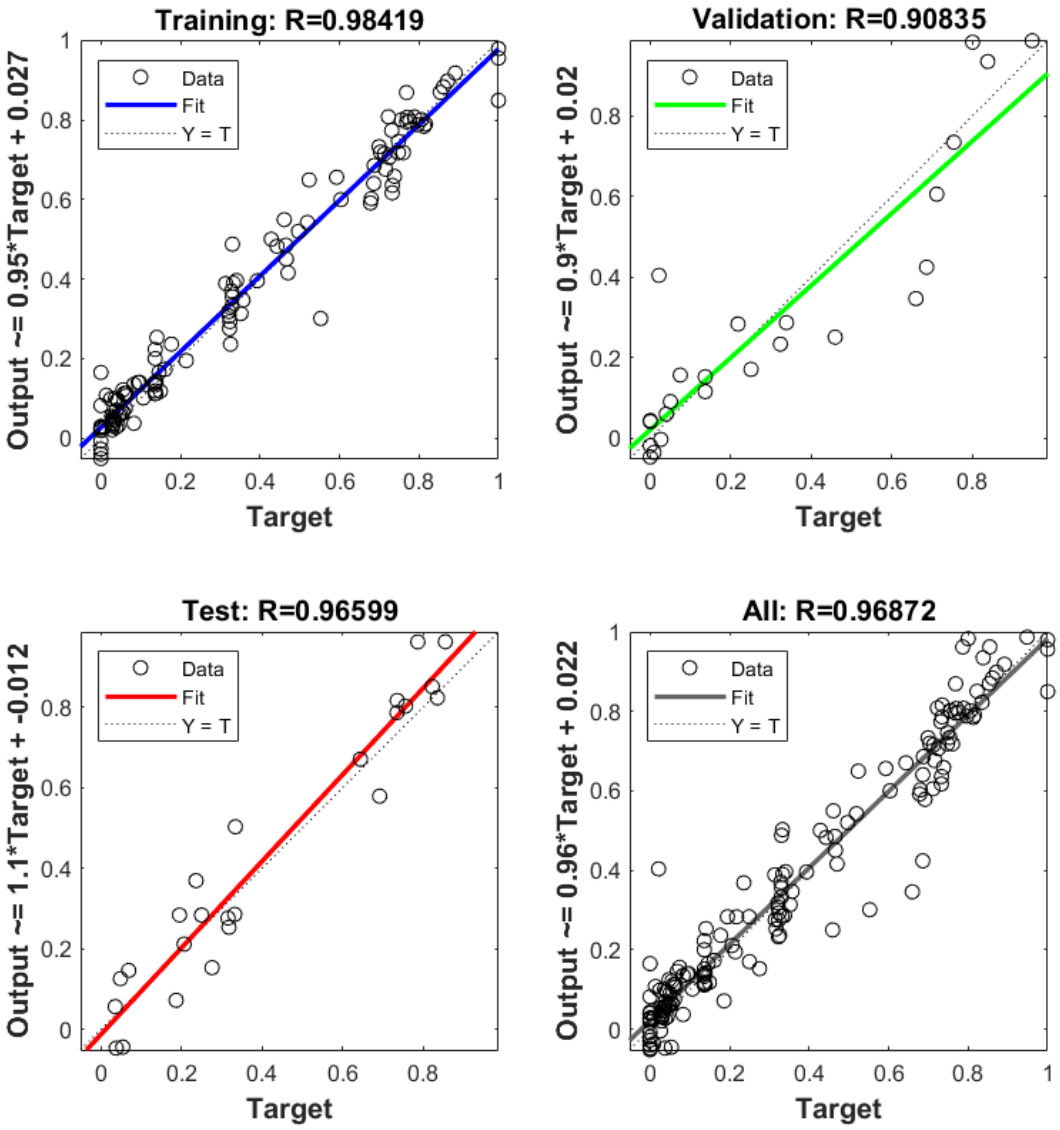

Fig. 9.7. Coefficient of correlation (R) values for training, testing, and validation of ANN with adaptive learning rate.

The 'R' values for the training, validation, and testing are 0.98419, 0.90835, and 0.96599, respectively and the overall R is 0.96872. These values indicate that the model developed with adaptive learning provides nearly similar correlation strength except for the validation R that is

lower than that produced with fixed LR of 0.2. However, the model developed with LR = 0.2 converged using a smaller number of epochs (=10). While the ANN developed with LR = 0.2 uses relatively smaller epochs, the adaptive learning rate may reduce the trouble of figuring out the best LR (by model training) by automatic adoption of LR based on the nature of CF gradient with some compromise of model strength (R value).

9.2.5. Prediction of Target Variables

The prediction of AFT, and emission of NO, CO were obtained from the optimized feed forward model using Levenberg–Marquardt backpropagation algorithm having the LR = 0.2.

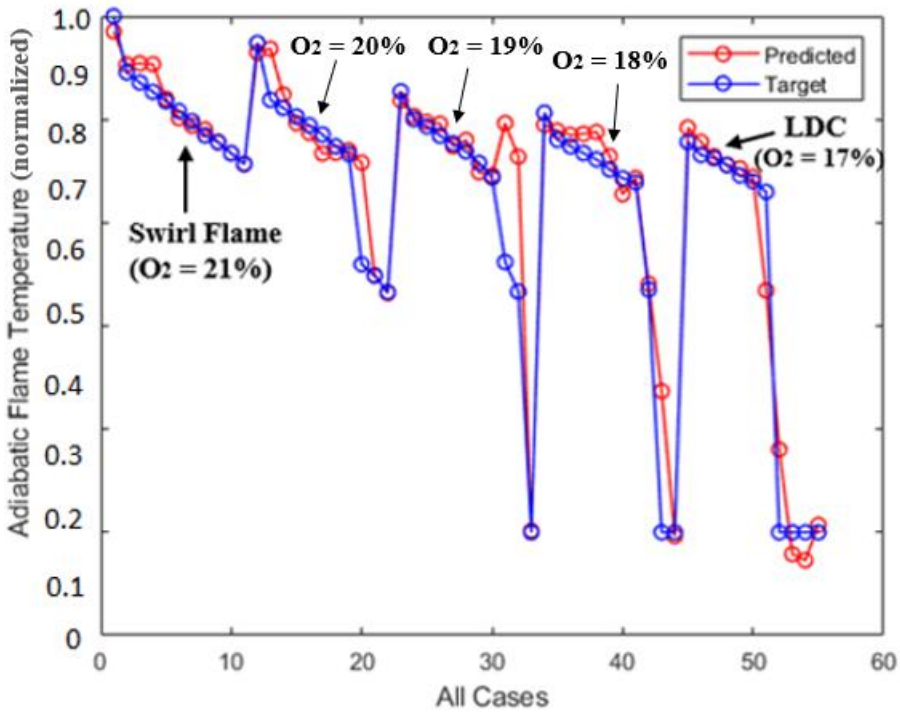

Fig. 9.8. Comparison between predicted and target adiabatic flame temperature (normalized) with LR = 0.2 and Levenberg–Marquardt backpropagation.

The predicted flame temperature (normalized with respect to the maximum temperature of 2190K) closely matched the target AFT obtained from Chemkin-Pro® simulation for every O_2 level. All the cases are demonstrated together (for O_2 = 21- 17%) with conventional swirl combustion (left side of figure) and lean distributed combustion, LDC (right side of the figure) in both Figs. 9.8 and 9.9. Noticeably, the temperature predicted in the distributed combustion regime matches closely with the target output. Furthermore, the model is capable of predicting the blowoff points indicated by the sudden drop in flame temperatures. The slight deviation of predicted values from the target temperatures observed for different air flowrates in the intermediate O_2 concentrations (18- 20%) is explained by the overall R value of 0.9842. Fig. 9.9. shows the prediction of normalized NO and CO concentrations in the range O_2 = 21- 17%.

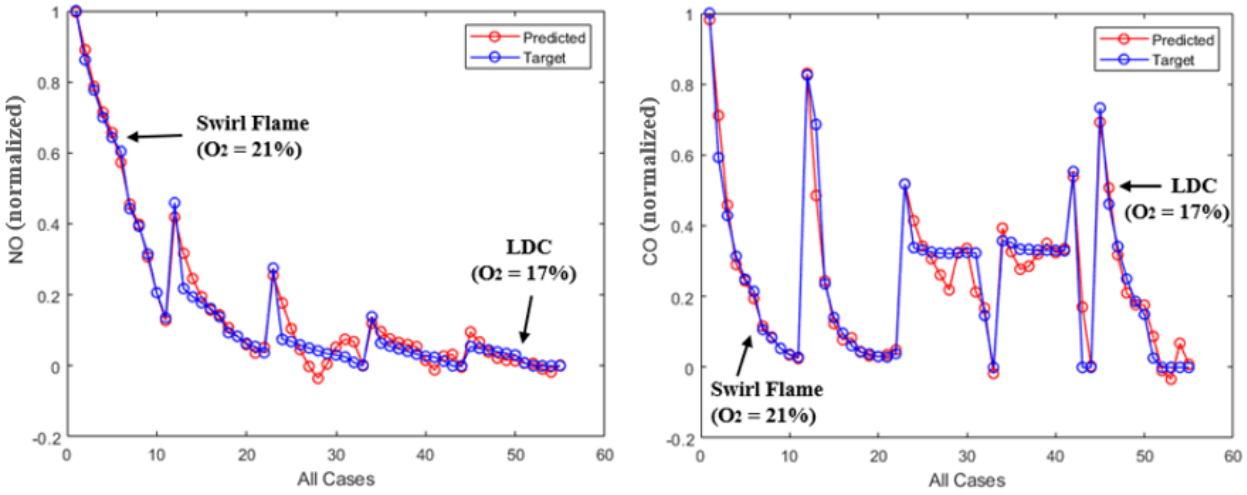

Fig. 9.9. Comparison between predicted and experimental (target) NO and CO concentrations (normalized) with LR = 0.2 and Levenberg–Marquardt backpropagation.

Similar observations of very well predicted output can be made in these cases as well. The model predicted concentrations closely matched the experimental concentrations in conventional swirl combustion and distributed combustion while slight deviation was observed in the range O_2 = 20-

18%. Hence, the current model has great potential for predicting various parameters in swirl-assisted distributed combustion (such as pollutant emission, flame temperature, flame acoustic signal at different dilution levels, pressure data, chemiluminescence intensities, etc.).

9.2.6. Comparison of Levenberg–Marquardt and Bayesian Regularization algorithm

A different backpropagation algorithm called Bayesian Regularization [135] was further used to compare the results predicted by the Levenberg–Marquardt algorithm (given in the previous section). Bayesian Regularization backpropagation was performed by using the 'trainbr' function in Matlab. Early stopping was applied in both cases to avoid any possible overfitting. Figure 9.10 shows the MSE characteristics of training and testing using Bayesian Regularization.

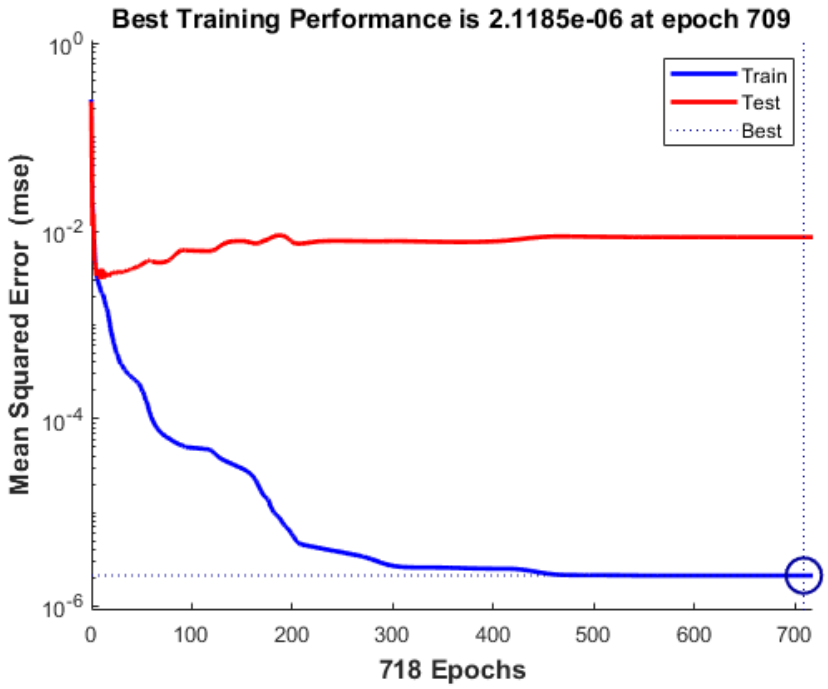

Fig. 9.10. Mean Square Error for training, testing using Bayesian Regularization.

This regularization algorithm does not necessitate a validation dataset to be separately prepared out of the training set unlike the Levenberg–Marquardt algorithm. All the data (except the test data) is used for training purposes in this case [136]. The Bayesian Regularization required more epochs (718 epochs) compared to the Levenberg–Marquardt algorithm (16 epochs) to converge. The best performance of training occurred in 709th epoch.

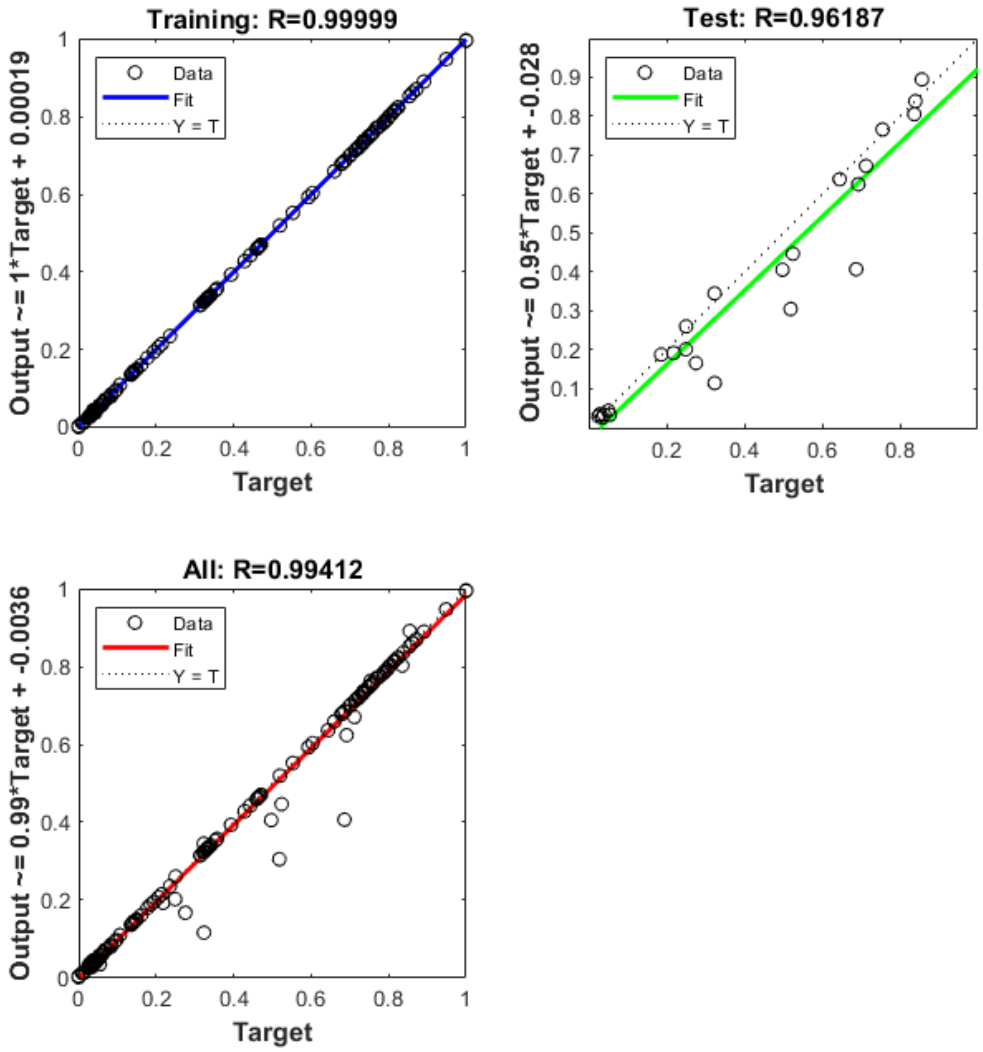

Fig. 9.11. Coefficient of correlation (R) values for training, testing, and validation of the ANN using Bayesian Regularization.

However, the training MSE was significantly reduced by using Bayesian Regularization. The R values for the Bayesian Regularization are shown in Fig. 9.11. The training, testing, and overall 'R' values are 0.99999, 0.96187, and 0.99412, respectively. Such observations indicate a very strong relationship generated with Bayesian Regularization for the current data.

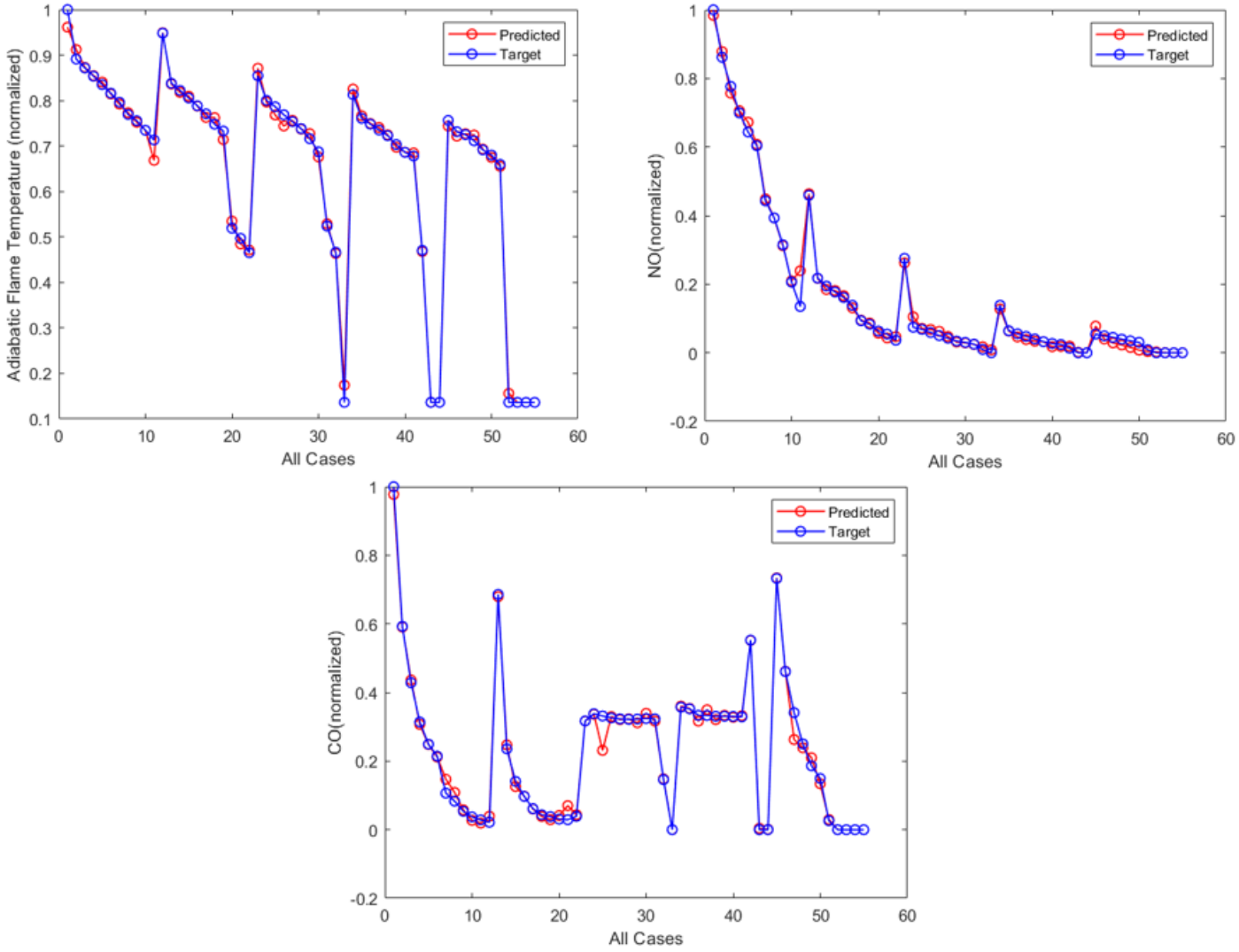

Fig. 9.12. Comparison between predicted and experimental (target) Adiabatic flame temperature, NO, and CO concentrations (normalized) with Bayesian Regularization.

This also indicates that the Bayesian Regularization is a better model compared to Levenberg–Marquardt algorithm although it took a relatively longer time of convergence for the current data. Figure 9.12 displays the prediction of AFT, and the concentration of exhaust NO and CO for different O_2 levels using Bayesian Regularization. The overall trend of this plot is similar to that of the one generated with Levenberg–Marquardt algorithm. However, this plot confirms the excellent agreement of predicted parameters with the target experimental parameters at almost every O_2 level as indicated by the R-values in Fig. 9.12.

9.3. Summary

An artificial neural network-based model was studied to predict flame temperature and emissions in distributed combustion established from a 5.72 MW/m^3-atm thermal intensity conventional swirl air flame at equivalence ratio of 0.9. The NO and CO concentrations collected with a gas analyzer and the adiabatic flame temperatures (AFT) obtained using Chemkin-Pro® simulations were selected as the output of the ANN. The airflow rates (in LPM) and O_2 levels at different dilution levels were considered as the input variables. Only one hidden layer, with 10, 15, and 20 neurons, was present in this ANN. Different transfer functions (Tansig and Logsig) along with feed forwards and cascade forward backpropagation network schemes were investigated. Hyperparameter optimization was considered using different learning rates. The best model was selected based on the mean square error (MSE) and the strength of the relationship (R) predicted by the model for individual outputs. An early stopping criterion was applied to avoid overfitting of data. The Levenberg–Marquardt backpropagation having Tansig transfer function and 15 neurons in the hidden layer produced the lowest MSE. An adaptive learning rate was

applied for automatic adoption of best LR values by the model at each iteration (or epoch) based on the local gradient of the CF curve. The optimized ANN showed strong correlation of the bestfit indicated by the 'R' values of the training, validation, and testing (0.99548, 0.95193, and 0.96391 respectively). Such predictive analysis was focused on developing an ANN-based smart virtual sensing in combustion. This chapter highlighted the importance of model optimization for better prediction of parameters.

Chapter 10: Recognition of Distributed Combustion Regime using Deep Learning (Computer Vision Technique).

While data-driven regression was demonstrated in the previous chapter, the image-based classification and feature extraction is investigated in swirl distributed combustion here. Image-based classification is widely used to develop deep neural networks capable of recognizing unknown images, audios, or the combination of both. The primary objective of such works is to gain enhanced autonomous decision-making using artificial intelligence to develop advanced combustion control systems. This chapter demonstrates the development of image-based perception to recognize unknown combustion images using deep learning. Flame chemiluminescence collected at high-speed (3000 kHz framing rate) was utilized to train the deep learning model. The fidelity of the optimized model was verified in terms of accuracy and loss. Finally, new combustion images (untrained) were tested to check the recognition capability of the current deep learning algorithm. The test conditions are given in appendix D.

10.1. Basic Concept of convolutional neural network:

The convolutional neural network (CNN) model was developed from the acquired chemiluminescence image data using a conventional swirl combustion and distributed combustion hardware devices. Teachable Machine by the Google Creative Lab was used extensively for the current CNN modeling. Teachable Machine is based on MobileNet, which aims to efficiently develop light weight deep learning models for mobile applications using depth wise separable convolutions [137]. While the MobileNet focuses on small model development, the Teachable Machine depends on transfer learning technique [138, 139]. Transfer learning is efficient in

transferring the knowledge from a pre-trained model to another model (generally of higher complexity) to be trained using the new available data. Transfer learning eliminates the requirement of initiating a fresh learning scheme every time with different datasets. The mathematical background of such learning was explained by Rehman [140]. For a specific domain $D = \{X, P(X)\}$ with X as the feature space and P(X) as marginal probability such that, $P(X) = \{x_1, x_2, ..., x_n\}$ for $x_i \in X$. With such domain definition, a task T can be defined as $T = \{y, P(y|X)\} = \{y, \eta\}$, where η is the objective function which can be denoted by P(y|X) as well. Now, if Dt, Tt represent the target domain and respective target task then D_s, Ts be the source domain with respective source tasks. The transfer learning aims at learning the target probability distribution $P(y_t|X_t)$ in Dt with information gained from Ds and T_s ($D_s \neq D_t$ or $T_s \neq T_t$). Figure 10.1 demonstrates the basics structure and different components involved in a CNN.

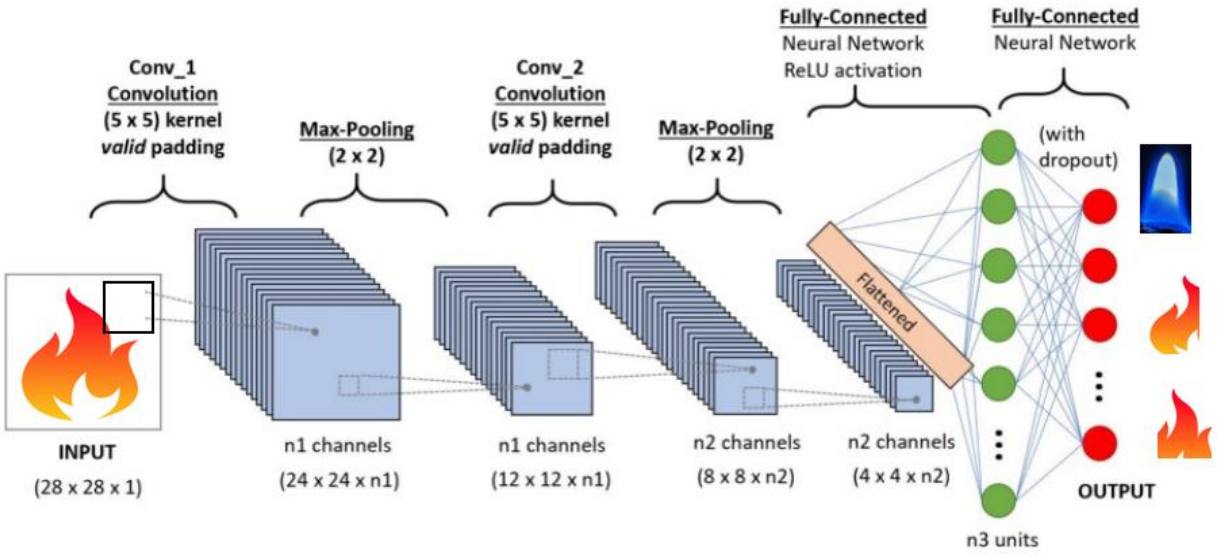

Fig. 10.1. Schematics of convolutional neural network

In addition to input, the CNN contains convolution layers, max-pooling, and output layer. The convolution and max pooling are explained below.

10.1.1. Convolution Layers

Convolution Layers act as filters on an image by allowing the extraction of visual features. Each neuron in a convolution layer is responsible for a small cluster of neurons from the preceding layer. The bounding box that determines the chunk of neurons is called a Kernel. Conceptually, convolution layers can be thought of as a filter moving across an image applying a convolution operation on individual regions of the image. The result is then sent to the corresponding neurons in the convolution layer. The mathematical formulation of 2D convolution is given by:

$$y[i,j] = \sum_{m=-\infty}^{+\infty} \sum_{n=-\infty}^{+\infty} h[m,n]\, x[i-m, j-n] \tag{10.1}$$

The example shown in Fig 10.2 has a kernel size of (3,3). Hence, $\begin{cases} m \in [\![-1,1]\!] \\ n \in [\![-1,1]\!] \end{cases}$ and the convolution for the upright pixel yields:

$$y[1,1] = \begin{matrix} 0\cdot 4 + 0\cdot 0 + 0\cdot 0 + \\ 0\cdot 0 + 1\cdot 0 + 1\cdot 0 + \\ 0\cdot 0 + 1\cdot 0 + 2\cdot(-4) \end{matrix} = -8 \tag{10.2}$$

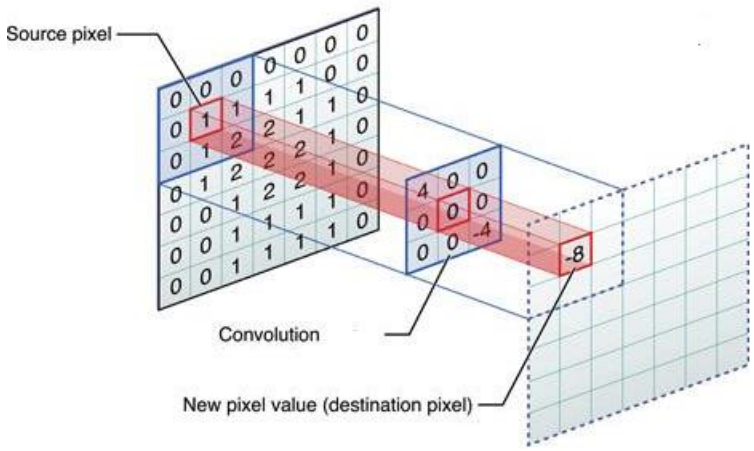

Fig. 10.2. Schematic representation of a convolution layer.

10.1.2. Max-Pooling Layers

As the names suggest, Max-pooling is a pooling operation that takes the maximum element from a region defined by the filter. Hence, the output of max pooling is a resized image containing the most dominant features of the input image. An example is shown below with a (2,2) filter size.

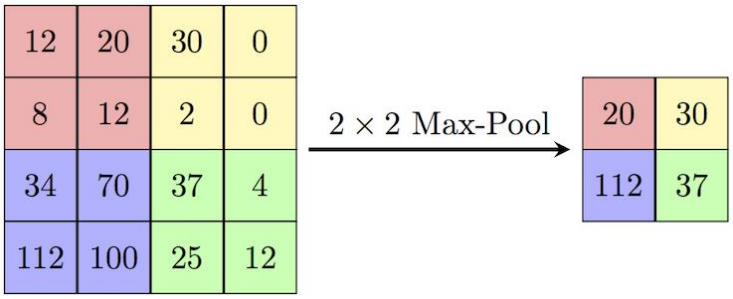

Fig. 10.3. Schematic representation of a Max-Pooling (2, 2) Layer.

Other types of Pooling Layer exist and can be used in Convolution Neural Network like Average Pooling or Min-Pooling to name but two.

10.2. Basic Concept of MobileNets:

The current CNN model was trained with image data for flames at O_2 = 21, 19, 18, and 16%. In each category, 300 chemiluminescence images (acquired at a rate of 2000 frames/sec.) were used for model training. Developing any good prediction model depends largely on model optimization scheme. Thus, model optimization was given importance for the current study.

The optimized classification model was chosen by repeated training of the model with hyperparameters variation (such as learning rate, batch size, and epochs). Image resizing was performed to convert the input images (of dimension 1280x720 pixels) dimension to at least 224x224 pixels and then normalized. Resizing is useful in developing a flexible neural network model capable of recognizing images of different sizes without affecting computational efficiency. These resized images were converted into array before initiating the prediction task for image recognition. Verification of image recognition capability of the model was tested by introducing new flame images. The optimized model was used to recognize the new flame images with original O_2~ 20% and 17% to verify the capability of the current model.

10.3. Results

Collecting the test data and labeling them individually is essential to such model development. Flame images were collected using high-speed imaging of chemiluminescence signatures at different dilution levels. The training process was performed using four different flames: conventional swirl flame (at O_2 = 21%), and three CO_2 diluted flames at O_2 = 19%, 18% and 16%, which were labelled as corresponding to their O_2 concentration levels. The training flames are exhibited in Fig. 10.4. These images showed different visible appearance of the reaction zone shape, chemiluminescence intensity, and standoff heights from the combustor base location.

Hence, such an image set is considered ideal for model training. A total of 300 instantaneous images were used to train the images in each category resulting in 1200 total images for the four flames used for training. Training was carried out using 85% of the total data while the testing used 15% of the data. While training the model, different learning rates (LR = 0.0001, 0.001, 0.01, 0.1, 1.0), epochs (20, 50, 100), and batch sizes (16, 32, 64) were tested to generate the best model. Generally, the best model was decided based on accuracy and loss during training. The accuracy of any CNN is defined as:

$$\boldsymbol{Accuracy} = \frac{\boldsymbol{Number\ of\ correct\ predictions}}{\boldsymbol{Total\ number\ of\ predictions\ made}} = \frac{\boldsymbol{TP+TN}}{\boldsymbol{TP+TN+FP+FN}} \tag{10.3}$$

where TP, TN, FP, and FN stand for true positive, true negative, false positive, and false negatives, respectively. The loss in this case is the cross-entropy loss that is generally used in multi-class classification tasks [141]. The binary cross-entropy loss is defined as the negative sum of the loss of corrected predicted probabilities.

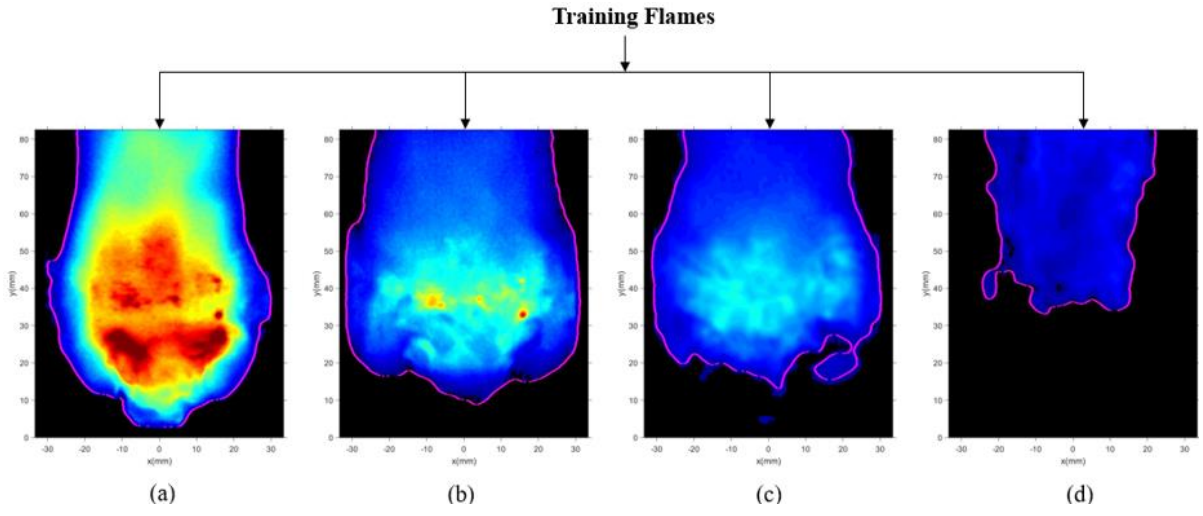

Fig. 10.4. Training flames at (a) O_2 = 21%, (b) O_2 = 19%, (c) O_2 = 18%, and (d) O_2 = 16% concentrations for the current computer vision model.

By definition the cross-entropy loss is the given by:

$$H_p = -\frac{1}{N}\sum_{i=1}^{N} y_i * \log\,(p(\,y_i) + (1 - y_i) * \log(1 - p(y_i)) \quad (10.4)$$

Here, $p(y_i)$ indicates the probability of prediction of any class of image.

10.3.1. Effect of Variation of Different Learning Rates on Flame Classification:

Different learning rates have been tested to investigate the performance of model training and accuracy of image recognition. The variation in loss function with respect to epochs for different LR has been tested to check the best training condition to achieve lower number of epochs as well as lowest loss value. The choice of the best working model was made based on the optimized loss value (of the testing data) and the number of training epochs. Table 10.2 outlines the loss values corresponding to the various learning rates, epochs, and batch sizes considered.

The confusion matrix [142] was plotted for all these cases to verify the performance of the trained model in flame image recognition. Figure 10.5 compares the variation of loss and the corresponding confusion matrix at different learning rates. As observed, the loss function gradually converged for LR = 0.0001 compared to the other learning rate cases. However, this case required more epochs to converge to lowest possible loss. The cases with LR = 0.001 and 0.01 converged with lower epochs. The higher LR cases (0.1 and 1) converge quickly, however, these cases included very high loss values. The bottom row of Fig. 10.5 showed the confusion matrices for the different LR cases considered during this study. As observed, the LR = 0.0001, 0.001, and 0.01 cases predicted different flame classes (at O_2 = 21, 19, 18, and 16%) very well.

Table 10.2. The loss values correspond to the various learning rates, epochs, and batch sizes.

Learning rate	Batch Size	Epochs	Loss
0.0001	16	20	0.004
0.001	16	20	0.00019
0.01	16	20	0.000105
0.01	16	50	0.0001002
0.01	16	100	0.00010074
0.01	32	50	0.0001053
0.01	64	50	0.00011
0.1	16	20	6.907
1.0	16	20	4.65

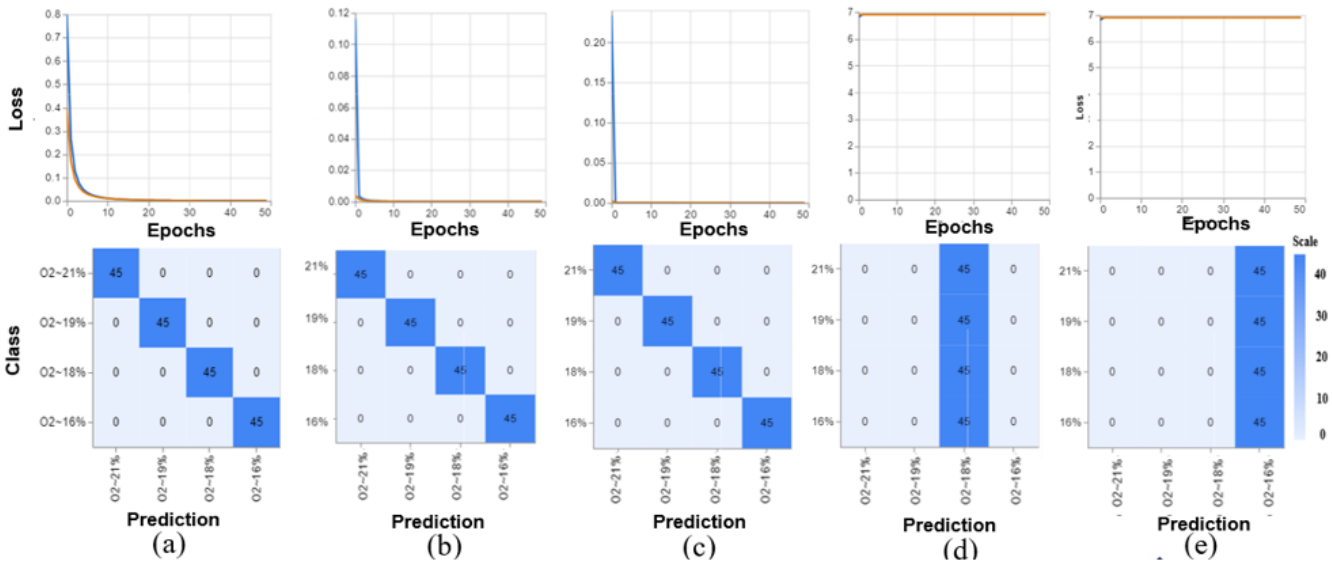

Fig. 10.5. Variation of Loss (top row) and the confusion matrix (bottom row) for learning rates (a) 0.0001, (b) 0.001, (c) 0.01, (d) 0.1, and (d) 1.

This is because all the testing samples (that is 15% of 300 total cases = 45 cases) were predicted as true positive (TP) for every class considered for training. For LR = 0.1 and 1, different classes were not predicted properly as seen from Fig. 10.5. This is because, the flame classes at O_2 = 21, 19, 16% and O_2 = 21, 19, 18% respectively were not predicted for LR = 0.1 and 1 as observed from the confusion matrix. Additionally, the loss of classification for these cases was significantly higher than the lower LR cases. Thus, the lower LR values were more favorable for the current flame image classification task. In order to receive the lowest loss as well as faster convergence of the CNN model, the LR = 0.01 was accepted as the optimized model for the current study. There can naturally be the question whether the perfect classification found for LR = 0.01 is due to the development of a good model or an overfitting tendency. A perfect classification comes due to overfitting, good model development or due to a smaller number of images. This issue was investigated by training models with larger image size to check the effect on model development. CNN models were also trained with 501, 2001, and 3001 images and LR = 0.01 under each category of training flames while keeping the epoch and batch size as 50 and 16 respectively. Figure 10.6 represents the confusion matrices for the above-mentioned image numbers. With a higher number of images in each category, misclassification was observed. For 501 images case, the class of O_2 = 19% was predicted as the O_2 = 18% and 21% classes. Such misclassification increased with higher images (2001 and 3001 images). The O_2 = 18% class was predicted as the O_2 = 19% class when model training was performed with 2001 and 3001 images. Such observations support that a perfect classification could be achieved when the number of images is less. With higher image data the model induces an increased tendency of misclassifying. Hence, it can be concluded that the current model developed with 300 images in each category with LR = 0.01 showed perfect classification due to moderately small number of images used for training.

This case was utilized for further modeling and detection of new flame images to develop an image-based perception algorithm.

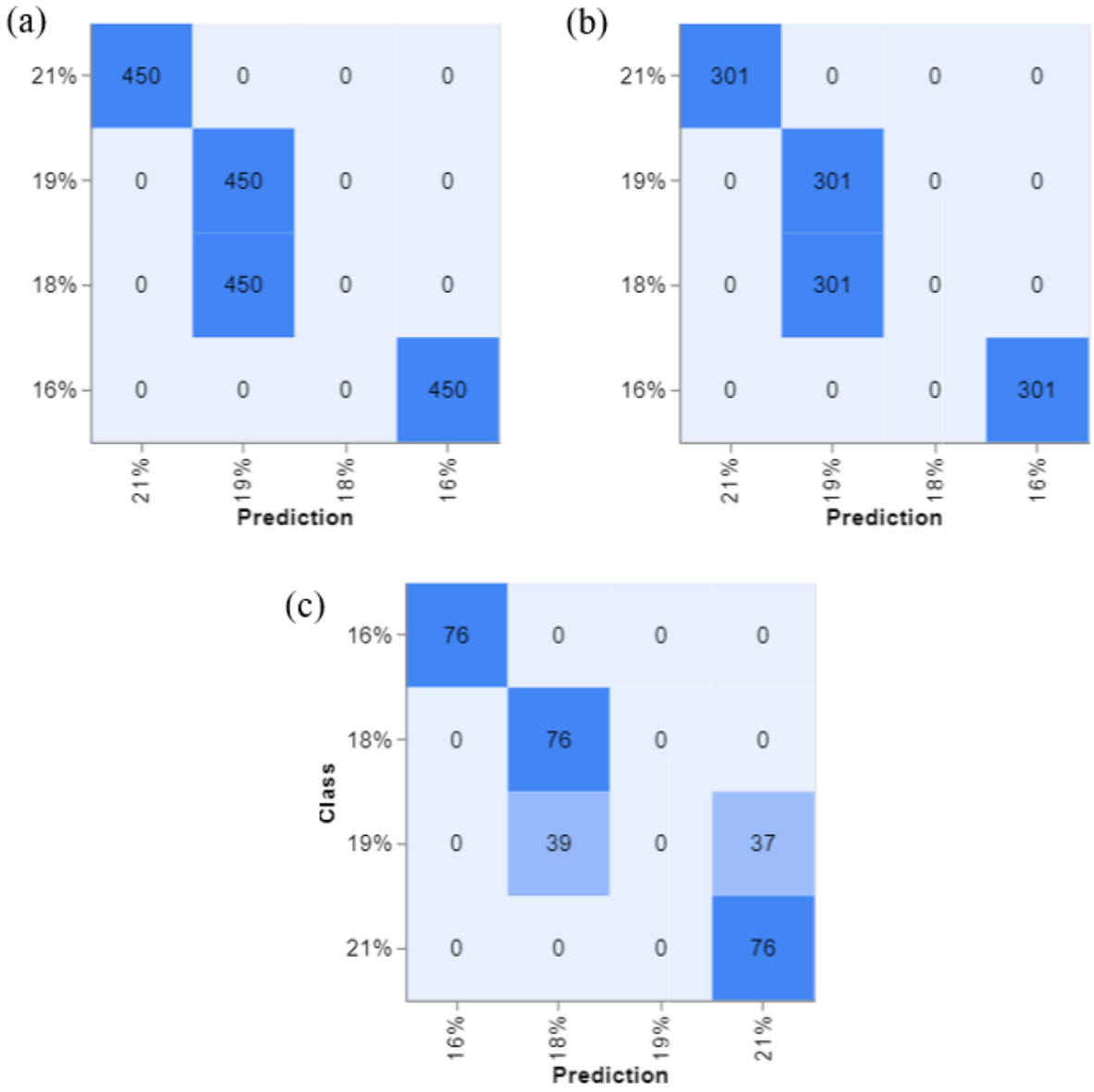

Fig. 10.6. Confusion matrix of CNN model training with (a) 3000, (b) 2000, and (c) 500 image at LR = 0.01, batch size = 16, and number of epochs = 50.

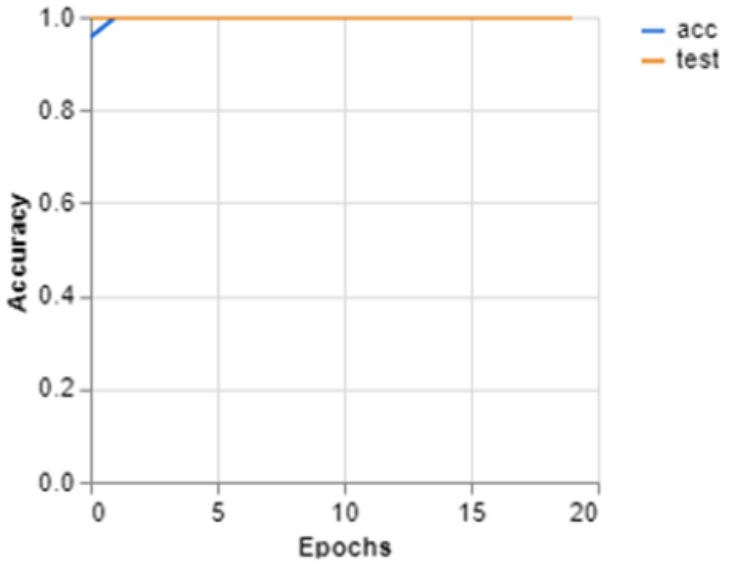

Fig. 10.7. Accuracy variation with epochs for the training data set.

Table 10.2 also confirms that the lowest loss was observed with a learning rate of 0.01, batch size 16, and epoch 50. The model with epoch 20 (with learning rate of 0.01, batch size 16) can also be used as the loss is comparable to that of the one with epoch 50. However, for smaller data sets, like the current one, the time of convergence is not much higher than that with epoch 20 case. Hence, the model with epoch 50 was considered for this study. Figure 10.7 shows the variation of accuracy with epochs for the training of flame data set with learning rate of 0.01, batch size 16, and epoch 50. As observed, the model accuracy reached near 1 at a very early stage of model training (~ epochs 2). The model training was still performed until epochs 20 to confirm the convergence of the model. Additionally, the loss function (in Fig. 10.5) did not rise after reaching the minimum value, so that the model was not overfitted. This was also verified by training the model for longer time that showed consistent nature of the loss function.

Next, the main task of developing this image classification model was to recognize and classify the image at its given O_2 level when any new image is introduced. The entire training process runs internally in Teachable Machine like a 'black box' and performs the image recognition task based on the input dataset. This model characterizes any given image in terms of the test image categories. The recognition task is shown by displaying what percentage of contribution from each the input image categories are contained by the image under verification. This is logical as the developed model was not expected to have the knowledge of the exact image label and should only predict the similarity of any image with the input image classes. Figure 10.8 demonstrates such prediction for the flames at O_2 = 20% and 17% in terms of the input images (at O_2 = 21%, 19%, 18% and 16%). The results showed that the current model predicted a combination of 60% characteristics from the O_2 = 19% flame and 40% characteristics from the O_2 = 21% conventional swirl flame for the flame at O_2 = 20% under verification. This is reasonable as this flame closely resembles the shape of flame at O_2 = 21% while the chemiluminescence intensity is very similar to the flame at O_2 = 19%. The prediction of this model for the flame originally at O_2 = 17% showed 76% characteristics from the O_2 = 18% reaction zone and 24% characteristics from the O_2 = 16% reaction zone. This is attributed to the fact that the shape and chemiluminescence intensity of the reaction zone at O_2 = 17% had relatively higher similarity with that of the O_2 = 18% reaction zone than the O_2 = 16% (which had a relatively higher standoff height). Such predictions slightly varied with different instantaneous images. Hence, the current model exhibited efficient recognition capability for the flames (mainly in distributed combustion) under study. Further, the model development can be performed with the acoustic signals acquired at various O_2 concentrations to make this technique more feasible for characterization of distributed combustion. The results

presented here are of significant importance in swirl combustion and distributed combustion [143, 144].

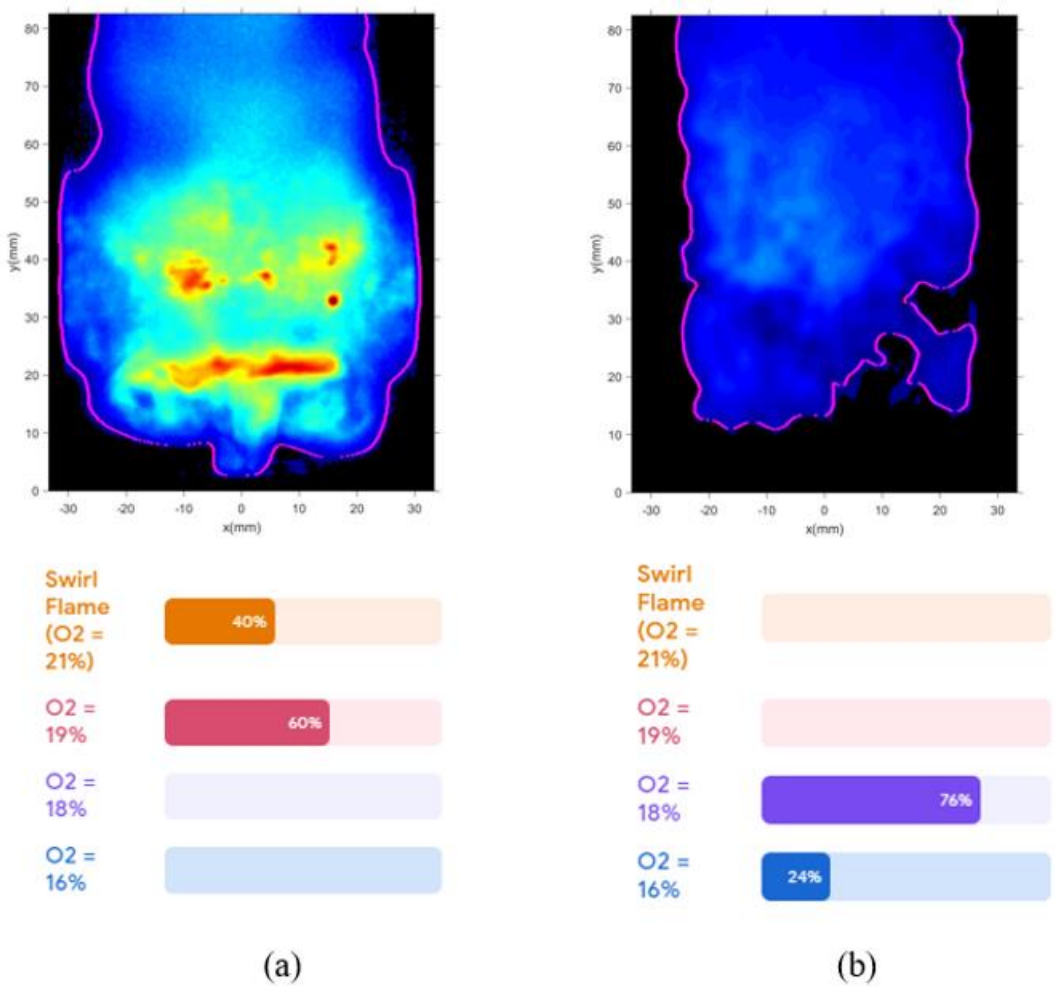

Fig. 10.8. Model based image recognition (a) O_2 = 20%, (b) O_2 = 17%.

The success of image-based recognition of new combustion regimes inspired to develop classification of combustion based on more inputs such as chemiluminescence and audio data from reaction zones. As images may not solely help to classify combustion regimes due to the highly complex, non-linear dynamics, and geometrical dependence of combustion systems additional input is conceptualized (audio in this case) to verify the confidence of classification. A combined image-audio CNN is conceptualized to classify swirl combustion at different O_2 levels (between 21-16%) corresponding to dilution levels. This work is under development and some of the initial developments are mentioned in appendix F.

10.4. Summary

Image feature-based recognition was investigated for the recognition of distributed combustion regime using deep learning-based convolutional neural network (CNN) framework. Distributed combustion regime was established from a 5.72 MW/m^3-atm thermal intensity swirl flame with methane (at equivalence ratio 0.9) by CO_2 dilution of the inlet airstream. The chemiluminescence images at different %O_2 = 21, 19, 18 and 16%) were used to train CNN model development with hyperparameter optimization such as learning rate, batch size, and epoch. The model with learning rate of 0.01, batch size 16, and epoch 50 was found to be the optimized one. The trained model recognized new flame images based on chemiluminescence signature, flame shape, and standoff distance features.

Chapter 11: Conclusions of The Present Research

This chapter is dedicated to provide the conclusions of the current research discussed in previous chapters (chapter 4- 10). Additionally, recommendation for future studies based on the current outcomes is also made to give future direction to the CDC research. The next few sections discuss the conclusions of different studies conducted as part of the current research. Chapter-wise conclusions are given below:

11.1. Conclusions of Chapter 4

Swirl distributed combustion using four different gaseous fuels such as propane, methane, 20% hydrogen enriched methane and 40% hydrogen enriched methane (with constant $\phi = 0.9$) at 5.72 MW/m^3-atm heat release intensity was investigated. Flames shape was obtained with OH* chemiluminescence using with nonlinear diffusion filtering. The conclusions of this work are:

1. Higher flowfield uniformity was attained in CDC (the rms OH* signal intensity fluctuation reduced from ~ 20% to only 2% of mean intensity in CDC).

2. The volumetric expansion of reaction zones with respect to their initial volumes showed a power law growth behavior of different flames. In CDC, the reaction zone showed over 4 and 5-times volumetric expansion with CO_2 and N_2 dilutions respectively.

3. Higher heat capacity value of CO_2 promoted greater reduction of flame speed that subsequently caused higher flame lift-off to occur. The normalized lift-off height for CO_2

diluted flowfield was observed to be higher than the N_2 diluted flowfield.

4. A significant reduction of NO and CO emissions were observed when the flames approached distributed combustion (~ 90% reduction of NO). High-temperature dissociation of CO_2 to CO increased the CO ppm at intermediate $\%O_2$ concentrations.

11.2. Conclusions of Chapter 5

Fundamental investigations of flame stability in swirl distributed combustion were compared to conventional swirl air combustion (at 5.72 MW/m^3-atm heat release intensity). This study was based on high-speed imaging of broadband chemiluminescence of reaction zones. The key findings of this work are:

1. Distributed reaction zones exhibited relatively stable RZ bases without much fluctuation. Shear layer vortex-shedding from swirl air flames were observed at frequencies in the range of 166- 187 Hz. A 174 Hz fluctuation of the RZ base was observed due to vortex shedding.

2. Analysis of dominant dynamic structures was performed with proper orthogonal decomposition (POD). Vortex shedding structures were confirmed in swirl air-flames with POD analysis. Mild spatial fluctuation observed in distributed combustion was due to the rotational effects associated with the precessing vortex cores (PVC) as well as the RZ stand-off.

3. Significant reductions of fluctuation energy (~ 60%) in distributed combustion compared to air-combustion contributed to higher RZ stability in distributed combustion. The POD

modes highlighted peak fluctuation frequencies at 176 Hz and 350 Hz in swirl air-combustion. However, the distributed combustion showed no such peak fluctuations.

4. Distributed combustion indicated decreased combustion noise. The power spectrum of heat release (q') and acoustic signal fluctuation (p') demonstrated a common peak at 174 Hz, which gradually diminished with the decrease in O_2 levels. The possibility of thermo-acoustic coupling in swirl air-combustion was indicated by the in-phase characteristics of p' and q' signals. These signals were out of phase in distributed combustion.

5. The effect of CO_2 dilution on RZ chemiluminescence at a constant adiabatic flame temperature (same as that of the undiluted flame of ~2100 K) showed the drop in flame luminosity was relatively higher for all the dilution levels with decrease in T_{ad} as compared to constant T_{ad} case.

6. Suppression of thermo-acoustic peak occurred relatively earlier along with a gradual decline of the PVC peak amplitude at constant T_{ad} compared to variable T_{ad} case. Instabilities in the present combustor were reduced with gradual dilution of the inlet air regardless of whether the T_{ad} was kept constant or not.

7. The global Rayleigh index calculated for different O_2 levels showed positive Rayleigh index values at O_2 = 21 and 20% signifying the continuation of self-sustained instability. However, distributed combustion demonstrated a negative Rayleigh index that indicated the dampening of such instability. The observed vortex shedding in normal swirl flame was primarily influenced by such thermo-acoustic instabilities and not by the existence of PVC.

11.3. Conclusions of Chapter 6

Performance of preheated and non-preheated swirl distributed combustion using hydrogen-enriched methane fuels (in the range volume = 0-40% H_2) was studied in this chapter. High-speed imaging was performed at 2000 frames per second for both swirl and distributed combustion with H_2 enrichment of methane fuel. Conclusions of this study are given below:

1. Enhancement of chemiluminescence intensity was observed with gradual increase of %H_2 in the fuel mixture. The stand-off distance gradually reduced with hydrogen enrichment to methane fuel due to enhanced flame speed.

2. The possible thermo-acoustic coupling in swirl air-combustion at different % H_2 was observed due to common peaks of $p'$and q' signals. No such common peaks near that frequency were observed in distributed combustion with H_2 = 0-20% enrichment.

3. Higher CO_2 flowrate (18.25 LPM) was required to establish distributed combustion with 40% H_2 enriched methane fuel. The POD analysis exhibited the influence of vortex shedding on thermo-acoustic fluctuations observed from the PSD of $p'$and q' signals.

4. The lean blowoff equivalence ratio (ϕ_{LBO}) measured for different %H_2-enriched cases showed decrease of ϕ_{LBO} of distributed reaction zones with gradual %H_2 enrichment (compared to the 0% H_2 enriched case) signifying the extension of lean operational limits of distributed combustion.
5. A gradual increase of NO ppm in conventional swirl combustion with increasing %H_2 was attributed to the increase of flame temperature. The NO concentration in distributed combustion gradually decreased for both the diluents.

6. Pollutant emission with inlet air preheats in the range 373- 573K also showed reduced pollutant emission (with gradual hydrogen enrichment) at any preheat temperature, like the non-preheated case. The increase in pollutants (NO and CO) observed with gradual preheating was attributed to higher flame temperature and high-temperature dissociation of CO_2 to CO.

11.4. Conclusions of Chapter 7

This chapter was primarily dedicated for measuring the lean blowoff limits (LBO) in swirl distributed combustion at different heat release intensities of 5.72, 7.63, and 9.53 MW/m^3-atm using propane and methane fuels at three different. Distributed combustion was fostered at $\phi = 0.9$ using CO_2 dilution. The ϕ was reduced by increasing the inlet airflow for each case. The important findings of this research are:

1. Near blowoff, significant quenching of distributed reaction zone led to nearly a V-shape (at $\phi_{LBO} + 0.06$) and thin thread-like shape with further reduction of ϕ (at $\phi_{LBO} + 0.02$). The LBO ϕ increased gradually with increase in heat release intensity, which was attributed to higher flowfield instability due to enhanced inlet turbulence.

2. Analysis of chemiluminescence signals at near and far-field locations (at y = 25 mm and 135 mm) confirmed the existence of lifted reaction zones at $\phi_{LBO} + 0.06$ while a heavily quenched thin reaction zone was inferred at $\phi_{LBO} + 0.02$. These results support the observations made from chemiluminescence images near the blowoff conditions.

3. Air preheats helped to extend the blowoff event to a lower equivalence ratio than no air preheats. Such decrease in LBO ϕ was primarily due to the additional flame stability (and enhanced flame speed) gained with air preheats.

4. Above 400 K, high temperature dissociation of CO_2 becomes an important factor leading to the weakened effect of dilution on T_{ad} reduction. High-temperature decomposition of CO_2 was confirmed from the CO and CO_2 mole fractions measurements (with experiment and simulation) near blowoff at different air preheats.

11.5. Conclusions of Chapter 8

This chapter demonstrates important distinctions between the non-reactive flow field characteristics between swirl air combustion and swirl distributed combustion using high frequency (3 kHz) particle image velocimetry (PIV) measurements using an Nd: YLF laser beam generating 527 nm wavelength to capture the Mie scattering images. The results obtained showed:

1. Higher axial velocity peaks near the swirl lobes at different axial locations near the burner exit were observed for distributed flow case. Axial velocity fluctuation (rms) was of relatively higher magnitude in distributed reaction zone indicating enhanced flow turbulence.

2. Radial velocity variation as a function of axial locations showed higher average values in distributed reaction zone case as compared to swirl flow case. The RMS fluctuation component of radial velocity also exhibited much higher value in distributed reaction regime indicating the existence of a healthy turbulence in all directions.

3. The existence of a conical flow field near the burner exit was seen due to vortex breakdown forming inner and corner recirculation zones. The corner recirculation was more prominent in distributed reaction flow case. In conventional swirl flowfield, vortex propagation was mainly observed along the average streamlines and within the inner recirculation zone, whereas in distributed reaction zone, the flowfield vortex rotation was observed in corner recirculation zone and inner recirculation zones and along the streamlines.

4. A higher magnitude of Reynolds stress distribution was found in distributed reaction zone due to enhanced turbulent fluctuation velocity in both radial and axial directions compared to traditional swirl flow case. Increased Reynold stress distribution signifies the hypothesis of better mixing characteristics in distributed reaction zone case.

5. Damköhler number (Da) showed values much higher than unity in swirl flow case. In contrast, the magnitude of Da was less than unity in all locations (axial and radial) within the entire flow field in CDC. This implied a shorter flow timescale involved than the chemical timescale in distributed reaction zone case. While conventional swirl flame is categorized within the corrugated flamelets regime, distributed reaction falls under the category of thickened reactions (with Da < 1) on the Borghi diagram.

11.6. Conclusions of Chapter 9

An artificial neural network-based model was developed to predict CDC parameters using experimental data at 5.72 MW/m^3-atm thermal intensity conventional swirl flame (with undiluted air) at O_2 ~ 21% with an equivalence ratio of 0.9 by gradually diluting the inlet airflow with

CO_2. Only one hidden layer, with 10, 15, and 20 neurons, was present in this ANN. Different learning rates of model training were investigated to decide the optimized model. The key findings of this study are as follows:

1. The lowest MSE was produced with feed forward network and Levenberg–Marquardt backpropagation having Tansig transfer function and 15 neurons in the hidden layer.

2. The learning rate (LR) of 0.2 produced the least MSE (among other LR values) and gradually converged while optimizing the cost function (CF) without any further abrupt increase of CF.

3. Adaptive LR was applied while training the current dataset showed automatic adoption of best LR values by the model at each iteration (or epoch) based on the local gradient of the CF curve. Such a strategy reduced the difficulties of figuring out the best model through repeated training.

4. The current ANN is capable enough to predict the target outputs in both conventional swirl combustion and distributed combustion regimes. The optimized ANN showed strong correlation of the best-fit indicated by the 'R' values of the training, validation, and testing (0.99548, 0.95193, and 0.96391 respectively).

5. The comparison of Levenberg–Marquardt algorithm with Bayesian Regularization showed the time of convergence with Bayesian Regularization to be longer than that of using Levenberg–Marquardt algorithm. However, the MSE with Bayesian Regularization decreased significantly compared to the Levenberg–Marquardt algorithm while improving the R value.

11.7. Conclusions of Chapter 10

Swirl-assisted distributed reaction zones were classified and recognized in this chapter using deep learning-based convolutional neural network (CNN) framework. The chemiluminescence images at different dilution levels (O_2 = 21, 19, 18 and 16%.) were used for CNN model development using various model hyperparameters such as learning rate, batch size, and epoch. The model with learning rate of 0.01, batch size 16, and epoch 50 was found to be the optimized one. While learning rates below 0.01 took higher epochs to converge, learning rates greater than 0.01 produced much higher loss values. The trained model recognized new flame images at O_2 levels 20 and 17% very well. Such recognition was performed based on chemiluminescence signature, flame shape, and standoff distances of the new images introduced with respect to the training images. This study assisted in image-based autonomous control system development to foster distributed combustion in lab scale without manual intervention.

The results show good promise for fostering distributed combustion in advanced high intensity gas turbines with the help of state-of-the-art experimental diagnostics and artificial intelligence approach to support the development of high performance and near zero emissions advanced gas turbine combustors.

11.8. Recommendations for Future Work

This dissertation provided some detailed fundamental understanding of swirl distributed combustion at moderately high heat release intensity of 5.72- 9.53 MW/m^3-atm. The results reported in this work discussed different aspects of distributed combustion such as flowfield behavior, flame shape and volumetric distribution ratio, flame stability in distributed combustion,

fuel-flexible operation, and emission reduction in CDC with detailed fundamental investigations using experimental diagnostics. These results will be important observations for future research directions in distributed combustion. Additionally, the use of machine learning demonstrated the possibilities for future investigations in these directions. Based on current research, recommendations are made to inspect some interesting aspects of distributed combustion.

11.8.1. **High Heat Release Intensity CDC Operation**

To investigate CDC for practical gas turbines, it is essential to perform experiments at higher heat release intensity above 20 MW/m^3-atm. Practical gas turbines run at much higher heat release intensity and the characteristic of CDC needs to be investigated in similar conditions. Specific cases of interest would be flame dynamics, combustion kinetics, and emission behavior with experimental diagnostics (imaging, PIV, laser-induced fluorescence).

11.8.2. **Elevated Pressure and Temperature Operations**

Another important aspect of this research is to examine CDC under high pressure conditions. This is an important consideration as gas turbine combustors operate at elevated pressure conditions (at the exit of the compressor). The specific topic of interest in this domain is to understand the role of diluents (CO_2/ N_2) in high-pressure conditions. Also, combustion kinetics can significantly be affected at high pressure. Preheating is another important aspect of gas turbine combustors. Although preheating was examined in this dissertation, the role of diluent at high-pressure, preheated condition CDC is not well-known. The role of preheating on Damköhler number in CDC needs to be examined in detail to understand whether Da remains < 1 in CDC with higher preheating cases. This is an important perspective as the reaction rate and flame shape

change significantly with preheating. Hence, careful observation is needed to see how these parameters affect the Damköhler number variation.

11.8.3. **Characterization of CDC with Low-Carbon Fuels**

The current thesis investigated CDC with hydrogen-enriched methane (%H_2= 0-40%vol) to demonstrate the stability and emission characteristics of CDC. Such a study strongly motivates future researchers to investigate CDC with gradually increasing hydrogen-enrichment up to 100% H_2 for decarbonization. Another zero-carbon fuel is ammonia which can be potentially studied in CDC. The challenge of using such fuels are safety aspects (flashback), combustion instability, and poor burning characteristics and toxicity (with ammonia). Care must be taken while imaging distributed reaction zones with CH* filters using hydrogen-enriched fuels. As the CH* signal changes with more hydrogen-enrichment to fuel, normalization of signals with respect to the peak signal will be needed in each case for calibration. It should also be noted that CH* filters may not represent actual heat release from reaction zones. Hence, care must be taken while imaging CH* chemiluminescence with hydrogen-enriched fuels. Subtraction of background signal is also required for receiving better signals when CH* imaging is performed.

11.8.4. **Improved Feature-based Classifications**

The objective of the current deep learning-based flame recognition task was to develop image-based autonomous classification for advanced combustion controls. Due to the complexity and non-linearity involved in combustion systems, a single feature is not adequate to predict combustion regimes. Image-based features showed favorable recognition capability in this

research. In the future, image and acoustic signatures need to be trained simultaneously to get a better understanding of recognition and prediction models in distributed combustion.

11.8.5. **Physics-based Modeling of Reactive Flow in CDC**

With the availability of state-of-the-art computational fluid dynamics (CFD) solvers, physics-based combustion modeling became very popular. CFD-based predictions can be conducted to benchmark with the available experimental data in CDC. The CFD modeling can be very useful in high-pressure conditions to get predictions of flowfields and reaction kinetics. Such data will be very useful to design high-pressure CDC combustors for actual testing. Additionally, the data obtained from CFD can also be used for predictive modeling using machine learning architectures. This is important because a purely data-driven model may not be able to explain the physical conditions in combustion systems. A physics-informed machine learning model can be very helpful in this context.

Appendix A: List of Papers

A.1. Published Journal Papers

1. R. Roy, A.K. Gupta, "Flame structure and emission signature in distributed combustion,", Fuel vol. 262, p. 116460, 2020.

2. R. Roy, A.K. Gupta, "Experimental investigation of flame fluctuation mitigation in distributed combustion,", *Experiments in Fluids,* vol. 62, p.62, 2021.

3. R. Roy, A.K. Gupta, "Lean blowoff limits in Distributed Combustion", *Journal of Energy Resources Technology*, vol. 144, Issue# 8, p. 0852301, 2022.

4. R. Roy, A.K. Gupta, "Data-driven prediction of flame temperature and pollutant emission in distributed combustion", *Applied Energy,* vol. 310, p. 118502, 2022

5. R. Roy, A.K. Gupta, "Recognition of Distributed Combustion Regime from Deep Learning," *Journal of Energy Resources Technology*# JERT-21-2021, 2022.

6. B. Yang, B., L. Hu, W. Ping, R. Roy, A.K. Gupta, "Boron-Nitride Nanosheet Based Thermal Barrier Coating for Micro-combustor Performance Improvement", *Journal of Energy Resources Technology,* vol. 144, Issue# 6, p. 062106, 2022.

A.2. Journal Papers Under Review/ Submitted

1. R. Roy, R. Roy, K. Nguyen, A.K. Gupta, "Performance Enhancement of Swirl-assisted Distributed Combustion with Hydrogen-enriched Methane," Under Review, Applied Energy.

2. R. Roy, K. Nguyen, A.K. Gupta, "Non-reactive Flow field Investigation in Conventional and Distributed Swirl Combustion Configuration," (To be submitted)

A.3. Peer Reviewed Conference Publications

1. R. Roy, K. Nguyen, T. Stuart, A.K. Gupta, "Performance of Swirl-Stabilized Distributed Combustion with Hydrogen Enriched Methane: Stability, Blowoff Limits, and Emissions," *ASME Turbo Expo Conference,* paper# GT2022-82062, June 13-17, Rotterdam, The Netherlands, 2022.

2. R. Roy, A.K. Gupta, "Effect of Hydrogen-enrichment to Methane in Swirl-assisted Distributed Combustion at Different Thermal Intensity," *Clearwater Clean Energy Conference*, paper# 71, August 1-4, Florida, 2022. (**Best Graduate Student Paper Award**)

3. R. Roy, A.K. Gupta, “Characteristics of Swirl-Stabilized Distributed Combustion with Hydrogen Enriched Methane,” *ASME Power Conference,* paper# POWER2022-85402, July 18-19, Pittsburg, 2022.

4. R. Roy, A.K. Gupta, “Detection of Distributed Combustion using Deep Learning Architecture,” *AIAA SciTech Forum*, Paper AIAA-2022-2062, 3-7 Jan, San Diego, 2022.

5. R. Roy, E. Melia, A.K. Gupta, “Investigation of Bluff-body Stabilized Methane, Propane and Ammonia Flames with Flowfield Dilution,” *AIAA SciTech Meeting*, Paper ID# 3772907, January 23-27, National Harbor, MD, 2023 (Accepted)

6. R. Roy, A.K. Gupta, “Feature-Based (Audio) Recognition of Swirl Combustion Regimes Using Convolutional Neural Network,” *ASME Turbo Expo Conference*, paper# GT2023-103231

Appendix B: Flame Image Processing and Noise Reduction

Extraction of flame boundary from OH* chemiluminescence image

The flame boundary was calculated from the binarized OH* chemiluminescence image set, generated by using the Otsu thresholding algorithm similar to Sweeney and Hochgreb [145]. The Otsu method is basically an adaptive thresholding technique where the threshold value is decided automatically from the gray-level image histogram analysis. The threshold value is optimized using discriminant criterion to maximize the separability of the background and foreground pixels [146]. Roy [147] demonstrated a user-defined threshold-based flame boundary detection technique for V-shaped turbulent premixed flames. The resultant OH* chemiluminescence image was filtered with a nonlinear anisotropic diffusion filter [148] modified by the diffusivity model proposed by Perona and Malik [149] for image noise smoothing and edge enhancement. Such image filtering is displayed in Fig. B.1 from sample OH* chemiluminescence image of swirling propane flame at two different conditions (O_2 ~ 21% and 15%). This helps to perceive the noise level and its subsequent reduction (from filtering) under normal air combustion and diluted flow conditions when approaching CDC. Figure B.1a shows the raw and nonlinear filtered OH* chemiluminescence signal of propane-air flame (O_2 ~ 21%) in color map representation (showing an array of red, green and blue intensities). Figure B.1b shows similar images of propane flame at O_2 ~ 15% in N_2 diluted flow field. The overall quality of the image improved significantly with diffusion filtering. The flame boundary became more defined with the edge smoothing (see zoomed window in Fig. B.1a). The effectiveness of such noise-filtering technique was further assessed in the context of distributed combustion by measuring the change in image noise levels at different O_2 concentrations using the approach of Liu et al. [150]. The corresponding signal to noise ratio (SNR) was also evaluated at different O_2 levels. Figure B.2 represents the noise levels

and SNR for the raw and nonlinear filtered chemiluminescence signals at different dilution levels towards distributed combustion. The mean noise level in the raw signal reduced from 39.67 a.u. to 19.35 a.u. using this filter (see Fig. B.2 a).

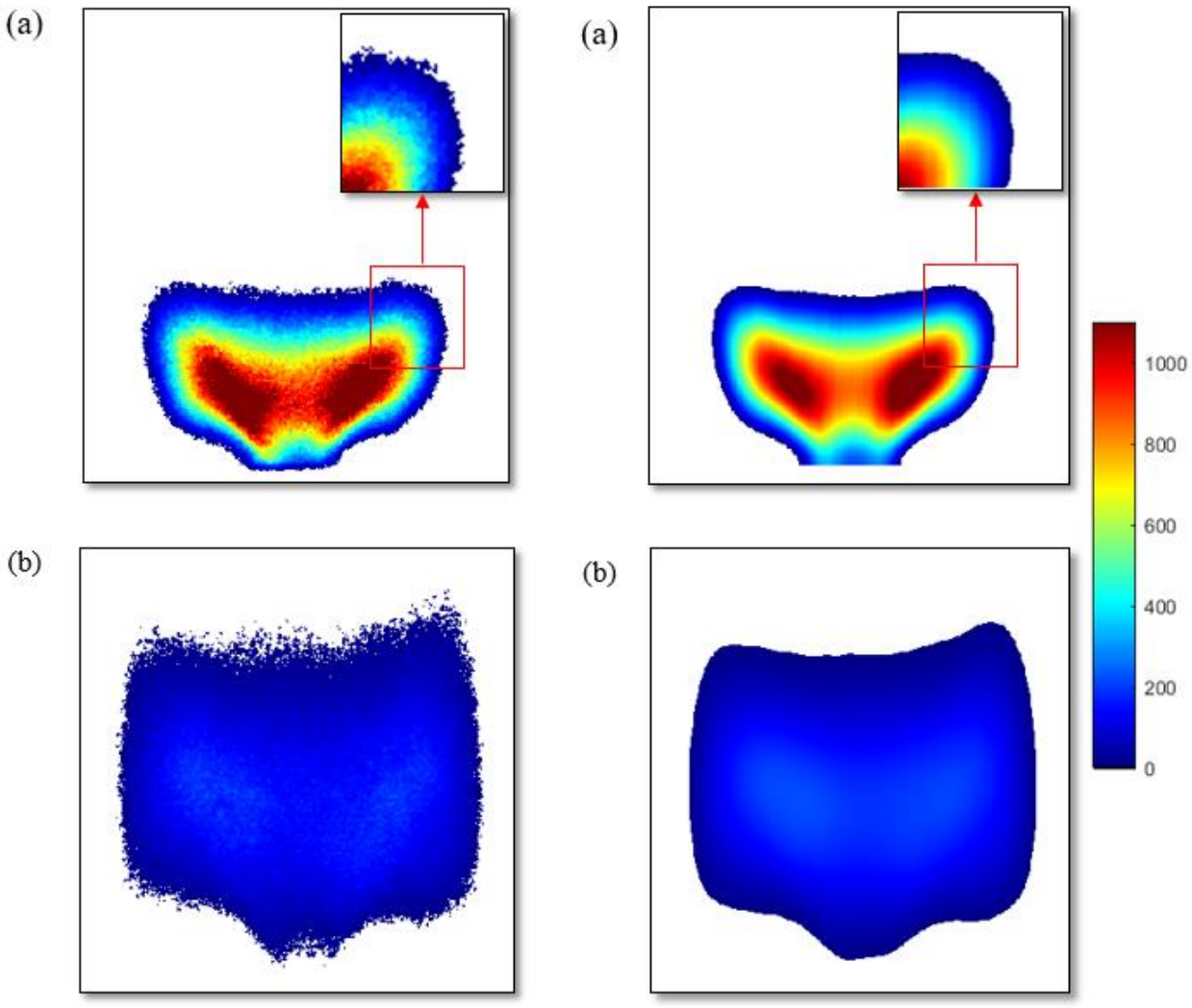

Fig. B.1. (a) Unfiltered, raw OH* chemiluminescence signal (left) and nonlinear diffusion filtered signal (right) of propane flame (at ϕ = 0.9) in air combustion (O_2 ~ 21%). (b) Unfiltered raw OH* chemiluminescence signal (left) and nonlinear diffusion filtered signal (right) of propane flame (at O_2 ~ 15%) using N_2 as the flow diluent (at ϕ = 0.9).

A remarkable increase of SNR for every O_2 concentration using nonlinear filtering can be observed (see Fig. B.2 b). The image noise filtering technique is therefore effective for flame visualization in this particular study since the OH* signal level continued to reduce with decrease in O_2 concentration. The observed trend of decrease in SNR is attributed to gradual reduction of chemiluminescence signals at lower O_2 concentrations.

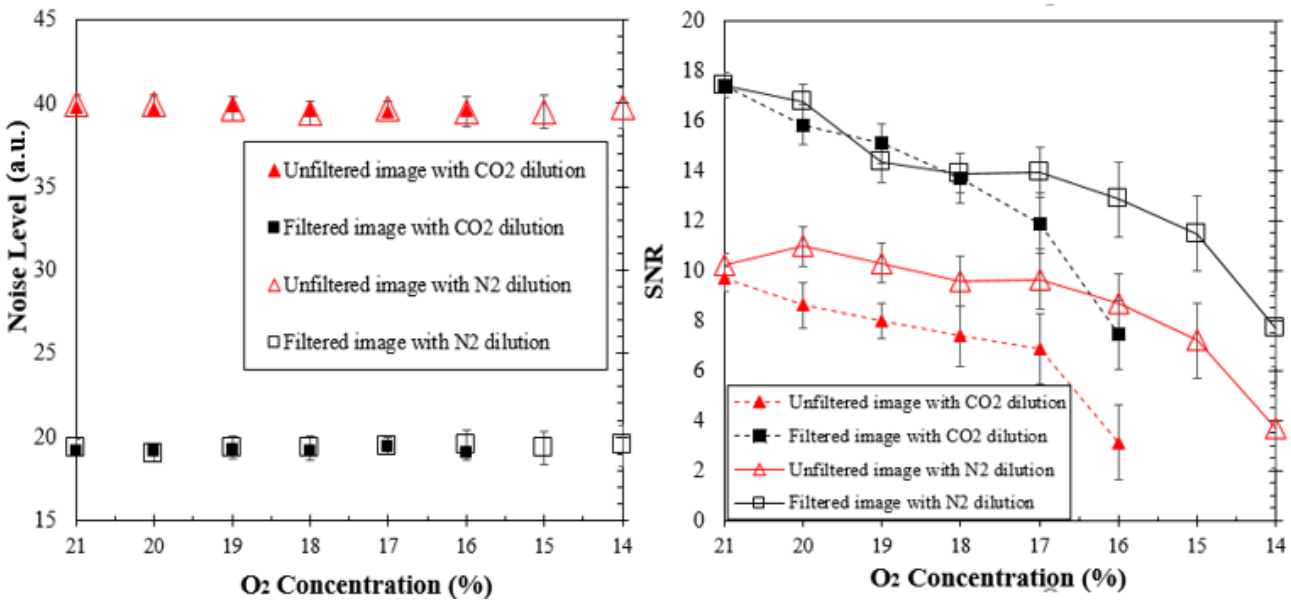

Fig. B.2. (a) Noise levels and (b) SNR at different O_2 concentrations of propane flame using CO_2 and N_2 as the inlet flow diluents.

The nonlinear diffusion filtering coupled with Perona and Malik diffusivity model provided effective edge enhancement and image noise reduction for better flame visualization while preserving essential flame features and edges of the actual image. Hence, the results calculated do not influence the derived flame boundary. For the OH* boundary detection, the filtered image at each O_2 concentration was converted into a binary map of background (unburned region) and

foreground (burnt region) pixels by calculating corresponding 'Otsu' threshold values. The final flame boundary was traced by tracking the intensity jump (from 0 to 1) across the entire span of the binarized image using Matlab© software. The boundary detection process was performed in a specific region near the edge of propane-air flame (at O_2 ~ 21%) to help assist in histogram analysis for the image pixel counts. The calculated value of the Otsu threshold was verified by locating it on the histogram distribution. The spatial resolution of imaging was measured as 5 pixels/mm. This technique was also verified on the other side of the flame, which showed good compatibility with the former side. The calculated Otsu threshold (represented by the vertical solid line) lies within the first two modes (of the intensity distribution) of the histogram representing the background and flame (OH*) signals, respectively. A reasonable flame boundary can be identified when the threshold value was visually compared in the zoomed flame front (middle image of Fig. B.3 a). Figure B.3 b and B.3 c represent the calculated flame boundary (magenta outlined) overlaid on the gray scale (normalized between black = 0 and white = 1) and color map appearance for the propane-air flame. A well-defined boundary that precisely matched with the observed contour of OH* emission in both the cases signifies the effectiveness of this technique to examine swirl stabilized flames. The sensitivity analysis of the flame edge location with respect to the image binarization threshold showed an approximate flame area change of 4% for every 10% offset of binarization threshold from the calculated Otsu threshold value. We used this approach to extract the flame boundary at different O_2 concentrations. Some apparent discontinuity of the flame boundary near to uppermost part of the flame is attributed to the presence of nearly flat flame at that region, for which the computational code was unable to find the above-stated intensity jump (0-1) that contributed to discontinuity in that region.

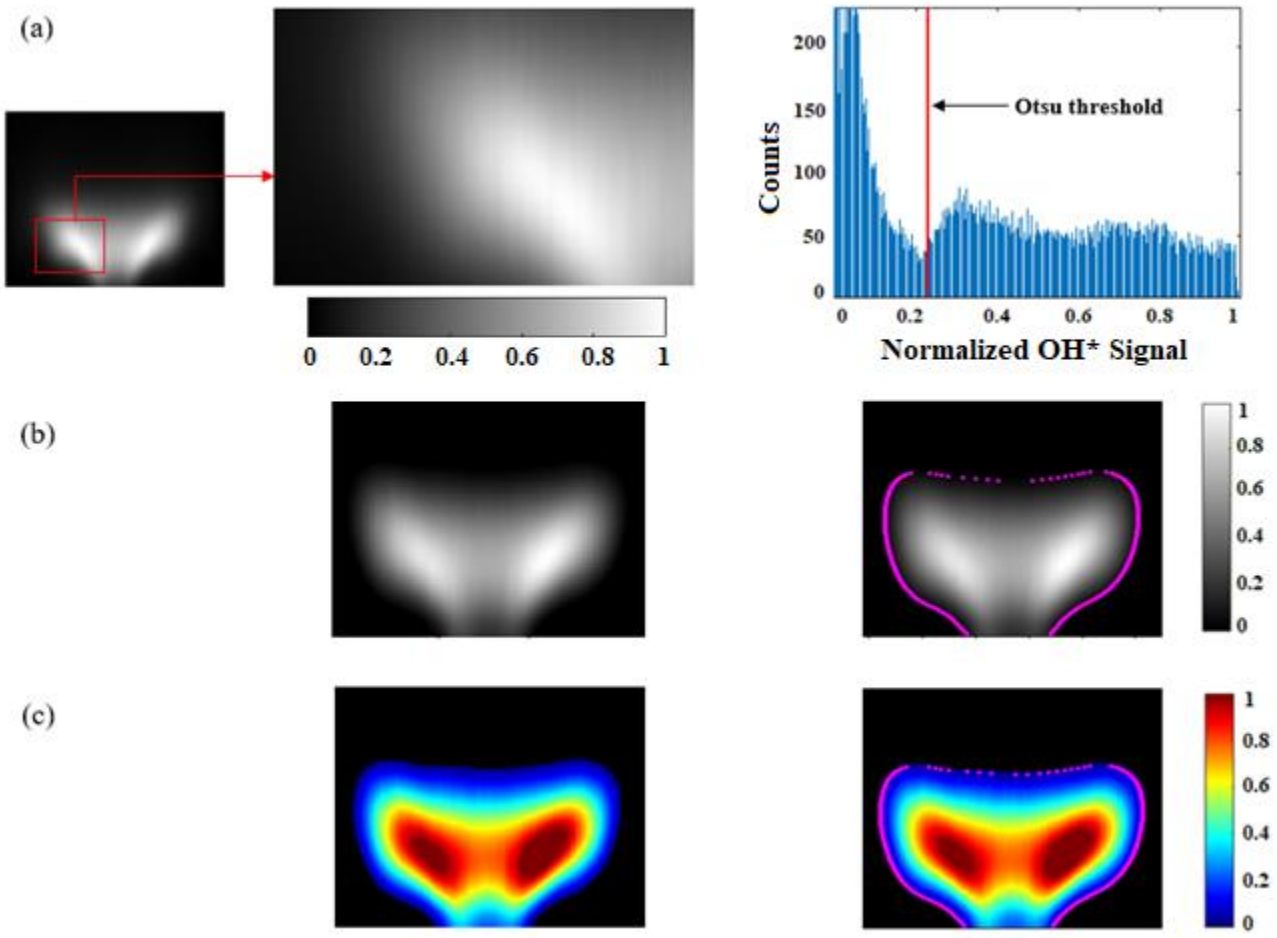

Fig. B.3. (a) Otsu threshold (—) overlaid on the histogram of filtered propane-air flame (ϕ = 0.9, O_2 ~ 21%) image. (b) Flame boundary (∿) overlaid on normalized (black = 0, white = 1) and (c) jet color map signal of OH* chemiluminescence of the similar propane-air flame.

Appendix C: Chemical Simulations for Flame Speed and Flame Temperature.

C.1. Computation of laminar flame speed

Flame speed in swirl sir combustion and with dilution was computed using 1D chemical simulations. Additionally, the variations of flame speed and adiabatic flame temperature (AFT) at different %H_2- enrichment was computed with Chemkin-Pro© simulation coupled with GRI-mech 3.0 reaction mechanism considering 53 species and 325 chemical reactions for computations. The results are shown in Figs. C.1 and C.2.

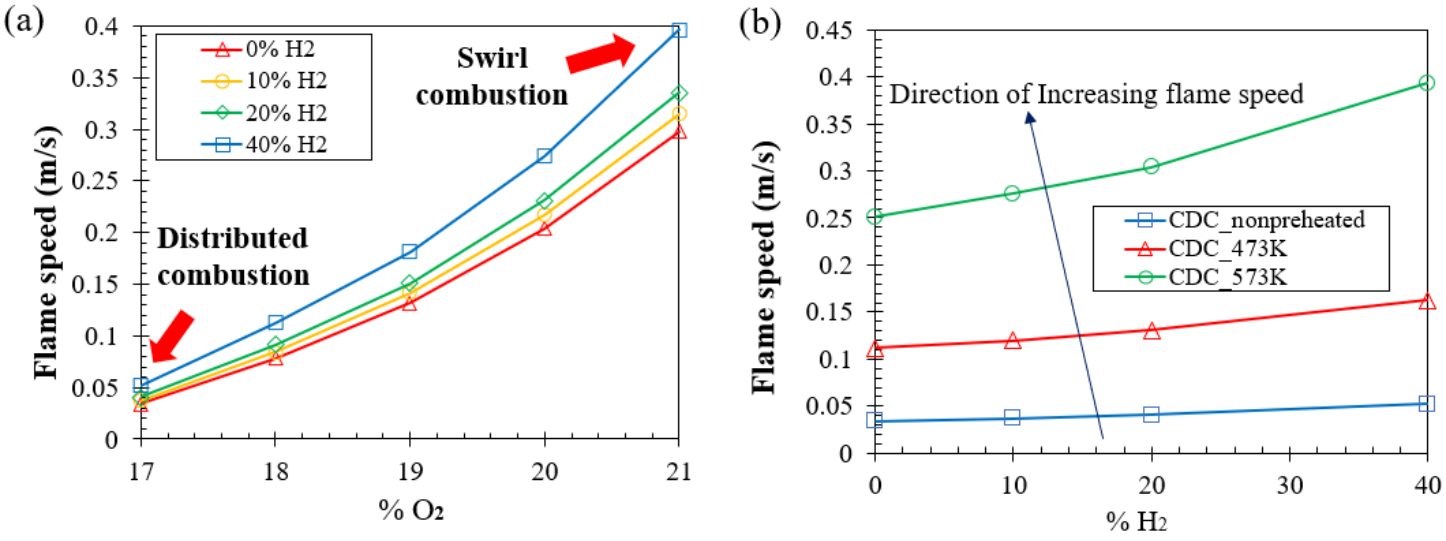

Fig. C.1. Laminar flame speed variation at (a) different O_2 concentrations (with CO_2 dilution) and (b) different air preheat temperature in distributed combustion with various H_2-enrichment to methane fuel.

Gradual reduction in flame speed can be observed with CO_2 dilution leading to reduction in $\%O_2$. Distributed combustion showed a low reaction rate compared to swirl air combustion. Figure C.1 shows an increase in flame speed with gradual increase in hydrogen enrichment ($\%H_2$=0 -40%) that is due to the enhanced flame temperature (at higher $\%H_2$) leading to reduced density. Hence, the flame speed increases in order to maintain continuity equation. When preheating is applied (up to 573 K), the flame speed increased gradually as seen from Fig. C.1 b. Preheating enhances the flame speed and mitigates the lift-off. Additionally, preheating helps to increase thermal efficiency which is important for gas turbines.

C.2. Computation of flame temperature with air preheats

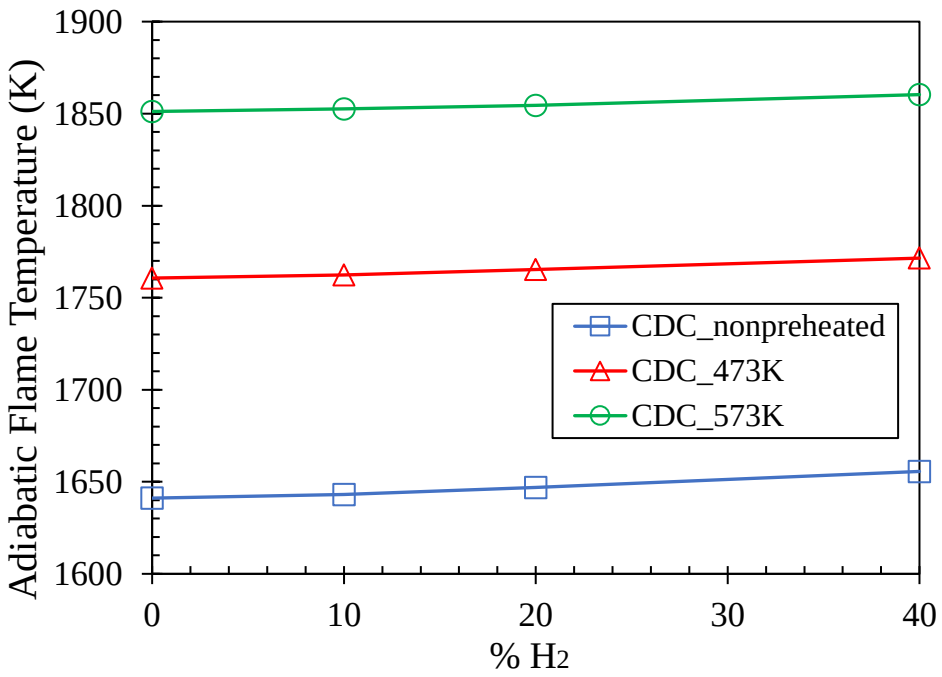

Fig. C.2. Adiabatic Flame Temperature variation at different air preheat temperature in distributed combustion.

C.3. Calculation of water vapor content in the combustion exhaust

The variation in vapor formation in the combustion exhaust (normalized with respect to the maximum) at different %H_2-enrichment was also calculated for the study of performance of distributed combustion with hydrogen-enriched methane. This was an important consideration when the hydrogen content of fuel gradually increases. Chemkin-Pro© simulation coupled with GRI-mech 3.0 reaction mechanism.

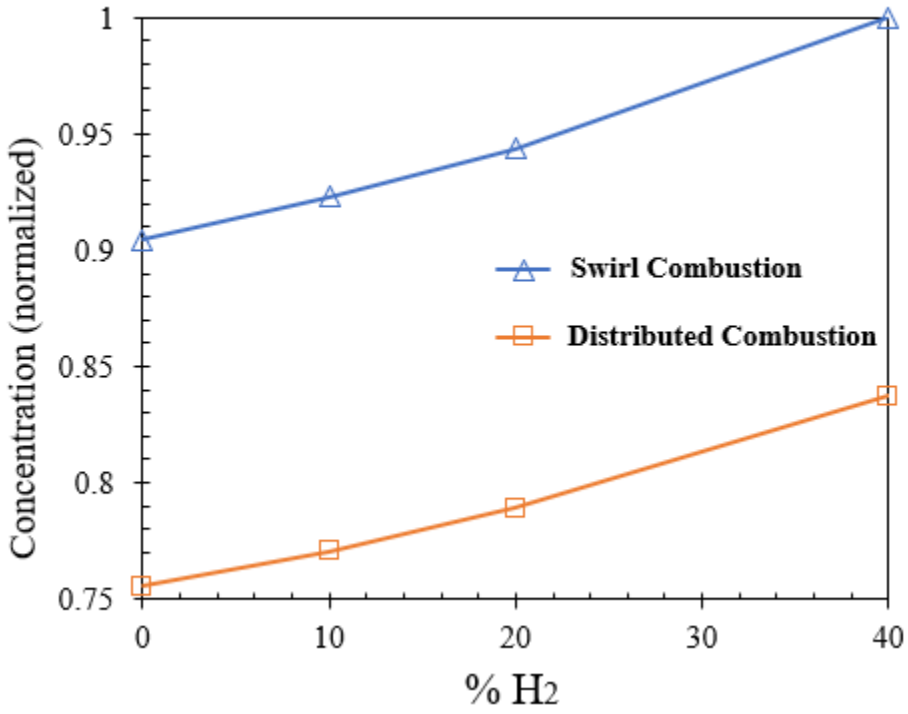

Fig. C.3. Variation of water vapor content at different air preheat temperature in distributed combustion with varying H_2-enrichment to methane fuel.

C.4. Sensitivity analysis of NO formation pathways with H2-enriched methane

This sensitivity analysis was performed using the results derived with Chemkin-Pro© simulation coupled with GRI-mech 3.0 reaction mechanism mentioned before. Figure A.4 shows the coefficient of reaction sensitivity at different hydrogen-enrichment levels in distributed combustion.

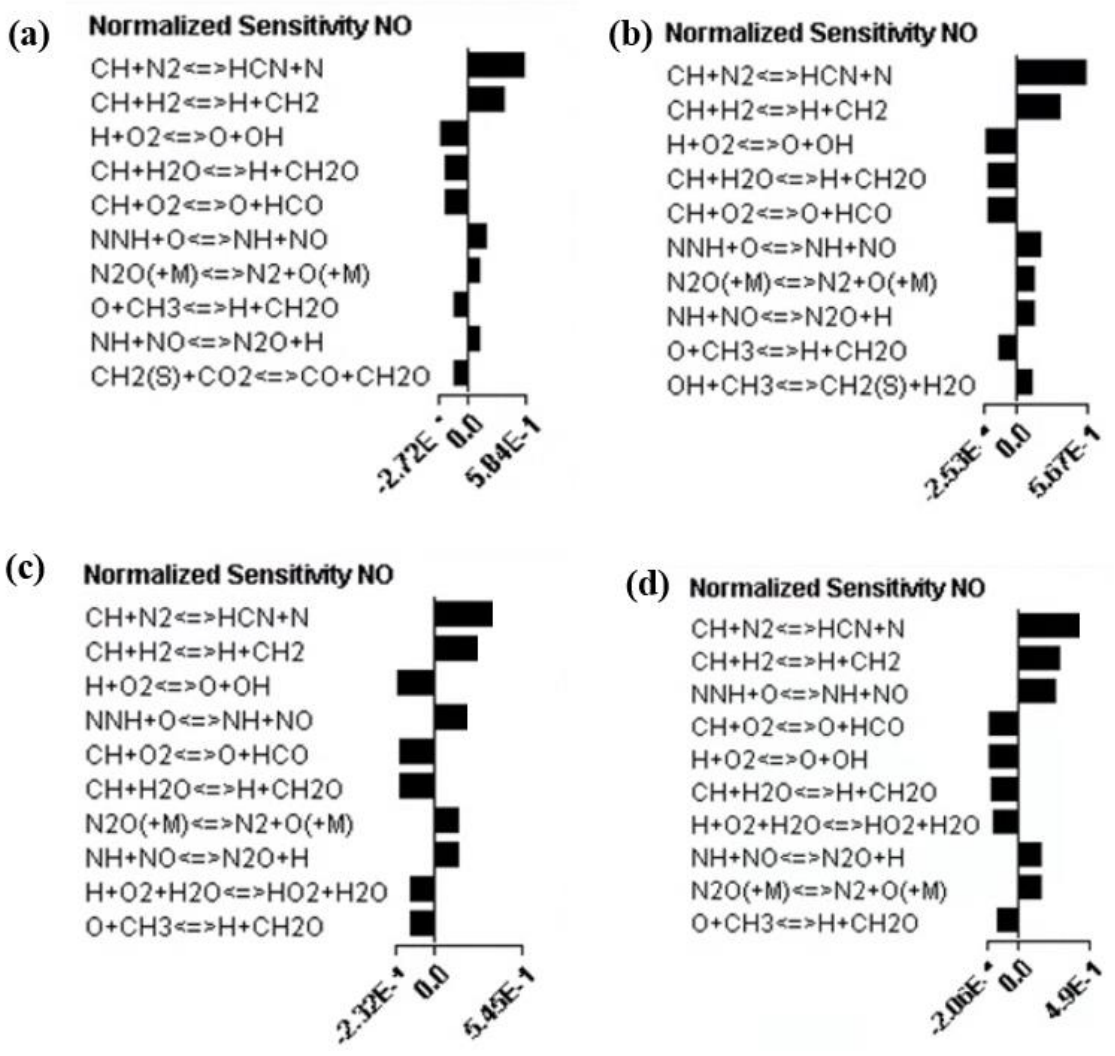

Fig. C.4. Coefficient of reaction sensitivity in distributed combustion with (a) 0%, (b) 10%, (c) 20%, and (d) 40% H_2-enriched methane.

Appendix D: Combustor Cross-section & Experimental Conditions.

The cross-sectional view of the swirl combustor used in this research is presented below. This cross-sectional view is obtained from the 3D model given in chapter 3. The combustion reaction occurs within the combustor volume enclosed by the quartz confinement and located near the burner exit nozzle. While the hub of the burner is manufactured with steel the top cover of the quartz tube is built from aluminum.

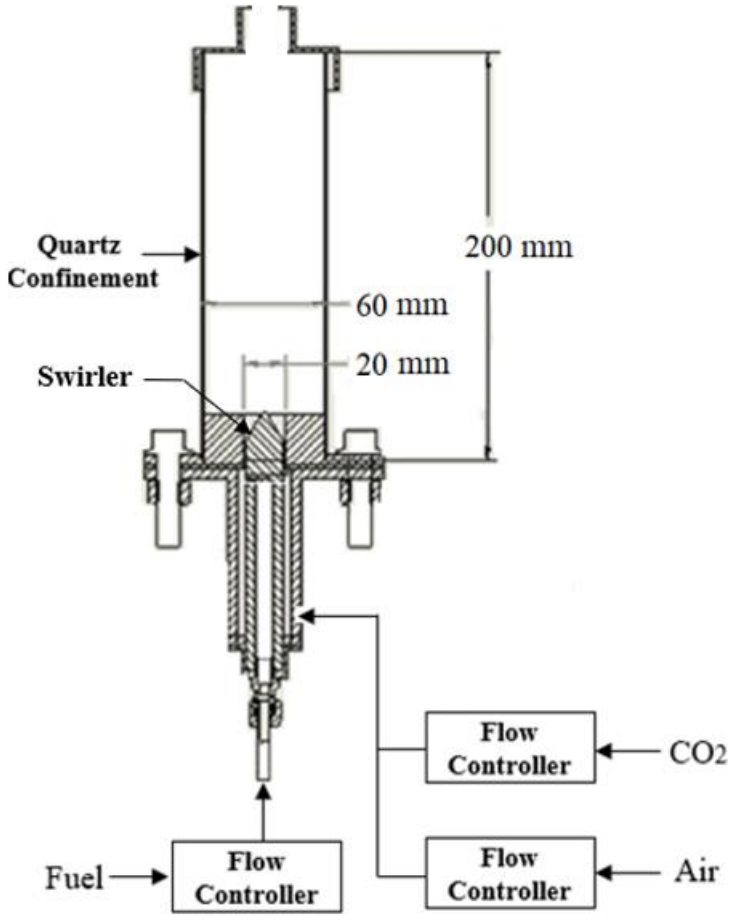

Fig. D. Cross-sectional view of the swirl combustor used in this research.

Table D.1. Experimental conditions used in chapter 5

Air [L/min]	CH_4 [L/min]	CO_2 [L/min]	Global oxygen concentrations (%)
52.20	4.93	0	21
		2.61	20
		5.49	19
		8.70	18
		12.28	17
		16.31	16

Table D.2. Experimental conditions used in chapter 6

%Hydrogen	Air Flowrate (LPM)	Methane Flowrate (LPM)	H_2 Flowrate (LPM)	CO2 Flowrate (LPM)	N_2 Flowrate (LPM)	Combustion mode
0%	57.948	5.48	0	0	0	Swirl
	57.948	5.48	0	14.55	13.63	Distributed
10%	57.48	5.29	0.59	0	0	Swirl
	57.48	5.29	0.59	14.55	13.53	Distributed
20%	57.09	5.08	1.27	0	0	Swirl
	57.09	5.08	1.27	14.55	13.43	Distributed
40%	56.18	4.55	3.04	0	0	Swirl
	56.18	4.55	3.04	14.55, 18.25	13.22	Distributed

Table D.3. Experimental conditions used in chapter 10

Air [L/min]	CH4 [L/min]	Diluent CO2 [L/min]	Global oxygen concentrations (%)
52.20	4.93	0	21
		2.61	20
		5.49	19
		8.70	18
		12.28	17
		16.31	16

Appendix E: POD Analysis for The Analysis of Distributed Combustion with Hydrogen-Enriched Methane At 7.63 MW/M3-Atm Heat Release Intensity.

The POD analysis was explained in chapter 5 and 6 that was used for obtaining the dynamic coherent structures in reactive flow fields in air combustion and distributed combustion at 5.72 MW/m^3-atm heat release intensity. The first four POD modes with 10% H_2-enriched methane is examined here at 7.63 MW/m^3-atm heat release intensity in order to understand the effect of hydrogen fuel on reaction zones shown in Fig. E.1. The first four modes contained significant energy of fluctuations (~ 5- 30%) and are presented according to decreasing energy levels. Hence, mode 1 possessed the highest fluctuation energy. Vortex shedding patterns were observed in the conventional swirl combustion at different thermal intensities (Fig. E.1 a and c). Shear layer vortex shedding near the burner exit was observed in conventional swirl air combustion regimes at 5.72 and 7.63 MW/m^3-atm thermal intensity. When the POD structure in mode 1 is compared between the reaction zone at different thermal intensity, wider reaction zones with thick shear layers were observed for the 7.63 MW/m^3-atm thermal intensity compared to the 5.72 MW/m^3-atm thermal intensity reaction zone. The structural appearance in mode 2 can be assumed to be the combination of shear layer vortex and ring vortex periodically shed from the burner exit (blue and yellow horizontal patches). Such vortex shedding was partly present in mode 3 also. Mode 4 in swirl air flame had structural appearance different from the other three modes. This pattern represents a rotational whirl structure (as observed on both sides) signifying the swirling nature of these flames. Hence, the swirl air flame showed a combination of vortex shedding and rotational patterns in the reaction zone. When the POD modes in distributed combustion are observed, there was no

observation of any prominent vortex shedding. This indicates reduced flame fluctuation in distributed combustion compared the swirl combustion. Further investigation was carried out to obtain the power spectral density (PSD) of these POD modes that can reveal the influence of vortex shedding and rotational structures in flame fluctuation behavior. Figure E.2 shows the PSD plots of POD modes for both swirl and distributed combustion with 10% H_2-enriched methane. The results show that 162 Hz frequency peak observed from the PSD of the POD modes in conventional swirl combustion is the source of flame fluctuations. In contrast, no significant peak was observed in distributed combustion resulting in reduced flame fluctuations. This observation was consistent for the other hydrogen-enrichment cases up to 40% hydrogen-enriched methane. Further, the POD modes were obtained for the distributed combustion case with 40% hydrogen-enriched methane and CO_2 dilution at 5.72 MW/m^3-atm thermal intensity. Figure E.3 exhibits the first 4 modes of both swirl and distributed combustion with 40% hydrogen-enriched methane and CO_2 dilution.

In this case, the swirl combustion also showed a high influence of vortex shedding. While the propagation of vortices along the reactive shear layers was observed in modes 1 and 2, modes 3 and 4 showed ring vortex at downstream locations.

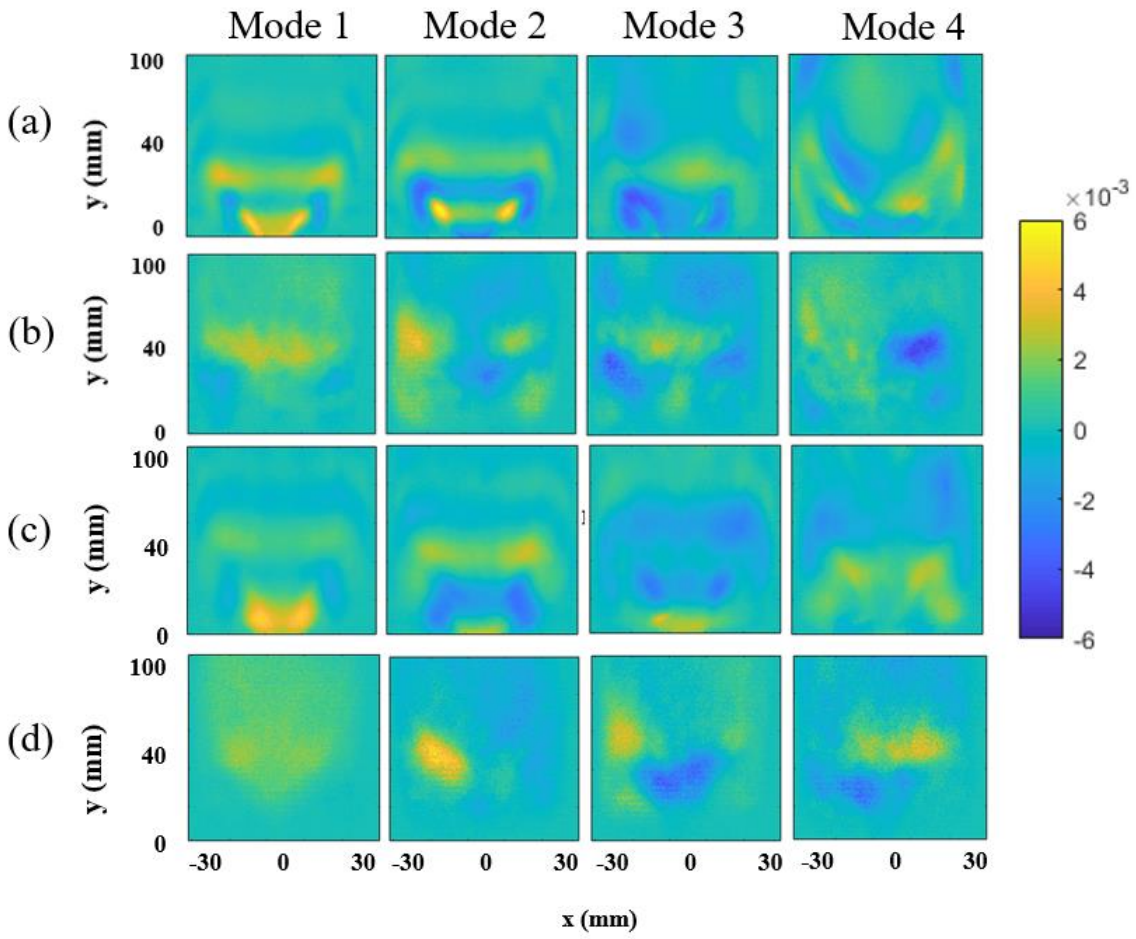

Fig. E.1. First four pod modes of the (a) conventional swirl combustion at 5.72 MW/m^3-atm (b) distributed combustion at 7.63 MW/m3-atm, (c) conventional swirl combustion at 7.63 MW/m3-atm and (d) distributed combustion at 7.63 MW/m3-atm with 10% H_2-enriched methane and CO_2 dilution.

For the present distributed combustion case, appearance of prominent structures was again observed. Such vortex shedding can be clearly observed in modes 3 and 4 of distributed combustion (small dark blue and yellow patches highlighted). The existence of structures may be attributed to the reappearance of vortex shedding resulting in fluctuating reaction zone in the examined case. This analysis was extended with the POD results obtained from the

chemiluminescence data obtained with the 7.63 MW/m^3-atm thermal intensity flames. Figure E.4 shows the POD images for the first 4 modes of the flame at 7.63 MW/m^3-atm thermal intensity (both swirl and CDC). This flame also showed the vortex shedding patterns for the first 2 modes in swirl combustion while the mode 3 and 4 showed more rotational patterns. Note that the distributed combustion showed relatively higher fluctuation structures for this case relative to the 10% H2-enriched methane fueled cases. In general, the fluctuation pattern at higher thermal intensity is more prominent than that of the lower thermal intensity cases. Further analysis was drawn up based on the PSD computations for this case as shown in Fig. E.5. The PSD plot showed an amplitude peak at 179 Hz in conventional swirl combustion while a small peak at 151 Hz was observed in distributed combustion. This observation is consistent with the results obtained for the lower thermal intensity case indicating reappearance of vortex-like structures in distributed combustion at higher hydrogen-enrichment.

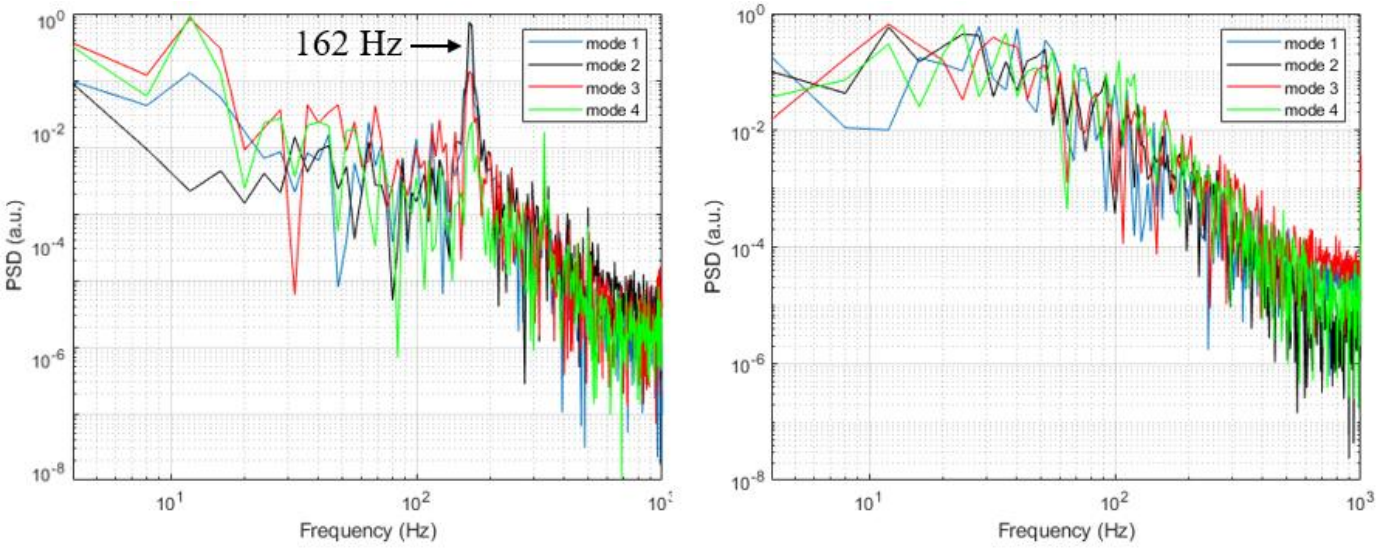

Fig. E.2. Power spectral density of the first four POD modes of the (a) conventional swirl combustion (top row) and (b) distributed combustion (bottom row) with 10% H_2-enriched methane at 5.72 MW/m3-atm thermal intensity.

Hence, the fuel property effect can play some role in fostering distributed combustion when hydrogen is used as the fuel at higher %vol in the blend. In our past study, we attributed this to the formation of higher water-vapor in the combustion exhaust that increases the specific heat of the combustion exhaust resulting in higher enthalpy content (of the product gases) resulting in localized thermal field fluctuations. Hence, more dilution was needed to mitigate such fluctuations.

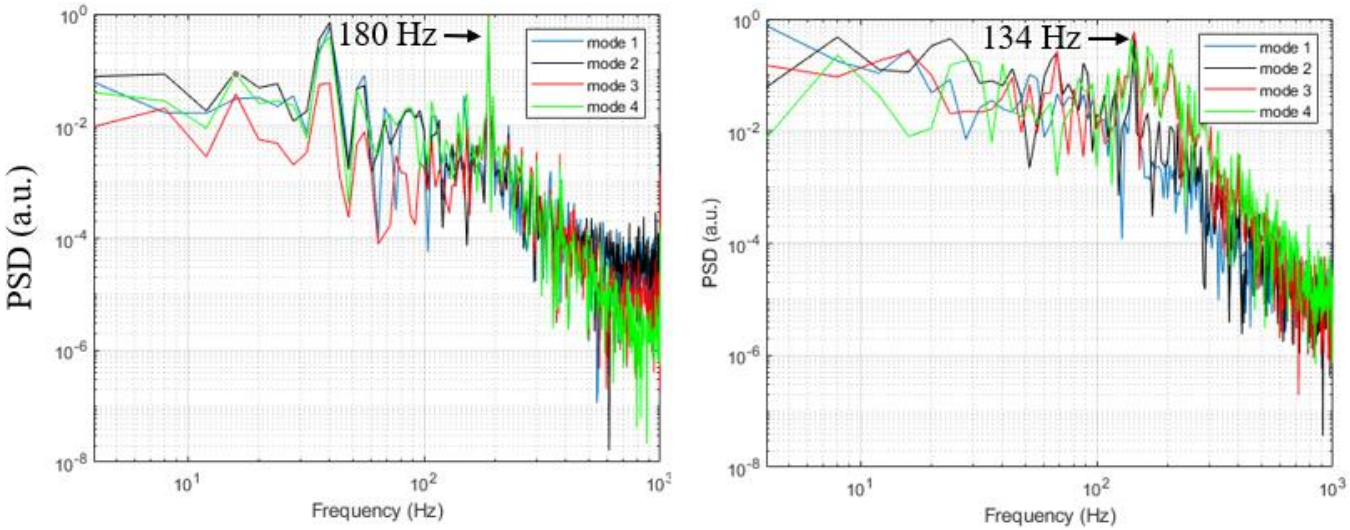

Fig. E.3. PSD of POD modes of the conventional swirl combustion (left) and distributed combustion (right) with 40% H_2-enriched methane at 5.72 MW/m^3-atm thermal intensity.

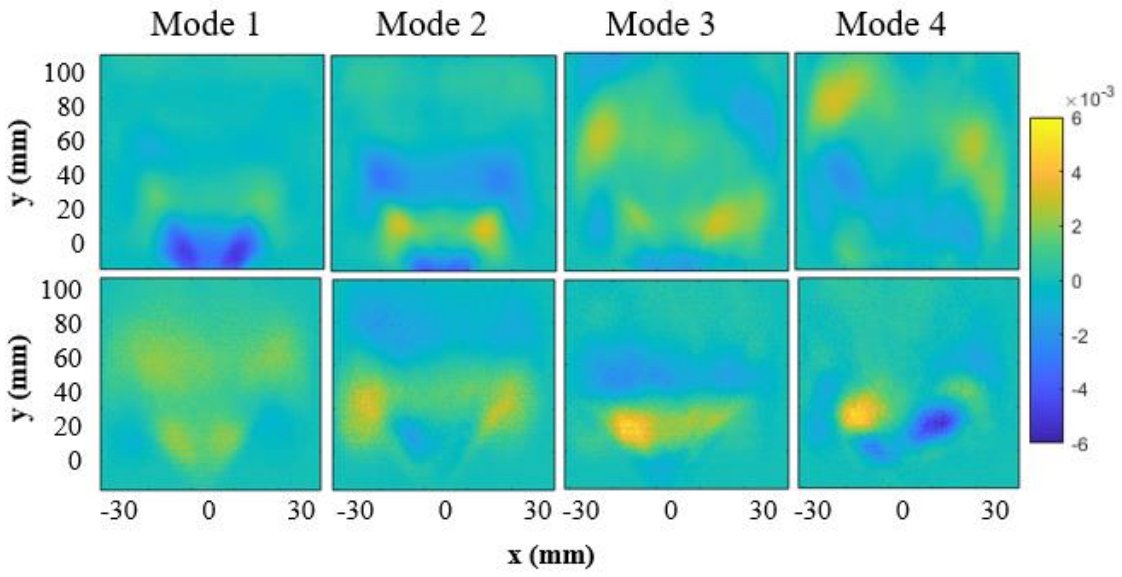

Fig. E.4. First four pod modes of the (a) conventional swirl combustion and (b) distributed combustion at 7.63 MW/m^3-atm thermal intensity with 40% H_2-enriched methane.

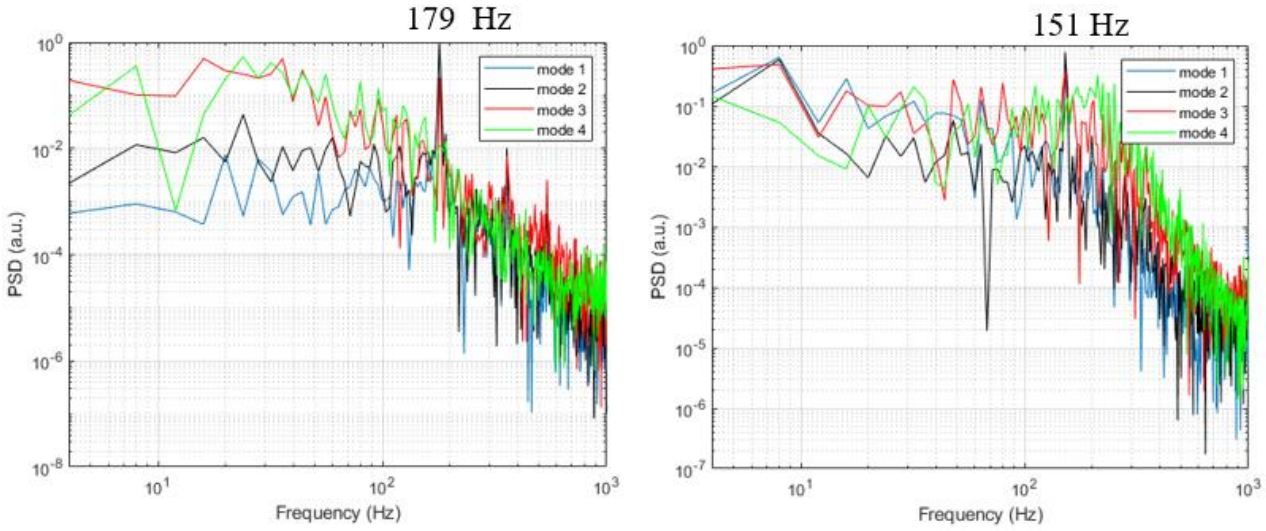

Fig. E.5. PSD of POD modes of the conventional swirl combustion (left) and distributed combustion (right) with 40% H_2-enriched methane at 7.63 MW/m^3-atm thermal intensity.

Appendix F: Image and Audio-based Recognition of Distributed Combustion.

This work is an extension of the image-based prediction explained in chapter 10. Model development was performed using an interactive cloud notebook called Google Colab with Python 3 language. This allows accessing online GPUs assigned by Colab. Open-source software libraries called 'Tensorflow' and 'Keras' were used for developing the convolution neural network.

F.1. Raw data collection

While the image data was gathered using high-speed imaging of chemiluminescence images (without spectral filtering) similar to the method explained in chapter 10, the acoustic signatures at different $\%O_2$ levels were gathered using the microphones. Preprocessing of data is crucial that includes obtaining good data to be used in the deep learning model. Data preparation is important to increase the accuracy and the efficiency of the latter.

F.1.1. Images data preparation

For image preprocessing Image Data-Generator from Keras' library was used. This involves generating batches of tensor image data with real-time data augmentation. Through this operation images were resized to a desired shape before being normalized. An image is a 3D tensor for which dimensions are $(\text{width} \cdot \text{height} \cdot \text{dimension of RGB})$. Every value in this tensor is a positive integer between 0 and 255 corresponding to a color tone.

F.1.2. Audio data preparation

For the audio data, the corresponding MEL-Spectrogram was generated from each raw audio spreadsheet. By doing this, a raw audio file can be changed into an image which can then be easily used for in the CNN followed by reshaping and normalization of spectrograms. The spectrogram size matches the image size used in this model. This later allows identical operations to be made on both image and spectrograms.

F.1.3. Convolution neural network (CNN) development

It has previously been explained in chapter 10 that CNNs are composed of convolution and pooling layers and choice of hyperparameter is dependent on the requirement of the model (accuracy, time of convergence). Figure

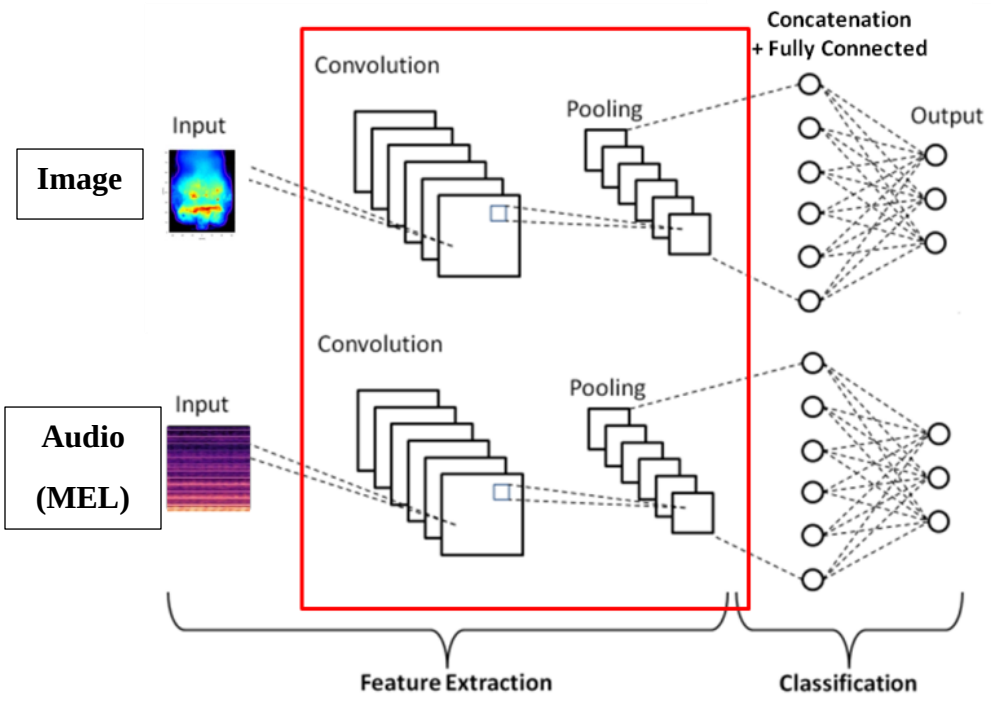

Fig. F.1. Schematic diagram for the CNN architecture with image and audio data.

The current model consists of 3 blocks of convolution and max-pooling layers with 8 filters for each convolution. These layers precede a concatenation layer that overlaps the information coming from both the image side and the audio side (MEL). A Flatten Layer reducing the dimensions of the network is present. Dense Layers with decreasing number of neurons finish the classification. Every Convolution and Dense Layer had ReLu activation functions except the very last Dense Layer which had a Softmax activation function for probabilistic classification of data. MaxPooling2D, Concatenation and Flatten Layers do not require any activation function.

$$\text{ReLU} = \begin{cases} \max(0, x), & for\ x \geq 0 \\ 0, & for\ x < 0 \end{cases} \tag{F.1}$$

$$\text{Softmax } (y_i) = \frac{e^{y_i}}{\sum e^{y_i}} \tag{F.2}$$

F.1.4. Data preprocessing

The data must be split into 'Training', 'Validation' and 'Testing' according to desired percentages in order to train and evaluate the model's performance. Different %O2 classes were used for training such as O2= 16, 18, 19, 21% with 500 data (image + audio) per class. The final image size was 224x224 pixels with batch size = 16, number of epochs = 50. 85% of total data was used for training and 15% used for testing. The learning rate = 0.01 was used with other parameters similar to that mentioned in chapter 10.

F.2. Prediction on training data

In a first attempt to test how well the deep learning model performs, predictions were conducted on the dataset used during training. The classification was performed on the training data, first. The results are shown on Fig. F.2. Here, the class 0 corresponds to 16% O_2, class 1 corresponds to 18% O_2, class 2 corresponds to 19% O_2 and the class 3 corresponds to 21% O_2.

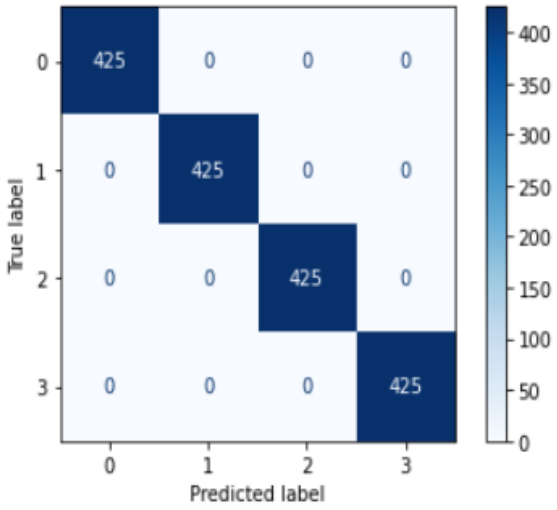

Fig. F.2. Confusion Matrix for the Training Dataset.

A perfectly diagonal confusion matrix was observed which means every data has been correctly classified by the CNN model. This was desired as similar data was used for the training purpose. Additionally, the 21% O_2 case (image + spectrogram) was run through the network. Note the image and the spectrogram used in this case was not included in the training process. The motivation was to check how well CNN predicted this case. The output for a small sample (two of them) was displayed on Fig F.3. The left figure (of Fig. F.3) shows the flame chemiluminescence and the right one exhibits MEL spectrogram.

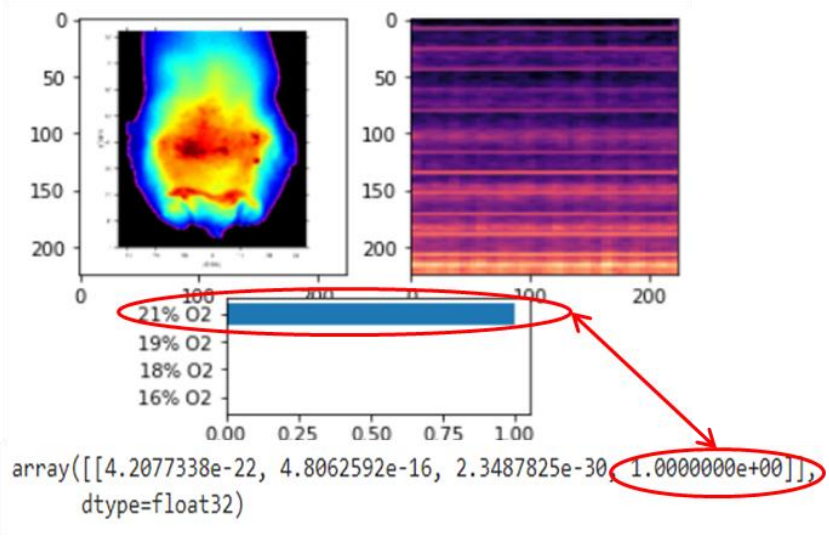

Fig. F.3. Prediction of 21%O_2 data not included in training.

The results showed very good agreement with the actual case. The bar plot at the bottom of figure shows probability of prediction of the image. As observed, the model predicts the considered case as 21% O_2 case with very high confidence.

F.3. Prediction of Untrained Classes

New untrained image classes were introduced to the model to verify the capability of such model prediction. Input dataset (image + audio) at 17% O_2 and 20% O_2 were introduced. The results for two of them are displayed in Fig. F.4. The model classified the 17% O_2 data as 18% O_2 with probability of ~100% each time. As a convolution neural network is supposed to recognize features from the training data such as shapes and luminosity, etc., the tested case in Fig F.4. what was expected to be predicted between 16% O_2 and 18% O_2. Hence, it is understood that the model is not capable of predicting unknown cases while trained cases (know combustion regimes) were predicted well. This can be attributed to the specific hyperparameters, dataset sizes, choice of

activation, etc. In order to achieve good predictions such parameters need to be optimized. Successful development of image and audio signature can develop a

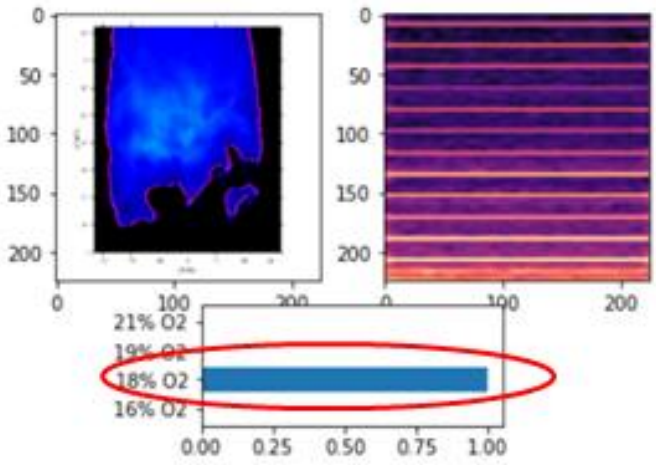

Fig. F.4. Prediction of 17%O_2 data.

Appendix G: Specification of Camera and Spectral Filters Used.

G.1. OS-9 camera (IDT)

High-speed imaging of flame has been extensively used during this research. The IDT OS-9 series camera was used for this purpose. The Specification of this camera is mentioned below.

Power requirement	18-36 V DC
Operating Temperature	-40 to + 50o C
Sensor	CMOS
Internal SSD	256 GB
Sensor Size	19.2 x 10.8 mm
Array Size	8 Megapixels
Pixel Size	7.5 x 7.5 µm
Aspect ratio	15:9

G.2. The chemiluminescence spectrum of flame

This section reports the radiation of important intermediate radicals from reaction zones which are of interest to the combustion community. Figure G.1. shows a typical chemiluminescence spectrum of lean flames under atmospheric conditions.

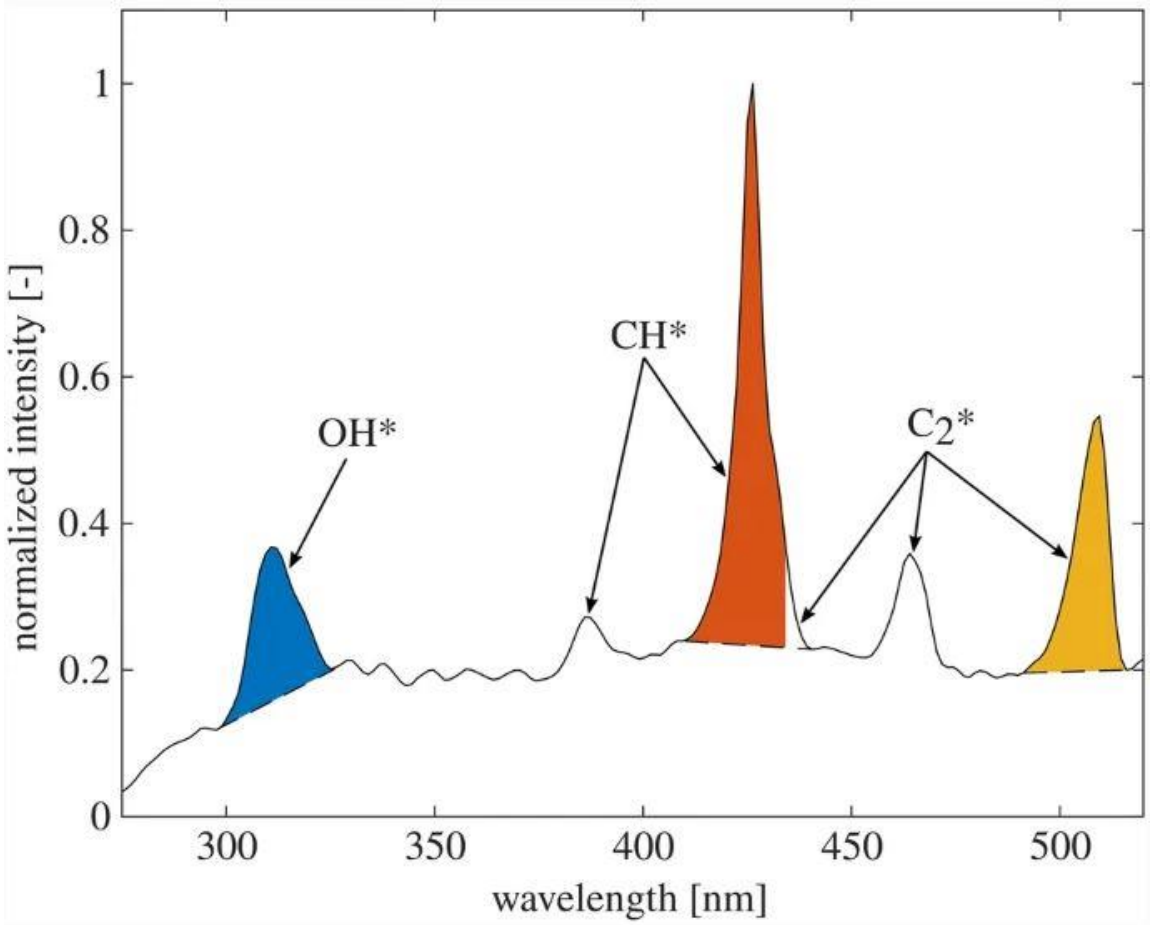

Fig. G.1. Chemiluminescence spectrum of lean flames under atmospheric conditions [151].

The peaks containing OH*, CH* and C2* radical emissions are superimposed on the broadband radiation. These areas are highlighted in Fig. 2. The intensity of the OH* radical is exhibited in blue, the intensity of the CH* radical in red and the intensity of the C2* radical in yellow. The OH* and CH* line-of-sight imaging was heavily performed during this research. Generally, a narrow band filter centered at 307 nm having FWHM (full width at half maximum) of ±10 nm is utilized for the OH* while bandpass filters centered at 430 ± 10 nm was used for CH*.

References

[1] K.K. Höinghaus, "Clean combustion: Chemistry and diagnostics," *Prog in Energy & Comb Sci*, vol. 65, pp. 1-5, 2017.

[2] C. Sourmehi, "EIA Projects Nearly 50% Increase in World Energy Use by 2050, Led by growth in renewables," *U.S. Energy Information Administration, International Energy Outlook*, 2021. https://www.eia.gov/todayinenergy/detail.php?id=49876#

[3] R. Lindsey, "Climate Change: Atmospheric Carbon Dioxide," *Climate.gov***,** 2022. https://www.climate.gov/news-features/understanding-climate/climate-change-atmospheric-carbon-dioxide

[4] R. Lindsey, Luann Dahlman, "Climate Change: Global Temperature**,"** *Climate.gov***,** 2022. https://www.climate.gov/news-features/understanding-climate/climate-change-global-temperature#:~:text=Earth%27s%20temperature%20has%20risen%20by,based%20on%20NOAA%27s%20temperature%20data.

[5] V. K. Arghode, "Development of Colorless Distributed Combustion for Gas Turbine Application," Ph.D. Thesis, University of Maryland, College Park, 2011.

[6] H. Tsuji, A.K. Gupta, T. Hasegawa, M. Katsuki, K. Kishimoto, M. Morita. "High temperature air combustion from energy conservation to pollution reduction,". 1st ed. Florida: *CRC Press*; 2003.

[7] A.E.E. Khalil, "Investigation of Colorless Distributed Combustion (CDC) with Swirl for Gas Turbine Application," Ph.D. Thesis, University of Maryland, College Park, 2013.

[8] A.H. Lefebvre, "Gas Turbine Combustion", *Taylor and Francis*, 1999.

[9] A.M. Steinberg, I. Boxx, M, Stöhr, W. Meier, "Effects of flow structure dynamics on thermoacoustic instabilities in swirl-stabilized combustion,". *AIAA J*, vol. 50, Issue# 4, pp. 952–967. https://doi.org/10.2514/1.J051466

[10] J.R. Dawson, V.M. Rodriguez-Martinez, N. Syred, T. O'Doherty, "The effect of combustion instability on the structure of recirculation zones in confined swirling flames,". *Combust Sci Tech*, vol. 177, Issue# 12, pp. 2349–2371, 2006.

[11] Y. Huang, S. Wang, V. Yang, "Systematic analysis of lean-premixed swirl-stabilized combustion,". *AIAA J*, vol. 44, Issue# 4, pp. 724–740, 2006.

[12] D. Fritsche, M. Füri, K. Boulouchos, "An experimental investigation of thermoacoustic instabilities in a premixed swirl-stabilized flame,". *Combust. Flame*, vol. 151, Issue# 1–2, pp. 29–36, 2007.

[13] R. Bompelly, "Lean blowout and its robust sensing in swirl combustors,". Ph.D. Thesis, Georgia Tech., 2013.

[14] Environmental Protection Agency, Standards of Perfromance for Stationary Combustion Turbines; Final Rule, vol. 71, Federal Regeister, 2006.

[15] S. Samuelsen, Conventional Type Combustion, The Gas Turbine Handbook, U.S. Department of Energy, Office of Fossil Energy, National Energy Technology Laboratory (NETL), Morgantown, WV, Report No. DOE/NETL-2006-1230, 2006.

[16] S. M. Correa, "A Review of NOx Formation Under Gas Turbine Combustion Conditions," Combustion Science and Technology, vol. 87, pp. 329-362, 1992

[17] C. P. Fenimore, "Formation of Nitric Oxide in Premixed Hydrocarbon Flames," Thirteenth Symposium (International) on Combustion, vol. 13, pp. 373-380, 1971.

[18] S.A. Mosier, R.M. Pierce, "Advanced Combustor Systems for Stationary Gas Turbine Engines, Phase I. Review and Preliminary Evaluation," vol. I, Contract 68-02-2136, FR-11405, Final Report, U.S. Environmental Protection Agency, 1980.

[19] S. Samuelsen, "3.2.1.3 Rich Burn, QuickMix, Lean Burn (RQL) Combustor," GTHandbook, pp. 227- 234.

[20] U.S. Department of Energy Office of Fossil Energy, NETL, Turbine Program, "Enabling Near-Zero Emission Coal-Based Power Generation," October 2005.

[21] K.M. Tacina, "Swirl-Venturi Lean Direct Injection Combustion Technology for Low-NOx Aero Gas Turbine Engines," 2018.

[22] K.M. Tacina, C. Chang, Z. J. He, P. Lee, H. C. Mongia, B. K. Dam, "A second generation swirl venturi lean direct injection combustion concept," in *50th AIAA/ASME/SAE/ASEE Joint Propulsion Conference*, 2014, p. 3434.

[23] K.M. Tacina, P. Lee, H. Mongia, B. K. Dam, Z. J. He, D. P. Podboy, "A Comparison of Three Second-Generation Swirl-Venturi Lean Direct Injection Combustor Concepts," in *52nd AIAA/SAE/ASEE Joint Propulsion Conference*.

[24] R. Tacina, C. Wey, P. Laing, and A. Mansour, "A low no (x) lean-direct injection, multipoint integrated module combuster concept for advanced aircraft gas turbines," 2002.

[25] D. J. Mavriplis, J. C. Vassberg, E. N. Tinoco, M. Mani, O. P. Brodersen, B. Eisfeld, R. A. Wahls, J. H. Morrison, T. Zickuhr, D. Levy, M. Murayama "Grid Quality and Resolution Issues from the Drag Prediction Workshop Series,", *Journal of Aircraft*, vol. 46, Issue# 3, p. 935-953, 2009.

[26] H. Mashhadimoslem, A. Ghaemi, A. Palacios, "Analysis of deep learning neural network combined with experiments to develop predictive models for a propane vertical jet fire," *Heliyon*, vol. 6, Issue# 11, p. e05511, 2020.

[27] Q. Li, W. Cai, X. Wang, Y. Zhou, D. D. Feng, M. Chen, “Medical Image Classification with Convolutional Neural Network,” *13th International Conference on Control Automation Robotics & Vision (ICARCV)*, Singapore, Dec. 12–14, pp. 844–848, 2014.

[28] V.K. Arghode, A.K. Gupta, K.M. Bryden, “High intensity colorless distributed combustion for ultra-low emissions and enhanced performance,” *Appl Energy*, vol. 92, pp. 822-830, 2012.

[29] A. K. Gupta, "Thermal Characteristics of Gaseous Fuel Flames using High Temperature Air," *Journal of Engineering for Gas Turbines and Power*, vol. 126, Issue# 1, pp. 9-19, 2004.

[30] A. K. Gupta, S. Bolz and T. Hasegawa, "Effect of Air Preheat and Oxygen Concentration on Flame Structure and Emission," *Journal of Energy Resources Technology*, vol. 121, pp. 209-216, 1999.

[31] J. A. Wunning and J.G. Wunning, "Flamless Oxidation to Reduce Thermal NO Formation," *Progress in Energy and Combustion Science*, vol. 23, pp. 81-94, 1997.

[32] A. F. Colorado, B. A. Herrera and A. A. Amell, "Performance of a Flameless Combustion Furnace using Biogas and Natural Gas," *Bioresources Technology*, vol. 101, pp. 2443-2449, 2010.

[33] R. Luckerath, W. Meier and M. Aigner, "FLOX Combustion at High Pressure with Different Fuel Compositions," *Journal of Engineering for Gas Turbines and Power*, vol. 130, Issue# 1, pp. 011505-1-7, 2008.

[34] O. Lammel, H. Schutz, G. Schmitz, R. Luckerath, M. Stohr, B. Noll, M. Aigner, M. Hase and W. Krebs, "FLOX Combustion at High Power Density and High Flame Temperature," Journal of Engineering for Gas Turbine and Power, vol. 132, p. 121503, 2010.

[35] A. Cavaliere and M. Joannon, "Mild Combustion," *Progress in Energy and Combustion Science*, vol. 30, pp. 329-366, 2004.

[36] I. B. Ozdemir and N. Peters, "Characteristics of the Reaction Zone in a Combustor Operating at Mild Combustion," *Experiments in Fluids*, vol. 30, pp. 683-695, 2001.

[37] R. Weber, J. P. Smart and W. vd Kamp, "On the (MILD) Combustion of Gaseous, Liquid, and Solid Fuels in High Temperature Preheated Air," *Proceedings of the Combustion Institute*, vol. 30, pp. 2623-2629, 2005.

[38] V.K. Arghode, A.K. Gupta, “Investigation of reverse flow distributed combustion for gas turbine application,” *Appl Energy*, vol. 88, Issue# 4, pp. 1096-1104, 2011.

[39] V.K. Arghode, A.K. Gupta, “Investigation of forward flow distributed combustion for gas turbine application,” *J Appl Energy*, vol. 88, Issue# 1, pp. 29-40, 2010.

[40] V.K. Arghode, A.K. Gupta, “Hydrogen addition effects on methane-air colorless distributed combustion flames,” *Int J Hydrogen Energy*, vol. 36, Issue# 10, pp. 6292-6302, 2011.

[41] S. Kumar, P. J. Paul and H. S. Mukunda, "Studies on a New High-Intensity Low-Emission Burner," *Proceedings of the Combustion Institute*, vol. 29, pp. 1131-1137, 2002.

[42] M. K. Bobba, P. Gopalakrishnan, K. Periagaram and J. M. Seitzman, "Flame Structure and Stabilization Mechanisms in a Stagnation-point Reverse-Flow Combustor," *Jounral of Engineering for Gas Turbine and Power*, vol. 130, Issue# 3, pp. 031505-1-8, 2008.

[43] P. Gopalakrishnan, M. K. Bobba and J. M. Seitzman, "Controlling Mechanisms for Low NOx Emissions in a Non-Premixed stagnation Point Reverse Flow Combustor," *Proceedings of the Combustion Institute*, vol. 31, pp. 3401-3408, 2007.

[44] K. Y. Hsu, L. P. Goss and W. M. Roquemore, "Characteristics of a Trapped Vortex Combustor," *Journal of Propulsion and Power*, vol. 14, pp. 57-65, 1998.

[45] D.L. Straub, K. H. Casleston, R. E. Lewis, T. G. Sidwell, D. J. Maloney and G. A. Richards, "Assesment of Rich-Burn, Quick-Mix, Lean Burn Trapped Vortex Combustor for Stationary Gas Turbines," *Journal of Engineering for Gas Turbines and Power*, vol. 127, pp. 36-41, 2005.

[46] R. A. Yetter, I. Glassman and H. C. Gabler, "Asymmetric Whirl Combustion: a New Low NOx Approach," *Proc. of the Combustion Instituite*, vol. 28, pp. 1265-1272, 2000.

[47] E.T. Vincent, "The Theory and Design of Gas Turbines and Jet Engines", *McGraw-Hill Book Co*., 1950.

[48] A. Cavaliere, M. de Joannon, "Mild Combustion", *Progress in Energy and Combustion Science*, vol. 30, pp. 329-366, 2004

[49] A. A.V. Perpignan, A. G. Rao, D. J.E.M. Roekaerts "Flameless combustion and its potential towards gas turbines," *Progress in Energy and Combustion Science*, vol. 69, pp. 28-62, 2018

[50] M.J. Evans, P.R. Medwell, H. Wu, A. Stagni, M. Ihme, "Classification and lift-off height prediction of non-premixed MILD and autoignitive flames," *Proceedings of the Combustion Institute*, vol. 36, Issue# 3, 2017, pp. 4297-4304.

[51] M. Oberlack, R. Arlitt, N. Peters, "On stochastic Damk€ohler number variations in a homogeneous flow reactor,". *Combust Theory Model*, vol. 4, pp. 495–509, 2000.

[52] J.A. Wunning, JG. Wunning, "Flameless Oxidation to Reduce Thermal NO-Formation", *Progress in Energy and Combustion Science*, Vol. 23, 1997, pp. 81-94.

[53] D. Lupant, B. Pesenti, P. Evrard, P. Lybaert, "Numerical and Experimental Characterization of a Self-Regenerative Flameless Oxidation Burner Operation in a Pilot-Scale Furnace", *Combustion Science and Technology*, Vol. 179, 2007, pp. 437-453.

[54] R. Weber, A. K. Gupta, S. Mochida, “High temperature air combustion (HiTAC): How it all started for applications in industrial furnaces and future prospects,” *Applied Energy*, vol. 278, p. 115551, 2020.

[55] A. S. Verrissimo, A. M. Rocha and M. Costa, "Operational Combustion and Emission Characteristics of a Small Scale Combustor," *Energy and Fuels*, vol. 25, pp. 2469-2480, 2011.

[56] S. Kumar, P. J. Paul and H. S. Mukunda, "Studies on a New High-Intensity Low-Emission Burner," *Proceedings of the Combustion Institute*, vol. 29, pp. 1131-1137, 2002.

[57] Vandervort, C. L., “9 ppm NO x /CO Combustion System for “F” Class Industrial Gas Turbines,” *Journal of Engineering for Gas Turbines and Power*, Vo. 123, pp. 317-321., 2001.

[58] M. J. Melo, J. M. Sousa, M. Costa and Y. Levy, "Experimental Investigation of a Novel Combustor Model for Gas Turbines," *Journal of Propulsion and Power*, vol. 25, pp. 609-617, 2009.

[59] X. Xing, B. Wang and Q. Lin, "Structure of Reaction Zone of Normal Temperature Air flamless Combustion in a 2 ton/h Coal-Fired Boiler Furnace," *Journal of Power and Energy*, vol. 221, pp. 473-480, 2007.

[60] “Dry Low NOx combustor upgrades,” https://www.ge.com/gas-power/services/gas-turbines/upgrades/dry-low-nox-dln-2-6-combustion-f-class

[61] “Japan claims world first: DLN gas turbine combustors verified on 100% hydrogen,”, Modern Power Systems, 2020. https://www.modernpowersystems.com/features/featurejapan-claims-world-first-dln-gas-turbine-combustors-verified-on-100-hydrogen-8185077/

[62] Environmental Protection Agency, "Alternative Control Techniques Document - NOx Emissions from Stationary Gas Turbines," North Carolina, 1993.

[63] W.R. Hawthorne, D.S. Weddell, H.C. Hottel HC, “Mixing and combustion in turbulent gas jets,” Third International Symposium on Combustion, *Flame and Explosion Phenomena*, pp. 266-288, Baltimore, USA, 1949.

[64] A.E.E. Khalil, A.K. Gupta, “Acoustic and heat release signatures for swirl assisted distributed combustion,” *Appl Energy*, vol. 193, pp. 125-138, 2017.

[65] A.E.E. Khalil, A.K. Gupta “Impact of internal entrainment on high intensity distributed combustion,” *Appl Energy*, vol. 156, pp. 241-250, 2015.

[66] A.E.E. Khalil, A.K. Gupta, “On the flame–flow interaction under distributed combustion conditions,” *Fuel*, vol. 182, pp. 17-26, 2016.

[67] A.E.E. Khalil, A.K. Gupta, "Flame fluctuations in Oxy-CO2-methane mixtures in swirl assisted distributed combustion,". *Appl Energy*, vol. 204, pp.303–317, 2017.

[68] A.E.E. Khalil, A.K. Gupta, "Acoustic and heat release signatures for swirl assisted distributed combustion," *Appl Energy*, vol. 193, pp.125–138, 2017.

[69] J.S. Feser, S. Karyeyen, A.K. Gupta. Flowfield impact on distributed combustion in a swirl assisted burner. *Fuel* 2020; 263: 116643.

[70] S. Karyeyen, J.S. Feser, A.K. Gupta, "Swirl assisted distributed combustion behavior using hydrogen-rich gaseous fuels," *Applied Energy*, vol. 251, p.113354, 2019.

[71] S. Karyeyen, J.S. Feser, A.K. Gupta, "Hydrogen concentration effects on swirl-stabilized oxy-colorless distributed combustion," *Fuel*, vol. 253, pp. 772-780, 2019.

[72] S. Karyeyen, J.S. Feser, E. Jahoda, A.K. Gupta, "Development of distributed combustion index from a swirl-assisted burner," *Applied Energy*, vol. 268, p. 114967, 2020.

[73] A.E.E. Khalil, A.K. Gupta, "Towards colorless distributed combustion regime," *Fuel*, vol. 195, pp. 113-122, 2017.

[74] A.E.E. Khalil, A.K. Gupta, "Hydroxyl radical distribution in distributed reaction combustion condition," *Fuel*, vol. 122, pp. 28-35, 2014.

[75] A.E.E. Khalil, A.K. Gupta, "Towards distributed combustion for ultra-low emission using swirling and non-swirling flowfields," *Applied Energy*, vol. 121, pp. 132-139, 2014.

[76] S. Karyeyen, J.S. Feser, E. Jahoda, A. K. Gupta, "Development of distributed combustion index from a swirl-assisted burner," Applied Energy, vol. 268, p.114967, 2020.

[77] S. Ethaib, R. Omar, M.K.S. Mazlina, A.B.D. Radiah, S. Syafiie, "Development of a hybrid PSO–ANN model for estimating glucose and xylose yields for microwave-assisted pretreatment and the enzymatic hydrolysis of lignocellulosic biomass," *Neural Comput Applic*, vol. 30, Issue# 4, pp. 1111-1121, 2018.

[78] S. Yao, B. Wang, A. Kronenburg, O.T. Stein, "Conditional scalar dissipation rate modeling for turbulent spray flames using artificial neural networks," *Proc Combust Inst*, vol. 38, Issue# 2, pp. 3371-3378, 2021.

[79] S. Joo, J. Yoon, J. Kim, M. Lee, Y. Yoon, "NOx emissions characteristics of the partially premixed combustion of H2/CO/CH4 syngas using artificial neural networks," *Appl Therm Eng*, vol. 80, pp. 436-444, 2015.

[80] S. Dey, N.M. Reang, P.K. Das, M. Deb, "Comparative study using RSM and ANN modelling for performance-emission prediction of CI engine fuelled with bio-diesohol blends: A fuzzy optimization approach," *Fuel*, vo. 292, p. 120356, 2021.

[81] X. Niu, C. Yang, H. Wang, Y. Wang, "Investigation of ANN and SVM based on limited samples for performance and emissions prediction of a CRDI-assisted marine diesel engine," *Appl Therm Eng*, vol. 111, pp. 1353-1364, 2017.

[82] R. Hernández, J. Ballester, "Flame imaging as a diagnostic tool for industrial combustion," *Combust Flame*, vol. 155, Issue# 3, pp. 509-528, 2008.

[83] G. Najafi, B. Ghobadian, T. Tavakoli, D.R. Buttsworth, T.F. Yusaf, M. Faizollahnejad, " Performance and exhaust emissions of a gasoline engine with ethanol blended gasoline fuels using artificial neural network," *Appl Energy*, vol. 86, Issue# 5, pp. 630-639, 2009

[84] Lamont WG, Roa M, Lucht RP. Application of artificial neural networks for the prediction of pollutant emissions and outlet temperature in a fuel-staged gas turbine combustion rig. *Proceedings of ASME Turbo Expo: Turbine Technical Conference and Exposition*, June 16-20, Paper: GT2014-25030, Düsseldorf, Germany.

[85] B.Z. Adewole, O.A. Abidakun, A.A. Asere, "Artificial neural network prediction of exhaust emissions and flame temperature in LPG (liquefied petroleum gas) fueled low swirl burner," *Energy*, vol. 61, pp. 606-611, 2013.

[86] L. Lourenco, S. Subramanian, Z. Ding, "Time series velocity field reconstruction from PIV data," Meas. Sci. Technol, vol. 8, p. 1533, 1997

[87] "Energy Information Administration, Alternatives to Traditional Transportation Fuels: An Overview," *U.S Department of Energy*, 1994.

[88] R.W. Schefer, D.M. Wicksall, A.K. Agrawal, "Combustion of hydrogen-enriched methane in a lean premixed swirl-stabilized burner," *Proceedings of the 29th symposium (international) on combustion*, vol. 29, Issue #1, pp. 843-51, 2002.

[89] A. Lantz, R. Collin, M. Aldén, A. Lindholm, J. Larfeldt, D. Lörstad, "Investigation of hydrogen enriched natural gas flames in a SGT-700/800 burner using OH PLIF and chemiluminescence imaging," *ASME J Eng Gas Turbines Power*, vol. 137, Issue #3, 2014.

[90] A.E.E. Khalil, A.K. Gupta, "Fuel property effect on distributed combustion," *Fuel*, vol. 171, pp. 116-124, 2016.

[91] J. Natarajan, T. Lieuwen, J. Seitzman, "Laminar flame speeds of H2/CO mixtures: effect of CO2 dilution, preheat temperature, and pressure," *Combust Flame*, vol. 151, Issue #1-2, pp. 104-19, 2007.

[92] M.D. Durbin, M.D. Vangsness, D.R. Ballal, V.R. Katta, "Study of flame stability in a step swirl combustor," *ASME J Eng Gas Turbines Power*, vol. 118, Issue #2, pp. 308-1, 1996.

[93] G.J. Rortveit, J.E. Hustad, S.C. Li, F.A. Williams, "Effects of diluents on NOx formation in hydrogen counterflow flames," *Combust Flame*, vol. 130, Issue #1-2, pp. 48-61, 2002.

[94] G.P. Smith, D.M Golden, M. Frenklach, N.W. Moriarty, B. Eiteneer, M. Goldenburg, et al. GRI 3.0 Mechanism, http://www.me.berkeley.edu/gri_mech/.

[95] M.E. Coltrin, D.S. Dandy, "Analysis of diamond growth in subatmospheric dc plasmagun reactor," *J Appl Phys,* vol. 74, Issue #9, p. 5803, 1998.

[96] R. Roy, A.K. Gupta, "Flame structure and emission signature in distributed combustion," *Fuel,* Vol. 262, p. 116460, 2020.

[97] J.P. Moeck, J.F. Bourgouin, D. Durox, T Schuller, "Tomographic reconstruction of heat release rate perturbations induced by helical modes in turbulent swirl fames," *Exp Fluids,* vol. 54, 1498, 2013.

[98] R. Rajasegar R, C.M. Mitsingas, E.K. Mayhew, J. Yoo, T. Lee, "Proper orthogonal decomposition for analysis of plasma-assisted premixed swirl-stabilized fame dynamics," *IEEE Trans Plasma Sci*, vol 44, Issue #12, pp. 2940–2951, 2016.

[99] N. Syred, V.I. Hanby, A.K. Gupta, "Resonant instabilities generated by swirl burners," *J Inst Fuel*, vol 1973, pp. 402-407, 1973.

[100] N. Syred, A.K. Gupta, J.M. Beér, "Temperature and density gradient changes arising with the processing vortex core and vortex breakdown in swirl burners," *Proc. 15th Symposium (Intl.) on Combustion,* The Combustion Institute, pp. 587–597, 1975.

[101] A.K. Gupta, D.G. Lilley, N. Syred, "Swirl Flows," *Abacus Press,* Gordon and Breach Publishers, Tunbridge Wells, 1984.

[102] S. Zhu, S. Acharya, "Flame dynamics with hydrogen addition at Lean Blowout Limits," *Proceedings of ASME Turbo Expo 2013: Turbine Technical Conference and Exposition*, Paper GT2013–95822. 2013.

[103] D. Durox, J.P. Moeck, J.F. Bourgouin, P. Morenton, M. Viallon, T. Schuller et al, "Flame dynamics of a variable swirl number system and instability control," *Combust Flame,* vol. 160, pp. 1729-1742, 2013.

[104] N. Syred, "A review of oscillation mechanisms and the role of the precessing vortex core (PVC) in swirl combustion systems," *Progress Energy Combust Sci*, vol. 32, Issue #2, pp. 93–161, 2006.

[105] D.M. Kang, F.E.C. Culick, A. Ratner, "Combustion dynamics of low-swirl combustor," *Combust Flame*, vol. 151, Issue# 3, pp. 412–425. 2007.

[106] R. Roy, A.K. Gupta, "Experimental investigation of flame fluctuation reduction in distributed combustion," *Experiments in Fluids*, vol. 62, p. 62, 2021.

[107] D.M. Wicksall, A.K. Agrawal, "Acoustics measurements in a lean premixed combustor operated on hydrogen/hydrocarbon fuel mixtures," *International Journal of Hydrogen Energy*, vol. 32, pp. 1103–1112, 2007.

[108] W. Zhang, J. Wang, R. Mao, W. Lin, B. Lin, Y. Wu, M. Zhang, Z. Huang, "Experimental study of compact swirl flames with lean premixed CH4/H2/air mixtures at stable and near blow-off conditions," *Experimental Thermal and Fluid Science*, vol. 122, p. 110294, 2021.

[109] P. Griebel, E. Boschek, P. Jansohn, "Lean Blowout Limits and NOx Emissions of Turbulent, Lean Premixed, Hydrogen-Enriched Methane/Air Flames at High Pressure," *ASME. J. Eng. Gas Turbines Power*, 129, Issue# 2, pp. 404–410, 2007.

[110] S. Marragou, H. Magnes, T. Poinsot, L. Selle, T. Schuller, "Stabilization regimes and pollutant emissions from a dual fuel CH4/H2 and dual swirl low NOx burner," *International Journal of Hydrogen Energy*, vol. 47, Issue# 44, pp. 19275-19288, 2022.

[111] T. Hussain, M. Talibi, R. Balachandran, "Investigating the effect of local addition of hydrogen to acoustically excited ethylene and methane flames," *International J. Hydrogen Energy, vol. 44*, Issue# 21, pp. 11168-11184, 2019.

[112] H.S. Kim, V.K. Arghode, A.K. Gupta, "Flame characteristics of hydrogen-enriched methane–air premixed swirling flames," *International J. Hydrogen Energy*, vol. 34, Issue# 2, pp. 1063-1073, 2009

[113] P. Kutne, B.K. Kapadia, W. Meier, M. Aigner, "Experimental analysis of the combustion behaviour of oxyfuel flames in a gas turbine model combustor," *Proc Combust Inst*, vol. 33, pp. 3383-3390, 2011.

[114] J.A. Miller, C.T. Bowman, "Mechanism and modeling of nitrogen chemistry in combustion," *Progress in Energy and Combustion Science*, vol. 15, Issue# 4, pp. 287-338, 1989.

[115] P. Li, F. Wang, J. Mi, B.B. Dally, Z. Mei, J. Zhang, A. Parente, "Mechanisms of NO formation in MILD combustion of CH4/H2 fuel blends," *International J. Hydrogen Energy*, vol. 39, Issue# 33, pp. 19187-19203, 2014.

[116] A.Palacios, D. Bradley, and L.Hu, "Lift-Off and Blow-Off of Methane and Propane Subsonic Vertical Jet Flames, With and Without Diluent Air," *Fuel*, vol. 183, Issue# 1, pp. 414–419, 2016.

[117] X. Yang, W. Yang, S. Dong, and H. Tan, "Flame Stability Analysis of Premixed Hydrogen/Air Mixtures in a Swirl Micro-combustor," *Energy*, vol. 209, Issue# 1, p. 118495, 2020.

[118] Z. Wang, B. Hu, A. Fang, Q. Zhao, and X. Chen, "Analyzing Lean Blow-Off Limits of Gas Turbine Combustors Based on Local and Global Damköhler Number of Reaction Zone," *Aerosp. Sci. Technol.*, vol. 111, Issue# 1, p. 106532, 2021

[119] Z. Wang, S.C Yelishala, G. Yu, H. Metghalchi, and Y.A. Levendis, "Effects of Carbon Dioxide on Laminar Burning Speed and Flame Instability of Methane/Air and Propane/Air Mixtures: A Literature Review," *Energy Fuels*, vol. 33, Issue# 10, pp. 9403–9418, 2019.

[120] N. Syred, A. K Gupta, and J.M Beér, "Temperature and Density Gradient Changes Arising With the Processing Vortex Core and Vortex Breakdown in Swirl Burners," *Proceedings of the*

15th Symposium (Intl.) on Combustion, Tokyo, Japan, Aug. 25–31, 1974, The Combustion Institute, pp. 587–597, 1975.

[121] N. Syred, V. I Hanby, and A. K Gupta, "Resonant Instabilities Generated by Swirl Burners," *J. Inst. Fuel*, vol. 46, Issue# 387, pp. 402–407, 1973.

[122] A. Mardani, B. A. Rekabdarkolaei, and H.R. Rastaaghi, "Experimental Investigation on the Effects of Swirlers Configurations and Air Inlet Partitioning in a Partially Premixed Double High Swirl Gas Turbine Model Combustor," *ASME J. Energy Resour. Technol*., vol. 143, Issue# 1, p. 012302, 2020.

[123] V.S Acharya, D.H. Shin, and T. Lieuwen, "Premixed Flames Excited by Helical Disturbances: Flame Wrinkling and Heat Release Oscillations," *J. Propul. Power*, vol. 29, Issue# 6, pp. 1282–1291, 2013.

[124] H. Yue, C. Guo-Biao, W. Hai-Xing, R. Bruno, B. Abdelkrim, "Flow Characterization and Dilution Effects of N2 and CO2 on Premixed CH4/Air Flames in a Swirl-Stabilized Combustor," *Chin. Phys*. B, vol. 23, Issue# 3, p. 034704

[125] A. De, S. Zhu, S. Acharya, "An Experimental and Computational Study of a Swirl-Stabilized Premixed Flame," *ASME. J. Eng. Gas Turbines Power*, vol. 132, Issue# 7, p. 071503, 2010.

[126] M. Stöhr, R. Sadanandan, W. Meier, "Phase-resolved characterization of vortex–flame interaction in a turbulent swirl flame," *Experiments in Fluids*, vol. 51, pp. 1153-1167, 2011

[127] Borghi R. On the structure and morphology of turbulent premixed flames. Recent Advances in the *Aerospace Sciences, Massachusetts: Springer*; 1985, p. 117-138. ISBN : 978-1-4684-4300-4

[128] Panda PP, Roa M, Slabaugh CD, Peltier S, Carter CD, Laster WR, Lucht RP. High-repetition-rate planar measurements in the wake of a reacting jet injected into a swirling vitiated crossflow. *Combustion and Flame,* vol. 163, p. 241-257, 2016.

[129] Slabaugh CD, Pratt AC, Lucht RP. Simultaneous 5 kHz OH-PLIF/PIV for the study of turbulent combustion at engine conditions. *Applied Physics* B, vol.118, p. 109-130, 2015.

[130] M. Mokhtarzad, F. Eskandari, N.J. Vanjani, A. Arabasadi, "Drought forecasting by ANN, ANFIS, and SVM and comparison of the models", *Environ Earth Sci*, vol. 76, p. 729, 2017.

[131] M. Kayri, "Predictive abilities of bayesian regularization and Levenberg–Marquardt algorithms in artificial neural networks: a comparative empirical study on social data", *Math Comput Appl*, vol. 21, Issue# 2, p. 20, 2016.

[132] C. Bishop, "Neural networks for pattern recognition", *Oxford University Press*, Oxford (1995).

[133] J. Jordan, "Setting the Learning Rate of Your Neural Network", *Data Science*, 2018.

[134] Yu CC, Liu BD, "A backpropagation algorithm with adaptive learning rate and momentum coefficient", *Proceedings of the 2002 International Joint Conference on Neural Networks*, IJCNN'02; vol. 2, pp. 1218-1223, 2002.

[135] D.JC. MacKay, "Bayesian interpolation", *Neural Comput*, 4, Issue# 3, pp. 415-447, 1992,

[136] H.Demuth, M. Beale, "Neural Network Toolbox User's Guide", the *MathWorks* 2000, Version 4.

[137] A. G. Howard, M. Zhu, B. Chen, D. Kalenichenko, W. Wang, T. Weyand, M. Andreetto, and H. Adam, "MobileNets: Efficient Convolutional Neural Networks for Mobile Vision Applications," *arXiv:1704.04861 2017— arxiv.org*.

[138] J.S Pan, and Q. Yang, "A Survey on Transfer Learning," IEEE Trans. *Knowl. Data Eng*., vol. 22, Issue# 10, pp. 1345–1359, 2009.

[139] K. Balasubramaniam, "Have You Taught Your Machine Yet?" *Towards Data Science*, 2019,

[140] U.O Rehman, "Multi Task Convolutional Learning for Flame Characterization," Master's thesis, *Linköping University*, Linkoping, Sweden, 2020.

[141] F. Culfaz, "Transfer Learning Using Mobilenet and Keras," *Towards Data Science*, 2018.

[142] S. Dabetwar, S. Ekwaro-Osire, J. P. Dias, "Damage Classification of Composites Using Machine Learning," Proceedings of the ASME 2019 *International Mechanical Engineering Congress and Exposition*, vol. 13: Safety Engineering, Risk, and Reliability Analysis, ASME, Salt Lake City, UT, Nov. 11–14, p. V013T13A017, 2019.

[143] J. Feser, A.K Gupta, "Performance and Emissions of Drop-In Aviation Biofuels in a Lab Scale Gas Turbine Combustor," *ASME J. Energy Resour. Technol.*, vol. 143, Issue# 4, p. 042103, 2021.

[144] R. Roy, A.K Gupta, "Measurement of Lean Blowoff Limits in Swirl-Stabilized Distributed Combustion With Varying Heat Release Intensities," *ASME J. Energy Resour. Technol.*, vol. 144, Issue# 4, p. 082301, 2022.

[145] M. Sweeney, S. Hochgreb, "Autonomous extraction of optimal flame fronts in OH planar laser-induced fluorescence images." *Applied optics*, vol. 48, Issue# 19, pp. 3866-3877, 2009.

[146] O. Nobuyuki, "A Threshold Selection Method From Gray-Level Histograms In IEEE Transactions On Systems, Man, And Cybernetics, Vol. IEEE," *Transactions on Systems, Man, and Cybernetics*, vol. 9, Issue# 1, pp. 62-66, 1979

[147] R. Roy, “Experimental investigation of the dynamics and blowoff characteristics of bluff-body stabilized 2D, V-shaped turbulent premixed flames with different gaseous hydrocarbon fuels.” *Master's Theses*. Article# 1318, 2018.

[148] H. Malm, G. Sparr, J. Hult, C.F. Kaminski, “Nonlinear diffusion filtering of images obtained by planar laser-induced fluorescence spectroscopy.” *Josa a*, vol. 17, Issue# 12, pp. 2148-2156, 2000.

[149] P. Perona, J. Malik, “Scale-space and edge detection using anisotropic diffusion.” *IEEE Transactions on pattern analysis and machine intelligence*, vol. 12, Issue# 7, pp. 629-639, 1990

[150] X. Liu, M. Tanaka, M. Okutomi, “Single-image noise level estimation for blind denoising.” *IEEE transactions on image processing*, vol. 22, Issue# 12, 5226-5237, 2013

[151] M. Vogel, M. Bachfischer, J. Kaufmann, T. Sattelmayer, “Experimental investigation of equivalence ratio fluctuations in a lean premixed kerosene combustor,” *Exp Fluids*, vol. 62, p. 93, 2021.